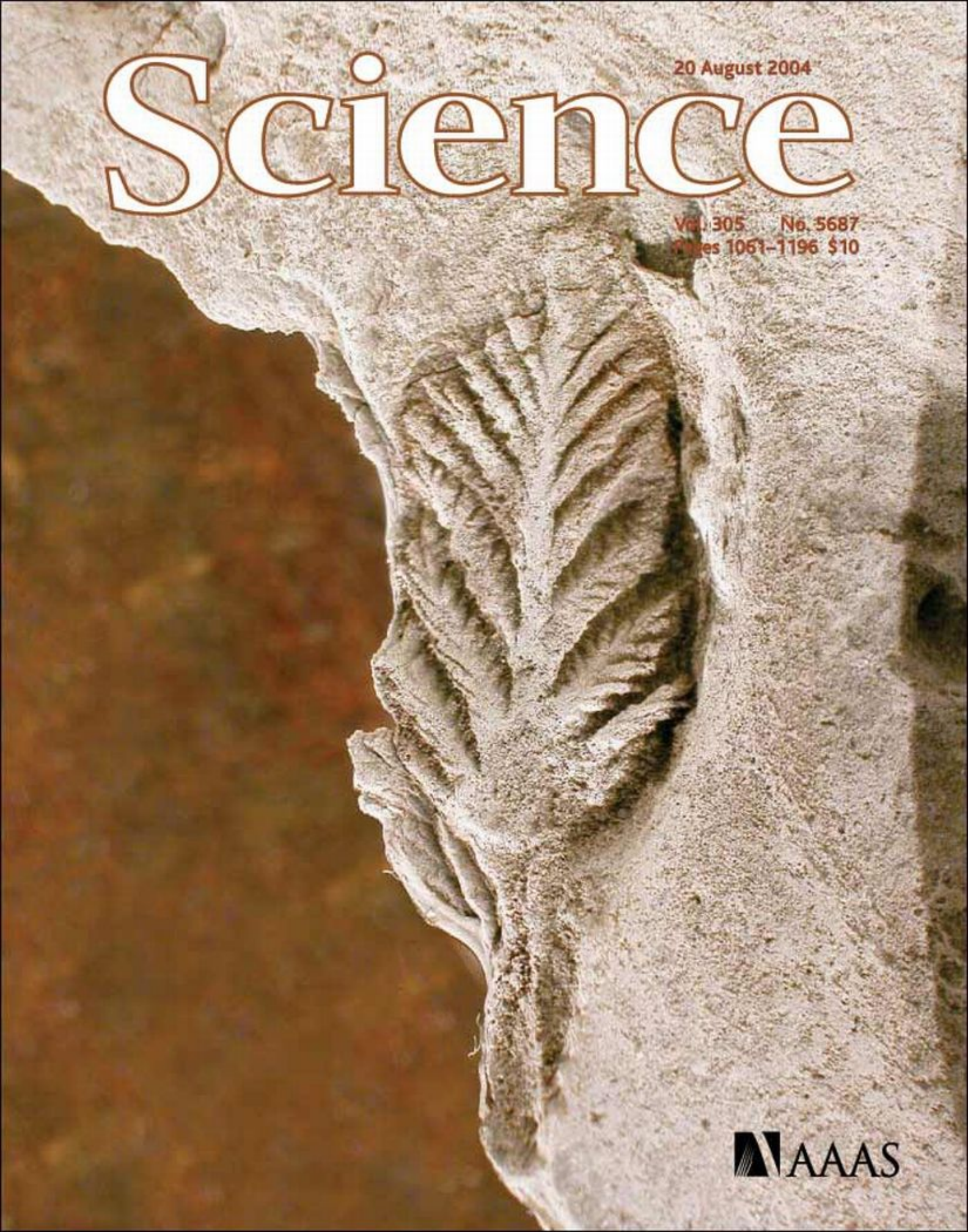
Science
20 August 2004
Vol. 305 No. 5687
Pages 1061–1196 $10
AAAS

Science

COVER This exquisitely preserved fossil from Spaniard's Bay, Newfoundland, is an example of the oldest known complex life forms on Earth. Frondlets 1 to 5 cm long with fractal-like branching (left) were combined as modules to form decimeter-to meter-scale frondose, plumose, and bush-shaped organisms that dominated marine ecosystems 575 to 560 million years ago. See page 1141. [Photo: G. Narbonne]

Volume 305
20 August 2004
Number 5687

DEPARTMENTS

NEWS OF THE WEEK

NEWS FOCUS

1094

1112 & 1144

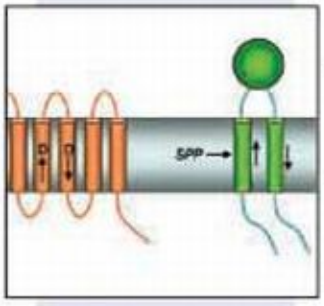

1119

LETTERS

BOOKS *ET AL.*

POLICY FORUM

PERSPECTIVES

REVIEW

Contents continued

Science

SCIENCE EXPRESS www.sciencexpress.org

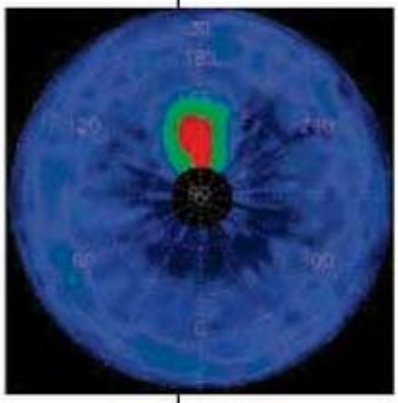

TECHNICAL COMMENT ABSTRACTS

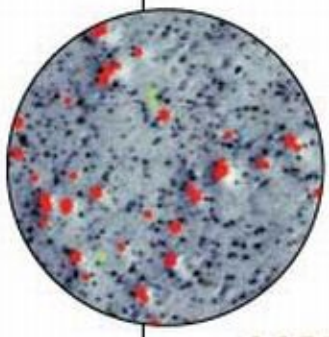

1133

BREVIA

REPORTS

Contents continued

REPORTS CONTINUED

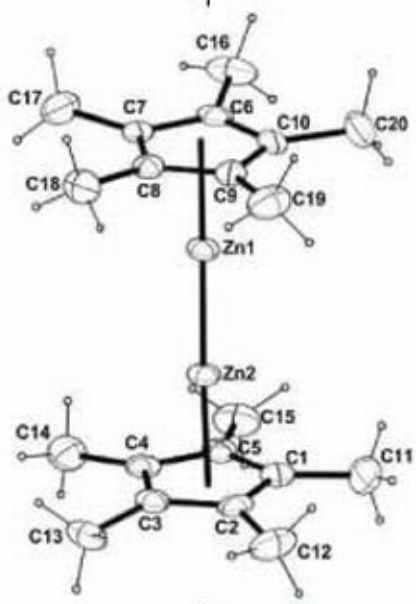

1117 & 1136

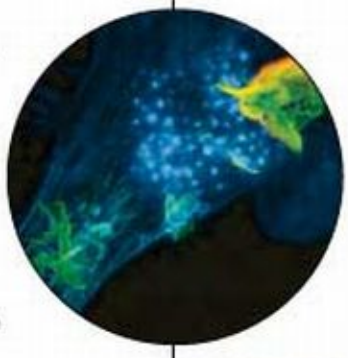

1150 & 1153

AAAS
ADVANCING SCIENCE, SERVING SOCIETY

SCIENCE (ISSN 0036-8075) is published weekly on Friday, except the last week in December, by the American Association for the Advancement of Science, 1200 New York Avenue, NW, Washington, DC 20005. Periodicals Mail postage (publication No. 484660) paid at Washington, DC, and additional mailing offices. Copyright © 2004 by the American Association for the Advancement of Science. The title SCIENCE is a registered trademark of the AAAS. Domestic individual membership and subscription (51 issues): $130 ($74 allocated to subscription). Domestic institutional subscription (51 issues): $500. Foreign postage extra: Mexico, Caribbean (surface mail) $55; other countries (air assist delivery) $85. First class, airmail, student, and emeritus rates on request. Canadian rates with GST available upon request, GST #125488122. Publications Mail Agreement Number 1069624. Printed in the U.S.A.

Change of address: allow 4 weeks, giving old and new addresses and 8-digit account number. Postmaster: Send change of address to Science, P.O. Box 1811, Danbury, CT 06813–1811. Single copy sales: $10.00 per issue prepaid includes surface postage; bulk rates on request. Authorization to photocopy material for internal or personal use under circumstances not falling within the fair use provisions of the Copyright Act is granted by AAAS to libraries and other users registered with the Copyright Clearance Center (CCC) Transactional Reporting Service, provided that $13.00 per article is paid directly to CCC, 222 Rosewood Drive, Danvers, MA 01923. The identification code for Science is 0036-8075/03 $13.00. Science is indexed in the *Reader's Guide to Periodical Literature* and in several specialized indexes.

Contents continued

Science
www.scienceonline.org

sciencenow www.sciencenow.org Daily News Coverage

New Doping Test Joins Olympics
Officials in Athens will check athletes for illicit human growth hormone.

Handwriting Analysis Goes 3D
Researchers use holograms to separate fact from forgery.

Evolving Ears as Whales Got Wet
Fossils show how ears adapted when the mammals left land behind.

Iris Mack is not your typical mathematician.

science's next wave www.nextwave.org Career Resources for Young Scientists

MiSciNet: Exceptional, Chic, Successful *C. Parks*
Iris Mack breaks common stereotypes about math and mathematicians.

Global/UK: Pushing the Boundaries of Elite Sport *T. Rooks*
Tegwen Rooks has witnessed the growth of sports science as a full-time athlete, rowing coach, and sports scientist.

Global/Canada: Funding Face-Off *A. Fazekas*
A McGill University professor offers young researchers advice on what it takes to start and stay in the corporate funding game.

US: Tooling Up—First Impressions *D. Jensen*
Potential employers often rely on first impressions, but there are a few things within your control.

US: The Other Side of the Table *R. Sonty*
The senior director of Worldwide Development at Pfizer Global Pharmaceuticals offers interviewing tips.

UK: Science as a Second Career Choice *P. Dee*
Phil Dee left the world of finance for a job in academia.

science's sage ke www.sageke.org Science of Aging Knowledge Environment

Genetically Altered Mice: Rtel$^{-/-}$ Mice *M. Russell*
The *Rtel* gene encodes a helicase-like protein that functions in the regulation of telomere length.

News Focus: Membranes of Death *M. Leslie*
Molecule prevents suicide triggered by cell's protein factories.

News Focus: Hardy Helper *R. J. Davenport*
Molecular partner urges worm protein to trigger survival pathway.

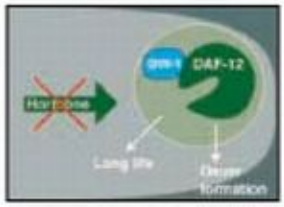

Teaming up to foster survival.

***Arabidopsis thaliana*, a model for plant signaling.**

science's stke www.stke.org Signal Transduction Knowledge Environment

Connections Map: *Arabidopsis* Ethylene Signaling Pathway *A. N. Stepanova and J. M. Alonso*
A MAPK cascade may mediate ethylene signals in *Arabidopsis*.

Connections Map: *Arabidopsis* Jasmonate Signaling Pathway *R. Liechti, A. Gfeller, E. E. Farmer*
Genetic analysis reveals links to the ethylene pathway.

Separate individual or institutional subscriptions to these products may be required for full-text access.

Academic Health I

Many of the readers of *Science* work in academic institutions, and it's likely that most of the others received their scientific training there. Universities also house a large fraction of basic research in the natural sciences. In the United States, recently published media critiques of the "competitiveness" of U.S. science have enhanced national concern about the health of research in the higher education sector. From time to time, therefore, we ought to stick a thermometer into the patient and see how our alma mater is faring. Herewith a handful of diagnoses of several indicators, some of which may be important for other nations as well.

In the 1980s, university administrators usually first examined the state of federal research funding. That habit is hard to break, so I turn first to next year's budget. The House of Representatives did well by the National Institutes of Health (NIH), matching the administration's request with an increase of 2.6%, although that's a painful comedown from the 15% annual increases of the past few years. The House's first look at the National Science Foundation's (NSF) budget was less salutory, however, proposing a drop of 2%. In the palmy days of big NIH increases, some bioenthusiasts were annoyed when I called editorial attention to the unbalanced nature of the science portfolio. That problem is more serious now, and that's unfortunate in view of the growing dependence of modern biology on the sister disciplines that are supported mainly by NSF.

The visa problem has only become more tangled. Fewer foreign students are applying for graduate or postdoctoral positions in U.S. universities, and that disruption of international exchange hurts science around the world. In a move that surprised many, Senator Norm Coleman (R-MN) introduced a bill (S.2715, "The International Student and Scholar Access Act of 2004") that could ease the situation by establishing a new science visa category, giving consular officers more training and more latitude to grant waivers, and reducing certain fees and requirements for students entering to complete a course of study. That's a promising beginning, and we hope it will receive serious consideration. Part of the problem, though, lies in organization and management in the Immigration and Naturalization Service and in the quality of interagency coordination, and the new law may not cure that.

A third issue has a long and troubled history. During the early 1980s, the Department of Defense (DOD) and the Department of Commerce attempted to apply various export control regulations, which were designed to prevent the distribution of military equipment and specifications to other countries, to basic research data and even to the movement of scientists. Negotiations between universities and DOD resolved some of the problems, and a National Academy of Sciences committee recommended that except for the "gray area" of dual-use technology, regulatory controls should not be used as a proxy for classification. President Reagan affirmed that in an Executive Order signed in 1985, National Security Decision Directive (NSDD) 189. That directive established classification as the only appropriate method of control over fundamental research.

Well, they're at it again, even though National Security Advisor Condoleezza Rice reaffirmed NSDD 189 in November of 2001. The Association of American Universities and the Council on Governmental Relations created a task force to collect information about troublesome provisions in research awards that appeared to violate the terms of NSDD 189. These included restrictions on publication and on distribution to foreign nationals. Especially disturbing was a common requirement that "if the Contractor will have access to or generate unclassified information that may be sensitive or inappropriate," the contract language must prohibit the contractor from releasing any of that unclassified information to anyone outside the organization. This clause was reported by 47 institutions; surprisingly, it was accepted without negotiation in 18 cases. Other institutions either negotiated acceptable language or rejected the award. Restraints on publication were found in 71 other cases in a total sample of 138 instances.

These indicators are not encouraging about the present state of the university/government relationship. Other important aspects of that partnership, as it was called in the old days, include restrictions on types of research that may be conducted, the upcoming reauthorization of the Higher Education Act, and the especially trying times imposed on state institutions by budget limitations. We'll have to save those for Part II, so stay tuned.

Donald Kennedy
Editor-in-Chief

Published by AAAS

This Week

PAGE 1090
Empty nests

1093
Counted out

HUMAN SUBJECTS RESEARCH

Pediatric Study of ADHD Drug Draws High-Level Public Review

A trial that would give healthy children an amphetamine is prompting heated debate among pediatricians and bioethicists. A divided review board at the National Institutes of Health (NIH), which is sponsoring the study, has sent the proposal outside the agency for additional scrutiny. Early next month, a newly formed Food and Drug Administration (FDA) advisory panel will meet in an unprecedented public session to discuss the proposal's safety and ethics—the first such review of a trial that involves giving a drug to healthy children.

The NIH study is designed to answer a long-standing question: Does a type of medication prescribed for hyperactivity affect the brains of children with attention deficit hyperactivity disorder (ADHD) differently than it does the brains of children without the condition? The scientist asking this question is Judith Rapoport, chief of child psychiatry at NIH's National Institute of Mental Health. Her project "could tell us a lot about what's dysfunctional in ADHD," says F. Xavier Castellanos, director of research at the New York University Child Study Center in New York City.

Still, "I can see why people are struggling" with the study, says Douglas Diekema, a pediatrician and bioethicist at Children's Hospital Regional Medical Center in Seattle, Washington, and chair of the institutional review board (IRB) that oversees clinical research at the hospital. On the one hand, he says, dextroamphetamine has been used for decades for ADHD and is generally considered safe. On the other, "you're actually giving [children] a psychoactive drug."

Rapoport and her colleagues aim to enroll 76 children, ages 9 to 18, including 24 sets of twins, only one of whom in each pair has the disorder. Subjects will receive a dose of dextroamphetamine and undergo functional magnetic resonance imaging scans. Participants will receive up to $570.

This isn't the first time Rapoport has tried to understand how stimulants calm down children with ADHD. In 1980, she and her colleagues ran a trial at NIH that gave children with ADHD and normal children a dose of dextroamphetamine and examined their responses to cognitive and psychological tests. She found that the drugs had virtually identical effects on all subjects, such as enhancing concentration.

Rapoport's findings prompted others to investigate. Chandan Vaidya and John Gabrieli of Stanford University added a layer of complexity in a 1998 study that gave a dose of Ritalin (an amphetamine-like drug) to 10 boys with ADHD and six controls. Brain scans showed differences in the drug's effects: In one area of the brain, the striatum, Ritalin boosted activity in ADHD children but suppressed it in healthy ones. That study sailed through the local review board without any problem, says Vaidya, now at Georgetown University in Washington, D.C.

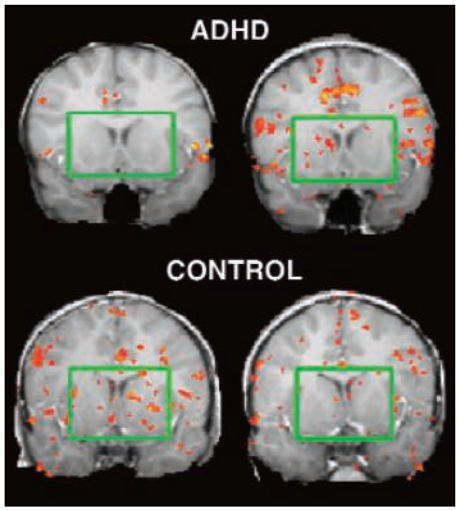

Lighting up disparities. A controversial NIH study hopes to replicate much of this 1998 experiment, in which healthy and ADHD children received brain scans both while on Ritalin (right column) and off it (left column).

However, the ▶

BIOSAFETY

Citizens Sue to Block Montana Biodefense Lab

Montanans have gone to federal court in Missoula to block construction of a National Institutes of Health (NIH) biodefense laboratory in the city of Hamilton. The 12 August lawsuit, filed by the Coalition for a Safe Lab and two other groups, says NIH needs to improve safety plans before the lab is built.

The new 600-square-meter facility, to be added to the National Institute of Allergy and Infectious Diseases' Rocky Mountain Laboratories, will be a biosafety level 4 (BSL-4), which means it could be used to study the deadliest pathogens, such as the Ebola virus (*Science*, 7 February 2003, p. 814). Officials have spent the past 2 years working with local groups on plans and drafting an environmental impact statement (EIS). NIH approved the project in June.

But opponents say the analysis lacks key elements, such as a plan for handling accidental releases. "The community would feel a whole lot better if there was a safety plan in place," says coalition leader Mary Wulff. The groups also say that NIH didn't release key documents that would help them evaluate the EIS or discuss alternate locations and has not considered the possibility that the lab might study weapons-grade pathogens.

Marshall Bloom, associate director of Rocky Mountain Labs, dismisses the concerns. The labs already have an emergency plan for the existing research space, he says, and can't fill in details for the new facility until it is built: "We don't even know the room numbers yet." The suit asks the judge to require NIH to redo the EIS and halt groundbreaking, scheduled for September. —JOCELYN KAISER

Safety suit. Montana activists worry that proposed BSL-4 lab won't be safe enough.

CREDITS: (TOP TO BOTTOM) C. J. VAIDYA *ET AL.*, *PNAS* **95**, 14494 (1998); CUHZA/SMITH CARTER

Published by AAAS

1094 When data aren't enough

1099 A deadly ocean current

1100 What makes a species invasive?

world of human-subject research has changed since then. In 2000, the Department of Health and Human Services created the Office for Human Research Protections (OHRP) and shut down noncompliant studies at several prominent universities. The local IRBs that approve clinical projects became more cautious. Nearly two dozen flooded OHRP with inquiries about pediatric trials that the review boards worried exceeded "minimal risk" for children—an issue unique to pediatric studies. Before 2000, only two pediatric studies had received additional scrutiny from OHRP, according to Lainie Friedman Ross, a pediatrician and bioethicist at the University of Chicago. Since then, the office has ruled on six, approving three of them with modifications.

The NIH board reviewing Rapoport's study arrived at a split verdict late last year. Ironically, many of the board's ethicists supported it, deeming one dose of the drug safe and nonaddictive; others familiar with dextroamphetamine compare this dose to a cup of coffee. "Research can't be risk-free," says Ezekiel Emanuel, who heads the clinical bioethics division at NIH but isn't a member of the IRB that weighed this trial. Although declining to comment on the case, Emanuel notes that "IRBs confronted with unfamiliar things just think they're more risky than they are."

In three meetings between last October and January, the NIH review board narrowly decided that the study exceeded minimal risk for healthy children and, therefore, required OHRP's blessing. Several members were concerned that the proposed financial compensation might affect parental judgment. In addition, "one member felt giving a child a controlled substance (in the absence of a medical indication) could not be justified," according to minutes from the IRB's November meeting. Indeed, many ethicists say privately that the use of an amphetamine—a drug that can be abused—raises more eyebrows than would a study involving a different, even riskier, medication, such as an antibiotic. Others say the study exceeds minimal risk simply because it calls for giving a prescription drug to healthy children.

FDA is involved because prescription drugs fall under its purview. Now that the public has been invited in, it may stay. Julie Kaneshiro of OHRP's Division of Policy and Assurances says that the agency, after coming under pressure from outsiders, has decided to make public all future pediatric trial reviews. **–JENNIFER COUZIN**

RESEARCH POLICY

Economist to Guide $22 Billion E.U. Science Programs

BERLIN—A Slovenian economist has been tapped to be Europe's next commissioner for science and research. Janez Potočnik, lead negotiator for Slovenia's entry into the European Union, is slated to take the reins of E.U. science policy, including the 5-year, $22 billion Framework 6 program that funds trans-European research.

The appointment surprised many E.U. watchers, because the 46-year-old Potočnik has no background in the natural sciences. (Outgoing commissioner Philippe Busquin studied physics before entering Belgian politics.) However, Potočnik's political savvy and negotiating experience should be an advantage for European science, says Robert Blinc, a physicist at the Jožef Stefan Institute in Ljubljana: "He will certainly do more than … a Nobel Prize winner in this position. He can sell science."

E.U. commissioners are chosen more for their political experience than their field of expertise. Each of the 25 E.U. member countries appoints a commissioner to serve in the E.U.'s executive branch for 5-year terms, and the commission president then divvies up responsibilities for specific policy areas. On 12 August, the incoming commission president, José Manuel Barroso of Portugal, announced the portfolio he had assigned each of the newly nominated commission members. Once approved by the parliament, the new commission will take office on 1 November.

Potočnik is saying little to the press before the European Parliament's confirmation hearings, expected next month. But many E.U. scientists hope that he will back a European Research Council (ERC), a program to fund basic research proposals from individual scientists—a shift from the past emphasis on funding large multinational collaborations. A commission proposal in June (*Science*, 25 June, p. 1885) called for doubling the E.U. research budget to an annual average of $12 billion over the period from 2007 to 2013 and using part of the increase to start an ERC.

Busquin, who in recent months has become a strong supporter of the idea, will leave some of the key negotiations with government ministers this fall to a temporary successor, incoming Belgian commissioner Louis Michel. Busquin was elected to the European Parliament this summer and will resign on 10 September to join the Parliament session that begins on 13 September.

Educated at the University of Ljubljana, Potočnik has been Slovenia's minister for European affairs since 2002. From 1993 to 2001, he was director of the Institute of Macroeconomic Analysis and Development in Ljubljana. In 1998, he was appointed head of the team negotiating Slovenia's treaty to join the E.U. That experience should help him work the Brussels bureaucracy, say observers. "He knows the E.U. inside and out," says economist Vladimir Gligorov of the Vienna Institute for International Economic Studies. He earned high marks, Gligorov says, for leading "what was largely thought to be the best negotiating team of all the new countries."

Brussels-bound. Slovenian Janez Potočnik has been appointed the new E.U. commissioner for science and research.

In light of that success, Potočnik is extremely well liked at home, Blinc says. "He has one of the highest approval rates of the former members of government," according to Blinc. "If he became prime minister, we would be happy." European scientists hope that his popularity will pay dividends for basic research. **–GRETCHEN VOGEL**

CREDIT: EUROPEAN COMMUNITY, 2004

Published by AAAS

ECOLOGY

Reproductive Failure Threatens Bird Colonies on North Sea Coast

CAMBRIDGE, U.K.—Warden Deryk Shaw can't believe what he's not hearing as he patrols the cliffs of Fair Isle. The usual cacophony of 250,000 sea birds has been replaced by an eerie silence. That's because the kittiwakes, arctic terns, guillemots, razorbills, arctic skuas, and great skuas that usually breed on this southernmost Shetland Isle have failed to do their job this season. "It's the worst year ever here, by a long way," says Shaw.

As the sea-bird breeding season draws to a close on Britain's North Sea coast, scientists report that many colonies are failing to rear any young. The situation is "unprecedented in terms of its scale and the range of species it's affecting," says ornithologist Eric Meek of the Royal Society for the Protection of Birds (RSPB) on the Orkney Islands. Many fear that rising sea temperatures and changing currents may be affecting the birds' food supplies, depressing reproduction.

Hard hit. Surface-feeding kittiwakes have experienced a 30% decline in North Sea colonies since 1988.

Although data on food supplies haven't yet been collated, anecdotal evidence suggests that the problem stems from a shortage of a key food source: sand eels, a small bottom-dwelling fish. Sea birds and humans alike appear to be having trouble finding them. The Danish fishing fleet, which catches 90% of the North Sea sand eel quota, caught only 36% of its 826,000-ton quota last year and has "undershot its quota quite substantially this year," says Euan Dunn, head of marine policy at the RSPB. Sea-bird biologist Martin Heubeck of Aberdeen University adds, "Anything that's dependent on sand eels last year and this year is pretty well knackered."

The northern Shetland and Orkney sea-bird colonies, which are the most dependent on sand eels, are the worst affected; everywhere, surface feeders such as terns and kittiwakes have been hardest hit. More robust species such as common guillemots can dive deeper in pursuit of fish and were able to cope when sand eel stocks crashed in the late 1980s, says sea-bird biologist Robert Furness of the University of Glasgow, U.K. "Guillemots are not a species that normally shows year-to-year variation in breeding success," explains sea-bird biologist Sarah Wanless of the Centre for Ecology and Hydrology (CEH) in Banchory, U.K. That they are now also succumbing is "causing everyone consternation," she says.

Experts say that the most likely causes for the decline in sand eels are past overfishing and rising sea temperatures. Previous research has linked rising temperatures to declines in the number of sand eels surviving to catchable size and to changes in their zooplankton prey. Sea temperatures have risen by about 1°C in the North Sea over the last 40-odd years, says marine ecologist Martin Edwards of the Sir Alistair Hardy Foundation for Ocean Sciences in Plymouth, U.K. And long-term plankton surveys indicate a "regime shift" in the North Sea in 1988, from a cold- to a warm-temperate ecosystem, explains Edwards. In particular, a cold-water species of copepod, a tiny crustacean that forms a key part of the North Sea food chain, has migrated 1000 km north, he says.

Recent modeling by CEH scientists indicates that rising sea temperatures and sand eel harvesting strongly affect kittiwakes, whose North Sea populations have declined by about 30% since 1988. "In terms of the North Sea, we're talking about a system that had almost the severest fishing pressure of any sea in the world," says Wanless. "Now it looks as if it's going to be subjected to severe pressure from climate change," too.

Furness, however, doubts that sea warming explains the pattern. He notes that the breeding crisis is worst in the northern North Sea, where sea temperatures are cooler. Instead, he suspects that adult herring, which have increased in numbers around Shetland, may be depleting the sand eel population. What's needed, he and others say, are studies linking oceanographic data with information on plankton, fisheries, and top marine predators such as sea birds.

Interdisciplinary research is just beginning. "We've got all the bits of the jigsaw" in long-term data sets, says Wanless, but people need to begin to "put all of them together fairly rapidly." The decline in kittiwake breeding populations, she fears, is "a sign that things have got into a serious state and may be very difficult to turn around." —FIONA PROFFITT

CONFLICTS OF INTEREST

Report Suggests NIH Weigh Consulting Ban

A new report from the federal Office of Government Ethics (OGE) hints that the National Institutes of Health (NIH) should consider a blanket ban on drug company consulting by intramural scientists. That suggestion runs counter to a proposal from NIH Director Elias Zerhouni that would concentrate on officials overseeing the extramural program and senior administrators.

The 26 July OGE report, addressed to Department of Health and Human Services (HHS) ethics official Edgar Swindell, found many lapses at NIH (*Science*, 13 August, p. 929). Of 155 outside activities that OGE reviewed, 39 were approved after the start date, and 35 apparently weren't approved at all. The problems, OGE acting director Marilyn Glynn concludes, highlight the "difficulties inherent in a case-by-case approval method."

In recommending that NIH craft supplemental regulations for its employees, the OGE report notes that "the most compelling argument that can be made for any absolute prohibition on consulting with drug companies is that some NIH officials actually are involved in making clinical decisions affecting the health and safety of patients." Even bench researchers studying drug products "could affect" the interests of companies, the report says.

Some observers warn against banning all consulting by intramural scientists. "That would just be unfair," says Paul Kincade, president of the Federation of American Societies for Experimental Biology. The report asks HHS to respond within 60 days.

Ironically, in 1995, then–NIH Director Harold Varmus eased up on consulting restrictions after the OGE said NIH's practices needed to be codified or made consistent with laxer government-wide rules. An OGE review since then found relatively minor problems with NIH's consulting policies, leading one biomedical research advocate to characterize the new report as an exercise in "CYA": covering your ass. —JOCELYN KAISER

CREDIT: MORTEN FREDERIKSEN, CENTRE FOR ECOLOGY AND HYDROLOGY

Published by AAAS

MEXICO

Government Uses Carrot, Stick to Retain Graduate Students

The Mexican government has cut back scholarships for graduate studies abroad while encouraging students to attend domestic programs. Officials say that the policy, which has been gathering steam over the past 5 years, is based not on the need to save money but on the ability of domestic institutions to offer graduate programs comparable to the best in the world. But critics say the move is depriving Mexican students of the best training in many fields and could hurt the country's scientific future.

Since 2000, Mexico's National Council of Science and Technology (CONACYT) has slashed by more than half the number of international scholarships it grants every year, from 1469 to 691 this year. The number of domestic scholarships has risen from 4806 in 2001 to an expected 8100 this year.

CONACYT officials argue that the quality of graduate-level scientific training has improved, making it less necessary for students to go overseas than was the case a generation ago. As evidence, Luis Gil, director of the CONACYT scholarship program, cites a jump in the number of "quality postgraduate programs," from 431 in 2000 to 654 in 2002 (the most recent year for which figures are available). The list is compiled by CONACYT based on the judgments of scientists using factors that include numbers of faculty publications and foreign collaborations. In addition, say CONACYT officials, a rise in graduate enrollments in science and engineering—from 43,700 in 2000 to 47,300 in 2002—shows that domestic programs have become more attractive to Mexican students.

René Drucker Colín, a physiologist and coordinator of scientific research at the National Autonomous University of Mexico, agrees. "Overseas graduate training is a necessary option only in a few fields, such as space science, where Mexico can't afford the infrastructure," he says. "Mexican universities can take care of everything else."

But although there is consensus between Mexico's scientific and academic communities that the country has made great strides in improving graduate education, many argue that not all fields are well represented. "We lack a critical mass of experts in many advanced disciplines such as genome sciences and nanotechnology," says biotechnologist Octavio Paredes-López, president of the Mexican Academy of Sciences. "It's good to attract more students into domestic programs, but we also need to send more students for training overseas."

The new policy is penny-wise and pound-foolish, says Mario Molina, the Nobel Prize–winning atmospheric chemist who was born and raised in Mexico. Molina says the real problem is making the country more attractive for young scientists, regardless of where they were trained. "It would be a very good investment for Mexico to continue sending good students overseas," says Molina, a professor at the Massachusetts Institute of Technology. "But it should be part of a larger strategy to build up scientific infrastructure so that these students can return to find satisfying career opportunities."

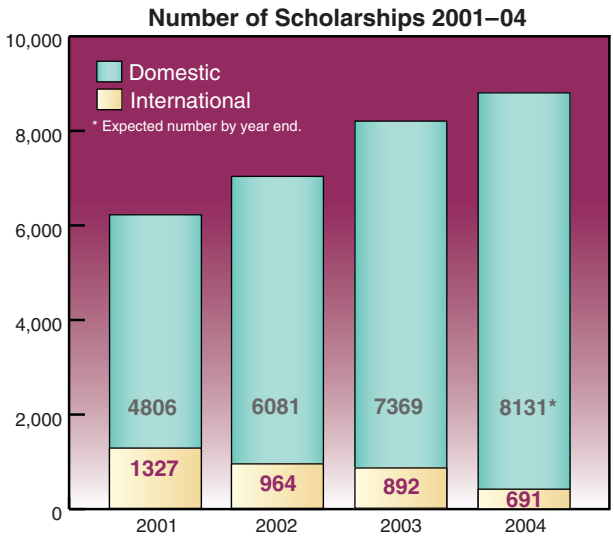

Homebound. Mexico has increased the total number of graduate scholarships while sending fewer students abroad.

SOURCE: CONACYT

That's the problem facing José Álvarez-Chávez, a CONACYT fellow who recently finished his Ph.D. in fiber optics at the University of Southampton in the U.K. "I've applied for an academic job in Mexico, but all the institutions I've talked to say they don't have any positions available because of budget cuts," he says. "And even if I did get a job at a university, I doubt that I'd have the resources to do experimental work." Instead, Álvarez-Chávez plans to pursue a research career in Europe or in the United States.

–YUDHIJIT BHATTACHARJEE

ScienceScope

German Panel Reportedly Supports Cloning Research

BERLIN—Support for human cloning experiments in Germany came from an unexpected corner this week. A slim majority of the German National Ethics Council may favor letting such experiments go forward in spite of the country's strict embryo protection laws, according to press reports.

The 25-member council, charged with advising Chancellor Gerhard Schröder on bioethics issues, was set to meet on 18 and 19 August in closed session. Before the meeting, members privately told reporters that the group is deeply divided on so-called research cloning—trying to create embryonic stem cells from cloned human embryos—but that a small majority seemed to favor allowing the practice.

That would put the panel at odds with leading German scientists, who have been more cautious. For instance, Ernst-Ludwig Winnacker, president of the DFG, the national research funding agency, has said that there is no pressing reason to allow therapeutic cloning in Germany. The chair of the ethics council, Spiros Simitis, has said that the German legislature should revisit the issue in light of Britain's recent decision to allow similar experiments (see p. 1102).

–GRETCHEN VOGEL

Royal Society Launches Ocean Acidification Study

LONDON—Call it the acid test. The U.K. Royal Society this week launched an investigation into how rising acidity may affect life in the world's oceans.

Recent studies conclude that Earth's oceans have absorbed almost half of the carbon dioxide (CO_2) produced by fossil fuel burning and cement production over the last 200 years (*Science*, 16 July, p. 367). The resulting chemical changes could produce a 0.4 drop in the pH of surface waters by the end of the century, scientists predict, possibly affecting corals and plankton that rely on calcium carbonate to form their skeletons. The increasing acidity could also reduce the ocean's future ability to absorb more CO_2.

Dundee University biologist John Raven, who will lead the study, says the oceans could be "doubly besieged" by rising temperatures and changing chemistry. The Royal Society is expected to publish its report early next year.

–FIONA PROFFITT

Published by AAAS

AIDS RESEARCH

Cambodian Leader Throws Novel Prevention Trial Into Limbo

The status of a planned AIDS prevention trial among Cambodian sex workers is unclear after the country's leader ordered it halted. The trial, backed by the U.S. National Institute of Allergy and Infectious Diseases (NIAID) and the Bill and Melinda Gates Foundation (*Science*, 19 September 2003, p. 1660), was scheduled to begin this fall.

The high-profile study, which would involve nearly 1000 sex workers in a novel use of the drug tenofovir, has been a target of community activists. On 12 August, Cambodian Ministry of Health officials notified U.S. and Australian collaborators that Prime Minister Hun Sen wanted the trial stopped. The researchers received scant information about the rationale for the decision. "It's really unclear," says co–principal investigator Kimberly Page-Shafer of the University of California, San Francisco (UCSF). "I'm shocked."

Prevention intervention. Oxfam's Rosanna Barbero led opposition to the study.

The unusual study asks whether tenofovir, an antiretroviral drug on the market to treat HIV infection, can *prevent* the transmission of the virus. For the past 2 years, researchers from UCSF and the University of New South Wales (UNSW) in Sydney, Australia, have worked with Cambodian collaborators to design the placebo-controlled study in 960 sex workers who are at high risk of becoming infected. "Our research in Cambodia has always been conducted directly in collaboration with the government and clearly could only continue with government endorsement," notes co–principal investigator John Kaldor of UNSW. The study already had received preliminary approval from a Cambodian ethics panel as well as one in the United States.

Concerns surfaced as early as June 2003, when Kaldor and collaborators from UCSF visited Cambodia to lay the groundwork for the study. Rosanna Barbero, who heads the Oxfam Hong Kong office in Phnom Penh and works closely with a large union of sex workers called the Women's Network for Unity, questioned why the researchers had come to Cambodia to do this trial in such a vulnerable group. "There's no culture of studies of any kind here," said Barbero, who suggested that the trial was "probably not feasible here."

Last March, the Women's Network for Unity said they would participate only if volunteers would receive health insurance for 30 years, a period they argued would protect them against possible side effects. Tenofovir was chosen for the 1-year study because it has a better safety profile than any anti-HIV drug on the market. In a somewhat incongruous second protest, ACT UP Paris and the Asian Pacific Network of Sex Workers denounced the trial at the World AIDS Conference held last month in Bangkok, accusing the sponsors of "a blackmail system" because it offered participants access to better treatment and health care than they otherwise would have received. A jointly issued press release by these groups also took aim at Gilead, the California manufacturer of the drug, contending that the company "organizes the infection of sex workers."

UCSF's Page-Shafer stresses that the study has the support of several other groups of sex workers: "If Cambodian women participate, they're the first ones to benefit," says Page-Shafer, who has worked on AIDS in Cambodia for several years.

The study is one of a handful of trials now planned in Africa and the United States to assess whether regularly taking tenofovir can derail HIV transmission, a novel approach to prevention, which now focuses mainly on education campaigns, condoms, vaccines, and microbicides. The Gates Foundation funds several of the studies through a grant to Family Health International, which until June supported the Cambodian study. NIAID then took over as the main funder, committing $2.1 million for the first year.

Mary Fanning, the NIAID medical officer in charge of the study, visited the trial headquarters in Phnom Penh in late July and said she had no inkling that Hun Sen had any reservations. In press accounts, Hun Sen suggested that the drug trials should be done in animals rather than in Cambodians. Tenofovir already has proven to be extremely effective as an HIV preventative in monkey experiments, and Fanning notes that it has passed the rigorous human studies required by the U.S. Food and Drug Administration.

Hun Sen and his staff apparently left Cambodia soon after making his views known. The researchers are hoping to receive clarification soon. **–JON COHEN**

ORGANIC CHEMISTRY

Druglike Molecules Mimic Gene Switches

It takes more than the right genes for good health. Those genes must also be switched on at the right times, a process known as transcription activation. When such activation goes awry, it can trigger diseases from cancer to diabetes.

Proteins typically serve as the genetic on-off switches. Researchers have long sought to make small druglike molecules to carry out the same task. Now researchers at the University of Michigan, Ann Arbor, report that they have succeeded. "It's really exciting that they have small molecules that can mimic natural activators," says Aseem Ansari, a biochemist at the University of Wisconsin, Madison.

In the body, an activator protein typically does its job in two steps: One "arm" binds to its genetic targets, and another arm grabs onto other proteins that turn on the gene. Smaller biomolecules, such as RNA snippets and protein fragments called peptides, can also work as activators. But these compounds can break down quickly and have other drawbacks, Ansari says. Because the new small molecules are more durable, he adds, they eventually might serve as scaffolds for a new family of gene-controlling drugs.

The research is described in the advance online publication of the *Journal of the American Chemical Society*. The Michigan team, led by chemist Anna Mapp, started by scrutinizing peptides known to activate particular genes. Although the peptides had different structures, they typically shared a handful of chemical features, such as phyenyl, hydroxyl, carboxylic acid, and isobutyl groups.

Mapp and her graduate students Aaron Minter and Brian Brennan synthesized a family of ring-containing compounds, known as isoxazolidines, that harbor the same groups. Then they grafted on gene-seeking "arms" by fastening each molecule to a protein known to target the DNA in a well-known engineered gene. The researchers added an extract made from the nuclei of human cells to test tubes containing the modified isoxazolidine molecules and measured an uptick in messenger RNA from the target gene. That increase was a sign that the small molecules had switched on gene transcription. **–ROBERT F. SERVICE**

CREDIT: MALCOLM LINTON

COGNITION

Life Without Numbers in the Amazon

To what extent can concepts exist without the words to express them? That question has long occupied philosophers and linguists. Now, in an article published online this week by *Science*, Peter Gordon of Columbia University has added to the debate with an unusual study on mathematical thought. Among members of a tiny tribe in the Amazon jungle that has no words for numbers beyond two, the ability to conceptualize numbers is no better than it is among pigeons, chimps, or human infants, the psycholinguist finds. The research suggests that "without a language for numbers, people don't develop an ability to perceive exact numerosities," he says.

The Pirahã, a hunter-gatherer tribe of about 200 people, live in small villages on a tributary of the Amazon. They have little social structure and no art, and they barter instead of using currency. They also have one of the world's most phonemically limited languages, with just 10 consonants and vowels. Although the Pirahã have words for one and two (hói and hoí), even those only indicate approximations, says Gordon.

A decade ago, Gordon visited the Pirahã to conduct fieldwork with linguist Daniel Everett, now at the University of Manchester, U.K., and his wife Keren, who spent 20 years with the tribe. Gordon gave a series of tests to the men (women and children were too shy to participate) to see how they dealt with concepts that have no representation in their language.

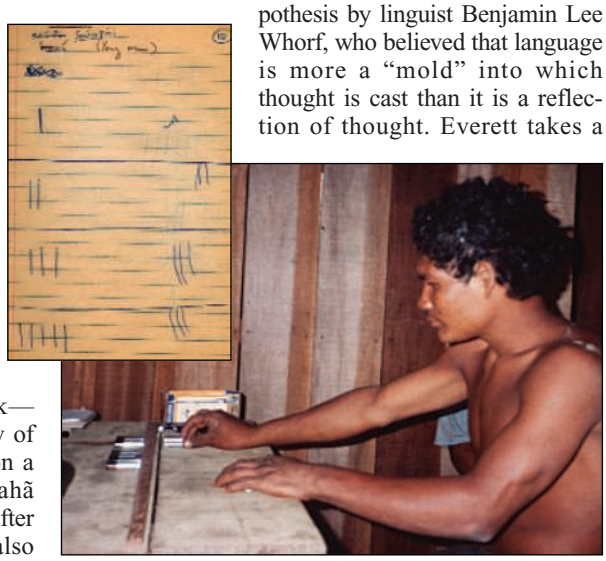

Tricky lineup. A Pirahã tribesman's number sense goes hazy after three.

Even in the simplest task—asking them to duplicate a row of up to 10 batteries he placed on a table—he found that the Pirahã performance started to decay after two or three batteries. They also did very poorly in a task requiring them to copy lines on a piece of paper (see picture). Tasks requiring cognitive manipulations of numbers were also beyond them. For example, the men could not retain the memory of a number, as demonstrated in a test where eight nuts were shown to them and then placed in a box.

Perhaps the most striking result came from a test in which the men saw a piece of candy being put into a box with a picture of several fish on the lid. They were then shown the box with the candy in it and another box that had either one more or one fewer fish on its lid and asked to choose a box. Even though a correct guess meant a candy reward, subjects did no better than chance. Their performance "looks like what you see in infants or animals; the notion of a precise one-to-one correspondence is not there," says Gordon.

Although some linguists have hypothesized that humans possess an innate number sense, Gordon contends that his results cast doubt on this theory. "What's innate is being able to see [specific numbers] up to three," says Gordon, who believes that this limitation is related to the fact that the Pirahã language is not recursive. For example, it is impossible for villagers to make comparisons such as "this pile of nuts is bigger than that pile." Instead they would say one pile is big and the other is small.

Calling the study "fantastic," psychologist Lisa Feigenson of Johns Hopkins University in Baltimore, Maryland, says that language must be causing the "drastic" difference in the number sense of the Pirahã. Feigenson notes, however, that other cultures with limited number terminology have developed ways of expressing the concepts.

Gordon says that the study favors a hypothesis by linguist Benjamin Lee Whorf, who believed that language is more a "mold" into which thought is cast than it is a reflection of thought. Everett takes a somewhat more interactive view, believing that the absence of both words and concepts for numbers is "the result of cultural constraints against quantification."

That view seems to be bolstered by the Everetts' attempts to teach the Pirahã numbers. Although children easily learned number words in Portuguese, the adults lost interest during the lessons. Everett also says years of attempts to teach adults to use the Brazilian currency came to naught, with adults telling him that "their 'heads were too hard' " for this type of thing. **–CONSTANCE HOLDEN**

CREDITS: (TOP TO BOTTOM) HOUSE COMMITTEE ON SCIENCE; P. GORDON *ET AL.*

ScienceScope

CIA Pick Puts Science Chair Boehlert on the Hot Seat

Science or spies? That's a choice facing Representative Sherwood Boehlert (R–NY), who heads the House Science Committee and was recently named temporary head of the House Intelligence Committee too.

Boehlert's double play was prompted by President George W. Bush's 10 August decision to nominate Representative Porter Goss (R–FL) to be the next head of the Central Intelligence Agency. Goss resigned from Congress, and House leaders asked Boehlert, a senior member of the intelligence panel, to take his place until they can pick a permanent successor.

Boehlert, however, says he's probably not interested in the intelligence job—in part because taking it would mean giving up his leadership of the science panel. "My choice right now is science," he told the *Ithaca* (NY) *Journal* last week. But that could change, he says, if the intelligence panel wins expanded powers during a pending overhaul of U.S. intelligence. A final decision could come as early as this month.

–DAVID MALAKOFF

Arizona Is Early Hot Spot as West Nile Virus Returns

The 2004 West Nile virus season is just starting to peak, but U.S. health officials are already seeing some trends. In what could be a shift from last year, 55% of all U.S. cases reported so far have been in Arizona—274 cases in all, according to the 13 August issue of the *Morbidity and Mortality Weekly Report* from the Centers for Disease Control and Prevention (CDC). That already represents a giant jump for the state, which reported only 13 cases last year, less than 1% of the 9862 total U.S. cases reported in 2003.

Because the disease hits hardest in the late summer and early fall, it's hard to say whether Arizona will retain its dubious distinction as a West Nile hot spot. At this time last year, Colorado was leading the pack and ended up with nearly one-third of the 2003 cases. Overall, 495 U.S. cases have been reported so far this year.

–JENNIFER COUZIN

Published by AAAS

With NASA's Earth Observing System complete, climate researchers are facing a confused and perilous future

Stormy Forecast for Climate Science

On 15 July, a spacecraft bristling with instruments to measure Earth's atmospheric chemistry soared into orbit. The successful launch of Aura rounds out NASA's Earth Observing System (EOS), an ambitious multibillion-dollar effort to understand global climate. The three large EOS platforms launched since 1999 join nearly a dozen smaller U.S. satellites monitoring everything from the world's ice sheets to solar radiation. The flotilla of instruments has left researchers awash in data. But they are learning that data alone won't buy happiness.

Next week, as a group of senior scientists gathers on the coast of Massachusetts to debate the future of space-based earth science, the mood will be grim. Despite receiving nearly $2 billion in annual funding from the U.S. government, climate researchers say their discipline is in trouble. A fractious community has failed to come up with a clear scientific agenda, they say, and political support for climate change research is waning. The combination has created a deep crisis. "Earth scientists say they are fighting for their lives," says Berrien Moore, a biogeochemical modeler at the University of New Hampshire in Durham, who will co-chair the National Research Council (NRC) meeting in Woods Hole, Massachusetts.

The NRC meeting is an attempt to do for climate change what has been done for astronomy, planetary science, and solar physics: create consensus on a realistic, long-term blueprint for the field, including the most important questions to be answered and the tools needed to explore them. It won't be an easy task. Although NASA and the National Oceanic and Atmospheric Administration (NOAA) have requested the study, authority for climate research is spread among many federal agencies with different agendas. The topic draws researchers from innumerable subdisciplines—from geophysics to oceanography—and with vastly different needs. A white paper prepared by NRC staff and outside researchers for next week's gathering concludes that diffuse objectives and a lack of priorities have already left the program "marginalized and politically expendable."

> "EOS has revolutionized earth sciences—but we can't fully appreciate it because we are inside the revolution."
>
> —Berrien Moore, co-chair, NRC panel on space-based climate research

Point of the spear

That blunt assessment would probably have shocked the earth scientists who, a generation ago, conceived of EOS as a way to gather massive amounts of data for use in unlocking the mysteries of the complex global climate system. That vision became the centerpiece of a global change research program created by the U.S. government in 1990. The initial plan called for NASA to build and launch six massive platforms that, over 15 years, would gather simultaneous data on a host of ground, ocean, and atmosphere parameters.

Then reality intervened. Staring at an estimated $30 billion price tag for building and operating the system, NASA delayed and scaled back its plans. The result is three smaller platforms—Terra, Aqua, and Aura—plus other more modest spacecraft. Even so, EOS accounted for half of the government's $1.6 billion climate change program by the time the first satellite, Terra, was launched in 1999 (see graphic, p. 1097).

The size of a school bus, Terra's package of five instruments is examining land-surface changes, atmospheric aerosols, global cloud cover, and ocean temperatures. Aqua followed in 2002, with a half-dozen instruments measuring stratosphere temperatures and Earth's thermal radiation budget, among other parameters. Aura completed the trio of satellites in July with its focus on atmospheric chemistry. Each satellite is designed to run for 6 years, although each could last longer.

The trio's scientific output has been staggering. From delivering 17 terabytes of data in 1999, EOS is expected to approach a delivery of 1000 terabytes this year. Despite those impressive data rates, the earth sciences community is bitterly divided over whether EOS has been worth the investment. Answering this question will be a difficult but important part of the NRC panel's job.

Advocates argue that it is too early to judge the system's impact, given the years needed to first calibrate instruments and then sift through mountains of complex data. Moore contends that EOS "has revolutionized earth sciences—but we can't fully appreciate it because we are inside the revolution." He expects that in a few years the data will help scientists produce much better climate models based on a better understanding of how the land surfaces, oceans, and atmosphere interact.

And even if the science may be lagging, the EOS data system alone is a huge leap forward, says Lawrence Smarr, a computer scientist at the University of California, San Diego, and chair of the panel that advises NASA on earth sciences. It's the largest data system in use in the world, he says, and could pave the way for applications in many fields. "The EOS program has been at the point of the spear," he adds. "They've been the pioneers."

Critics, however, say that the NASA satellite and data system has failed to deliver on its promise to be a coordinated system providing long-term coverage. "EOS is an

CREDITS: (TOP TO BOTTOM) NASA/GSFC; K.DONAHUE/UNH-EOS

Published by AAAS

unmitigated disaster," says William Rossow, an atmospheric scientist at NASA's Goddard Institute for Space Studies in New York City. "I don't believe it has done much of anything." He and others insist that EOS is actually an expensive and haphazard bevy of instruments with relatively short lives. They fear that the vast majority of EOS data, produced at such a high cost, is not being used—and will never prove useful.

Few dispute, however, that satellites have given researchers a view of global systems that is far more sweeping than that obtained from in situ measurements taken on ocean buoys or balloons. But they have their foibles. Orbits decay and satellites drift. If an instrument measures temperatures in a region later in the day because of a change in orbit, for example, an apparent cooling trend may simply be a result of diurnal variation. As instruments become more sensitive, they also become more vulnerable to the harsh conditions of space. And calibrating instruments is still a painstaking process, which one scientist describes as "a black art." Satellites also have their limits; they cannot provide detailed views of the ocean depths or what's happening under Antarctic ice sheets.

Many of NASA's smaller, cheaper, and more focused earth science satellites of the past decade have won plaudits from researchers. They include the 7-year-old Tropical Rainfall Measuring Mission, whose fate is up in the air (*Science*, 13 August, p. 927); a joint U.S.-French ocean observing satellite called TOPEX/Poseidon; and a mission to examine the elevation of Earth's ice sheets. NASA's earth science chief Ghassem Asrar notes that his agency has plans for 10 new missions—although none is on the scale of EOS.

Just Say NOAA

At the heart of the debate is how to satisfy researchers' needs for long-term, accurate, and continuous data streams. A related question is which federal agency should take the lead role for that next generation of climate research. Asrar argues that NASA is in the business of providing research satellites, not long-term operational spacecraft. He suggests that NOAA, which operates U.S. weather satellites, is in a better position to take charge of a post-EOS observation program. "The problem is that NASA wants to move on, but we say we need 20 to 30 more years of records," says Mark Abbott, an oceanographer at Oregon State University in Corvallis.

Scientists also fear that earth sciences at NASA are no longer seen as an up-and-coming enterprise. Asrar was just named deputy for a new science office that subsumes the old independent earth science office created in 1992. "A lot of earth scientists are afraid astronomy will eat their lunch when their lunch is already a quarter-sandwich short," quips Charles Kennel, director of Scripps Institution of Oceanography in La Jolla, California, and chair of NASA's advisory council.

Meanwhile, the agency's budget for earth science is projected to decline from today's $1.6 billion to $1.3 billion in 2008. And earth science's star seemed to pale further in January, when President George W. Bush told NASA to focus on astronaut missions to the moon and Mars. "If the Bush initiative goes somewhere, earth science will take it on the chin," predicts John Townsend, former director of NASA's Goddard Space Flight Center in Greenbelt, Maryland.

NOAA Administrator Conrad C. Lautenbacher Jr. says his agency is ready and willing to take on the job of continuous climate monitoring. He sees that task as a natural extension of NOAA's long history of monitoring the weather, although he acknowledges that "I don't believe the process we have today is optimal." But weather and climate science are not the same, say researchers, many of whom are skeptical of NOAA's ability to come up with the money and expertise to take over climate monitoring from NASA.

NOAA's first big step into the field will be the National Polar-Orbiting Environmental Satellite System (NPOESS). A decade ago, NOAA and the Defense Department agreed to merge their two weather-monitoring systems, and the first of the $7 billion series is slated for launch by 2010, around the time EOS is winding down. Originally slated to be solely a weather satellite, NPOESS has added climate elements as well.

In part to smooth the transition from EOS's research instruments to an operational system, NASA and NOAA plan to

Mount Vesuvius reigns over Italy's west coast in this view from a Terra instrument, one of five examining a wide range of earth, ocean, and air parameters.

This glimpse of last fall's forest fires in southern California comes from one of six instruments monitoring clouds, atmosphere, humidity, and sea-surface temperatures.

Scientists are still calibrating the five instruments that will probe Earth's atmosphere, including the Antarctic ozone hole.

CREDIT: (TOP) NASA/GSFC

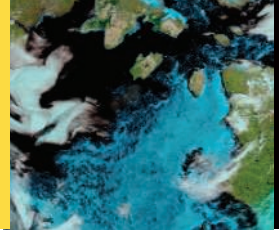

Fields of sea ice melt in northeastern Canada's Hudson Bay

U.S. coastal areas along the Gulf of Mexico

launch NPP—the NPOESS Preparatory Project—in 2006. The spacecraft will include four instruments derived from EOS. Greg Withey, who manages NOAA's satellites, says that "climate will get a nice ride" with NPP and NPOESS. And NASA's Asrar says the satellites will provide climate researchers with a continuity of data beyond EOS—as well as sufficient overlap to calibrate delicate climate instruments.

But many researchers hotly dispute Asrar's assertion. "He is changing facts to fit his view," complains Richard Goody, a Harvard University emeritus climate researcher. "Weather and climate systems are different." Weather work typically requires high-resolution images without the absolute accuracy and stability that climate researchers say they need to do their jobs. Whereas a weather forecaster has little need to store data, climate researchers depend heavily on an organized and accurate long-term database. And weather and climate needs can conflict. For example, some EOS spacecraft are rolled in orbit so they can spot the moon and use it to calibrate delicate climate instruments. Although NASA is willing to take such risks, Withey admits that such a maneuver might be too dangerous for an operational satellite critical for national weather forecasting.

Researchers are convinced that the needs of the weather program inevitably must trump those of climate. "There's a lot of angst about NPOESS," says Bruce Wielicki of NASA's Langley Research Center in Hampton, Virginia. "It is not actually tasked to do climate." And scientists' skepticism extends beyond NPOESS itself. They fear that NOAA—part of the U.S. Commerce Department—is ill equipped to handle the expensive and long-term task of climate observation. NOAA's $3.3 billion budget is less than one-fourth the size of NASA's, and it lacks a lab like the one at Goddard, which manages EOS, with the necessary talent and resources to handle a complex environmental research data and satellite system. "NOAA is the problem," says Goody. "It has the mandate" on climate, he adds. "But it is not really a good research agency."

Wielicki also wonders who will pay for the extensive ground-based research, information systems, and infrastructure that NASA currently funds. "NOAA spends very little on these now," he says. "I hope we can find a way to work with NASA and maybe the National Science Foundation." Others suggest that NASA and NOAA should share Goddard's facilities to smooth the transition from NASA's research satellites to an operational system run by NOAA. Getting agencies to cooperate more closely, however, will be difficult, and researchers fear that their needs will fall through the government cracks.

Cats and dogs

But eliminating the confusion about agency roles won't resolve all the problems plaguing climate researchers. "I don't think the community has produced plans and programs which can be funded and supported," says Lautenbacher. Adds Asrar: "There has been an absence of unified support in the [scientific] community." Both men say they want earth scientists to come up with a clear list of future missions that federal agencies and Congress can support.

Part of the problem is that climate research remains a fragmented business. Rossow maintains that the vast majority of research is actually old-fashioned earth sci-

Stitching Together a Global System of Systems

Keeping an eye on the planet is no simple task. NASA alone is currently flying 15 satellites designed to understand various aspects of the Earth system. Europe and Japan also have large spacecraft carrying out climate research, and there is a fleet of weather satellites operated by countries including India and China. And that's only what is in space: Many nations also deploy ocean buoys, balloons, and aircraft to gather additional climate and weather data on everything from atmospheric temperature to deep-ocean currents.

Scientists have long dreamed of flowing together these many rivulets of data to create a common stream from which all climate researchers may drink. And last summer in Evian, France, leaders of the eight richest nations pledged to create a comprehensive, continuous, and coordinated system of global observation systems. Since then, 50 nations—from Argentina to Uzbekistan—have signed up to take part in what Charles Kennel, director of Scripps Institution of Oceanography in La Jolla, California, calls "a remarkable and profound event."

In February, ministers from around the world will gather in Belgium, the third such meeting since the one in Evian, to draw up a 10-year plan to coordinate observation plans, involve developing countries in data gathering, and exchange all data quickly and openly. But many researchers, frustrated by what they see as a lack of progress, fear that the entire exercise is part of an attempt by U.S. President George W. Bush to talk about climate change rather than take action. They also worry that further delays will produce a proliferation of redundant instruments and a chaotic sea of data. "How can this work when U.S. agencies aren't even able to coordinate?" asks Kevin Trenberth of the National Center for Atmospheric Research in Boulder, Colorado. Adds another climate researcher: "They've just created a new acronym and a new committee."

Slow going. NOAA's Conrad Lautenbacher is working on a coordinated plan for Earth observation.

Such cynicism is unwarranted, says Conrad C. Lautenbacher Jr., chief of the National Oceanic and Atmospheric Administration (NOAA), which is the U.S. representative to the talks. The mere presence of so many high-level officials shows that governments are taking the issue seriously, argues NOAA's Greg Withey, who is in charge of satellite systems. "You don't get 40 to 50 ministers coming to a conference just because they like to travel," he says. But Withey predicts "it is going to take another year" to come up with an approach that will iron out the technical difficulties of creating common data sets and calibrating instruments.

Withey says that by the end of this year, NOAA will have a plan for U.S. observation strategy for the next decade to present at the February meeting. Japan is working on its own document, and Europe has just wrapped up work on a global system that combines environmental and security monitoring. **–A.L.**

CREDITS: (TOP TO BOTTOM) NASA/GSFC/LARC/JPL, MISR TEAM; NASA GSFC, MITI, ERSDAC, JAROS, AND U.S./JAPAN ASTER SCIENCE TEAM; NOAA

Published by AAAS

A stretch of the Yangtze River in China, including the Wu Gorge

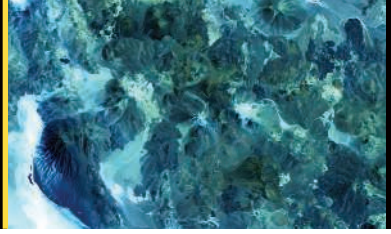

Volcanoes along the Chilean-Argentinean border

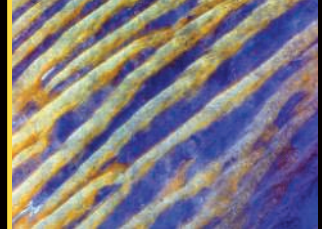

A great sea of linear dunes in Saudi Arabia

ence in disguise. He says that scientists, instead of working on a problem such as how clouds interact with radiation, aerosols, and general planet circulation, too often simply extend previous work on cloud physics. "Our community blinds itself if it thinks it is doing climate," he says. Goody agrees that the community jumped on climate research because that is where the money is and that it has failed to transform itself into an interdisciplinary powerhouse. Unlike an area such as systems biology, climate research remains too focused on small-scale issues, he and others say.

> "EOS is an unmitigated disaster. I don't believe it has done much of anything."
>
> —William Rossow, NASA Goddard Institute for Space Studies

Kevin Trenberth of the National Center for Atmospheric Research in Boulder, Colorado, recalls being "astonished and appalled" to learn that members of different Aqua instrument teams were not communicating with one another, although one of the reasons for launching several instruments on one platform was to compare simultaneous data. "We have a pile of numbers," says Rossow. "But we need a structure to take these measurements and analyze them."

Wielicki says that taking the necessary interdisciplinary approach is tough work. To understand the global radiation budget, for example, his team is using 11 instruments on seven spacecraft. "It's a huge job," he adds, despite the fact that they have data from an instrument that flew before EOS. "Other fields in most cases are doing this for the first time." The diverse interests of earth scientists complicate the picture. "We're not like the astronomy community; our disciplines range from solid Earth to upper atmosphere to weather, climate, ecosystems, and oceanography," says Richard Anthes, president of the University Corporation for Atmospheric Research in Boulder, Colorado, who is co-chairing the NRC panel with Moore. In the past few years, astronomers, solar system researchers, and solar physicists reached consensus on long-term plans and priorities for their respective fields. But reconciling the many and competing desires of climate researchers is a formidable task. Says Anthes: "The challenge is to hold this community of cats and dogs together."

Climate awakening

Both NASA and NOAA want the NRC panel to review recent advances in Earth-system science, pose the principal scientific questions that need answers, and suggest which measurements and systems are needed. "We've got the foundation. We've got to figure out what kind of house we are going to build," says Moore.

A central question is how to create and deploy a climate-observing system that can provide consistent and accurate data. Moore, Trenberth, Thomas R. Karl, director of the National Climatic Data Center in Asheville, North Carolina, and Carlos Nobre, director of Brazil's Center for Weather Forecasting and Climate Studies, recently proposed a climate observation and data system that would tie together all the world's environmental satellites, along with in situ data, a global telecommunications network, comprehensive models of the land, ocean, and atmosphere, and a center to monitor data quality.

Karl says the space portion of such a system could instead use existing capabilities from many nations (see sidebar). Wielicki, however, estimates that a complete climate satellite system could cost $5 billion to $10 billion annually—more than triple what NASA now spends on Earth observation.

Given the U.S. political climate, such an investment, even with contributions from other countries, seems highly unlikely. "What a waste of money! What would you do with the knowledge?" says one congressional aide. Whereas fiscal conservatives would attack any massive new research program as unaffordable, liberals are likely to see it as a ruse to delay action on the underlying problems that are causing global warming. Congressional "enthusiasm has waned," adds the congressional aide. "It doesn't seem at all sexy or interesting."

A clear and comprehensive vision statement might help persuade skeptical politicians, says Withey. But Goody and others aren't convinced of the need for a bigger budget, especially with the trend toward microsatellites and miniature instruments. "The money in global change research is ample for what we need to do," says Goody.

Given these long-standing problems, climate researchers aren't sure how to regain the enthusiasm and high hopes of the early 1990s. Wielicki fears that it will take a disaster—"a really bizarre weather event such as a Category 6 storm or a falling ice sheet"—to alert the public and the politicians to the perils facing the planet. Without such a catastrophe, earth scientists will have to find another way to make their case that understanding climate change is every bit as important as finding life on Mars or warning citizens of an approaching hurricane.

—Andrew Lawler

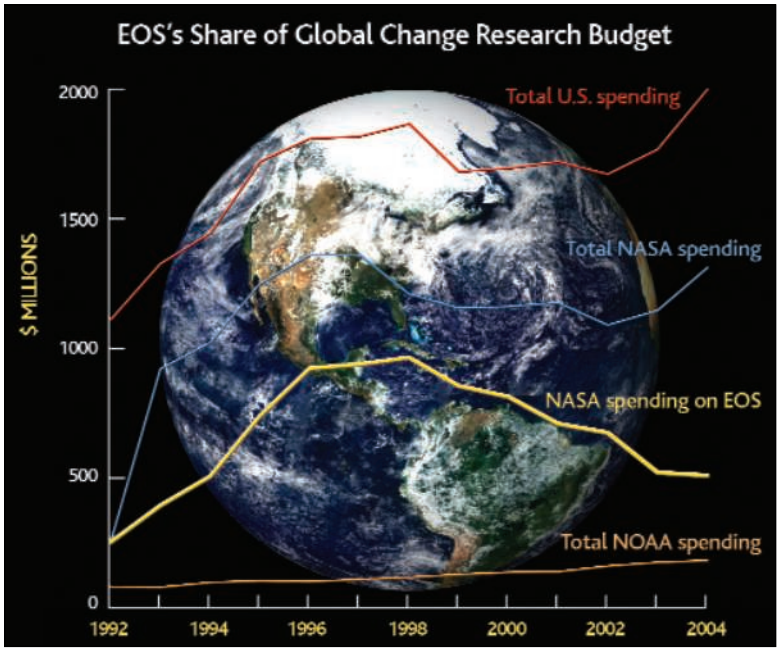

Lion's share. NASA's EOS budget has consumed the largest single chunk of U.S. Global Change Research Program funds since the early 1990s.

CREDITS: (TOP TO BOTTOM) USGS; NASA GSFC, MITI, ERSDAC, JAROS, AND U.S./JAPAN ASTER SCIENCE TEAM; SOURCE: NASA/NOAA

Published by AAAS

New Dead Zone Off Oregon Coast Hints at Sea Change in Currents

Ocean scientists are scratching their heads about an apparently natural, seasonal onslaught of deadly water in the northeastern Pacific

NEWPORT, OREGON—The data scroll in from an instrument cage being towed through the deep blue-green waters off the central Oregon coast. The meter-long cage, called an acrobat for its ability to "fly" below the water's surface, holds monitors that track the water's temperature, salinity, and levels of dissolved oxygen, chlorophyll, and organic matter. Anthony Kirincich, a physical oceanography graduate student at Oregon State University (OSU), Corvallis, toggles a black switch that tilts the cage's "wings," pitching the acrobat toward the ocean bottom. Red, blue, and green lines on one of the laptop monitors aboard the research vessel *Elakha* start snaking.

"We're diving, and you can see the dissolved oxygen is making a beeline toward the lower levels," says Francis Chan, a marine ecology postdoctoral assistant at OSU. As the acrobat crosses the 50-meter mark, the green line representing dissolved oxygen sinks below the magic number of 1.43 milliliters of oxygen per liter of water, the minimum needed to support most marine life. The acrobat has just entered the "dead zone."

The zone is a several-kilometer-wide swath of nutrient-rich but oxygen-depleted water from the North Pacific that has recently welled up off the coast of Oregon. A similar dead zone first appeared for 2 months in the summer of 2002, suffocating vast numbers of crabs, rockfish, and other marine organisms that couldn't flee fast enough. Last year, oxygen-depleted "hypoxic" waters feigned another approach, but the winds that drive it onshore relaxed, causing it to slink off the coastal shelf. Now the dead zone is back, and Chan, Kirincich, and others think they may be witnessing the birth of a new seasonal ocean circulation phenomenon. But their excitement about doing new science is mixed with concern that the phenomenon may wreak havoc on Oregon's highly productive marine ecosystems.

"It happened once, and [people thought] it was a fluke," Chan says of the 2002 dead zone. "Now that we're seeing it again, it makes you at least curious and at worst alarmed at how fast these shifts can happen." Adds Jane Lubchenco, a marine ecologist at OSU and one of the leaders of the team working to track the dead zone: "This coastal ecosystem off Oregon seems to be changing in a way we have never seen."

Most dead zones are the result of human-induced pollution. Fertilizer and other nutrient-rich pollutants trigger blooms of phytoplankton, which suck oxygen out of the water when they decay. There are more than 30 such regions around the world. Naturally recurring dead zones fed by the upwelling of oxygen-poor waters, however, are known only off the coasts of Peru and South Africa, Lubchenco says.

Lubchenco's team began tracking the emergence of this year's dead zone in June after coastal residents reported seeing dead crabs and fish washing up on beaches. Since then, the team has conducted shipboard monitoring surveys in a region that lay at the heart of the 2002 dead zone to gauge ocean conditions. By mid-July, the group had confirmed that a band of hypoxic water at least several kilometers wide had moved in off the coast. And in early August, their instruments reported the lowest dissolved oxygen levels of the season, 0.55 ml/liter at a depth of 90 meters. Videos of the ocean floor and the rare appearance of hundreds of dead crabs in an intertidal zone have added weight to the notion that a new dead zone has returned, although so far it's weaker than the one 2 years ago.

The long-term effect of the dead zone hinges on whether it becomes a regular summertime fixture. Fish and crab populations seemed to recover quickly after the 2002 spell. But George Boehlert, who heads the Hatfield Marine Science Center in Newport, Rhode Island, says recurring hypoxic waters could harm juvenile fish, with serious but delayed impacts on adult populations. A persistent dead zone, says OSU physical oceanographer Jack Barth, could also mean that ocean circulation patterns in the Pacific may be changing. The nutrient-rich waters are part of a normal ocean current that carries water eastward across the North Pacific toward the North American coastline. That current splits near Vancouver Island, carrying some water northward along the coast of British Columbia and the rest south toward California. Temperature, salinity, and other measurements, Barth says, suggest that a change in wind conditions is forcing more of this North Pacific water southward, where some of it is lapping up onto the continental shelf off central Oregon. Once on the shelf, the cold hypoxic water is pulled up near the shore if winds blow surface waters away from the coast—as happened in 2002 and again this year.

It's not clear what might be triggering the changing wind conditions and sea circulation patterns, Barth says. So far they don't appear to be linked to either El Niño or La Niña, which alter ocean and atmospheric circulation patterns across the Pacific. Another possibility is the Pacific Decadal Oscillation (PDO), a large-scale circulation change over as long as 4 decades. Evidence suggests that the PDO may have entered a new phase in 1998, but Barth says "we simply don't have enough evidence yet" to finger it as the cause of the new dead zone.

Barth, Lubchenco, and others plan to keep a close eye on the waters here. "It's a bad thing that's happening," Lubchenco says. "But it's so interesting that it's very exciting to watch." **–ROBERT F. SERVICE**

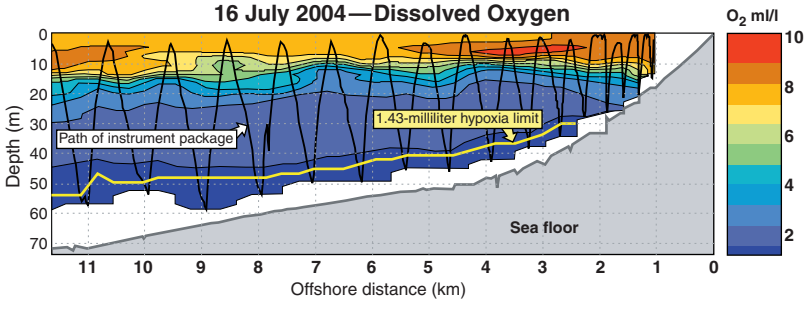

Pacific grim. Low-oxygen water creeping along the continental shelf killed bottom-dwelling crabs (*top*)—to the delight of scavenging starfish.

CREDITS: (TOP TO BOTTOM) OSU; ADAPTED FROM PISCO AND A. KIRINCICH, J. BARTH, OCEANIC AND ATMOSPHERIC SCIENCES, OSU

Published by AAAS

Bees From the Rainforest Add Up To a $62,000 Coffee Buzz

PORTLAND, OREGON—A record number of ecologists—more than 4000—gathered here from 1 to 6 August for the 89th annual meeting of the Ecological Society of America (ESA). They discussed everything from ecosystem services to invasive species to fire ecology.

In recent years, some economists and conservation biologists have tried to estimate the monetary value of natural ecosystems to people. In the best-known example, ecological economist Robert Costanza of the University of Maryland, College Park, and his colleagues calculated in 1997 that the planet's "ecosystem services"—air and water purification, nutrient cycling, waste decomposition, and more—are worth $33 trillion per year, an amount nearly twice the global gross domestic product. And in 2002, a team led by conservation scientist Andrew Balmford of the University of Cambridge, U.K., calculated that a worldwide network of nature reserves would be worth roughly $5 trillion, 100 times the value of exploiting the resources in them (*Science*, 9 August 2002, p. 950).

Bee profitable. Pollination from nearby bees is worth $62,000 to a coffee farmer.

Such global estimates, however, have little meaning to the farmer, rancher, industrialist, or city planner who makes land-use decisions based on considerations closer to home. So a team led by Taylor Ricketts of the World Wildlife Fund tackled a discrete local example. Their answer may help save patches of rainforest.

The researchers homed in on a single coffee plantation in Costa Rica and measured the value of one ecosystem service, the pollination of the coffee crop by bees. Ricketts's team examined 11 bee species that visited coffee flowers from stands of rainforest that bordered the farm. Flowers near the forests received twice as many bee visits and twice as much pollen deposition as did flowers far from forests, they found. As a result, coffee plants near the forests had 20% greater yields and 27% fewer deformed beans. Combining these data with market prices for coffee, the team calculated that bee pollination accounts for $62,000, or 7%, of the farm's annual income. In addition, by providing multiple species of native bees, the forest patches served to stabilize pollination services year to year against the severe population fluctuations typical of feral honeybees.

Just looking at the benefit from pollination, the value of preserving the natural forest stands is greater than the value of cutting down the forest for other uses, Ricketts told ESA attendees. For instance, cattle grazing would yield only $24,000 per year.

The team's full cost-benefit analysis appears in the *Proceedings of the National Academy of Sciences* online on 11 August and in the upcoming issue of *Conservation Biology*. Ricketts and his colleagues plan to return to Costa Rica this winter to spread word of their findings among coffee farmers, government officials, and agricultural extension agents.

The bee study "provides a tangible example of the benefits of [forests] in a way that's immediately relevant to the coffee farmers," Balmford says. "The key to getting ecosystem services on the table for decision-making is to begin to quantify them in a locally relevant way."

Are Invasive Species Born Bad?

Honoring the bicentennial of Lewis and Clark's expedition through the newly acquired western territories, the official theme of this year's ESA meeting was the ecological exploration of inhabited landscapes. Based on the number of presentations, however, it might have been a conference devoted to invasive species.

One key question for ecologists is what makes these interlopers so invasive. Do certain species simply have an innate potential to grow and reproduce rapidly? Or does invasiveness result from evolutionary changes that occur after an introduction? As ecologist Kristina Schierenbeck of California State University in Chico puts it, "Are invasive species 'born' or 'made?' "

Most ecologists have long assumed that invasiveness was just a matter of being in a favorable environment. If an organism introduced into a new region leaves behind its natural predators, competitors, and parasites, its chances of reproductive success increase. Recently, however, ecologists have explored whether species may also evolve to become invasive in their new homes. This "evolution of increased competitive ability" (EICA) hypothesis, proposed in 1995 by ecologists Bernd Blossey and Rolf Nötzold, is just now being tested rigorously.

The meeting showcased "very compelling examples and evidence that EICA can occur," says ecologist Dana Blumenthal of the U.S.D.A. Agricultural Research Service in Fort Collins, Colorado. But "the jury is still definitely out" on the extent of the phenomenon, he adds.

The EICA hypothesis predicts that once an organism escapes its natural enemies, it no longer needs the defenses it had evolved against them. If these defenses use up precious energy or resources, natural selection should favor the organism investing instead in traits that give it a competitive edge over its new neighbors. For a plant, this could mean larger size, faster

Less is not more. Using fewer resources for defenses doesn't enable St. John's wort to grow faster in the United States.

CREDITS: (TOP TO BOTTOM) TAYLOR RICKETTS/WWF; S. PETERSON/USDA NRCS NPDC

Published by AAAS

growth, or greater reproductive capacity, all adding to its invasive nature.

Evidence for EICA was offered by Evan Siemann and William Rogers of Rice University in Houston, Texas, who work with the Chinese tallow tree, *Sapium sebiferum*. They have found that trees from introduced southern U.S. populations show faster growth and reduced investment in chemicals that defend against leaf-eating insects compared with trees from native Asian populations. As with most EICA studies, the work featured "common garden experiments," in which native and introduced plants are grown side by side to control for environmental variables. The investigators found that Asian trees outperform American trees in settings with native Asian herbivorous insects, whereas American trees outperform Asian ones in settings without these insects. Many scientists, Blumenthal says, consider this evidence the strongest so far in support of the EICA hypothesis.

However, a study of the European plant garlic mustard, *Alliaria petiolata*, which arrived in North America 150 years ago, failed to support the hypothesis. Experiments presented by Oliver Bossdorf of the UFZ Centre for Environmental Research in Halle, Germany, and colleagues did show that American populations had lost their resistance to a European weevil that specializes on the plant. But when the group then grew American and European populations in side-by-side competition, plants from native European populations outgrew those from introduced American populations.

Perhaps the most extensive common garden experiments thus far involve St. John's wort, *Hypericum perforatum*, the plant of alternative medicine fame, which was introduced from Europe to America 2 centuries ago. Ecologist John Maron of the University of Montana, Missoula, and his colleagues collected seeds from 50 St. John's wort populations across Europe and North America and then grew European and American plants in common gardens on both continents. Maron's group then measured levels of three chemicals the plants make to deter insects. The American plants exhibited lower levels of the chemicals, indicating they had lost defenses since their introduction. When grown in Europe, the American plants also suffered more infection and mortality than the natives, revealing that the apparently weakened defenses did have a real effect.

Did the American plants that saved on defense invest their new gains into competitive ability, as the EICA hypothesis predicts? Apparently not. The American plants showed no trend toward larger size or greater reproductive ability when growing in the United States.

Maron's work tested EICA more comprehensively than any previous study, according to some ecologists. "He did exactly the experiments that needed to be done," says Marc Johnson of the University of Toronto.

Maron doesn't perceive his results or those of Bossdorf's group as undermining EICA, however. He says that circumstances will vary for every species. Indeed, in Portland, both Blossey and Blumenthal summarized previous tests of the EICA hypothesis and found that of 14 studies, five supported EICA, one rejected it, and the remainder were inconclusive. "One flaw of EICA," says ecologist Peter Kotanen of the University of Toronto, "is that it envisions a very simple tradeoff between defense and growth. The real world is more complicated."

Nonetheless, the ongoing rigorous assessment of the hypothesis demonstrates that the study of invasive species has come of age. "What I found striking at this meeting is how much invasion biology has matured," says Kotanen. "We've gone from case histories and compilations to people finally doing experiments, and we've probably learned more in the last 10 years than in the 5 decades before."

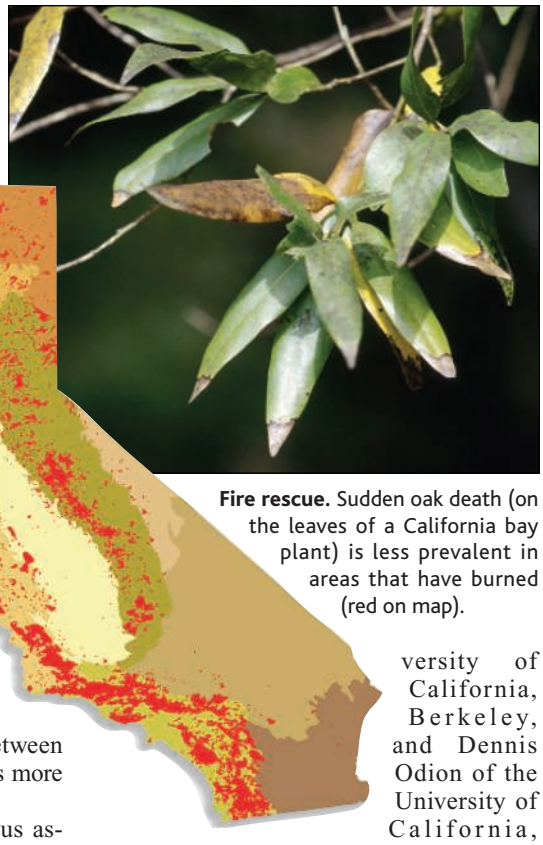

Fire rescue. Sudden oak death (on the leaves of a California bay plant) is less prevalent in areas that have burned (red on map).

CREDITS: (TOP TO BOTTOM) JOSEPH O'BRIEN/USDA FOREST SERVICE; ADAPTED FROM M. A. MORITZ/ESPM/UNIV. OF CALIFORNIA, BERKELEY

Fighting Sudden Oak Death With Fire?

One of the most destructive invasive species these days is the water mold *Phytophthora ramorum*, the pathogen that causes sudden oak death (SOD). The suddenness with which it began ravaging trees in California's oak woodlands just a decade ago led researchers to suspect that it was introduced from elsewhere, although no one yet knows for sure.

What is certain is that SOD threatens to drive several oak species into oblivion and profoundly alter the landscape of these woodlands. And the oak forests of eastern North America, where red oaks are known to be susceptible, could be next. The meeting, however, offered some possible good news for SOD researchers: Controlled fires might just provide a way to limit the spread of the troublesome pathogen.

Fire ecologists Max Moritz of the University of California, Berkeley, and Dennis Odion of the University of California, Santa Barbara, collected data from state agencies on the pathogen's presence at different sites in California, as well as historical data on forest fires. They discovered that the disease was much less prevalent in areas that had burned since 1950. "You almost never see infections in [those] areas," says Moritz. One reason, he and Odion speculate, could be that plant defenses against pathogens become weaker in older, unburned stands; trees need to invest more in competition with neighbors as stands age, and production of some defensive chemicals declines in older plants, for instance.

Whatever the mechanism, the findings indicate that California's fight against forest fires over many decades may have precipitated or accelerated the SOD outbreak. However, the findings also suggest that controlled burning might help halt the disease. Moritz and Odion warn that careful experiments would be needed to determine whether prescribed burns have the desired effect.

The rapid spread of SOD is "such a dynamic system that a lot of our tools in ecology for understanding and predicting patterns are inadequate," says Richard Ostfeld of the Institute of Ecosystem Studies in Millbrook, New York. That's why the fire findings, he adds, are "both interesting and important" for battling the disease.

–JAY WITHGOTT

Jay Withgott writes from Portland, Oregon.

LETTERS

Another Group at High Risk for HIV

JON COHEN'S ARTICLE "ASIA AND AFRICA: on different trajectories?" (Special Section on HIV/AIDS in Asia, 25 June, p. 1932) gives prominence to those who argue that by aggressively targeting high-risk groups—intravenous drug users (IDUs), sex workers, and gay men—with prevention and anti-retroviral therapy, a "generalized epidemic" (defined as a national prevalence rate of 2% or more) will be averted in most Asian countries. An earlier article by Cohen ("Two hard-hit countries offer rare success stories," 19 Sept. 2003, p. 1658) presented convincing evidence that targeting has reversed the spread of the epidemic within these groups, most notably in Thailand and Cambodia. We are concerned, however, that Cohen places too much emphasis on these particular high-risk groups and not on a larger risk group that is mentioned only in passing—mobile and migrant workers and their sexual contacts.

> **"[F]ishermen and other seafarers (and their casual and long-term sexual partners)... are thought to be among the groups with highest prevalence rates of any occupational group other than commercial sex workers, in Asia as well as in some African countries..."**
>
> –ALLISON AND SEELEY

Cohen refers to the presence of "huge populations of migrant workers" in the region, and his earlier article on Myanmar identifies gem miners and loggers as migrant workers that are a "major conduit" of infection into the general population ("The next frontier for HIV/AIDS: Myanmar," 19 Sept. 2003, p. 1650). He does not mention fishermen and other seafarers (and their casual and long-term sexual partners) who are thought to be among the groups with highest prevalence rates of any occupational group other than commercial sex workers, in Asia as well as in some African countries (*1*). Among many passing references to high incidences of HIV/AIDS in ports and fishing communities are three studies from southeast Asia that have surveyed seroprevalence. The results are worrying. A sample of 818 Thai, Khmer, and Myanmar fishermen working in the Thai trawler fleet in the late 1990s were 15.5% HIV positive, with the highest rates being for the cross-border migrants (20.2% for Khmer and 16.1% for Myanmar fishermen) (*2*). In the port of Sihanoukville, Cambodia, in a survey of 446 fishermen, 17% of those who claimed to regularly use condoms were HIV positive, and 20% of irregular condom users were HIV positive (*3*). In Malaysia, fishermen are estimated to make up around 2% of the total adult population, but they account for between 6 and 7.8% of people known to be living with HIV (*4*, *5*). Almost 29 million fisherfolk, 84% of the world total, work in Asia (*6*), with perhaps three or four times that number of dependents, so the high seroprevalence rates observed in fishing communities are likely to be regionally significant. If the epidemic has already taken a significant hold in these migrant and mobile subpopulations, then targeting IDUs and sex workers to contain the epidemic may prove to be too little, too late.

EDWARD H. ALLISON AND JANET A. SEELEY
School of Development Studies, University of East Anglia, Norwich NR4 7TJ, UK.

References
1. E. H. Allison, J. A. Seeley, *Fish Fish.* **5**, 215 (2004).
2. A. T. Entz, V. P. Ruffolo, V. Chinveschakitvanich, V. Soskolne, G. J. P. van Griensven, *AIDS* **14**, 1027 (2000).
3. A. Kim *et al.*, poster presented at the XIV International AIDS Conference, Barcelona, Spain, 7 to 12 July 2002 (available at http://ari.ucsf.edu/ari/pdf/Posters/barcelona/shafer2.pdf).
4. Asian Business Coalition (Malaysia), www.abconaids.org/ABC/asp/view.asp?PageID=48&SiteID=7&LangID=0&MenuID=5&SubMenuID=69&SponsorID=50 (2004).
5. M. Huang, in *Global Symposium on Women in Fisheries* (World Fish Centre, Penang, Malaysia, 2002), pp. 49–53.
6. Data from Food and Agriculture Organisation, Fisheries Information Division; see www.fao.org.

Taxonomists and Conservation

Q. D. WHEELER *ET AL.* ARGUE FOR A redefinition of the role and job of taxonomists in order "to create a legacy of knowledge for a planet that is soon to be decimated" ("Taxonomy: impediment or expedient?", Editorial, 16 Jan., p. 285). At some time in the past, scientists, and by extension their professional organizations, defined the role of scientists as dispassionate providers of information for policy-makers. Values need not intrude, as they might bias the information. For scientists and their societies to promote the description of what is being decimated, without attempting to stop it, can only be seen as blind adherence to an obsolete and dangerous perception of their role in society. Like all other groups in society, scientists have self-interest; they have descendants and values. They are far better trained to predict the future than politicians, and the public understands this. If AAAS and other scientific organizations fail to advocate sensible population, conservation, and environmental policies, then their silence will certainly equal death. Wheeler *et al.* have not gone far enough in their call for redefining the role of taxonomists. It is time for scientific societies to step up to the plate and commit their considerable clout to the public debate about preservation of the planet. Otherwise, they invite the destruction that looms on the horizon.

JAMES T. MARTIN
College of Osteopathic Medicine of the Pacific, Western University of Health Sciences, 309 East 2nd Street, Pomona, CA 91766, USA.

Response

MARTIN SUGGESTS THAT A FOCUS BY taxonomists on documentation of species and clade diversity possibly invites a greater level of species extinction by not couching its arguments explicitly in terms of conservation. Knowledge of Earth's species diversity and its patterns of distribution is precisely what conservation biologists and decision-makers need to make scientifically informed priorities in efforts to preserve life on Earth. Nothing could be more important, noble, or urgent than to conserve as much of life's diversity as possible for the future. However, there is a parallel and equally pressing need to explore life on Earth to assure as much baseline knowledge as possible, to document those components of diversity that will ultimately not survive. This burden of discovery and documentation rests heavily on taxonomists and the museum community. We seem to have condemned future generations to confront growing numbers of environmental problems in a world biologically impoverished to a greater or lesser extent; we need not ask them to do so in utter ignorance of the products of billions of years of evolution. This exploration of the life of an entire planet is a tall order for an ill-supported community. Taxonomists are unique and essential partners in successful plans to preserve life and its diversity, but to do so at the expense of what they alone

Letters to the Editor

Letters (~300 words) discuss material published in *Science* in the previous 6 months or issues of general interest. They can be submitted through the Web (www.submit2science.org) or by regular mail (1200 New York Ave., NW, Washington, DC 20005, USA). Letters are not acknowledged upon receipt, nor are authors generally consulted before publication. Whether published in full or in part, letters are subject to editing for clarity and space.

can contribute to the advance of knowledge would be a tragic mistake.

QUENTIN D. WHEELER,[1] PETER H. RAVEN,[2]
EDWARD O. WILSON[3]

[1]Department of Entomology, Cornell University, Ithaca, NY 14853, USA. [2]Missouri Botanical Garden, St. Louis 63166–0299, MO, USA. [3]Museum of Comparative Zoology, Harvard University, Cambridge, 02138 MA, USA.

Taxonomists and the CBD

IN THEIR EDITORIAL "TAXONOMY: IMPEDIMENT or expedient?", Q. D. Wheeler *et al.* make a strong case for the internationalization of taxonomy through a cyber-infrastructure that would give taxonomists and museums access to the right tools for documenting species diversity (16 Jan., p. 285). Most biologists are familiar with the biodiversity crisis, but not with the Convention on Biological Diversity (CBD), not mentioned by Wheeler *et al.*, which would govern such a globalized taxonomy (*1*). The CBD was instrumental in creating a global awareness of the "taxonomic impediment"—the incomplete knowledge of taxa and the dearth of taxonomists worldwide (*2*). This impediment is most acute in tropical, developing nations, which contain most of the world's biodiversity, yet produce far fewer taxonomists than developed countries. Two crucial ways to address the problem are (i) increased study of taxa in developing nations and (ii) increased taxonomic training in developing nations. The CBD provides a regulatory framework for these solutions (*3*), yet most taxonomists are little aware of this new "global regime" that affects their professional lives.

With the highest percentage of taxonomists of developed nations, the United States must shoulder much of the responsibility in overcoming the incomplete knowledge of taxa and the dearth of taxonomists in biodiversity-rich countries. This necessitates an understanding of the CBD by U.S. taxonomists. Because of greater institutional engagement, U.S. taxonomists at herbaria, museums, botanic gardens, and zoos tend to be more aware of the CBD than those at universities; however, U.S. universities need to become more engaged with the CBD because most U.S. taxonomists work at universities.

Universities, taxonomists, and funding agencies must work together to build the institutional support necessary to address CBD-related issues, such as the regulatory maze associated with collecting biological samples, and the international collaboration and training required to do so. If not seen in a larger context, these regulations tend to be viewed as annoying bureaucratic hurdles whose ethical and sociopolitical dimensions are invisible (*4*).

R. GEETA, ANDRE LEVY, J. MATT HOCH,
MELISSA MARK

Department of Ecology and Evolution, State University of New York, Stony Brook, NY 11794, USA.

References

1. See www.un.org/geninfo/bp/enviro.html.
2. See CBD Conference of the Parties II/8 decision (available at www.biodiv.org/decisions/default.aspx?m=cop-02&d=08) "The Darwin Declaration" of the Australian Biological Resources Study (available at www.deh.gov.au/biodiversity/abrs/publications/other/darwin/).
3. See related article of the CBD: Article 7, Identification and Monitoring; Article 12, Research and Training; Article 15, Access to Genetic Resources; Article 16, Access to and Transfer of Genetic Resources; Article 17, Exchange of Information; Article 18, Technical and Scientific Co-operation (available at www.biodiv.org/convention/articles.asp).
4. A. C. Revkin, "Biologists sought a treaty; now they fault it," *N.Y. Times*, 7 May 2002, p. F1.

Response

GEETA *ET AL.* EXPRESS CONCERN THAT OUR call for a taxonomic cyber-infrastructure was made without cognizance of the CBD or the urgent needs for taxonomic capacity in developing nations. Space constraints prohibited acknowledgment of the impressive and important gains made as a result of international activities growing from the CBD. The so-called taxonomic impediment can only be removed when taxonomy is transformed into a modern, efficient science. Our proposal is to address what taxonomists need to do so that they can work rapidly and efficiently through a virtual cyber-tool that opens access to sophisticated digital instruments, specimens, data, and literature—the sum of taxonomic and natural history knowledge. While this "tool" would permit taxonomists in the United States to do their work much better and faster, a major impact of the proposal would be to help level the playing field for scientists at smaller institutions and in developing nations, through remote access to virtual libraries, museums, and knowledge bases. Another positive impact would be the facilitation of multi-investigator, multi-institutional, and multi-national collaborations to accelerate the pace of species discovery, description, analysis, and classification, again to the immediate benefit of colleagues and students in developing nations. The kind of community cooperation described by Geeta *et al.* is, as they suggest, essential to success on all these fronts.

QUENTIN D. WHEELER,[1] PETER H. RAVEN,[2]
EDWARD O. WILSON[3]

[1]Department of Entomology, Cornell University, Ithaca, NY 14853, USA. [2]Missouri Botanical

Garden, St. Louis 63166–0299, MO, USA. [3]Museum of Comparative Zoology, Harvard University, Cambridge, 02138 MA, USA.

Taxonomy: Exploring the Impediment

THE POSSIBILITIES FOR DRAMATICALLY improving taxonomic output painted by Q. D. Wheeler *et al.* in their Editorial ("Taxonomy: impediment or expedient?", 16 Jan., p. 285) are exciting and necessary. However, unless these technical enhancements are matched by sociological changes by both providers and users of taxonomic information, their vision is unattainable.

The 1.78 million of Earth's species that have been described represent at best 42% of the total, and the expectation that taxonomists can rapidly name any sample is unrealistic. Wheeler *et al*. address this. However, an increase in taxonomic output must be matched by products that meet the needs and expectations of the wider user community. Despite this, the ratio between numbers of taxonomists and available funding to the number of species to be studied drives taxonomists to focus on core tasks rather than on developing "user-friendly" products.

Identifications, identification aids, and inventories require considerable time and museum resources, although funding bodies, holding the perception that these are available, rarely fund them. Funders recognizing the scale of work find it difficult to prioritize and may see the problem as intractable and unfundable.

Furthermore, career development and peer recognition accrue more from papers in *Science* and peer-reviewed journals than from field guides, Web pages, or identification handbooks. Career progression and institutional recognition exert selection pressure in favor of traditional research products. Many funding bodies also expect outputs of high-impact, cutting-edge science, published in key journals. This tendency leads to grants for developing novel methodologies rather than for implementing existing ones.

Solving these problems will require agreement about priorities. The CBD has highlighted many of these issues and the U.S. National Science Foundation, the UK Darwin Initiative, and Australian Biological Resources Study are leading the way in recognizing the trade-off between methodology development and implementation. Users must also ensure that their needs for taxonomic products are addressed in their project design and grant applications.

Taxonomic institutions should reconsider their functions, performance indicators, and appraisal criteria. The importance of outputs for nontaxonomists should be raised and impact assessment mechanisms devised. Because taxonomic and other institutions compete for funds, the process must involve discussions with supporting government departments and universities to ensure that novel performance indicators are agreed upon. If constructive action is not taken, we fear that, improved methodologies or not, taxonomy will fail to meet its users' needs and expectations, leading to further loss of a vital science, biodiversity, and human well-being.

CHRISTOPHER H. C. LYAL[1] AND ANNA L. WEITZMAN[2]
[1]The Natural History Museum, Cromwell Road, London SW7 5BD, UK. [2]The National Museum of Natural History, Smithsonian Institution, Washington, DC 20560, USA.

Museum Collections and Taxonomy

TAXONOMY IS A CRITICAL TOOL IN understanding biodiversity, and we applaud the view taken by Q. D. Wheeler *et al.* ("Taxonomy: impediment or expedient?", Editorial, 16 Jan., p. 285) that natural history collections and an evolving cyberinfrastructure are central to the taxonomic mission. But their vision needs to be even bolder if we are to accomplish related grand challenges such as documenting the diversity of life, deciphering the Tree of Life, determining how biotas and their ecosystems shape global environmental systems, and creating a universal biioliteracy that enables practical outcomes and education for society.

Innovative tools such as genomic and biodiversity informatics and molecular-based identification can, for the first time, make these grand challenges attainable while there is still enough biodiversity left to matter. One critical piece of data is the 300 years of information associated with approximately 3 billion specimens of animals and plants in museums and herbaria worldwide (*1*–*5*). Wheeler *et al.* worry about some of these data being "outdated or unreliable." Yes, specimen collections and their databases are imperfect, requiring taxonomic and geospatial updating and verification. But these improvements are now ongoing, while at the same time we deploy verified collections data for powerful analyses of environmental and societal phenomena, such as the spread of invasive and disease species, biosecurity, and the effect of climate change on species distributions and conservation. When museums use modern infor-

matics tools to digitize and fully share specimen data, they are fostering the collections and their information for research on the very biodiversity phenomena that those collections were intended to help elucidate (*6*–*9*).

Informatics complements expertise in taxonomic and morphological research, which is essential to understanding the complexity of life. But the biodiversity community needs to automate large segments of the process of species discovery and documentation using rapid identification with unique gene sequences and informatics-mediated taxonomic tools (*5*, *8*–*10*). From the onset, large-scale floral and faunal studies should be Web-mediated digital library projects, with species treatments published online, and the biotic information disseminated by instant, open-access networks that empower the scientific community, the public, and policy-makers.

DOUGLAS CAUSEY,[1] DANIEL H. JANZEN,[2] A. TOWNSEND PETERSON,[3] DAVID VIEGLAIS,[3] LEONARD KRISHTALKA,[3] JAMES H. BEACH,[3] EDWARD O. WILEY[3]

[1]Museum of Comparative Zoology, Harvard University, 26 Oxford Street, Cambridge, MA 02138, USA. [2]Department of Biology, University of Pennsylvania, 415 South University Avenue, Philadelphia, PA 19104, USA. [3]Biodiversity Research Center, University of Kansas, Lawrence, KS 66045, USA.

References

1. S. E. Miller, W. J. Kress, C. Samper K., *Science* **303**, 310 (2004).
2. A. V. Suarez, N. D. Tsutsui, *BioScience* **54**, 66 (2004).
3. L. Krishtalka, P. S. Humphrey, *BioScience* **50**, 611 (2000).
4. J. Kaiser, *Science* **284**, 888 (1999).
5. D. H. Janzen, in *Plant Conservation: a Natural History Approach*, J. Krupnick, J. Kress, Eds. (Univ. of Chicago Press, Chicago, IL, in press).
6. E. Pennisi, *Science* **289**, 2306 (2000).
7. A. T. Peterson, V. Sanchez-Cordero, C. B. Beard, J. M. Ramsey, *Emerg. Infect. Dis.* **8**, 662 (2002).
8. A. T. Peterson *et al.*, *Nature* **416**, 626 (2002).
9. D. A. Vieglais, E. O. Wiley, C. R. Robins, A. T. Peterson, *Oceanography* **13**, 10 (2000).
10. P. D. N. Hebert, A. Cywinska, S. L. Ball, J. R. deWaard, *Proc. R. Soc. London B* **270**, 313 (2003).

Taxonomy and Natural History

ALTHOUGH I WHOLEHEARTEDLY CONCUR WITH the vital message in Q. D. Wheeler *et al.*'s Editorial "Taxonomy: impediment or expedient?" (16 Jan., p. 285), I would also argue the case for natural history. A taxonomic understanding of biodiversity is clearly an essential complement to the study of ecosystem structure and dynamics, but good, reliable natural history studies of organisms, often relegated to a backstage in setting research funding priorities, provide yet another essential underpinning of understanding biodiversity. To answer the challenging question about an organism, "what does it do for a living?", is a compelling and necessary partner to a plea for strengthening the research infrastructure for taxonomic studies. Museum natural history collections and studies on the lifestyles of the taxonomic units that comprise them must go hand in hand when defining funding priorities for biodiversity studies.

ALLEN M. YOUNG

Milwaukee Public Museum, 800 West Wells Street, Milwaukee, WI 53233, USA.

CORRECTIONS AND CLARIFICATIONS

Special section on Immunotherapy: News: "Putting tolerance to the test" (9 July p. 194). The name of Lloyd Kasper of Dartmouth College was misspelled.

TECHNICAL COMMENT ABSTRACTS

COMMENT ON "Network Motifs: Simple Building Blocks of Complex Networks" and "Superfamilies of Evolved and Designed Networks"

Yael Artzy-Randrup, Sarel J. Fleishman, Nir Ben-Tal, Lewi Stone

Milo *et al.* (Reports, 25 October 2002, p. 824, and 5 March 2004, p. 1538) used network randomization schemes to test statistically for the presence of evolutionary design principles in complex biological and synthetic networks. The method identified significant "network motifs" (nonrandom recurring patterns of interconnections) to imply that evolutionary selection has been at play. We show that the approach may be inappropriate in a number of circumstances.

Full text at www.sciencemag.org/cgi/content/full/305/5687/1107c

RESPONSE TO COMMENT ON "Network Motifs: Simple Building Blocks of Complex Networks" and "Superfamilies of Evolved and Designed Networks"

Ron Milo, Shalev Itzkovitz, Nadav Kashtan, Reuven Levitt, Uri Alon

Our approach detects network motifs; it does not explain why they appear. That network motifs are selected for their function is one possible hypothesis, which is supported by recent experiments on gene networks. The toy hypotheses used in the comment, a random-lattice model for neurons and a preferential-attachment model for gene networks, do not capture the subgraph profiles of the corresponding real networks.

Full text at www.sciencemag.org/cgi/content/full/305/5687/1107d

Turn to page 1171

Comment on "Network Motifs: Simple Building Blocks of Complex Networks" and "Superfamilies of Evolved and Designed Networks"

Recently, excitement has surrounded the application of null-hypothesis approaches for identifying evolutionary design principles in biological, technological, and social networks (*1*–*13*) and for classifying diverse networks into distinctive superfamilies (*2*). Here, we argue that the basic method suggested by Milo *et al*. (*1*, *2*) often has limitations in identifying evolutionary design principles.

The technique is relevant for any network that can be notated schematically as a directed graph of N nodes (for example, representing neurons) and a set of edges or links between pairs of nodes (for example, synaptic connections). In particular, the approach is able to identify unusually recurring "network motifs"—patterns of interconnections among a small number of nodes (typically three to five) that are significantly more common in real networks than expected by chance (*1*–*13*). Overabundance is taken to mean that the motifs are the manifestation of evolutionary design principles favored by selection in biological or synthetic systems (*1*–*8*).

In statistical parlance, the basic method [which has a long history in theoretical biology (*10*–*13*)] tests a "random null hypothesis" by statistically comparing the distribution of motifs in an observed network with that found in a computer-generated ensemble of appropriately randomized networks. Over and above the realistic constraint that the degree distribution of incoming and outgoing links to every node must be maintained (*14*), the edges in the randomized network are connected between nodes completely at random and without preference. Such randomized networks are considered null in that their structure is generated by a process free of any type of evolutionary selection acting on the network's constituent motifs. Rejection of the null hypothesis has thus, in many studies, been taken to represent evidence of functional constraints and design principles that have shaped network architecture at the level of the motifs through selection (*1*–*13*).

However, the method outlined above can lead to the wrong interpretations if the underlying null hypothesis is not posed carefully. For example, using this approach, Milo *et al*. (*1*) identified several significant network motifs in the neural-connectivity map of the nematode *Caenorhabditis elegans*. However, in the case of *C. elegans*, neurons are spatially aggregated and connections among neurons have a tendency to form in local clusters (*15*). Two neighboring neurons have a greater chance of forming a connection than two distant neurons at opposite ends of the network. This feature of local clustering, though, is not reflected in the baseline randomized networks used by Milo *et al*. (*1*, *2*), in which the probability of two neurons connecting is completely independent of their relative positions in the network (Fig. 1). The test is not null to this form of localized aggregation and will thus misclassify a completely random but spatially clustered network as one that is nonrandom and that has significant network motifs.

Analysis of a "toy network" (Fig. 1) illustrates what can go wrong. In this network, the nodes are randomly connected preferentially to nearby neighbors, but with a probability that falls off for more distant neighbors (a Gaussian distribution is used). Although the toy network is built devoid of any rule selecting particular motifs for their functions, we find that the same network motifs identified by Milo *et al*. (*1*) for *C. elegans* are present, and the random null hypothesis must be rejected (Fig. 1). Thus, the statistically significant motifs found in *C. elegans* (*1*) are more likely to be the result of the inherently localized partitioning of the nematode's connectivity network than a property that emerges from the action of evolutionary forces selecting particular motifs for their specific functions. It is not our goal in this case to construct a model that realistically captures the distribution of motifs as found in *C. elegans*, but merely to explore the implications of choosing an incomplete null model. Having said that, it is still somewhat surprising that the simple "toy model" reproduces the distribution (significance profile) of all three-node motifs with reasonable realism.

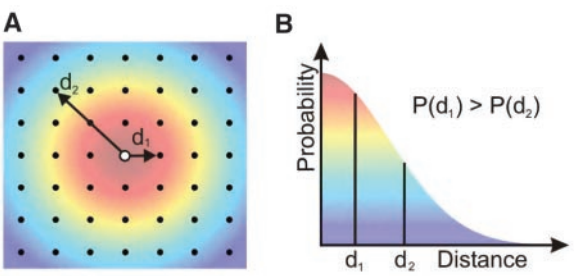

C

Motif	Feed-forward	Bi-fan	Bi-parallel
Observed	42	347	65
Mean	27.1	18.83	43.32
Std.	5.33	8.63	6.4
Z score	2.79	38.02	3.38

Fig. 1. (**A**) Construction of Gaussian "toy network." We used a 30 by 30 grid of 900 nodes. Edges were added on the basis that the probability P of two nodes being connected reduces with the distance d between them. Thus, $P(d_1) > P(d_2)$ when $d_1 < d_2$. This feature will be present to some degree in neural networks such as that of *C. elegans* (*14*). (**B**) Color-coded probability $P(d)$ of connecting to a node as a function of distance for the Gaussian toy network. (**C**) Overrepresentation of motif patterns in the Gaussian toy network. We focused on three motif patterns (feedforward, bi-fan, and bi-parallel) found in (*1*) to be significantly overrepresented in the *C. elegans* neural map. The observed number of each motif, as counted in the Gaussian toy network of (A), was compared with the mean number of motifs counted in 2000 randomized networks (*14*). For all three cases, the Z scores $\left(\frac{\text{Observed - Mean}}{\text{Std.}}\right)$ were larger than 2, signifying that the null hypothesis can be rejected and all motifs are significantly overrepresented.

Many biological and synthetic networks, such as the metabolic and transcription networks (*9*) and the World Wide Web (*16*), are characterized by a scale-free distribution of links to every node. In scale-free networks, the probability of a node having k connections obeys the power law $p(k) \sim k^{-\gamma}$ (with $\gamma > 2$)—that is, most nodes have few connections and a few nodes have many connections. It has been argued (*16*) that some biological scale-free networks are generated by the rule of preferential attachment, a

rule that in itself does not include any type of selection for or against particular motifs. We have used two variants of the preferential-attachment rule (*17*) to generate toy networks, and have then analyzed their motif structure. Using the first variant, we find that the feedforward loop (FFL, shown schematically in Fig. 1C) is always significantly overrepresented ($>2\sigma$ from the mean) compared with the randomized null networks, which implies that the motif has been favored by evolution. In contrast, for the second variant, the FFL is significantly underrepresented, which indicates that the motif has been disfavored. As such, the actual process by which a network is generated, even if it is free of selection for or against particular motif functions, can strongly bias an analysis that seeks to determine the quantitative significance of motifs.

Similar problems arise when applying the approach to studying complex ecological food webs (*10*–*13*). In these systems, each node represents an organism, and an edge between two organisms indicates that one feeds on the other. Food webs are nonrandom structures largely governed by trophic relationships; randomizing feeding links in a food-web network and testing the random null hypothesis serves at best only to trivially prove this point. Unsurprisingly, Milo *et al*. (*1*) find nonrandom overrepresented network motifs that are consistent with simple trophic relationships such as predator–prey–resource interactions. From an ecological perspective, little can be learned from rejecting the possibility that the food web is random. It may be worthwhile in the future to seek ways of posing the null hypothesis in a more sophisticated ecological framework (*10*–*13*).

In summary, for all of these examples, the null hypothesis test suggested the involvement of evolutionary design principles in random toy networks that were generated without the involvement of any fitness-based selection process. The only possible resolution to this problem is to reformulate the test in a manner that is able to identify functional constraints and design principles in networks and to discriminate them clearly from other likely origins, such as spatial clustering.

There is no denying that the network randomization approach has a certain charm in facilitating diverse and multidisciplinary cross-system comparisons in the search for common universal network motifs, design principles, and characteristics defining distinctive network superfamilies (*1*, *2*). Indeed, this approach has stimulated theoretical and experimental work that has demonstrated the utility of certain motifs in tasks such as information processing (*18*, *19*). However, given the dangers sketched above, any cross-system analysis may be very fragile and will be prone to comparing network motifs that are found to be statistically significant because of an ill-posed null hypothesis. Moreover, the method described in (*2*) forces a common reference frame for comparing motif significance profiles (distribution and significance of all possible motifs) of networks, even if they are of different origins—for example, neural networks, for which a null model based on spatial clustering may be justified, versus transcription networks, for which such a null model would be unsuitable. Thus, comparisons mediated through a common but inappropriate reference frame may give the wrong impression that different networks are in fact similar with respect to their motif significance profile. Clearly, these techniques need to be developed further before design principles can be deduced with confidence (*20*).

Yael Artzy-Randrup*
Biomathematics Unit
Department of Zoology
Tel Aviv University
Ramat Aviv, Tel Aviv, 69978, Israel

Sarel J. Fleishman*
Department of Biochemistry
Tel Aviv University

Nir Ben-Tal
Department of Biochemistry
Tel Aviv University

Lewi Stone†
Biomathematics Unit
Department of Zoology
Tel Aviv University
**These authors contributed equally to this work.*

†*To whom correspondence should be addressed. E-mail: lew521@yahoo.com*

References and Notes

1. R. Milo *et al*., *Science* **298**, 824 (2002).
2. R. Milo *et al*., *Science* **303**, 1538 (2004).
3. S. Maslov, K. Sneppen, *Science* **296**, 910 (2002).
4. T. I. Lee *et al*., *Science* **298**, 799 (2002).
5. S. Shen-Orr, R. Milo, S. Mangan, U. Alon, *Nature Genet*. **31**, 64 (2002).
6. G. C. Conant, A. Wagner, *Nature Genet*. **34**, 264 (2003).
7. N. Kashtan, S. Itzkovitz, R. Milo, U. Alon, *Bioinformatics*, in press.
8. S. Wuchty, Z. N. Oltvai, A. L. Barabasi, *Nature Genet*. **35**, 176 (2003).
9. N. Guelzim, S. Bottani, P. Bourgine, F. Kepes, *Nature Genet*. **31**, 60 (2002).
10. E. F. Connor, D. Simberloff, *Ecology* **60**, 1132 (1979).
11. A. Roberts, L. Stone, *Oecologia* **83**, 560 (1990).
12. L. Stone, A. Roberts, *Oecologia* **85**, 74 (1990).
13. N. J. Gotelli, G. R. Graves, *Null Models in Ecology* (Smithsonian Institution Press, Washington, DC, 1996).
14. Randomized networks were generated by randomly shuffling edges in the graph while leaving the number of ingoing and outgoing edges of every node unchanged. This was achieved (*1*–*13*) by randomly selecting a pair of edges, U→V and X→Y, and switching them to U→Y and X→V if these edges did not already exist. The switching procedure was implemented typically thousands of times to create a randomized matrix. The random switching ensures that the probability of two nodes being connected is effectively independent of the distance between them.
15. J. G. White, E. Southgate, J. N. Thomson, S. Brenner, *Philos. Trans. R. Soc. London Ser. B* **314**, 1 (1986).
16. A. L. Barabasi, R. Albert, *Science* **286**, 509 (1999).
17. The preferential-attachment rule builds up networks so that each new node added to the system connects preferentially to well-connected nodes (hubs). In the first variant of the rule we used, toy networks were built up with older nodes directed to newer ones; in the second variant, edges were directed randomly.
18. S. Mangan, A. Zaslaver, U. Alon, *J. Mol. Biol*. **334**, 197 (2003).
19. S. Mangan, U. Alon, *Proc. Natl. Acad. Sci. U.S.A*. **100**, 11980 (2003).
20. A possible resolution to the problem in the context of molecular networks would require waiting for the availability of sufficient data on networks from several organisms. It might then be possible to test (*8*) whether some functions, such as the transcriptional control of a particular protein, in diverse organisms are preferentially governed by a certain motif, which in turn would strengthen the case for the role of selection.
21. We thank A. Ayali for his very helpful advice and suggestions. We are grateful for the support of the James S. McDonnell Foundation and the Internal Tel Aviv University Research Fund.

19 April 2004; accepted 21 July 2004

Response to Comment on "Network Motifs: Simple Building Blocks of Complex Networks" and "Superfamilies of Evolved and Designed Networks"

Our previous work (*1*) presented a phenomenological observation on real-world networks: They show distinct subgraph significance profiles (SP) when compared with randomized networks with the same degree sequence as the real networks. This observation calls for a theory—a model that prescribes evolutionary dynamics or constraints that, once used to evolve a network, yield the observed SPs. The SP method also provides a way to test whether a given theoretical model actually reproduces the local structure of the real network. Selection of network motifs for their function is one such possible theory, which, as we mention below, can and should be tested experimentally; it is certainly not the only possible theory (*1*, *2*).

Along these lines, Artzy-Randrup *et al.* (*3*) comment that the observed network motifs (*2*) can arise by various different mechanisms, not only by evolutionary selection for function. They proposed two such theoretical models ("toy networks") as counterexamples, showing some of the network motifs found in the neuronal synaptic network of *Caenorhabditis elegans* and in the transcription network of *Escherichia coli*. The models were (i) a random-lattice (geometrical) model, in which neurons that are close in space tend to form synapses and (ii) a preferential-attachment (PA) model for transcription networks, in which networks are grown so that genes preferentially link to genes that already have many connections. These models were shown in the comment to display some of the same network motifs (overrepresented subgraphs) as do the real-world networks. Here, we demonstrate that if one wishes to test whether these toy mechanisms can explain the real-world networks, one may compare the structure they produce more fully to the real networks, using the SP approach. We demonstrate that both models give SPs that are quite different from the SPs of the real networks: They produce many strong motifs that do not appear in the real networks.

We begin with the random-lattice model for the neuronal network. The random-lattice model (*1*) yields feedforward loops, just as does the real neuronal network. However, the SP of lattice models shows two three-node subgraphs that are not found in the real network (Fig. 1A). One is the 3-loop, a cycle made of three nodes (subgraph 8), and the second is a 3-loop with one mutual edge (subgraph 11). These subgraphs are generally overrepresented in random-lattice models, regardless of the dimensions of the lattice. For example, based on symmetry, the ratio of feedforward loops and 3-loops can be generally shown to be 3:1 in lattice models. In the real neuronal network, the ratio is 22:1 (about 1500:70). Thus, geometry or clustering alone does not seem to explain the structure of the neuronal network of *C. elegans*. It seems more likely to us that the spatial arrangement and the connectivity of the neurons coevolved to supply the needed, highly designed circuitry (for example, the scarcity of 3-loops in the real neuronal network may be the result of evolutionary selection against unwanted designs within a geometrically constrained neural architecture). The hypothesis that the neuronal network motifs function as recurring circuitry elements should be tested experimentally.

We now consider the PA model, which can produce feedforward loops, a common motif in the *E. coli* transcription network. However, when considering four-node subgraphs, one finds that the PA model shows many subgraphs that are not found in the real network (Fig. 1B). This includes feedforward loops connected to form four-node patterns in different ways (Fig. 1B, subgraphs 3 and 6 to 9) that are not realized in the natural network. These subgraphs are generally found in other variants of PA models that generate feedforward loops. Thus, PA processes do not seem sufficient to explain the evolution of this real transcription network. Again, it seems likely that transcription networks rapidly rewire over evolutionary time scales to adapt to the environment (*4*, *5*), and thus that their connectivity is not just a vestige of frozen history based on attachment rules.

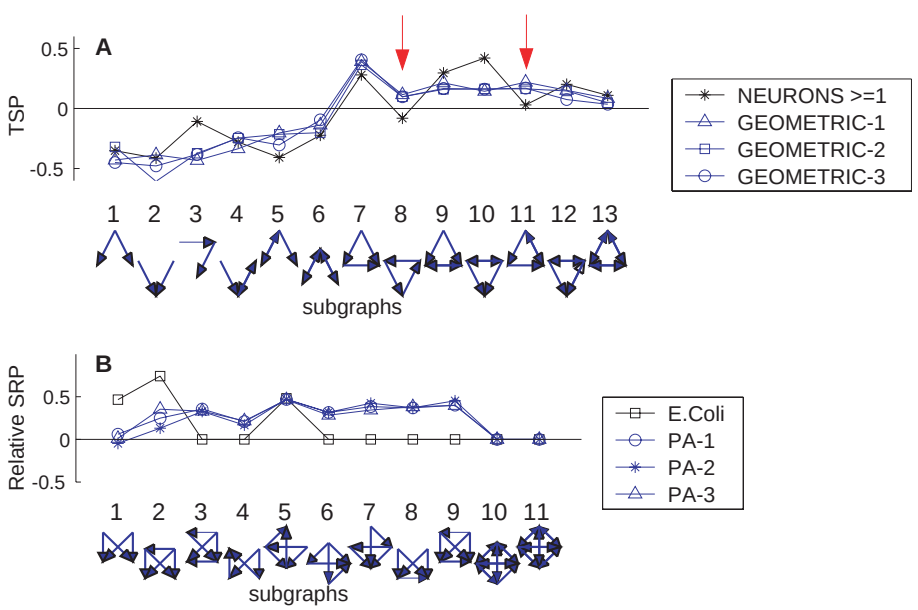

Fig. 1. Comparison of the local structure of real-world networks and theoretical model networks. (**A**) Triad significance profile (TSP) of the *C. elegans* neural network (*13*) (black) and of three instances of random-lattice networks (blue). In the lattice networks, directed connections were formed at random between neighboring nodes arranged on a two-dimensional lattice (*1*). Red arrows indicate subgraphs that occur in the random-lattice network much more often than in the real network. (**B**) The four-node subgraph ratio profile (SRP) for the *E. coli* transcriptional network (*14*) (black) and three instances of model networks created by a directed preferential-attachment (PA) process (*15*) (blue). The PA networks are grown by adding new nodes, such that the probability of connecting a directed edge to an existing node increases with the number of edges it already has.

It is notable that thinking of biological network motifs as information-processing units is not an assumption of the present approach, but rather a

hypothesis that is, in principle, experimentally testable. Indeed, experimental and theoretical work on network motifs in transcription networks has yielded support for their role as information-processing units, performing tasks such as asymmetric filtering [coherent feedforward loop motif (*6*)], response acceleration [negative autoregulation motif (*7*)], pulse production [incoherent feedforward loop motif (*8*, *9*)], and temporal pattern generation [single-input module motif (*10*, *11*)]. It is therefore possible to suggest that these wiring patterns were selected based on their functions.

We believe that the search for theoretical models to explain the observed SPs will be a fruitful one and will help identify the mechanisms or evolutionary principles that lead to the observed local structure (or at least rule out evolutionary hypotheses that do not). Care should be taken, because distinct models could give rise to very similar structures; SPs of higher order subgraphs as well as topological generalizations of motifs (*12*) may help give increasing resolution to distinguish between models and real networks.

The present approach based on degree-preserving randomized networks is a simple first step for comparing networks and for discovering potentially interesting overrepresented and underrepresented patterns for further analysis. More elaborate null-hypothesis models could in principle be used to help highlight interesting patterns and to test models for their origin.

Ron Milo
Shalev Itzkovitz
Nadav Kashtan
Reuven Levitt
Uri Alon*
Departments of Molecular Cell Biology and Physics of Complex Systems, Weizmann Institute of Science Rehovot 76100, Israel
**To whom correspondence should be addressed. E-mail: urialon@weizmann.ac.il*

References

1. R. Milo *et al.*, *Science* **303**, 1538 (2004).
2. R. Milo *et al.*, *Science* **298**, 824 (2002).
3. Y. Artzy-Randrup, S. J. Fleishman, N. Ben-Tal, L. Stone, *Science* **305**, 1107 (2004); www.sciencemag.org/cgi/content/full/305/5687/1107c.
4. S. A. Teichmann, M. M. Babu, *Nature Genet.* **36**, 492 (2004).
5. G. C. Conant, A. Wagner, *Nature Genet.* **34**, 264 (2003).
6. S. Mangan, A. Zaslaver, U. Alon, *J. Mol. Biol.* **334**, 197 (2003).
7. N. Rosenfeld, M. B. Elowitz, U. Alon, *J. Mol. Biol.* **323**, 785 (2002).
8. S. Mangan, U. Alon, *Proc. Natl. Acad. Sci. U.S.A.* **100**, 11980 (2003).
9. S. Basu, R. Mehreja, S. Thiberge, M. T. Chen, R. Weiss, *Proc. Natl. Acad. Sci. U.S.A.* **101**, 6355 (2004).
10. A. Zaslaver *et al.*, *Nature Genet.* **36**, 486 (2004).
11. M. Ronen, R. Rosenberg, B. I. Shraiman, U. Alon, *Proc. Natl. Acad. Sci. U.S.A.* **99**, 10555 (2002).
12. N. Kashtan, S. Itzkovitz, R. Milo, U. Alon, *Phys. Rev. E.*, in press.
13. J. G. White, E. Southgate, J. N. Thomson, S. Brenner, *Philos. Trans. R. Soc. London Ser. B* **314**, 1 (1986).
14. S. Shen-Orr, R. Milo, S. Mangan, U. Alon, *Nature Genet.* **31**, 64 (2002).
15. A. L. Barabasi, R. Albert, *Science* **286**, 509 (1999).

19 May 2004; accepted 2 August 2004

CHEMISTRY

Molecular Topographies

David C. Clary

Is it possible to understand in simple pictures how glasses form, how proteins fold, and how atoms bond together to form clusters? Can a unifying description be developed that explains these seemingly different scientific problems? What is the link between understanding these processes and palms, willows, and banyan trees? If you want the answers to these questions, you should read *Energy Landscapes*.

The energy of interaction between molecules depends on the coordinates of all the constituent atoms, and an understanding of the variation of this energy explains many of the thermodynamic and kinetic properties of molecular systems. Being able to understand how systems of atoms and molecules relax to give particular forms of crystals or native states of proteins requires a global understanding of these energies. "Energy landscapes" is a term that is now commonly used to describe the topography of these energies, borrowing the geographically familiar concepts of valleys, ridges, and cols, saddle-like high passes across mountain ranges. This beautifully illustrated book provides a detailed background and description of energy landscapes and gives many examples of how they can be used to explain the properties of atomic and molecular clusters, biomolecules, glasses, and supercooled liquids.

Energy Landscapes
Applications to Clusters, Biomolecules and Glasses
by David J. Wales
Cambridge University Press, Cambridge, 2004. 691 pp. $85, £55. ISBN 0-521-81415-4.

Energy landscapes commonly refer to representations of either potential energy surfaces (that is, the energies of electrons plus nuclear-repulsion energies for fixed atom positions) or free-energy surfaces that also include entropy. As atomic and molecular systems in equilibrium take up positions of the minimum possible free energy, the minima in the complicated topology of the free-energy landscapes play the key role. Furthermore, because processes such as phase transformations in glasses and the folding of proteins depend explicitly on atomic motions, it is necessary to understand how systems move from one minimum to another on the energy landscape via cols (or, in the chemical context, transition states).

The reviewer is in the Department of Physical and Theoretical Chemistry, University of Oxford, South Parks Road, Oxford, OX1 3QZ, UK.

E-mail: david.clary@chem.ox.ac.uk

NOTA BENE: MUSEUMS

Education Can Be Fun

Who better to put together a new science museum in Washington, D.C., than the U.S. National Academy of Sciences (NAS). The recently opened Marian Koshland Science Museum is the brainchild of National Academies member Daniel Koshland Jr. (photo A), who was editor-in-chief of the journal *Science* from 1985 to 1995. Wishing to honor his wife of 52 years, who was also a member of the NAS, Dr. Koshland created an endowment to open a science museum in her name. After 5 years of careful planning by a committee of National Academy members cochaired by Dr. Koshland and his successor at *Science*, Don Kennedy, Washington, D.C.'s newest museum is now open for business.

Marian Koshland Science Museum of the National Academy of Sciences
6th and E Streets NW, Washington, DC.
www.koshland-science-museum.org.


A

In a departure from other science museums and centers, the Marian Koshland Science Museum presents visitors with actual scientific data and examples drawn from published National Academy reports. Geared for adults and children 13 or older, the museum hopes that the exhibits will generate discussion between parents and their adolescent children.

Constrained by space (the museum is only 6000 square feet), the National Academy scientists decided to concentrate on two themes representing scientific research areas that are of direct relevance to policy-makers and the general public. Dr. Koshland in particular is keen to show "how science is relevant to the general public in their everyday lives."

The two principal exhibits explore climate warming and the applications of DNA technology and will be on display until 2006, when they will tour other U.S. cities. They will be replaced by two new exhibits currently in the planning stages whose themes will be drawn from among 75 published NAS reports. With report titles such as "Microbial Threats to Health," "Stem Cells," "The Polygraph and Lie Detection," and "Making the Nation Safer," it is unlikely that the museum will run out of exhibit ideas any time soon.

The first part of the museum is a permanent exhibit that reveals the wonders of science, from the subatomic to the cosmic. A short introductory film takes viewers on a swirling journey through a microscope and telescope. Next are three interactive visual displays that explore several themes introduced in the film, including DNA replication and expansion of the cosmos. The most stunning visual display, however, is "The Lights at Night," derived from NOAA global satellite data, which shows regional hotspots of rampant energy consumption even as we sleep.

The climate warming exhibit opens with a globe coated with two different kinds of plastic that enables visitors to literally feel climate warming in action. The temperature difference between the two halves of the globe represents the temperature 200 years ago (at the start of the Industrial Revolution) and the predicted temperature in 2100. Text panels explain how scientists measure climate change using tree rings; cores of ice, sediment, or coral; and balloon-borne sensors that provide daily readings of upper-air temperature, wind, and humidity. An ingenious sliding plasma screen (photo B) enables visitors to observe year-to-year variations in temperature worldwide, from 1900 to 2000. It is startling to see the map of the United States in 1930 with a large swathe of the country glowing bright orange—a sobering reminder of the devastation wrought by the dust bowl drought. Behind the plasma screen are plotted the actual temperature change data used to compile the interactive video. An adjacent sliding visual shows predicted regional temperature changes up to the year 2100 based on computer modeling.

Wherever possible, video interactives challenge visitors to question their own willingness to address climate warming by per-

CREDIT: MARIAN KOSHLAND SCIENCE MUSEUM

Published by AAAS

For this reason, the early part of the book is largely involved with a description of the computational methods used to determine stationary points and transition states—"exploring the landscape." Later sections of the book describe the detailed structure of such landscapes as well as methods for classifying their properties. A powerful approach exploits disconnectivity graphs. As shown in the figure, these graphs enable the complicated multidimensional topologies of the energy landscapes to be reduced to very simple pictorial forms that connect stationary points. The graphs can be classified into tree-like patterns (such as the palms, willows, and banyans) (see the figure). David Wales, a chemist at Cambridge University, has been a pioneer in exploiting these graphs, and he demonstrates their considerable value in simplifying the description of systems that can depend on thousands of variables.

The book has the particular merit of many excellent figures, which are displayed to develop the ideas of the energy landscape; these allow the rather complicated underlying quantum mechanics and statistical mechanics to be given clear and natural graphical representations. This feature will make the book valuable for those who are not familiar with the theory but who wish to use the energy-landscape concept to help understand the results obtained in their research.

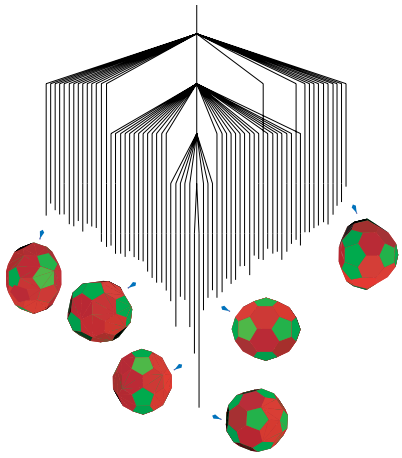

Willow tree depiction of the pathways linking various isomers of C_{60}.

CREDIT: COURTESY DAVID J. WALES

The most difficult aspect of describing molecular interactions for complicated systems is the accurate calculation of their electronic energies. *Energy Landscapes* does not address this aspect, which is essential for the reliable prediction of the properties of molecules. Furthermore, the prediction of many atomic and molecular properties that relate to current cutting-edge experiments requires detailed dynamics calculations that turn the energy landscapes into thermodynamic and kinetic quantities. In the book, Wales hardly touches on the methods used for these calculations. These are areas on the frontiers of molecular simulation research, and they are essential for understanding how systems change their structure with variations of temperature. Also missing from the book is a description of the ultrafast time-resolved experiments that are now starting to provide quantitative information on the stationary points of potential surfaces for condensed phases and biomolecules. Nonetheless, Wales makes an important contribution: *Energy Landscapes* provides a pictorial language that simplifies complicated calculations to a form that can be understood and used by many scientists interested in molecular problems, from undergraduates to those at the frontier of research.

CREDIT: MARIAN KOSHLAND SCIENCE MUSEUM

sonally helping to reduce carbon dioxide levels. In "Consider the Alternatives," visitors are asked to vote on the trade-offs they would be willing to accept, and the display collects the data as part of a Penn State University study. Although many visitors may encourage the planting of more trees or the design of energy-efficient buildings, they are shown by just how much these incentives would increase their monthly household costs. Having noted the number of children who, intrigued by their parents' absorption, commandeered the controls of the display and began randomly pressing buttons, I hope that the museum's computer wizards have introduced sufficient filters to remove erroneous data.

The "Putting DNA to Work" exhibit reveals the many applications of DNA technology. In the section on DNA forensics, an elaborate interactive allows visitors to see how the FBI's combined DNA index system (CODIS) is used to solve crimes. Video screens compare real DNA sequences from several suspects with a DNA sample from the crime scene. As the DNA sequences flash up, visitors can easily see how an exact match at 13 genomic sites clearly identifies the real culprit. In the next example, visitors learn how DNA microarray technology led to the rapid identification of a coronavirus as the cause of the 2002 SARS outbreak.

Visitors are also introduced to the notion of genetically modified organisms: By sliding a knob along a series of corn chromosomes, they can select genes that imbue corn with beneficial traits. The adjacent text panel explains the importance of improving crop yields. It is sobering to discover that to match today's U.S. production of corn, which is grown over just 4% of the continental United States, ancient corn (teosinte) would have to be planted over 12 times as much land.

A great favorite with the younger visitors that I observed is a giant screen that allows users to pick a random six-base DNA sequence and then do a rapid scan of all 3 billion bases in the human genome to see how many matches can be found. One of the simplest displays in the museum (photo C) also evoked more than a few smiles: Visitors must guess how many of their genes match those of a fellow human, a chimp, a mouse, a fruit fly, and a plant.

Looking beyond its elegant displays, the museum is seeking other ways to bring science to the general public. Determined not to be left out of the Washington social scene, the museum is launching a series of evening public programs where visitors can meet the experts. The first of these events will feature a murder scene in the museum, and visitors will be able to quiz several forensic experts about how they would solve the crime using current DNA technology. In another event that combines climate change, genetics, and oenology, visitors will learn about the origins of popular grape varieties and how climate change affects grape quality while sipping local Virginian vintages. The museum is also working with local high schools and has set up a popular intern program in which local high school students are trained to run hands-on science activities at the museum on weekends. With help from these budding young scientists, visitors can enjoy extracting DNA from their cheek cells or examining computer microprocessors under a handheld microscope.

With over 10,000 visitors in 3 months, DC's newest museum proves what all scientists know and the general public always suspected: Science is fun.

–ORLA SMITH

Published by AAAS

INTELLECTUAL PROPERTY

Commons-Based Strategies and the Problems of Patents

Yochai Benkler

The role of intellectual property in science has dramatically increased in the past 25 years. U.S. law has encouraged universities to patent their discoveries and license them commercially, judicial reforms have increased patent protection, and the trend has expanded internationally through trade treaties. The expansion occurred even though economic theory is ambivalent about the effects of patents on welfare and innovation (*1*). Empirical evidence suggests that patents are important in few industries, mostly pharmaceutical (*2*, *3*), and that aggregate effects of strong protection are small and often negative (*4*, *5*). Excessive patent protection has been criticized as impeding scientific research through "anticommons" effects (*6*) and as imposing cost barriers on access to medicines. Proposed solutions usually take the form of legal change, but the emerging model of commons-based production can be implemented by the scientific community without waiting for law reform.

Commons-Based Production

Property, contract, and managerial commands are the basic tools of managing mainstream production. By contrast, production is "commons-based" when no one uses exclusive rights to organize effort or capture its value, and when cooperation is achieved through social mechanisms other than price signals or managerial directions. Large-scale instances of such cooperation are "peer production" (*7*).

Free software is the paradigm of commons-based production, as is the Linux kernel for peer production. Free software is based on a legal innovation, the GNU General Public License (GPL), which has been adopted with variations by 85% of open source projects (*8*). It permits anyone to use the software and to develop it, but no one can appropriate outputs exclusively. It requires improvers to share access to their improvements. The Linux kernel development process added an organizational innovation: It modularized the work and thereby harnessed thousands of volunteer developers and testers (*9*). The measurable quality of free software and its wide adoption have proved its value.

Beyond software, the Internet abounds with commons-based peer production. Wikipedia (http://wikipedia.org) is a multilingual encyclopedia produced by 20,000 volunteers. A major Web index, the Open Directory Project (http://dmoz.org), is produced by 60,000 volunteers. SETI@Home processes radio astronomy data (http://setiathome.ssl.berkeley.edu), combining the excess computer cycles of 4.5 million PCs to create a supercomputer.

Why do people do it? How do they organize without property and contract? Peer production modularizes work so that individuals can contribute at different levels of effort consistent with their motivation; contributions are then integrated into a usable whole. Instead of direct payment, commons-based production relies on indirect rewards: both extrinsic, enhancing reputation and developing human capital and social networks; and intrinsic, satisfying psychological needs, pleasure, and a sense of social belonging. Instead of exclusive property and contract, peer production uses legal devices like the GPL, social norms, and technological constraints on "antisocial" behavior.

Nonproprietary frameworks for scientists. Science has long been the quintessence of nonproprietary production (*10*). Academic freedom to choose one's goals and open distribution of the inputs and outputs of the scientific process are its organizational norms. Some academic projects already offer working models for using the culture of science to solve the problems of patents.

The open bioinformatics movement has focused on developing an open source model, providing open access to tools and research outputs. Visible successes include the Ensembl Genome Browser (www.ensembl.org) and resources offered by the National Center for Biotechnology Information (www.ncbi.nlm.nih.gov).

The Public Library of Science (www.plos.org), based on the e-Biomed proposal (*11*), offers a model of commons-based, peer-reviewed scientific publication. It has a professional staff funded by philanthropic giving and author page charges. Papers published are freely available under a Creative Commons Attribution license. Creative Commons is an organization that created a menu of licenses that provide authors several ways to license their work openly (*12*).

The ArXiv.org e-Print Archive offers a more radical alternative (*13*). Authors post physics papers on a server with no prepublication peer review. Postpublication criticism, a facility for version updating, and a tight-knit academic community where reputation effects are substantial provide accreditation and quality control.

Harnessing nonscientists. National Aeronautics and Space Administration (NASA) clickworkers was an experiment (http://clickworkers.arc.nasa.gov/top) to see if volunteers, working in small increments, could do analysis normally done by a scientist or graduate student. Users were provided an interface that enabled them to mark craters on Mars images. In 6 months, over 85,000 users visited the site, many contributing to the effort. Their automatically computed consensus was equivalent in quality to the markings of a trained scientist (*14*).

Folding@home may be the best-documented distributed computing project. It harnesses contributions of over 572,000 CPUs from 272,000 users. The processing power is used to simulate protein folding without a dedicated supercomputer and has resulted in multiple scientific publications (*15*).

Proposal 1: Publicly Minded Licensing

Patent royalty and licensing revenue provides an insignificant portion of total university revenues (see the table, p. 1111). Revenue from government-sponsored research outweighs patent revenues by an order of magnitude. These facts make it fiscally feasible and likely advantageous for universities to use their intellectual property rights to alleviate impediments of the patent system when applied to research tools and distribution in poor nations. Universities could cooperate to seek wide adoption of open licensing provisions. One model is PIPRA (Public Intellectual Property for Agriculture), a collaboration among agricultural research universities to share their intellectual property and retain rights to use their technologies for subsis-

Yale Law School, Yale University, 127 Wall Street, New Haven, CT 06520, USA. E-mail: yochai.benkler@yale.edu

tence and specialty crop development (*16*). Collectively, universities would have substantial negotiating power with the biotechnology and pharmaceuticals industries.

Universities could adopt two varieties of license: an open research license (ORL) and a developing country license (DCL). An ORL would include two core elements:

Reservation for research. The university would reserve a right to use and nonexclusively sublicense its technology for research and education. This is more permissive than, but consistent with, emerging practice since *Madey* clarified that the research exemption in patent law was illusory (*17*).

Reciprocal nonexclusive license to research. The licensee and any sublicensee would grant back a nonexclusive license to the university to use and sublicense all technology that the licensee develops based on university technology, again, for research and education only.

A DCL would add development, manufacture, and distribution of end-product drugs if distribution is limited to developing nations. It would permit generics to manufacture for developing nations, using the same licensing technique as the GPL.

This approach would alleviate anticommons effects and patent-based limits on global distribution without significantly impacting pharmaceutical revenues. Universities and scientists would lose almost no revenue from end products, but would lose the remote likelihood of appropriating a basic enabling technology. Their gains would be reduced research impediments and improved public perception of universities as public interest organizations, not private businesses. This gain is far from symbolic. Minor increases in public funding of university science would make up for loss of the small probability of striking gold in research tools patents.

SELECTED REVENUES FROM U.S. UNIVERSITIES*

Institution	Revenues (millions $)		
	Total	Licensing and royalties	Government grants and contracts
All universities	227,000	1,270	31,430
Univ. California	14,166	81	2,372
Harvard	2,473	48	416
Stanford	3,475	43	860
Univ. Minn.	1,237	39	324
Florida State	2,646	36	238
Cal Tech	531	27†	268

*Sources for this information are as described (*19*). †Almost half of this amount is in income from a single initial public offering; without that offering, the revenue would be $15.7 million.

Proposal 2: Peer Production

Scientists can complement university licensing practices by adopting peer-production strategies. Although many think that science is too expensive to be done this way, people once thought the same of supercomputing. It would require identification of the components of scientific production and modularization of tasks to minimize the burden on any single contributor.

Initially, anything that can be computer modeled has the same economic characteristics as free software and distributed computing. This is where current proposals for peer production of biomedical research for tropical diseases primarily focus (*18*). Adapting peer production to the laboratory is harder, but specifying its components can mark feasible paths. First, graduate students, post-docs, and scientists are parallel in life-cycle and motivational profile to free software developers. Scientists may be busier, but anyone who can find days to work on unexpected grant applications can find a few minutes or hours to contribute to other goals they value. Second, experiments that can be done with widely available equipment can be designed to fit peer production. Some equipment is ubiquitous and offers redundant capacity. Scientists interested in starting a project must specify the research program in fine-grained modules, preferably executable on widespread equipment—like discrete polymerase chain reaction (PCR) analyses. These could be placed on a Web site to allow contributors to perform analyses when their equipment is free and to upload results to the project site. Others could review and analyze results. In principle, this process could be used for abundant materials, perhaps including some laboratory organisms and animals. The person who builds the platform will require greater investment of effort, but will reap greater rewards. Repeat contributors may become coauthors on papers based on the results. Many contributors could add smaller contributions—spending 2 hours using an otherwise idle machine—for the benefit of finding a new treatment, gaining experience, or mention as a contributor.

Experiments that require expensive equipment that has no downtime, or rare materials, may resist modularization. Some perceived bottlenecks may, however, merely be convenience-oriented and time-saving. A high-throughput process, such as automated sequencing, might be replaced by many scientists working in discrete increments using simpler equipment to achieve acceptable throughput (if sample and reagents availability and cost were solved). As distributed computing has shown, seemingly insurmountable equipment costs may sometimes be resolvable by reorganizing a process. Ultimately the problem of high-cost bottlenecks may limit the extent to which some processes can be made amenable to peer production. If small enough, however, residual costs may be covered by philanthropic and government funding.

Scientists can learn from peer production how to organize their research projects to modularize research tasks and to integrate contributions from many low-intensity collaborators. This will increase their ability to pursue science that affects millions of lives, but cannot pay its way under the present system.

References and Notes

1. K. Arrow, in *The Rate and Direction of Inventive Activity: Economic and Social Factors* [National Bureau of Economic Research (NBER), Cambridge, MA, 1962], p. 609.
2. R. Levin *et al.*, *Brookings Pap. Econ. Activ.* **1987**, 783 (1987).
3. W. M. Cohen *et al.*, *NBER Work. Pap. Ser.* **2000** (w7552) (2000).
4. A. Jaffe, *Res. Policy* **29**, 531 (2000).
5. J. Lerner, *Am. Econ. Rev.* **92** (2), 221 (2002).
6. M. A. Heller, R. S. Eisenberg, *Science* **280**, 698 (1998).
7. Y. Benkler, *Yale Law J.* **112**, 369 (2002).
8. J. Lerner, J. Tirole, *J. Law Econ. Org.* **21**, in press; *NBER Work. Pap. Ser.* **2002** (w9363) (2002).
9. E. Raymond, *The Cathedral and the Bazaar* (O'Reilly, Cambridge, MA, 2001).
10. R. Merton, *The Sociology of Science* (Univ. of Chicago Press, Chicago, 1973).
11. H. Varmus, *E-Biomed: A Proposal for Electronic Publication in the Biomedical Sciences* (NIH, Bethesda, MD, 1999); available at www.nih.gov/about/director/pubmedcentral/ebiomedarch.htm.
12. L. Lessig, *Free Culture* (Penguin, New York, 2004).
13. M. Sincell, *Science* **293**, 419 (2001).
14. B. Kanefsky *et al.*, *32nd Lunar and Planetary Science Conf. Abstr.*, Houston, TX, 12 to 16 March 2001, 1272 (2001); available at www.lpi.usra.edu/meetings/lpsc2001/pdf/1272.pdf.
15. C. D. Snow *et al.*, *Nature* **420**, 102 (2002).
16. R. C. Atkinson *et al.*, *Science* **301**, 174 (2003).
17. *Madey* v. *Duke University*, 307 F.3d 1351 (Fed. Cir. 2002).
18. S. M. Maurer, A. Rai, A. Soli, in *Biotechnology: Essays from Its Heartland* (BASIC & QB3, San Francisco and Santa Cruz, CA, 2004), p. 33; available at www.qb3.org/pdfs/biotech1.pdf.
19. Sources: Aggregate revenues: National Center for Education Statistics, U.S. Dept. of Education, *Enrollment in Postsecondary Institutions, Fall 2001, and Financial Statistics, Fiscal Year 2001* (2003), Table F; Association of University Technology Management, *Annual Survey Summary FY 2002* (AUTM 2003), Table S-12. Individual institutions: publicly available annual reports of each university and/or its technology transfer office for FY 2003.

Published by AAAS

PHYSIOLOGY

Lactic Acid—The Latest Performance-Enhancing Drug

David Allen and Håkan Westerblad

The 2004 Athens Olympics will undoubtedly see many records broken. Improved performances will be attributed to better training, superior genes, or the use of performance-enhancing drugs, both legal and illegal. From a physiological perspective, one of the major limits to improved performance is the decline in muscle function as muscles are used intensively and repeatedly—a phenomenon called muscle fatigue. Many of the approaches used by athletes to enhance their performance, such as creatine supplementation, carbohydrate loading, and training at high altitude, are targeted at the various pathways that contribute to muscle fatigue. For many athletes, coaches, and sports commentators, muscle fatigue and the accumulation of lactic acid (generated from the anaerobic breakdown of glycogen) are more or less synonymous. However, the importance of lactic acid in muscle fatigue is now under scrutiny (*1*). On page 1144 of this issue, Pedersen *et al*. (*2*) present a further challenge to the traditional view with their demonstration that lactic acid, in fact, has beneficial effects on the performance of fatigued muscles. They show in rat muscle fiber preparations that lactic acid influences the activity of chloride ion (Cl^-) channels, which in turn sustains the action potentials that are necessary for muscle contraction.

Enhanced online at www.sciencemag.org/cgi/content/full/305/5687/1112

It was A. V. Hill in 1929 who proposed that the accumulation of lactic acid in muscles contributes to muscle fatigue (*3*). Using preparations of isolated frog muscle removed from solution and kept in nitrogen, Hill showed that, following electrical stimulation, mechanical performance gradually declined as the muscle accumulated large amounts of lactic acid. However, if the muscle preparation was transferred to a saline solution equilibrated with nitrogen, which enabled the lactic acid to diffuse away, muscle performance improved. Such experiments, and their equivalents in mammalian muscle, suggested that accumulation of intracellular lactic acid might be a principal cause of muscle fatigue. The theoretical basis for this idea was provided by Fabiato (*4*), who showed that increased intracellular acidification (acidosis) of muscle due to accumulation of lactic acid blocked force production by the muscle's contractile proteins.

Doubts about the importance of lactic acid in muscle fatigue, however, have accrued since these early studies. For instance, humans deficient in the enzyme myophosphorylase are unable to break down glycogen or accumulate lactic acid, but their muscles fatigue more rapidly than normal (*5*). The direct depressant effect of acidosis on contractile proteins, clearly evident at or below room temperature, is greatly reduced at body temperature (*6*). Work on single muscle fibers has shown that when muscle cells are intentionally rendered acidic, the rate of fatigue remains unchanged (*7*).

It was Nielsen and his colleagues who ushered in a new phase in our understanding of the effects of muscle acidosis (*8*). They argued that the accumulation of extracellular potassium ions (K^+) is a key component of muscle fatigue and showed that force in an isolated muscle declined steeply when the K^+ concentration increased. Importantly, if the muscle was rendered acidic, much of the decline in force was reversed and was accompanied by recovery of action potential generation.

In the new study, Pedersen *et al*. (*2*) take this observation a step further using a preparation of "skinned" single muscle fibers from the rat. In their preparation, the surface membrane of the muscle fiber is removed (mechanical skinning), but the internal network of tubules in the fiber (T-tubules) seals over and retains its functional connection to the sarcoplasmic reticulum. This intriguing preparation can be activated in various ways. Crucially for these experiments, electrical stimulation generates action potentials in the sealed T-tubules and causes normal release of calcium ions (Ca^{2+}) from the sarcoplasmic reticulum, resulting in muscle contraction.

The investigators noted that when action potentials stimulated Ca^{2+} release, mild depolarization of the T-tubules caused a large reduction in contractile force but, as Neilsen *et al*. found (*8*), this effect could be partially reversed by acidosis. Their key observation is that this effect could be eliminated by removing Cl^- from the solution bathing the muscle preparation, suggesting that acidosis exerts a beneficial effect on Cl^- channel activity. A central feature of the new mechanism is that the accumulation of extracellular K^+ results in action potentials becoming a less effective trigger of Ca^{2+} release in working muscles. Acidosis reduces this effect by decreasing the contribution of Cl^- channels, which act to clamp the membrane potential near the chloride reversal potential. Because the chloride reversal potential is near the resting membrane potential, the effect of Cl^- channel activity is to increase the amount of sodium ion (Na^+) current necessary to generate an action potential, which then triggers Ca^{2+} release. This mechanism will only operate under conditions in which the amplitude of the action potential has become a rate-limiting step for muscle activity. Unfortunately, it is not easy to establish whether this is the case in different types of muscle fatigue.

The Pedersen *et al*. findings add to the complexity of the contribution of intracellular and extracellular acidosis to muscle performance. Generated by the anaerobic breakdown of glycogen, lactic acid is, from the standpoint of active muscle, an inefficient way to produce ATP. An increase in intracellular acidosis will affect the function of many intracellular proteins besides contractile proteins, but we do not yet know which of these are important for muscle contraction. Lactic acid is ferried out of muscle cells by lactate transporter proteins, creating an extracellular acidosis, which probably contributes to the painful sensations of muscle fatigue experienced by athletes. Once in the circulation, lactate

D. Allen is at the Institute of Biomedical Research, University of Sydney, NSW 2006, Australia. H. Westerblad is at the Karolinska Institute, S-171 77 Stockholm, Sweden. E-mail: davida@physiol.usyd.edu.au, hakan.westerblad@fyfa.ki.se

can be metabolized by other tissues and may be involved in the regulation of the respiratory and circulatory systems.

Fatigue has many sources that may be present at different sites in muscle cells. Many constituents of muscle metabolism (lactic acid, glycogen, phosphocreatine, inorganic phosphate, ATP, Ca^{2+}, Na^{+}, K^{+}) change during fatigue and, for each of these, we need to know which proteins are affected and how these proteins regulate muscle contraction. Equally important is the effect of multiple cellular changes on muscle activity in the intact animal. Athletes and trainers who keep abreast of these issues may potentially be able to modify aspects of their training or performance in ways that give them a competitive edge.

References

1. H. Westerblad *et al.*, *News Physiol Sci.* **17**, 17 (2002).
2. T. H. Pedersen *et al.*, *Science* **305**, 1144 (2004).
3. A. V. Hill, P. Kupalov, *Proc. R. Soc. London Ser. B* **105**, 313 (1929).
4. A. Fabiato, F. Fabiato, *J. Physiol. (London)* **276**, 233 (1978).
5. E. B. Cady *et al.*, *J. Physiol. (London)* **418**, 311 (1989).
6. E. Pate *et al.*, *J. Physiol. (London)* **486**, 689 (1995).
7. J. D. Bruton *et al.*, *J. Appl. Physiol.* **85**, 478 (1998).
8. O. B. Nielsen *et al.*, *J. Physiol.* **536**, 161 (2001).

IMMUNOLOGY

UNGstoppable Switching

Shyam Unniraman, Sebastian D. Fugmann, David G. Schatz

Antibodies are the frontline in our defense against pathogens. These Y-shaped molecules produced by B cells recognize and bind to foreign substances inside the body. The immunoglobulin (Ig) genes encoding antibodies show an extremely high degree of variability, because they are initially assembled from different gene segments in an ordered but random process. After an antibody encounters its corresponding antigen, two cellular programs that alter Ig genes become activated in the B cell: somatic hypermutation (SHM) and class switch recombination (CSR). A key player in both processes is the DNA-repair enzyme uracil DNA glycosylase (UNG) (*1*, *2*). On page 1160 of this issue, Begum and co-workers (*3*) present their surprising observation that the only known enzymatic activity of UNG—the removal of the "RNA base" uracil from DNA—is not required for CSR.

Antibodies have two functional domains: the "variable" (V) region that binds to antigen and the "constant" (C) region that activates the immune response. SHM introduces point mutations in the exon encoding the variable region, allowing selection of high-affinity antibodies. CSR, however, exchanges the generic Cμ region for more specialized Cγ, Cε, or Cα variants. Recombination occurs between highly repetitive switch (S) repeats that precede the downstream C cassettes, resulting in looping out and deletion of intervening constant regions (see the figure). Despite having completely different outcomes, CSR and SHM have similar molecular requirements, and mystery enshrouds the mechanism of both events (*4*).

It is well established that a single protein, the activation-induced cytidine deaminase (AID), is essential for CSR (*5*), but how this protein works and the subsequent steps downstream of its activity remain a black box (see the figure). The current hypothesis is that transcription of the S regions leads to the exposure of single-stranded DNA, and that AID then converts cytosine bases into uracils within these regions (the DNA deamination model). Subsequently, the glycosylase UNG (which is expressed by all cells) removes the uracil bases, leaving only the sugar backbone behind. Such abasic sites then are removed by the apurinic/apyrimidinic endonuclease 1 (APE1), resulting in a single-strand break. A similar nearby lesion on the opposite strand would result in a DNA double-strand break (DSB). A DSB in each of two switch regions would lead to the excision of the intervening DNA segment. A crucial prediction of this model is that UNG is necessary for the generation of DSBs during CSR.

In agreement with this model, UNG-deficient B cells show a striking defect in their ability to undergo CSR (*1*, *2*, *4*). But in sharp contrast to the prediction of the DNA deamination model, Begum *et al.* (*3*) now report that activation of DNA DSB-repair pathways, as assessed by the formation of DNA-repair foci, is not impaired when UNG activity is blocked with a specific inhibitor (Ugi). Their finding suggests that in CSR, UNG acts downstream of DSB formation. Even more surprising, B cells ex-

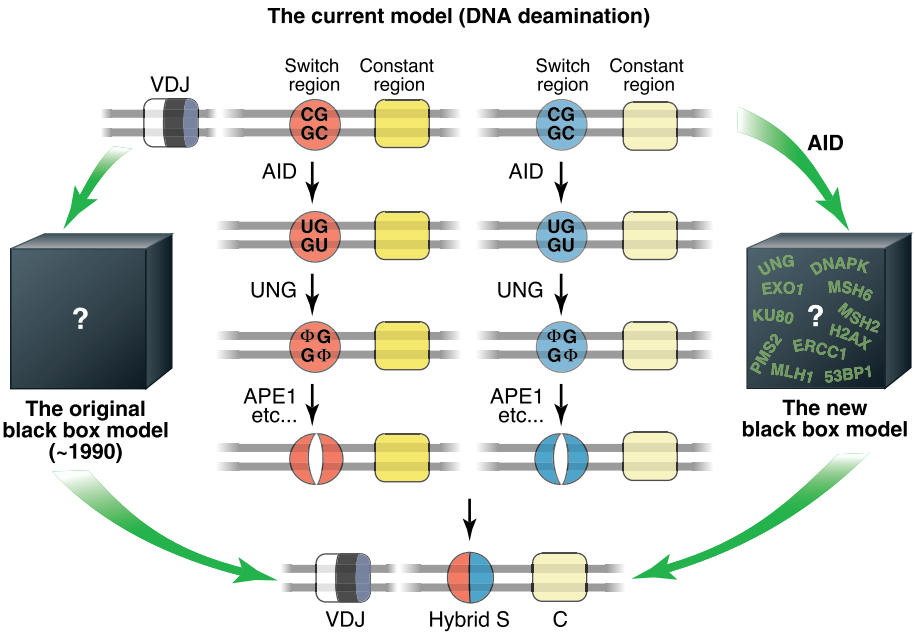

What's going UNG? Different models of class-switch recombination (CSR). A decade ago, little was known about CSR except the germline configuration of the Ig genes—switch (S) regions (red and blue circles) and constant (C) regions (yellow boxes)—and the final recombined structure of the genomic locus (the original black box model). In the current DNA deamination model, AID deaminates cytosines to uracils on both DNA strands in the switch region. UNG then converts these uracils to abasic sites (Φ), which are acted upon by APE1 and other enzymes to generate DSBs. Other proteins may also be involved, but their function remains unclear. Begum *et al.* (*3*) show that the generation of DSBs is independent of UNG activity, contradicting the DNA deamination model and leaving us with nearly a dozen proteins implicated in CSR but little idea of where to place them in the pathway (the new black box model).

CREDIT: KATHARINE SUTLIFF/*SCIENCE*

The authors are at the Howard Hughes Medical Institute, Section of Immunobiology, Yale University School of Medicine, New Haven, CT 06520, USA. E-mail: shyam.unniraman@yale.edu, sebastian.fugmann@yale.edu, david.schatz@yale.edu

pressing a catalytically inactive version of UNG are still able to perform CSR at normal rates (*3*). So, what's going on?

Given that Ugi blocks UNG activity by mimicking its DNA substrate (*6*) and that the B-cell UNG catalytic mutants retain their DNA binding ability, one plausible explanation is that UNG acts as the lesion-recognition subunit of a unique multi-enzyme CSR recombinase complex. This recombinase complex would facilitate the recombination of S regions containing uracils rather than the generation of DSBs. Such a scenario is unlikely, however, because UNG catalytic mutants that no longer bind to uracil are still able to support CSR. Perhaps UNG has an as yet unknown activity that does not require the glycosylase active site but is still blocked by Ugi. If this were true, we would lose the best evidence for uracils as intermediates in CSR, which in turn implies that AID might not act by deaminating cytosines in DNA to begin with. Begum *et al*. (*3*) favor a role for AID in editing the mRNA of a CSR endonuclease, a model that is neither supported nor negated by their results. We are thus brought back to the CSR black box.

How do the Begum *et al*. findings fit into current models of SHM? As in CSR, AID is proposed to act on cytosines that are exposed by transcription of the V region. Again, the coordinated action of UNG and APE1 would create abasic sites that are filled in by error-prone DNA polymerases carried forward by replication. The absence of UNG (or a block in UNG activity due to Ugi) creates a strong bias toward C to T (and G to A) mutations (*1*, *2*, *7*), potentially as a result of replication over a G:U mismatch. Whether this model withstands the challenge posed by catalytically inactive UNG mutants remains to be seen.

The Begum *et al*. study raises serious questions about a critical step in the prevailing model of CSR, and sends us almost back to the starting line in our thinking about how CSR works. The key to the riddle of CSR (and SHM) will be the characterization of the DNA intermediates formed along the reaction pathway. This will help us to understand how the DNA-repair machinery gets hijacked to cause surprisingly beneficial modifications rather than performing its traditional part in counteracting any alterations to the genome.

References

1. C. Rada *et al*., *Curr. Biol.* **12**, 1748 (2002).
2. K. Imai *et al*., *Nature Immunol.* **4**, 1023 (2003).
3. N. A. Begum *et al*., *Science* **305**, 1160 (2004).
4. Z. Li *et al*., *Genes Dev.* **18**, 1 (2004).
5. M. Muramatsu *et al*., *Cell* **102**, 553 (2000).
6. C. D. Mol *et al*., *Cell* **82**, 701 (1995).
7. J. Di Noia, M. S. Neuberger, *Nature* **419**, 43 (2002).

PHYSICS

Arrival of the Fermion Superfluid

Tin-Lun Ho

All particles are either bosons or fermions. Bosons behave like each other, whereas fermions refuse to act the same. In their lowest energy state, bosons form a Bose-Einstein condensate (BEC) in which all particles behave identically. As a result, quantum phenomena are magnified, becoming observable even at macroscopic length scales. Fermions cannot perform this feat. However, a bound pair of fermions behaves like a boson. A collection of bound fermion pairs should therefore be able to Bose-condense as bosons do. Two reports in this issue make a strong case for the realization of such a fermion superfluid in cold atoms.

Since the dramatic discovery of Bose-Einstein condensation in 1995, many groups have tried to create fermion superfluids. Recent experimental advances indicated that the realization of a fermion superfluid was imminent (*1*–*3*). In January 2004, Greiner and colleagues reported evidence for pair condensation in a Fermi gas of ^{40}K (*4*). Reports by other groups on similar (*5*) and related properties (*6*, *7*) in a different Fermi gas (^{6}Li) soon followed. However, theories for pair condensates are considerably more complex than those for Bose-Einstein condensates. Confirmation of fermion superfluid is therefore less straightforward. On page 1128 of this issue, Chin *et al*. (*8*) present direct evidence of a pairing gap in the Fermi gas of ^{6}Li, which is a key property of a pair condensate. On page 1131, Kinnunen *et al*. provide a theoretical explanation for this observation (*9*). These results, together with the evidence in (*1*–*7*), make the case for a fermion superfluid difficult to challenge.

As pointed out by Bardeen, Cooper, and Schrieffer (BCS), the condensation of electron pairs is the origin of superconductivity in solids (*10*). The electron pairs (called Cooper pairs) are very big, with diameters about 100 times the mean distance between electrons. They therefore overlap strongly with each other. The condensates in Fermi gases are generated with "Feshbach resonance" (*11*), which allows the size of the pairs to be varied from much larger than the mean distance between atoms to about the size of an atom. As a result, a change from a superfluid with large pairs to a BEC of molecules can occur on a continuum.

Feshbach resonance works as follows. When two fermion atoms interact in a vacuum, they can jump between a "closed channel" and an "open channel." In the closed channel, they form a small (atomic-scale) molecule, whereas they are unbound in the open channel. The energy difference between the two states can be tuned with a magnetic field. Feshbach resonance occurs when the energy difference is tuned to zero, at which point a bound pair is about to emerge. When

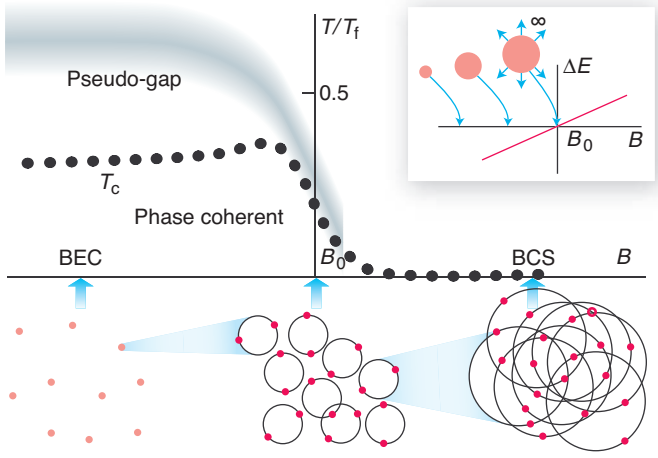

Schematic phase diagram for a fermion superfluid. The main figure and the inset reflect the many-fermion and the two-fermion cases, respectively. **Main figure:** T_c is the transition temperature, below which the system is a superfluid and has phase coherence. T_c is very low on the BCS side (right), where the pairs are much larger than interparticle spacing. It increases to the order of the Fermi temperature T_f near resonance, where the size of the pair is of the order of the interparticle spacing. Far below resonance, the system is a molecular BEC (left). In the pseudo-gap region above T_c, bound pairs exist but are not phase-coherent. Above the gray line, the number of bound pairs becomes very small. It represents a crossover and not a phase transition. **Inset:** Energy difference ΔE between the closed-channel molecule and the open-channel scattering state for a two-fermion system. As the resonance (at magnetic field B_0) is approached from below, the pair size grows to infinity.

The author is in the Department of Physics, Ohio State University, Columbus, OH 43210, USA. E-mail: ho@mps.ohio-state.edu

the closed channel lies below the open channel, the fermions form a bound pair that includes both closed- and open-channel contributions. As the resonance is approached from below, the closed channel component is reduced. The pair grows in size toward infinity (see the figure, inset). Above resonance, the fermion pair remains unbound.

The situation for many fermions is very different from that for two fermions. The current BCS-BEC crossover theory (*12*) gives the following picture. As the resonance is approached from below, the pairs grow in size and overlap. At resonance, the pair size is reduced to interparticle spacing, independent of the details of atomic potentials. This is remarkable because it implies that all Fermi gases with the same density have identical properties at resonance, even though their atomic interactions are very different. Such universality was observed in 2003 (*13*, *14*). Above resonance, fluctuations between closed- and open-channel states continue to bind fermions into pairs, although the binding force decreases with increasing distance from resonance, and the pairs become much larger than interparticle spacing (see the figure).

With increasing temperature, the superfluid will be destroyed by thermal effects. The destruction takes place sharply at a temperature T_c at which the pairs stop acting in unison, such that the system loses "phase coherence." Bound pairs can still exist above T_c, but they will break up gradually as temperature increases. The region above T_c with a substantial number of bound pairs is referred to as the pseudo-gap region.

In the experiment by Chin *et al*., a radial frequency radiation is applied to a Fermi gas of ^{6}Li consisting of equal numbers of fermions in atomic states **1** and **2**. The radiation excites **2** to a different atomic state **3**. If there is no pairing between **1** and **2**, only radiation with frequency equal to the energy difference between **2** and **3** will be absorbed. If there is pairing, another absorption frequency will appear, corresponding to the breakup of the pair **1**+**2**. Such a double-peak structure is indeed observed as the temperature is lowered. Moreover, the atomic peak (due to **2**-to-**3** transition) gradually disappears at lower temperatures, leaving only the "pairing" peak, which implies that all fermions are transformed into pairs [see figure 3 in (*8*)]. This behavior above resonance provides strong evidence for a fermion superfluid, because there are no stable closed-channel molecules in that regime, and the pairs must come from pairing in an open channel. Kinnunen *et al*. show that these phenomena are well accounted for by theoretical calculations based on the BEC-BCS crossover picture (*9*).

The discovery of a Fermi superfluid will not only enable the study of many difficult problems in solid-state physics in well-controlled settings; it will also further strengthen the cold atom connection to other fields such as nuclear physics and quantum information theory. Research into fermion superfluids is only just beginning, but even at this early stage, new and exciting directions are emerging. A recent preprint (*15*) reported reversible production of "*p*-wave" molecules across Feshbach resonance. These are molecules that carry orbital angular momentum. Even fermion superfluids with rotating pairs may be possible in the near future. The best is yet to come.

References and Notes

1. S. Jochim *et al*., *Science* **302**, 2101 (2003); published online 13 November 2003 (10.1126/science.1093280).
2. M. Greiner *et al*., *Nature* **426**, 537 (2003).
3. M. W. Zwierlein *et al*., *Phys. Rev. Lett.* **91**, 250401 (2003).
4. C. A. Regal *et al*., *Phys. Rev. Lett.* **92**, 040403 (2004).
5. M. W. Zwierlein *et al*., *Phys. Rev. Lett.* **92**, 120403 (2004).
6. J. Kinast *et al*., *Phys. Rev. Lett.* **92**, 150402 (2004).
7. M. Bartenstein *et al*., *Phys. Rev. Lett.* **92**, 203201 (2004).
8. C. Chin *et al*., *Science* **305**, 1128 (2004); published online 22 July 2004 (10.1126/science.1100818).
9. J. Kinnunen, M. Rodríguez, P. Törmä, *Science* **305**, 1131 (2004); published online 22 July 2004 (10.1126/science.1100782).
10. J. Bardeen *et al*., *Phys. Rev.* **104**, 844 (1956).
11. M. Holland *et al*., *Phys. Rev. Lett.* **87**, 120406 (2001).
12. P. Nozieres, S. Schmitt-Rink, *J. Low Temp. Phys.* **59**, 195 (1985).
13. K. M. O'Hara, S. L. Hemmer, M. E. Gehm, S. R. Granade, J. E. Thomas, *Science* **298**, 2179 (2002); published online 7 November 2002 (10.1126/science.1079107).
14. T. Bourdel *et al*., *Phys. Rev. Lett.* **91**, 020402 (2003).
15. J. Zhang *et al*., *Phys. Rev. A*, in press (http://arxiv.org/abs/quant-ph/0406085).

PALEOBIOLOGY

Decoding the Ediacaran Enigma

Martin Brasier and Jonathan Antcliffe

Fossils and Egyptian hieroglyphs share daunting similarities: Both consist of arcane geometries, glyphs in rock that conceal deeper meanings from the rude enquirer, and are capable of false translation. Remember Shelley's fakery "*And on the pedestal the words appear: 'My name is Ozymandias, King of Kings: Look on my works ye Mighty and despair!*" and take note of recent fossil feuds (*1*, *2*). To read the fossil runes correctly, the paleontologist craves the stimulus of fresh fossil finds, channeled by insightful methodology to catalyze productive thought. The recent discovery of remarkably well-preserved, three-dimensional Ediacaran fossils in Newfoundland reported by Narbonne (*3*) on page 1141 of this issue may provide such a stimulus. The new fossil find raises the question of whether the study of the life history and growth plan of these fossil animals could provide a Rosetta stone for decoding Ediacaran animal evolution (*4*–*6*).

The Ediacara biota remains one of the greatest enigmata within evolutionary paleobiology (see the figure, top). Discovered in 1946 by R. C. Sprigg in the Flinders Ranges of southern Australia, the Ediacara biota—which is 580 to 543 million years old (Ma)—represents the most ancient complex organisms on Earth. Martin Glaessner provided the first insights into Ediacaran biology (*7*). He saw in the fossils of Ediacaran animals (so remarkably preserved in late Precambrian sandstones) the ancestors of Phanerozoic animal phyla. The Cambrian is the first period with abundant fossils and marks the start of the era of the Phanerozoic or "visible life" that continues through to the present. Before this came the vast interval of the Precambrian, which ranges back to the origins of the Earth about 4600 million years ago.

Paleontologists eagerly sought relationships between Ediacaran fossils and living seapens and worms, jellyfish and crabs. This "great ancestral" view has held sway for almost 40 years (*8*, *9*), but a growing number of paleontologists argue that Ediacaran creatures were not ancestral to Cambrian life at all. They suggest that members of the Ediacara biota were uniquely fashioned beasts that met their doom at the end of the Precambrian (*10*–*12*). Ediacaran animals—each "quilted" like a mattress—take many forms, resembling desiccated lichens, underwater fungi, enormous ferns, or giant deep-sea single-celled protists (*10*–*12*).

We believe the time has come to raise difficult questions about the methodology used to analyze Ediacaran fossils. Ediacaran forms once thought to be "jellyfish" by Glaessner (*7*) have been reinterpreted as the attachment discs of fernlike fronds (*13*). And fronds once placed in discrete taxa now seem to be part of a much wider spectrum of intergrading forms (*3*). Could it be that other "Glaessnerian species" are not biological species in the sense of Mayr (*14*) at all, but mere organs, different growth stages, or ecophenotypes of a single taxonomic unit? For example, the archetypal taxon of the Ediacara biota is a frondlike (frondose) organism called *Charnia*. In this organism, each "branch" of the frond is further subdivided at least three times into tiny, self-similar *Rangea*-like elements called rangeo-

M. Brasier and J. Antcliffe are in the Department of Earth Sciences, Oxford University, OX1 3PR, UK. E-mail: martin.brasier@earth.ox.ac.uk

morph frondlets by Narbonne (*3*). In *Charnia*, these rangeomorph frondlets appear to be folded over so that only half is visible from one side (see lower figure, D). Both small (about 0.2 m) and large (>0.7 m) specimens of *Charnia* frond are known to coexist in England (see lower figure, C and D), and even smaller *Charnia*-like units can also be seen clustered together within the coexisting bushlike fossil *Bradgatia* (see lower figure, B). In Newfoundland, coexisting fossil "spindles" contain rows of little *Bradgatia*-like bushes, each branch of which looks like a tiny *Rangea* (see lower figure, A). Could these intergrading rangeomorphs represent different stages of the *Charnia* growth cycle, with bushlike forms (such as *Bradgatia*) and spindle-shaped forms acting as a creche that produces other forms, and large *Charnia grandis* surviving as an example of gigantism? If such intergradation can be proved, what does this imply about the biology of the Ediacara biota? This question tests our assumptions about the fundamental unit of Ediacaran fossil architecture: Is it the *Charnia* frond, the rangeomorph frondlet (*3*), or the smaller quilted pneu (*10*–*12*)?

Our concern is that the current "Ediacaran species concept" is no longer tenable. It is based on a "typological" approach using type specimens rather than populations (*14*), and on an "analog" approach that compares fossil morphologies with modern organisms according to assumed similarities. But these similarities could well have evolved independently. This approach is therefore unsound for deciphering long-extinct groups and, unlike cladistics, is an insecure basis for classification. We need quantitative studies of fossil populations, with analysis of morphological gradients in the same geological successions and bedding planes (*15*), as well as detailed analyses of growth programs (morphospace), life history (ontogeny), and evolutionary history (phylogeny) (*4*–*6*). It is premature to put forth any evolutionary history for fossils whose diagnosis has been conceived without reference to a postulated growth program observed through successive stages of ontogeny. Without such reference, both the taxonomic pattern and the evolutionary processes responsible for it will remain obscure.

Several recent studies reveal the dangers of the popular "analog" approach. Extant frondose seapens, which often provide a model for extinct Ediacaran fronds (*8*, *9*), comprise colonies of coral-like polyps that multiply by the antapical insertion of branches around the base of the colony; the Ediacaran *Charnia* most likely grew by apical insertion of these elements (*4*–*6*). Xenophyophores, which provide yet another model for Ediacaran fronds (*10*–*12*), are larger benthic forams that grow in quite another way (*4*, *6*). The fields of morphospace that each of these groups occupies are different so that similarities among Ediacaran fossils, seapens, and xenophyophores may be convergent and misleading (*4*–*6*).

How then can we decode the evolution of the long-extinct Ediacara biota? As with the Rosetta stone, one may begin with a well-known "cartouche" or pattern from the fossil record—in this case, the pattern of "heterochronic evolution." Many extinct fossil groups—such as the younger graptolites after the Cambrian and larger foraminifera after the Devonian (*16*, *17*)—ran a predictable evolutionary race in which architectural novelty arose through accentuation of adult or juvenile growth stages (heterochrony). Such evolutionary trends are often iterative and convergent. Do the Ediacaran fossils follow this trend? We can only answer this question by tracing changes in the fossil record over time that are consistent with heterochronic evolution. *Charnia*, the core taxon of the Ediacaran Period, is found throughout most

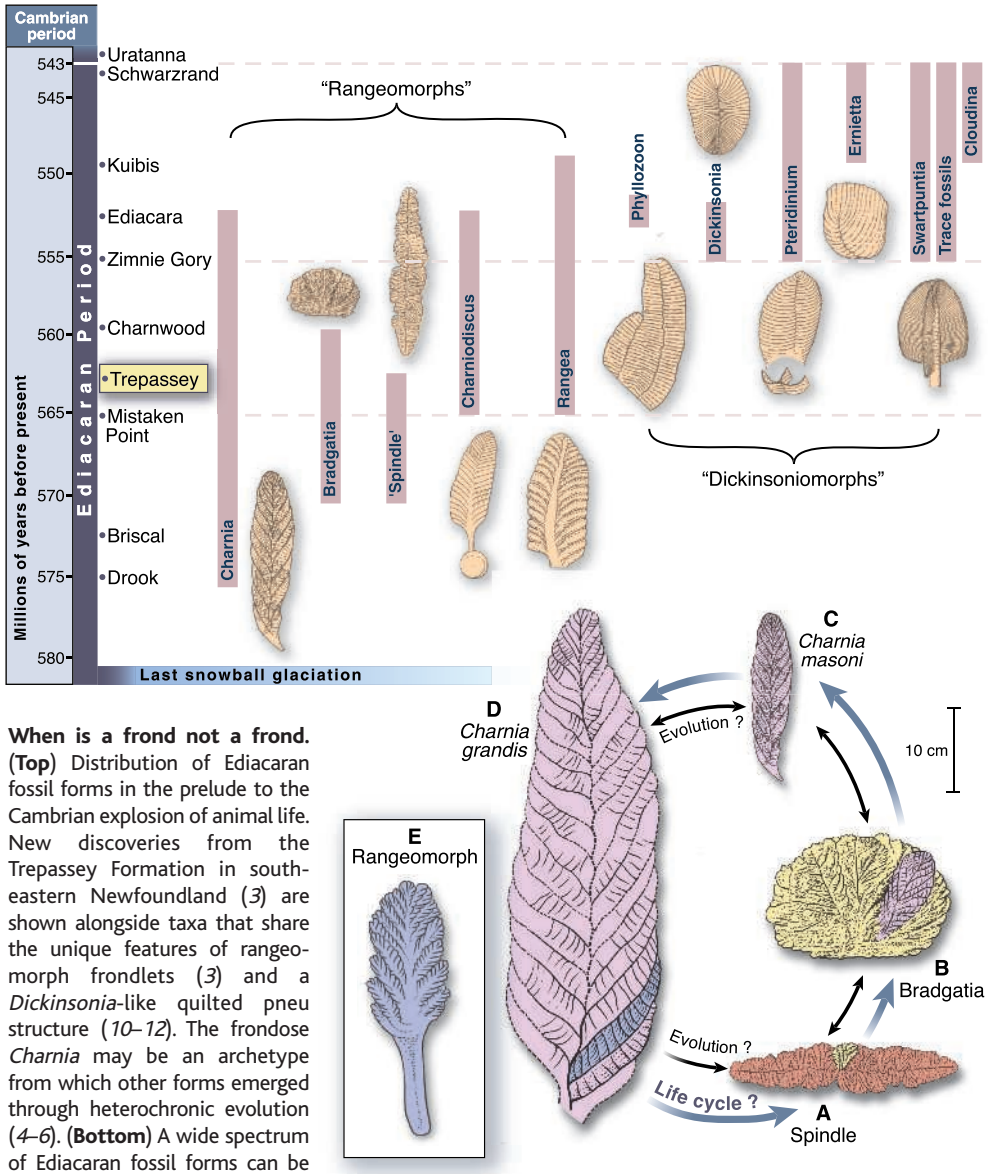

When is a frond not a frond. (**Top**) Distribution of Ediacaran fossil forms in the prelude to the Cambrian explosion of animal life. New discoveries from the Trepassey Formation in southeastern Newfoundland (*3*) are shown alongside taxa that share the unique features of rangeomorph frondlets (*3*) and a *Dickinsonia*-like quilted pneu structure (*10*–*12*). The frondose *Charnia* may be an archetype from which other forms emerged through heterochronic evolution (*4*–*6*). (**Bottom**) A wide spectrum of Ediacaran fossil forms can be found clustered in the same geological bedding plane. Depicted are four such forms from the new fossil finds in Newfoundland, as well as fossil forms found in England, Russia, and Australia (*3*–*6*, *15*). Their intergrading morphologies may be related in one of three ways: through growth stages within the whole life cycle (ontogeny), ecologically controlled phenotypes, or sister taxa that have evolved by suppressing or expanding different parts of the life cycle (heterochrony). The basal segments of *Charnia grandis* are reconstructed to show up to four levels of inferred "fractal" quilting. The fossils are shown at a comparable scale except the rangeomorph frondlet [Inset (E), 4 cm long].

CREDIT: KATHARINE SUTLIFF/*SCIENCE* AND TAINA LITWAK

of the 40 million years that define this period. Early Ediacaran fossil assemblages from Newfoundland and England (dated 580 to 559 Ma) contain clustered colonies of *Charnia*-like elements—called rangeomorphs by Narbonne (*3*), or *Rangea* and *Bradgatia* by others—which are bushlike, plumose, or fusiform (see the figure, top). Late assemblages, such as those from Namibia dated at 549 to 543 Ma, lack these rangeomorph colonies. Instead, they contain a variety of simpler forms (called "dickinsoniomorphs") such as *Pteridinium* and *Ernietta*, whose architecture resembles simplifications of the archetypal *Charnia* (see the figure, top). Assemblages of intermediate age from Russia and Australia also tend to contain simple "dickinsoniomorphs" such as *Phyllozoon* and *Dickinsonia* (see the figure, top).

Perhaps innovations in Ediacaran body architecture about 580 to 543 Ma were enabled by a process of developmental change in which some aspects of *Charnia* morphology were suppressed (see the figure, bottom) while others became enhanced and dominant. Such heterochronic forms could have exploited different modes of existence—from tethered or reclining on the sea floor (older assemblages) to forms embedded in the sediment (younger assemblages), or from offshore to onshore habitats (*4*–*6*, *10*–*12*, *15*, *18*). Each of these modes of existence requires that some kind of evolution took place. If this sequence of evolutionary development (heterochrony) is correct, then perhaps we are about to break the code to the evolution of the Ediacara biota, the earliest animals. Watch this space.

References and Notes

1. J. W. Schopf, *The Cradle of Life* (Princeton Univ. Press, New York, 1999).
2. M. D. Basier *et al.*, *Nature* **416**, 76 (2002).
3. G. M. Narbonne, *Science* **305**, 1141 (2004).
4. J. Antcliffe, M. D. Brasier, Workshop on the Rise and Fall of the Vendian (Ediacaran) Biota, International Commission of Stratigraphy, Prato, Italy, August 2004.
5. J. Slack, thesis, University of Oxford (2003).
6. J. Antcliffe, thesis, University of Oxford (2004).
7. M. F. Glaessner, *The Dawn of Animal Life* (Cambridge Univ. Press, Cambridge, 1984).
8. J. Gehling, *Geol. Soc. India Mem.* **20**, 181 (1991).
9. R. Jenkins, in *Origin and Early Evolution of the Metazoa*, J. Lipps, P. Signor, Eds. (Plenum, New York, 1992), pp. 131–176.
10. A. Seilacher, *J. Geol. Soc. London* **149**, 607 (1992).
11. Seilacher's work (*10*) followed the pioneering work of Pflug in 1972 and Fedonkin in 1983. The giant protist hypothesis is given in (*12*).
12. A. Seilacher *et al.*, *Palaeontol. Res.* **7**, 44 (2004).
13. G. Narbonne, *GSA Today* **8**, 1 (February 1998).
14. E. Mayr, *What Evolution Is* (Wedenfield & Nicholson, London, 2002), p. 318.
15. M. Clapham, G. Narbonne, *Geology* **30**, 627 (2002).
16. R. A. Fortey, A. Bell, *Paleobiology* **13**, 1 (1987).
17. M. D. Brasier, *J. Micropalaeontol.* **1**, 95 (1982).
18. D. Grazhdankin, *Paleobiology* **30**, 203 (2004).

CHEMISTRY

Zinc-Zinc Bonds: A New Frontier

Gerard Parkin

The ability of metal atoms to bind to other atoms of the same element in molecular compounds plays an important role in chemistry. Furthermore, the nature of such "homonuclear" metal-metal bonds is often unusual. For example, molybdenum and tungsten can form metal-metal quadruple bonds (*1*), compared to the triple-bond maximum for nonmetals. Other metals, such as gold, can form metal-metal bonds even when there are no unpaired electrons available to do so (*2*).

However, not all metals readily form homonuclear metal-metal bonds. Zinc is one metal that was not known to form such bonds—until now. On page 1136 of this issue, Resa *et al.* (*3*) report the synthesis and structure of the dinuclear pentamethylcyclopentadienyl (Cp*) compound $Cp^*_2Zn_2$, a landmark discovery in the chemistry of zinc (see the figure).

To place this result in context, compare the chemistry of zinc with that of the other two elements in group 12 of the periodic table, cadmium and mercury. In marked contrast to zinc, compounds with mercury-mercury bonds are quite common. Hg_2Cl_2—called "calomel" and used in electrochemistry and early medicines (such as laxatives)—is one of many compounds with a dinuclear $[Hg_2]^{2+}$ core (*4*).

Progressing up the periodic table from mercury to cadmium, the ability to form metal-metal bonded compounds diminishes rapidly. The first structurally characterized compound with cadmium-cadmium bonds, $Cd_2(AlCl_4)_2$, was reported as recently as 1986 (*5*). It is therefore no surprise that compounds with zinc-zinc bonds have been elusive.

Resa *et al.* obtained their zinc-zinc bonded compound by reacting Cp^*_2Zn with Et_2Zn at –10°C in diethyl ether solution (*3*). As noted by the authors, the formation of $Cp^*_2Zn_2$ is unforeseen, requiring the formal loss of two ethyl radicals (the fate of which was not determined). In view of the unprecedented nature and unusual synthesis of $Cp^*_2Zn_2$, Resa *et al.* have given considerable attention to its characterization, particularly to the possibility that it could be the hydride-bridged derivative $[Cp^*Zn(\mu\text{–}H)]_2$. Such caution is warranted because the Co–Co bond in the cobalt analog $Cp^*_2Co_2$ (*6*) was later shown to be bridged by three hydride ligands (*7*).

It is experimentally very difficult to disprove the presence of a bridging hydride ligand (especially by x-ray diffraction), but excellent evidence is provided by the high-resolution mass spectrum, which is consistent with the formula of $Cp^*_2Zn_2$ and not with that of $[Cp^*Zn(\mu\text{–}H)]_2$. The possibility that the compound could be the hydride complex and lose H_2 in the gas phase is discounted by the fact that $Cp^*_2Zn_2$ may be sublimed without much decomposition.

Structural evidence for the absence of hydride bridges is provided by the observation that the zinc-zinc bond length in $Cp^*_2Zn_2$ is 2.31 Å, much shorter than the value of 2.45 Å in a known hydride-bridged dimer (*8*). For further comparison, the cadmium-cadmium bond length in $Cd_2(AlCl_4)_2$ is 2.58 Å (*5*), and mercury-mercury bond lengths are typically between 2.49 and 2.67 Å (*4*). The shorter zinc-zinc bond distance in $Cp^*_2Zn_2$ is in line with the single-bond metallic radii of Zn (1.25 Å), Cd (1.41 Å), and Hg (1.44 Å).

Resa *et al.* also provide chemical evidence against the formulation as a hydride compound. For example, alcoholysis of $Cp^*_2Zn_2$ is accompanied by the deposition of metallic zinc; if the compound were a hydride-bridged dimer, alcoholysis would not be expected to be accompanied by deposition of zinc, but rather by elimination of H_2.

An often cited analog of the Cp* ligand is the tris(pyrazoly)hydroborato (Tp) ligand. Both are five-electron donors in their neutral form and occupy three coordination sites. The dinuclear compounds $[Tp^{Me}_2]_2Cd_2$ (*9*) and $[Tp^{Me}_2]_2Hg_2$ (*10*) have previously been synthesized (see the figure). The work of Resa *et al.* raises the intriguing possibility that the

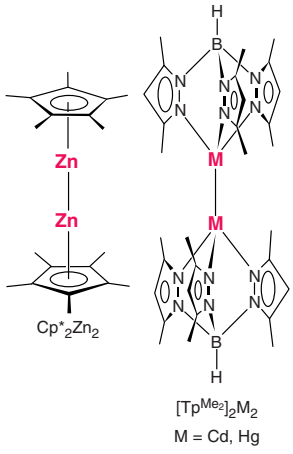

The first zinc-zinc bond. The molecular structure of the first molecular compound with a zinc-zinc bond (**left**) and related compounds with cadmium-cadmium and mercury-mercury bonds (**right**).

The author is in the Department of Chemistry, Columbia University, New York, NY 10027, USA. E-mail: parkin@chem.columbia.edu

zinc compound $[Tp^{Me}_2]_2Zn_2$ could also be synthesized, thereby completing the series of isostructural molecules with zinc-zinc, cadmium-cadmium, and mercury-mercury bonds.

Resa *et al.* note that the oxidation state of zinc in $Cp^*_2Zn_2$ is +1, in marked contrast to the +2 oxidation state that is observed for zinc in its stable compounds. However, it is important to emphasize that the assignment of a +1 oxidation state for zinc in $Cp^*_2Zn_2$ is merely a consequence of the fact that homonuclear element–element bonds are not considered in the evaluation of oxidation states. The +1 oxidation state thus does not convey any information about the electronic configuration of the zinc atoms in $Cp^*_2Zn_2$. Despite the +1 oxidation state, the valence of zinc is two: Zinc has used both of its valence electrons in bonding to the Cp* ligand and the other zinc atom.

Paramagnetic monovalent zinc species are extremely unusual, although it has recently been reported that Zn^+ ion may be trapped within a molecular sieve (*11*). However, the zinc-zinc bond in $Cp^*_2Zn_2$ illustrates that the molecular chemistry of zinc can still yield surprises. The next frontier for zinc chemistry will be the isolation of a simple molecular compound that features a bona fide monovalent zinc center.

References

1. F. A. Cotton, R. A. Walton, *Multiple Bonds Between Metal Atoms* (Oxford Univ. Press, Oxford, ed. 2, 1993).
2. M. Bardaji, A. Laguna, *J. Chem. Educ.* **76**, 201 (1999).
3. I. Resa, E. Carmona, E. Gutierrez-Puebla, A. Monge, *Science* **305**, 1136 (2004).
4. D. Bravo-Zhivotovskii, M. Yuzefovich, M. Bendikov, K. Klinkhammer, Y. Apeloig, *Angew. Chem. Int. Ed.* **38**, 1100 (1999).
5. R. Faggiani *et al.*, *Chem. Commun.* 517 (1986).
6. J. J. Schneider *et al.*, *Angew. Chem. Int. Ed.* **30**, 1124 (1991).
7. J. L. Kersten *et al.*, *Angew. Chem. Int. Ed.* **31**, 1341 (1992).
8. H. Hao *et al.*, *Chem. Commun.* 1118 (2001).
9. D. L. Reger, S. S. Mason, A. L. Rheingold, *J. Am. Chem. Soc.* **115**, 10406 (1993).
10. G. G. Lobbia *et al.*, *Gaz. Chim. Ital.* **121**, 355 (1991).
11. Y. Tian, G.-D. Li, J.-S.Chen, *J. Am. Chem. Soc.* **125**, 6622 (2003).

RETROSPECTIVE: MOLECULAR BIOLOGY

Francis Crick (1916–2004)

Leslie E. Orgel

In the latter half of the 1950s, I had the good fortune to be accepted by Francis Crick and his co-workers as an observer of, and occasional verbal contributor to, their efforts to understand DNA replication, protein synthesis, and other aspects of classical molecular biology. Francis and I became good friends, so I have had the opportunity to observe his mind at work in Cambridge, England, and later at the Salk Institute, where he served in an advisory capacity until 1977, and then as a faculty member until his death.

I will not attempt to summarize Francis' scientific achievements in detail; that is a task for historians of science. My list of favorite papers that he authored or coauthored would include those on diffraction by a helix, coiled-coils, the adaptor hypothesis, wobble pairing, the three-letter code, the structure of collagen, the prediction of an "RNA world" and, of course, the two short papers on the structure of DNA that launched many thousands of manuscripts. I would include selfish DNA but, since I was a coauthor, I realize that I may be prejudiced. Success in science may depend on many factors: imagination, intellectual power, experimental skill, persistence and, of course, luck. The series of important contributions that Francis made to structural and molecular biology rules out luck as a major factor in his case.

If luck didn't come into it, what explains Francis' extraordinary achievements? His intellectual power and remarkable intuition in all matters structural and biological are by now legendary. Watching him in action, I was always amazed at his ability to get his mind around a set of disparate and sometimes contradictory facts and in very little time force them to order. He seemed to know instinctively which facts he should take seriously and which he could ignore. He often advised that one should not abandon a good theory because of a few contradictory facts—not good advice for most of us, but it seemed to work for Francis.

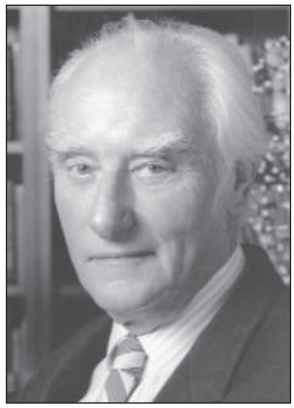

I never saw Francis Crick in a pompous mood. He was always confident in public debate and, at the beginning of his career, he was sometimes assertive, but he never resorted to reputation or seniority to further his point of view. He had no interest in becoming part of the power structure of science, but was generous with his time when he thought his advice might be useful. The Salk Institute benefited greatly from his numerous suggestions.

Francis did not suffer fools gladly. In his younger days he may have dismissed them a little harshly, but he became gentler as he grew older. He liked new ideas, and he didn't care where they came from. Surprisingly, he was always prepared to give careful consideration to ideas that seemed lunatic fringe to most of us, if he thought that they might possibly contain even a grain of truth. If he decided that they didn't, he would patiently explain to the authors what was wrong—but rarely more than once. He had a nose for any results that "smelled fishy" and would make an appropriate facial gesture when describing them.

At the Salk Institute, Francis switched from molecular biology to the neurosciences. I heard him say on a number of occasions that he did not expect to make a major contribution himself, but that he hoped to point younger scientists in the right direction. He was convinced that understanding consciousness, or at least its neural correlate, was the most important goal in neuroscience and that the time was ripe for an experimental approach. I am not competent to judge the importance of the contributions that he and his longtime collaborator, Christof Koch, have made; I suspect that the jury is still out. However, there is no doubt about his success in attracting other scientists to the field. When Francis began writing about consciousness, mention of the subject would probably have doomed a grant application. Nowadays, conferences on consciousness attract thousands.

The last few months of Francis' life were among the most striking. He was suffering serious discomfort from the side effects of chemotherapy and was sometimes slowed down mentally by the effects of painkillers. Knowing that time was short, he concentrated almost entirely on his work. He became interested in the role that a relatively little understood part of the brain, the claustrum, might play in consciousness. Within a few months he had mastered the literature to the point that he was writing a paper that included a lengthy review section. The last time we talked about science, 2 weeks before his death, he was as excited as a schoolboy about two new ideas that had occurred to him in the past day or two. On the last day of his life he was correcting the manuscript on the claustrum. Francis died as he had lived, striving to understand how the biological world works.

CREDIT: THE SALK INSTITUTE

The author is at the The Salk Institute, La Jolla, CA 92037, USA. E-mail: orgel@salk.edu

Intramembrane Proteolysis: Theme and Variations

Michael S. Wolfe[1]* and Raphael Kopan[2]*

Proteases that reside in cellular membranes apparently wield water to hydrolyze the peptide bonds of substrates despite their water-excluding environment. Although these intramembrane proteases bear little or no sequence resemblance to classical water-soluble proteases, they have ostensibly converged on similar hydrolytic mechanisms. Identification of essential amino acid residues of these proteases suggests that they use residue combinations for catalysis in the same way as their soluble cousins. In contrast to classical proteases, however, the catalytic residues of intramembrane proteases lie within predicted hydrophobic transmembrane domains. Elucidating the biological functions of intramembrane proteases, identifying their substrates, and understanding how they hydrolyze peptide bonds within membranes will shed light on the ways these proteases regulate crucial biological processes and contribute to disease.

Nature is an endless combination and repetition of very few laws. She hums the old well-known air through innumerable variations. – Ralph Waldo Emerson

In musical composition, a simple harmonized melody can be repeated many times with varied treatment so that at least some semblance of the general melodic or harmonic theme is evident. Analogous themes and variations occur in biochemistry, in which general mechanisms and conserved catalytic amino acid residues can be found among many different types of enzymes. For example, the study of proteases reveals how nature exploits a relatively simple process in myriad ways. Proteases catalyze the hydrolysis of the amide bonds that link amino acids together into peptides and proteins, and this process requires the concerted effort of key residues within the enzyme's active site. The context in which these conserved catalytic residues are found determines the substrate to be cleaved and can affect the rate, location, and timing of the substrate's hydrolysis.

Proteases are classified into four general types based on their catalytic residues and mechanism of action: (i) serine/threonine proteases, (ii) cysteine proteases, (iii) aspartyl proteases, and (iv) metalloproteases. Each of these four protease categories contains hundreds of known examples with representatives in all forms of life (*1*). Until recently, all proteases identified were water-soluble enzymes: Either the entire enzyme is normally found in an aqueous environment, or a membrane anchor holds down an otherwise aqueous protease. However, a new cadre of proteases has been discovered that seem to be embedded within the hydrophobic environment of the lipid bilayer. Despite the water-excluding environment of the lipid bilayer, these intramembrane proteases somehow are able to hydrolyze their transmembrane substrates (Fig. 1). The substrates themselves also are unusual: They are typically folded into an α-helix, a conformation that makes the backbone amide bonds inaccessible to nucleophilic attack because of steric hindrance by the amino acid side chains. The intramembrane-cleaving proteases (I-CLiPs) (*2*) therefore must create a microenvironment for water and the hydrophilic residues needed for catalysis, then bend or unwind their substrates to make the amide bonds susceptible to hydrolysis. Nevertheless, despite the novelty of being membrane-embedded and cleaving transmembrane domains, the I-CLiPs apparently are variations on old, familiar themes found in protease biochemistry: The essential catalytic residues of these I-CHiPs are virtually the same as those found in aqueous proteases.

The S2P Family: Variation on a Metalloprotease Theme

The first discovery of an I-CLiP arose from studies on the regulation of sterol and fatty acid metabolism. Sterol regulatory element binding proteins (SREBPs) are transcription factors that promote the expression of genes involved in the synthesis of cholesterol and fatty acids (*3*). Coordinated gene expression is controlled through negative feedback inhibition by cholesterol to ensure that lipids and sterols are produced only when needed. SREBPs are synthesized as precursor proteins that contain four distinct domains: a domain exposed to the cytosol that binds DNA and activates transcription, two transmembrane regions, and a regulatory domain involved in feedback control by cholesterol (Fig. 1A). When cholesterol levels are high, the SREBP precursor is kept in the endoplasmic reticulum (ER) by a multipass membrane protein called SCAP (SREBP cleavage-activating protein) (*4*) that is bound to a small membrane protein called Insig (*5*). Reduced cholesterol levels result in dissociation of Insig from SCAP, allowing SCAP to shepherd SREBP to the Golgi apparatus. Proteolysis of SREBP in the Golgi results in release of the transcription factor and its translocation to the nucleus. Control of subcellular localization also regulates the intramembrane serine protease Rhomboid (Fig. 1D): The substrate Spitz is ushered from the ER to the Golgi by a membrane protein called Star. In this case, however, the released Spitz is not a transcription factor, but is rather a secreted growth factor (see below).

Proteolytic release of SREBPs occurs in two steps (Fig. 1A). First, the luminal loop between the two transmembrane regions is cleaved by the membrane-tethered Site-1 protease (S1P) (*6*). Release of the transcription factor requires subsequent cleavage by the Site-2 protease (S2P), which hydrolyzes an amide bond predicted to lie three residues within the transmembrane domain (*7*). The requirement for a prior proteolytic event is a common theme among the I-CLiPs. For example, γ-secretase processing of the amyloid β-protein precursor (APP) or the receptor Notch cannot take place without initial shedding of the extracellular domain from the membrane by other enzymes (Fig. 1B). Similarly, proteolysis of remnant signal peptides by signal peptide peptidase (SPP) requires prior processing of nascent membrane proteins by signal peptidase (Fig. 1C). Rhomboid, however, appears to be an exception: It cleaves full-length Spitz without the need for preceding proteolysis.

Complementation cloning has identified S2P as a multipass membrane protein containing a conserved HEXXH sequence characteristic of zinc metalloproteases (*8*). The two histidines and the glutamate are required for S2P activity, consistent with known metalloprotease biochemistry in which the two histidines coordinate with zinc and the zinc in turn activates the glutamate for interaction

[1]Center for Neurologic Diseases, Harvard Medical School and Brigham and Women's Hospital, Boston, MA 02115, USA. [2]Department of Molecular Biology and Pharmacology and Department of Medicine, Washington University in St. Louis, St. Louis, MO 63110, USA.

*To whom correspondence should be addressed. E-mail: mwolfe@rics.bwh.harvard.edu (M.S.W.) and kopan@wustl.edu (R.K.)

with the catalytic water. Further analysis led to the discovery of a conserved aspartate located ~300 residues from the HEXXH sequence that is likewise critical for S2P activity and thought to be a third residue involved in zinc coordination (*9*). The involvement of zinc in S2P activity has not been demonstrated, and a cell-free assay for S2P activity has not yet been reported; therefore, S2P has not been directly shown to act as a protease. Nevertheless, extensive genetic analysis has not uncovered any other proteins required for S2P cleavage of SREBP.

Further support for the proteolytic function of S2P comes from the discovery of a family of related proteins in bacteria (*10*). These prokaryotic proteins are essential for the proteolysis of an otherwise membrane-bound transcription factor needed for sporulation. This factor, σ^k, controls gene expression in the mother cell after engulfment of the forespore. Cleavage of pro-σ^k and release of the transcription factor requires the multipass membrane protein SpoIVFB, and this protein likewise contains the HEXXH motif and a second conserved region with an aspartate, both of which are essential for proteolysis. Another bacterial S2P family member, YaeL in *Escherichia coli*, similarly requires HEXXH and a conserved aspartate to coordinate cell growth and cell division through intramembrane proteolysis of RseA, a factor critical for responding to extracytoplasmic stress (*11*). The membrane orientations of the substrates SREBP and σ^k are opposite to each other, correlating with that of their respective enzymes, S2P and SpoIVB, which apparently have opposite orientations (*10*). This implies that the catalytic region must align with the peptide substrate with proper relative directionality.

The α-helical conformation of the transmembrane substrate renders the amide bonds inaccessible to attack by a catalytic residue or water, requiring some bending or unwinding of the helix before proteolysis takes place. The SREBP substrate contains a conserved asparagine-proline (NP) sequence within its transmembrane region that is critical for proteolytic processing by S2P (*12*). These two residues have the lowest propensity to form α-helices, suggesting that the NP-containing SREBP transmembrane region may be metastable. After S1P cleavage and dissociation of the other transmembrane region, the NP sequence may facilitate unwinding of the residues immediately upstream, including the leucine-cysteine bond that gets cleaved. Unwinding may result in protrusion of this bond to the membrane surface and access by the active-site residues of S2P. Substrates for SPP and Rhomboid also require helix-disrupting residues, suggesting a general strategy for intramembrane proteolysis and a means of substrate specificity. In contrast, γ-secretase substrates do not appear to contain such residues; thus, this enzyme may be able to carry out helix bending or unwinding.

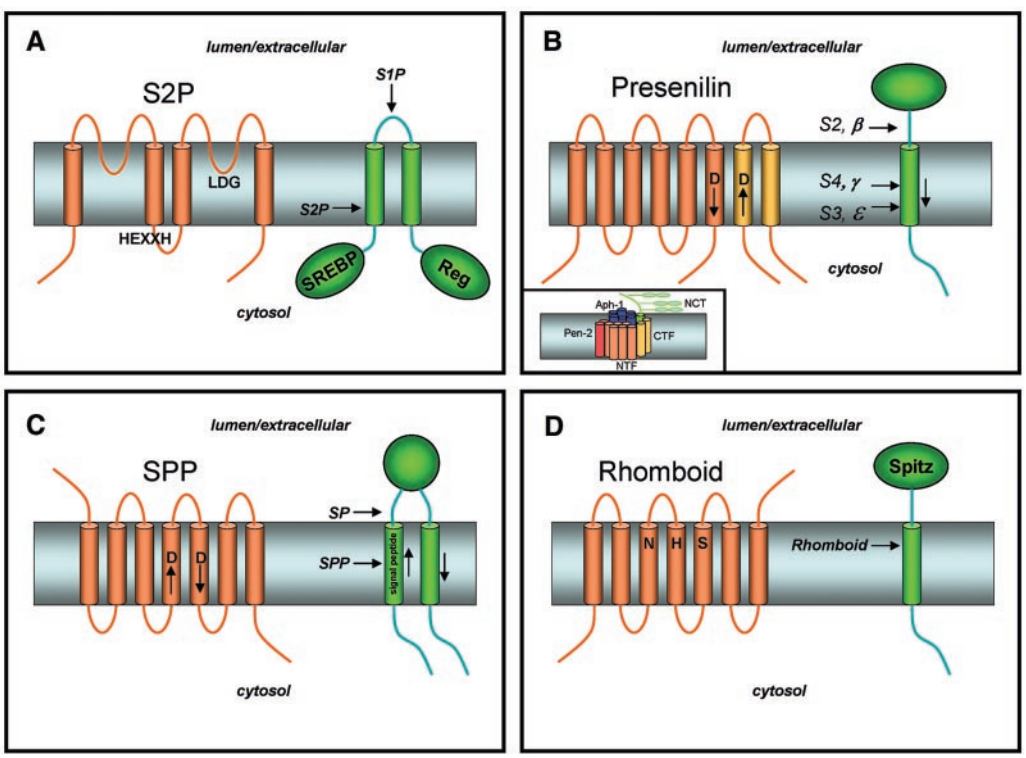

Fig. 1. Membrane topology of I-CLiPs and their substrates. (**A**) S2P contains conserved HEXXH and LDG (*74*) motifs found in metalloproteases. SREBP is first cleaved by S1P in the luminal loop. The regulatory domain (Reg) interacts with the cholesterol-sensing SCAP protein to ensure that S1P proteolysis occurs only when cholesterol levels are low. Subsequent intramembrane proteolysis releases this transcription factor, which then switches on expression of genes required for cholesterol and fatty acid synthesis. (**B**) Presenilin is processed into two pieces, an N-terminal fragment (NTF, dark orange) and a C-terminal fragment (CTF, light orange) that remain associated. Each fragment donates one aspartate essential for γ-secretase activity. APP and other substrates are first cleaved in the extracellular domain (APP by β-secretase, Notch by a metalloprotease), and the remnant is cleaved twice within the membrane by γ-secretase to produce the Aβ peptide of Alzheimer's disease (secreted) and the intracellular domain (freed into the cytosol). Inset: Presenilin interacts with three other membrane proteins (nicastrin, Aph-1, and Pen-2) to form active γ-secretase. [The model is redrawn from Fraering *et al.* (*45*).] Although the stoichiometry of these components is unclear, evidence suggests that two presenilin molecules lie within a single γ-secretase complex (*53*). NCT, nicastrin. (**C**) SPP, like presenilin, contains two aspartates that are essential for protease activity. Signal peptides are removed from membrane proteins by signal peptidase (SP) and these peptides are released from the membrane by SPP-mediated intramembrane proteolysis. (**D**) Rhomboids contain a conserved serine, histidine, and asparagines that compose a putative catalytic triad of a serine protease. Rhomboid-1 cleaves within the transmembrane region of the *Drosophila* EGF-like growth factor Spitz.

Presenilin Aspartyl Proteases: Composition for Quartets

A key step in the pathogenesis of Alzheimer's disease is APP proteolysis resulting in the formation of the amyloid-β peptide (Aβ), the principle protein component of the characteristic cerebral plaques of the disease (*13*). The N terminus of Aβ is produced from APP by the action of β-secretase, which leads to membrane shedding of the large luminal or extracellular APP domain (Fig. 1B). The 99-residue remnant (C99) is then cleaved in the middle of its transmembrane region by γ-secretase, releasing Aβ, and again near the inner leaflet at the S3 or ε site to release the APP intracellular domain (AICD). The requirement for prior cleavage is a common theme among the intramembrane proteases, with Rhomboid so far the only exception.

Two contemporaneous observations provided critical clues for the identification of the elusive γ-secretase, a subject of intense interest as a potential therapeutic target. First, knockout of presenilin genes eliminated γ-secretase cleavage of APP (*14*). Second, the types of compounds that could inhibit γ-secretase contained moieties typically found in aspartyl protease inhibitors (*15*). These findings led to the identification

of two conserved transmembrane aspartates in the multipass presenilin that are critical for γ-secretase cleavage of APP (Fig. 1B), suggesting that presenilins might be the responsible aspartyl proteases (*16*). Presenilin is cut into two pieces, an N-terminal fragment (NTF) and a C-terminal fragment (CTF), the formation of which is gated by limiting cellular factor(s) (*17*). The NTF and CTF remain physically associated in a high–molecular weight complex and are metabolically stable (*18*–*20*). These and other results suggest that the NTF-CTF heterodimer is the biologically active form (*21*). The NTF and CTF each contribute one of the critical and conserved aspartates, suggesting that the γ-secretase active site might be at the interface between these two presenilin fragments. In strong support of this hypothesis, transition-state analog inhibitors of γ-secretase (compounds designed to interact with the active site of the protease) were found to bind directly to presenilin NTF and CTF (*22*, *23*). However, presenilins are apparently part of a larger multiprotein complex that constitutes γ-secretase (see below).

At the same time presenilins were discovered as susceptibility loci for Alzheimer's disease, they were also shown to be required for Notch signaling (*24*), a pathway essential for cell differentiation during development and beyond (*25*). After Notch is synthesized in the ER, the receptor is cleaved in its extracellular domain during its passage through the secretory pathway, and the two pieces so generated remain associated (*26*). Upon interaction with a cognate ligand, Notch becomes susceptible to a second extracellular proteolysis near the membrane (S2/β in Fig. 1B) (*27*, *28*). The membrane-associated remnant is then cleaved at the S4/γ and S3/ε sites by γ-secretase (*29*), releasing the Notch intracellular domain (NICD). NICD translocates to the nucleus and activates transcription after associating with the nuclear partner CSL (*30*). Knock-in of a Notch-1 transmembrane mutation that greatly reduces presenilin-mediated proteolysis at S3 leads to a lethal phenotype in mice that is similar to that seen in Notch-1 knockout mice, indicating that efficient γ-secretase cleavage is essential for Notch signaling during development (*31*). By analogy, it has been suggested that the intracellular domain of APP is likewise implicated in cell signaling, but whether it acts in the nucleus (*32*) or at the cell membrane before its release by γ-secretase (*33*) is not yet resolved.

The highly conserved role of γ-secretase in Notch signaling and its importance in development enabled genetic screens in worms that identified two Notch modifiers, a single-pass membrane protein APH-2 (nicastrin) and a multipass protein APH-1 (*34*–*36*). Nicastrin was independently isolated biochemically as a presenilin-associated protein and later found to be essential for γ-secretase processing of both APP and Notch (*37*, *38*). A saturation screen in *Caenorhabditis elegans* for presenilin modifiers netted these proteins and added Pen-2. All four proteins (presenilin, nicastrin, Aph-1, and Pen-2) associate with one another (*39*, *40*) and with an immobilized γ-secretase inhibitor (*40*, *41*). Moreover, their coexpression increased γ-secretase activity in both *Drosophila* and mammalian cells (*39*, *40*) and reconstituted activity in yeast (*42*). Because yeast have no such protease activity and contain no apparent orthologs of these metazoan proteins, these findings strongly suggest that this quartet of proteins is necessary and sufficient for γ-secretase activity. γ-Secretase is so far unique among intramembrane proteases in being composed of several different proteins: S2P, SPP, and Rhomboid do not appear to require other proteins for the proteolytic event per se. Coexpression, RNA interference, and the identification of assembly intermediates suggest the order in which these four subunits come together (*39*, *43*, *44*), and partial dissociation of the protease complex with detergent offers a model for how these subunits interact (Fig. 1B, inset) (*45*). Nicastrin and Aph-1 together can stabilize full-length presenilin, and the final addition of Pen-2 apparently triggers presenilin endoproteolysis and γ-secretase activity (*39*). Pen-2 is also required to stabilize the presenilin subunits (*46*). However, the specific biochemical functions of these presenilin cofactors are presently enigmatic.

Since the discovery that Notch is cleaved by γ-secretase, a plethora of other substrates have been identified, including Erb-B4, E- and N-cadherins, CD44, the low-density lipoprotein receptor, Nectin-1, and the Notch ligands Delta and Jagged (*47*). Knowledge of the cellular functions of these proteolytic events vary, but in the case of N-cadherin, the produced intracellular domain associates with the transcriptional activator CREB binding protein (CBP) and promotes its migration to the cytosol and degradation by the proteasome (*48*). Although cellular function can be ascribed in some cases, the ability of γ-secretase to cleave so many different substrates and its apparently poor sequence specificity raise the question of whether a major role of this enzyme is to serve as a general degrading protease for membrane-bound protein remnants. Indeed, γ-secretase appears to be unique among intramembrane proteases in its ability to process so many different substrates: S2P, SPP, and Rhomboid all display some degree of sequence specificity near their respective sites of proteolysis. The broad substrate recognition by γ-secretase is likely related to the fact that, unlike the other intramembrane proteases, the enzyme does not require helix-breaking residues near the cleavage sites within the substrates.

Exactly how do substrates interact with the enzyme? For proteolysis to occur within the boundaries of the membrane, the active site would be expected to be inside the protease complex, sequestering the catalytic water and hydrophilic aspartates from the lipid hydrocarbon tails. As a corollary, the enzyme should have a substrate docking site on the outer surface of the complex, because the substrates are themselves confined to two-dimensional movement within the bilayer. Evidence for such a docking site includes the fact that an APP substrate coelutes with γ-secretase components upon affinity isolation with an immobilized inhibitor directed to the protease active site (*41*). Moreover, biophysical methods that allow detection of APP-presenilin interactions in cells demonstrate that the interaction occurs in the presence of an active site–directed inhibitor (*49*). This interaction, however, is prevented by a helical peptide that mimics the APP transmembrane domain and blocks γ-secretase activity by a unique mechanism (*50*, *51*), perhaps by binding to the docking site. Important unresolved issues include the location of the docking site on the protease complex [co-immunoprecipitation of C99 with truncated presenilins suggests that the first and eighth transmembrane regions may contribute to this site (*52*)], the substrate path from docking site to active site, and how substrate conformation is altered during the enzymatic process. Other I-CLiPs would be predicted to contain substrate docking sites for similar reasons, but this hypothesis remains untested.

An alternative model for γ-secretase that could potentially address these considerations is that the active site forms not within a single presenilin but at the interface of two presenilin molecules composing a dimer. Recent evidence suggests that two presenilin molecules lie at the core of the γ-secretase complex. This includes the coimmunoprecipitation of differently tagged presenilins and the crosslinking of two NTF fragments by modified γ-secretase inhibitors (*53*). This idea is corroborated by findings on a presenilin-related protein, signal peptide peptidase (see below). Whether S2Ps or Rhomboids are dimers is unknown: Perhaps this is a particular characteristic of the aspartyl I-CLiPs. How the two presenilins might interact within the complex and what this means for substrate processing are important questions for future studies. The issue of the stoichiometry of the γ-secretase complex members is presently unclear. Estimates of the complex size range from 250 kD (*40*) to 2 MD (*54*), although most studies suggest 400 to 600 kD (*55*–*57*). This could mean that some or all components are found at least twice in a single complex or that unidentified modulator

proteins are present. These possibilities are not mutually exclusive.

SPP Aspartyl Proteases: Variation on a Variation

The concept of presenilin as the catalytic component for γ-secretase was considerably strengthened when signal peptide peptidase (SPP) was found to be a similar intramembrane aspartyl protease. SPP clears remnant signal peptides from the membrane after their production by signal peptidase (Fig. 1C). However, this process apparently also plays a role in immune surveillance, during which signal peptides from the major histocompatibility complex (MHC) type I molecules are cleaved by SPP and the peptide products are presented on the cell surface as an indication to natural killer cells that MHC synthesis is proceeding normally (*58*). In addition, SPP is exploited by the hepatitis C virus for the maturation of its core protein, suggesting that this protease may be a suitable target for antiviral therapy (*59*). SPP was identified by affinity labeling with a peptidomimetic inhibitor, and the protein sequence displayed parallels with presenilin (Fig. 1C) (*60*). SPP contains two conserved aspartates, each predicted to lie in the middle of a transmembrane domain, and the aspartate-containing sequences resemble those found in presenilins. The predicted topology of SPP also resembles that of presenilins, placing the key aspartates in the same relative position to each other in the membrane. As with S2P compared with its bacterial relatives, the orientation of the aspartate-containing transmembrane domains of SPP is apparently opposite to that of presenilins, again in correlation with the orientation of SPP substrates, which is opposite that of γ-secretase substrates. Before the identification of SPP, a computational search for presenilin-like proteins netted an entire family of so-called presenilin homologs (PSHs) (*61*); however, it is not yet clear if all of these proteins have catalytic activity.

SPP appears to be less complicated than γ-secretase. Expression of human SPP in yeast reconstituted the protease activity, suggesting that the protein has activity on its own and does not require other mammalian protein cofactors (*60*). Moreover, unlike presenilins, SPP is not processed into two pieces. Thus, SPP may be a more tractable enzyme for understanding this type of intramembrane aspartyl protease and may shed light on γ-secretase structure and function. Indeed, the catalytic sites of the two proteases appear remarkably similar: their activities are inhibited by some of the same active site–directed peptidomimetics (*51*, *62*). SPP forms a homodimer very rapidly in cells, and this dimer is stable enough to allow isolation and analysis (*63*). Moreover, this dimer can be specifically labeled by a transition-state analog inhibitor, suggesting that the dimer is catalytically active. The functional importance of this dimer and how it is assembled remains to be determined. However, another SPP-like protein, PSH4, also forms a stable homodimer (*64*), suggesting that this may be a general property of the PSH family. In terms of substrate recognition, however, SPP does display an important difference with γ-secretase: the apparent requirement for helix-breaking residues that should facilitate the ability of the enzyme to access the site of hydrolysis (*65*). In this respect, SPP shows more similarity to S2P and Rhomboid.

Rhomboid Serine Proteases: Playing Solo?

The study of a conserved growth factor signaling pathway also led to intramembrane proteolysis. Epidermal growth factor (EGF) receptor ligands are synthesized as single-pass membrane proteins, but signaling requires proteolytic release and secretion of the ligand for interaction with its cognate receptor. In vertebrates, this is accomplished by membrane-tethered metalloproteases. Genetic analysis in *Drosophila*, however, identified two essential players, dubbed Star and Rhomboid-1, in the proteolysis of the EGF ortholog Spitz. No other components are apparently required. Full-length Spitz remains in the ER until it is ushered by Star to the Golgi apparatus, where it encounters Rhomboid-1 (*66*). Rhomboid-mediated proteolysis in the Golgi is then followed by secretion for intercellular communication. But how does Rhomboid allow cleavage of Spitz?

Mutational analysis of conserved nonglycine residues revealed a requirement for a serine, a histidine, and an asparagine, which together might serve as a catalytic triad typically found in serine proteases (Fig. 1D) (*67*). These three residues are predicted to reside about the same depth within the membrane and thus have the potential to interact with each other. Consistent with this idea, the cleavage site of Spitz was estimated to be at an equivalent depth in the transmembrane region, and Spitz cleavage was sensitive only to serine protease inhibitors. Moreover, a careful analysis of concentration dependence revealed that expression of catalytic amounts of Rhomboid-1 still allowed Spitz proteolysis. Taken together, these findings suggest that Rhomboid-1 is a novel intramembrane serine protease.

What determines Rhomboid substrate specificity, and how is this proteolytic event regulated? Most of the Spitz transmembrane region could be swapped with that of a non-substrate protein without affecting cleavage by Rhomboid; however, the N-terminal quarter of the transmembrane region is critical for substrate recognition (*68*). Indeed, incorporation of this substrate motif into Delta allowed this Notch ligand to be processed by Rhomboid. Further examination of the substrate motif led to the tentative identification of a critical glycine-alanine, suggesting that, as with S2P and SPP, Rhomboid seems to require helix-destabilizing residues within the transmembrane domain of its substrates. Rhomboid activity is distinguished from that of the other I-CLiPs because Rhomboid does not require prior substrate cleavage by another protease. Rhomboid regulation apparently occurs mainly by translocation of the substrate from the Golgi to the ER (mediated by Star) and control of Rhomboid transcription.

Like S2P, Rhomboid genes have been conserved throughout evolution. In spite of overall low homology with eukaryotic Rhomboids, a number of bacterial Rhomboids are capable of cleaving *Drosophila* Rhomboid substrates, and mutation of the putative catalytic triad residues abolished protease activity, illustrating the evolutionary conservation of the serine protease function of Rhomboid (*69*). The natural substrates for the bacterial Rhomboids are unknown. As for substrates of eukaryotic Rhomboid-1 homologs, two mitochondrial membrane proteins have been identified as substrates for yeast Rhomboid RBD1 (*70*–*72*). RBD1-mediated release of one of these substrates is essential for remodeling the mitochondrial membrane, and the human ortholog of RBD1, PARL, could restore substrate proteolysis, proper growth rates, and mitochondrial morphology in a yeast RBD1 mutant (*71*), suggesting that the role of these Rhomboids in mitochondrial function has been evolutionarily conserved. This finding expands the role of intramembrane proteolysis beyond cell signaling, implicating such proteases in a broad range of biological functions.

Conclusions and Perspective

I-CLiPs are multipass membrane enzymes that apparently hydrolyze transmembrane substrates, and these proteases possess essential residues that reside within the boundaries of the lipid bilayer. But apart from this, what do they have in common? All appear to recapitulate the mechanisms of soluble proteases, although this has not been formally demonstrated. Such proof demands a high-resolution crystal structure, a primary challenge for this field of investigation. All I-CLiPs are predicted to contain an initial substrate docking site, but to date evidence for such a docking site has only been provided for γ-secretase. The I-CLiPs discovered so far are important biologically and are closely regulated, but the means of control vary. They are all involved in cell signaling, but some release specialized transcription factors (S2P), whereas others generate transcriptional modulators and/or contribute to degradation of their substrates (γ-secretase and SPP). Other I-CLiPs generate fragments that can act as immune system surveillance molecules (SPP) or secreted growth factors (Rhomboid). Membrane topology seems to dictate the types of substrates that can be cleaved, but

this concept remains speculative. Most I-CLiPs appear to require helix-breaking residues near the cleavage sites of their substrates, although γ-secretase may be an exception.

The next step is to identify substrates for I-CLiP family members whose functions are unknown. For instance, although an entire family of PSHs and Rhomboids have been discovered, natural substrates are known only for a handful of these proteins. The conservation of putative catalytic residues implies conservation of proteolytic function, but the search for substrates is far from trivial. A computational approach for sequence motifs that are apparently required for substrate proteolysis by Rhomboids led to identification of adhesion proteins in the protozoan pathogen *Toxoplasma* as potential substrates (*68*). A similar approach led to the identification of the anticoagulant cell-surface protein thrombospondin as a substrate for a human rhomboid (*73*), but again, the physiological significance of this finding is unknown. Another key issue is understanding the specific mechanisms of these proteases (for example, elucidating conformational changes that take place in both enzyme and substrate during proteolysis, determining if these changes require the input of energy, and identifying enzyme residues that directly interact with substrate). Such understanding should facilitate the identification of new members of this protease class and the design of specific inhibitors. New members will likely display interesting variations on themes already evident from the study of I-CLiPs, enzymes that have transposed the well-known tune of proteolysis into the context of cellular membranes.

References and Notes

1. A. J. Barrett, J. F. Woessner, N. D. Rawlings, Eds., *Handbook of Proteolytic Enzymes* (Academic Press, New York, 1998).
2. M. S. Wolfe, J. De Los Angeles, D. D. Miller, W. Xia, D. J. Selkoe, *Biochemistry* **38**, 11223 (1999).
3. M. S. Brown, J. L. Goldstein, *Cell* **89**, 331 (1997).
4. A. Nohturfft, R. A. DeBose-Boyd, S. Scheek, J. L. Goldstein, M. S. Brown, *Proc. Natl. Acad. Sci. U.S.A.* **96**, 11235 (1999).
5. R. B. Rawson, *Nature Rev. Mol. Cell Biol.* **4**, 631 (2003).
6. J. Sakai *et al.*, *Mol. Cell* **2**, 505 (1998).
7. E. A. Duncan, U. P. Dave, J. Sakai, J. L. Goldstein, M. S. Brown, *J. Biol. Chem.* **273**, 17801 (1998).
8. R. B. Rawson *et al.*, *Mol. Cell* **1**, 47 (1997).
9. N. G. Zelenski, R. B. Rawson, M. S. Brown, J. L. Goldstein, *J. Biol. Chem.* **274**, 21973 (1999).
10. D. Z. Rudner, P. Fawcett, R. Losick, *Proc. Natl. Acad. Sci. U.S.A.* **96**, 14765 (1999).
11. K. Kanehara, Y. Akiyama, K. Ito, *Gene* **281**, 71 (2001).
12. J. Ye, U. P. Dave, N. V. Grishin, J. L. Goldstein, M. S. Brown, *Proc. Natl. Acad. Sci. U.S.A.* **97**, 5123 (2000).
13. J. Hardy, D. J. Selkoe, *Science* **297**, 353 (2002).
14. B. De Strooper *et al.*, *Nature* **391**, 387 (1998).
15. M. S. Wolfe *et al.*, *Biochemistry* **38**, 4720 (1999).
16. M. S. Wolfe *et al.*, *Nature* **398**, 513 (1999).
17. G. Thinakaran *et al.*, *J. Biol. Chem.* **272**, 28415 (1997).
18. G. Yu *et al.*, *J. Biol. Chem.* **273**, 16470 (1998).
19. A. Capell *et al.*, *J. Biol. Chem.* **273**, 3205 (1998).
20. J. Zhang *et al.*, *J. Biol. Chem.* **273**, 12436 (1998).
21. H. Laudon *et al.*, *J. Neurochem.* **89**, 44 (2004).
22. Y. M. Li *et al.*, *Nature* **405**, 689 (2000).
23. W. P. Esler *et al.*, *Nature Cell Biol.* **2**, 428 (2000).
24. D. Levitan, I. Greenwald, *Nature* **377**, 351 (1995).
25. S. Artavanis-Tsakonas, M. D. Rand, R. J. Lake, *Science* **284**, 770 (1999).
26. F. Logeat *et al.*, *Proc. Natl. Acad. Sci. U.S.A.* **95**, 8108 (1998).
27. C. Brou *et al.*, *Mol. Cell* **5**, 207 (2000).
28. J. S. Mumm *et al.*, *Mol. Cell* **5**, 197 (2000).
29. B. De Strooper *et al.*, *Nature* **398**, 518 (1999).
30. E. H. Schroeter, J. A. Kisslinger, R. Kopan, *Nature* **393**, 382 (1998).
31. S. S. Huppert *et al.*, *Nature* **405**, 966 (2000).
32. X. Cao, T. C. Sudhof, *Science* **293**, 115 (2001).
33. X. Cao, T. C. Sudhof, *J. Biol. Chem.*, **279**, 24601 (2004).
34. C. Goutte, W. Hepler, K. M. Mickey, J. R. Priess, *Development* **127**, 2481 (2000).
35. R. Francis *et al.*, *Dev. Cell* **3**, 85 (2002).
36. C. Goutte, M. Tsunozaki, V. A. Hale, J. R. Priess, *Proc. Natl. Acad. Sci. U.S.A.* **99**, 775 (2002).
37. G. Yu *et al.*, *Nature* **407**, 48 (2000).
38. H. M. Chung, G. Struhl, *Nature Cell Biol.* **3**, 1129 (2001).
39. N. Takasugi *et al.*, *Nature* **422**, 438 (2003).
40. W. T. Kimberly *et al.*, *Proc. Natl. Acad. Sci. U.S.A.* **100**, 6382 (2003).
41. W. P. Esler *et al.*, *Proc. Natl. Acad. Sci. U.S.A.* **99**, 2720 (2002).
42. D. Edbauer *et al.*, *Nature Cell Biol.* **5**, 486 (2003).
43. M. J. LaVoie *et al.*, *J. Biol. Chem.* **278**, 37213 (2003).
44. Y. Hu, M. E. Fortini, *J. Cell Biol.* **161**, 685 (2003).
45. P. C. Fraering *et al.*, *Biochemistry* **43**, 323 (2004).
46. S. Prokop, K. Shirotani, D. Edbauer, C. Haass, H. Steiner, *J. Biol. Chem.* **279**, 23255 (2004).
47. B. De Strooper, *Neuron* **38**, 9 (2003).
48. P. Marambaud *et al.*, *Cell* **114**, 635 (2003).
49. O. Berezovska, P. Ramdya, M. S. Wolfe, B. Bacskai, B. T. Hyman, *J. Neurosci.* **23**, 4560 (2003).
50. C. Das *et al.*, *J. Am. Chem. Soc.* **125**, 11794 (2003).
51. A. Y. Kornilova, C. Das, M. S. Wolfe, *J. Biol. Chem.* **278**, 16470 (2003).
52. W. G. Annaert *et al.*, *Neuron* **32**, 579 (2001).
53. E. H. Schroeter *et al.*, *Proc. Natl. Acad. Sci. U.S.A.* **100**, 13075 (2003).
54. Y. M. Li *et al.*, *Proc. Natl. Acad. Sci. U.S.A.* **97**, 6138 (2000).
55. H. Steiner *et al.*, *J. Biol. Chem.* **277**, 39062 (2002).
56. M. R. Farmery *et al.*, *J. Biol. Chem.* **278**, 24277 (2003).
57. O. Nyabi *et al.*, *J. Biol. Chem.* **278**, 43430 (2003).
58. M. K. Lemberg, F. A. Bland, A. Weihofen, V. M. Braud, B. Martoglio, *J. Immunol.* **167**, 6441 (2001).
59. J. McLauchlan, M. K. Lemberg, G. Hope, B. Martoglio, *EMBO J.* **21**, 3980 (2002).
60. A. Weihofen, K. Binns, M. K. Lemberg, K. Ashman, B. Martoglio, *Science* **296**, 2215 (2002).
61. C. P. Ponting *et al.*, *Hum. Mol. Genet.* **11**, 1037 (2002).
62. A. Weihofen *et al.*, *J. Biol. Chem.* **278**, 16528 (2003).
63. A. C. Nyborg *et al.*, *J. Biol. Chem.* **279**, 15153 (2004).
64. T. Golde, personal communication.
65. M. K. Lemberg, B. Martoglio, *Mol. Cell* **10**, 735 (2002).
66. J. R. Lee, S. Urban, C. F. Garvey, M. Freeman, *Cell* **107**, 161 (2001).
67. S. Urban, J. R. Lee, M. Freeman, *Cell* **107**, 173 (2001).
68. S. Urban, M. Freeman, *Mol. Cell* **11**, 1425 (2003).
69. S. Urban, D. Schlieper, M. Freeman, *Curr. Biol.* **12**, 1507 (2002).
70. K. Esser, B. Tursun, M. Ingenhoven, G. Michaelis, E. Pratje, *J. Mol. Biol.* **323**, 835 (2002).
71. G. A. McQuibban, S. Saurya, M. Freeman, *Nature* **423**, 537 (2003).
72. M. Herlan, F. Vogel, C. Bornhovd, W. Neupert, A. S. Reichert, *J. Biol. Chem.* **278**, 27781 (2003).
73. O. Loh, S. Urban, M. Freeman, *Curr. Biol.* **14**, 236 (2004).
74. Single-letter abbreviations for the amino acid residues are as follows: A, Ala; C, Cys; D, Asp; E, Glu; F, Phe; G, Gly; H, His; I, Ile; K, Lys; L, Leu; M, Met; N, Asn; P, Pro; Q, Gln; R, Arg; S, Ser; T, Thr; V, Val; W, Trp; and Y, Tyr.

75. We thank S. Urban for helpful comments on the manuscript. Supported by NIH and the Alzheimer's Association.

Intercontinental Spread of Pyrimethamine-Resistant Malaria

Cally Roper,[1]* Richard Pearce,[1] Shalini Nair,[2] Brian Sharp,[3] François Nosten,[4] Tim Anderson[2]

Here we present molecular evidence demonstrating that malaria parasites bearing high-level pyrimethamine resistance originally arrived in Africa from southeast Asia. Chloroquine (CQ) is being replaced by sulfadoxine pyrimethamine (SP) for treatment of *Plasmodium falciparum* malaria in Africa. Mutations in the dihydrofolate reductase (*dhfr*) gene of *P. falciparum* underlie resistance to pyrimethamine. *Dhfr* alleles with one (108N) or two (108N plus 51I or 108N plus 59R) mutations result in increased parasite clearance times. Infections bearing triple-mutant *dhfr* (108N, 51I, and 59R) have high treatment failure rates, and quadruple-mutant *dhfr* alleles (108N, 51I, 59R, and 164L) render parasites untreatable (*1*). Parasites with one to three mutations occur in Africa, whereas all four mutations are common in southeast Asia (*2*) and South America (*3*). Triple-mutant alleles are replacing other alleles in Africa (*4*).

It is generally assumed that pyrimethamine resistance has evolved multiple times (*1*), because it is selectable in the laboratory, has a simple genetic basis, and appears rapidly after SP introduction. However, analysis of microsatellites that flank *dhfr* in African parasites sampled from sites 4000 km apart demonstrate just three independent origins of double mutants and a single origin of the triple mutant (*4*). Similarly, *dhfr* alleles with two to four mutations have a single evolutionary origin across five southeast Asian countries (*2*).

Genotyping of eight microsatellite markers flanking *dhfr* in both southeast Asian and African parasites shows that the triple-mutant *dhfr* allele in Africa shares a common origin with *dhfr* alleles bearing two to four mutations in southeast Asia (Fig. 1). The predominant five-locus microsatellite haplotype (–10 kb to +0.5 kb) associated with triple-mutant *dhfr* in Africa is identical to that associated with *dhfr* alleles carrying two to four mutations in southeast Asia. In contrast, these five loci show high levels of variation (mean expected heterozygosity = 0.76) around sensitive *dhfr* alleles. Markers situated further from *dhfr* (–20 kb and >+6 kb) show higher polymorphism on chromosomes that carry resistant *dhfr* alleles, as expected, in a selective sweep (*2*, *5*). However, the predominant alleles are the same on resistant chromosomes from both continents. In contrast, African double-mutant *dhfr* alleles have dissimilar flanking alleles, indicating independent origins (*4*). Because all southeast Asian *dhfr* alleles carrying >1 mutation have a single origin, the simplest explanation is that triple-mutant *dhfr* alleles spreading in Africa originated in southeast Asia.

Alleles at the major CQ-resistance locus *pfcrt* also have a common origin in African and Asian parasites (*5*, *6*). CQ-resistant *pfcrt* alleles and triple-mutant *dhfr* alleles may have arrived in Africa in the same parasite genome. Pyrimethamine resistance was widespread in Asia when CQ resistance was first recorded in Africa (*7*). Import of southeast Asian parasites has thus led to the demise of the two affordable drugs that have been the mainstay of malaria treatment in Africa.

Why did the triple-mutant allele not arise independently in Africa? Assuming a mutation rate of 10^{-9} per base per generation, we would expect 10 to 1000 independent origins of triple-mutant parasites in every infection ($10^{10–12}$ parasites) containing double-mutant *dhfr* alleles. The implication is that complex compensatory mutations are required to restore parasite fitness.

Every year 30,000 malaria cases are imported into industrialized countries (*8*). The numbers of cases imported into Africa is unknown but likely to be substantial. Given that 67% of parasites sampled in Thailand, Cambodia, and Myanmar carry the 164L mutation in *dhfr* (*2*), as well as high levels of mefloquine and quinine resistance, it is only a matter of time before these invade and establish in Africa. We suggest that careful thought should be given to preventing further import of resistant parasites, perhaps by screening and treatment of passengers traveling from southeast Asia or South America to Africa. Widespread introduction of artemisinin-based combination therapy (*9*) could also help to minimize the foci from which resistant parasites can spread. Importantly, these data demonstrate that antimalarial drug resistance is an international problem requiring a coordinated international response.

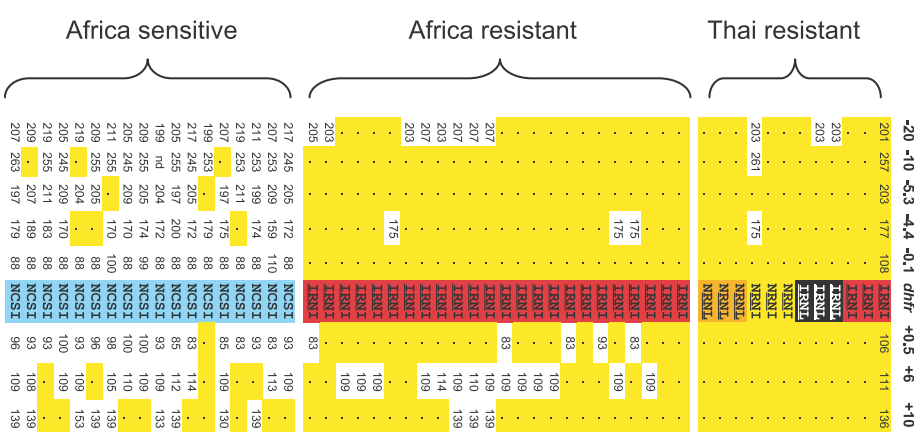

Fig. 1. *dhfr* alleles and flanking microsatellites of parasites from Africa and Thailand. The figure comprises data from 12 Thai parasites with two to four resistance mutations, 24 African parasites with triple-mutant alleles, and 18 African parasites with sensitive *dhfr* alleles. The four-letter codes describe amino acids present at positions 51, 59, 108, and 164 in the predicted *dhfr* protein (*10*). Amino acids conferring resistance are underlined, and *dhfr* alleles are shaded yellow, orange, red, and black in order of increasing resistance. Sensitive alleles are shaded turquoise. Allele lengths are shown for eight microsatellites positioned at –0.1, –4.4, –5.3, –10, and –20 kb upstream and +0.5, +6, and +10 kb downstream of *dhfr*. Dots and yellow shading indicate identical allele size to the predominant resistant haplotype (shown at right).

References and Notes

1. C. V. Plowe *et al.*, *J. Infect. Dis.* **176**, 1590 (1997).
2. S. Nair *et al.*, *Mol. Biol. Evol.* **20**, 1526 (2003).
3. J. F. Cortese, A. Caraballo, C. E. Contreras, C. V. Plowe, *J. Infect. Dis.* **186**, 999 (2002).
4. C. Roper *et al.*, *Lancet* **361**, 1174 (2003).
5. J. C. Wootton *et al.*, *Nature* **418**, 320 (2002).
6. D. A. Fidock *et al.*, *Mol. Cell* **6**, 861 (2000).
7. N. J. White, *J. Antimicrob. Chemother.* **30**, 571 (1992).
8. E. T. Ryan, K. C. Kain, *N. Engl. J. Med.* **342**, 1716 (2000).
9. N. White, *Philos. Trans. R. Soc. London Ser. B* **354**, 739 (1999).
10. Single-letter abbreviations for the amino acid residues are as follows: C, Cys; I, Ile; L, Leu; N, Asn; R, Arg; S, Ser.
11. Supported by NIH and the Wellcome Trust.

Supporting Online Material
www.sciencemag.org/cgi/content/full/305/5687/1124/DC1
Materials and Methods
References and Notes

7 April 2004; accepted 22 June 2004

[1]London School of Hygiene and Tropical Medicine, Keppel Street, London WC1E 7HT, UK. [2]Southwest Foundation for Biomedical Research, San Antonio, TX, USA. [3]Medical Research Council, Durban, South Africa. [4]Shoklo Malaria Research Unit, Mae Sot, Tak, Thailand.

*To whom correspondence should be addressed. E-mail: cally.roper@lshtm.ac.uk

Observation of a One-Dimensional Tonks-Girardeau Gas

Toshiya Kinoshita, Trevor Wenger, David S. Weiss*

We report the observation of a one-dimensional (1D) Tonks-Girardeau (TG) gas of bosons moving freely in 1D. Although TG gas bosons are strongly interacting, they behave very much like noninteracting fermions. We enter the TG regime with cold rubidium-87 atoms by trapping them with a combination of two light traps. By changing the trap intensities, and hence the atomic interaction strength, the atoms can be made to act either like a Bose-Einstein condensate or like a TG gas. We measure the total 1D energy and the length of the gas. With no free parameters and over a wide range of coupling strengths, our data fit the exact solution for the ground state of a 1D Bose gas.

At zero temperature, dense, weakly interacting bosons in a 1D trap form a Bose-Einstein condensate (BEC) (*1*). Dilute, strongly interacting bosons in 1D, however, act in a completely different manner. Rather than condensing into a single quantum state, they are expected to repel each other, as if they were noninteracting fermions (*2*, *3*). Known as a Tonks-Girardeau (TG) gas (*4*, *5*), this system provides a textbook example of the critical role played by coupling strengths in many-body physics (*6*). Recent cold atom experiments have made observations of a TG gas a possibility (*7*), substantially increasing the already extensive body of theoretical research. Strongly coupled 1D atomic gases, and similarly accessible 2D gases, are poised to experimentally elucidate many subtleties of many-body quantum systems (*8*–*17*).

The gradual transition between the BEC and TG regimes is usually characterized by the parameter $\gamma = \varepsilon_{int}/\varepsilon_{kin}$, where ε_{int} and ε_{kin} are the average interaction and kinetic energies calculated with mean field theory. A BEC (low γ) in a 1D trap is qualitatively like a BEC in 3D (*18*, *19*). By trapping atoms in red-detuned 2D optical lattices, which create 2D arrays of atoms in tightly confined tubes (*20*), three recent experiments have approached the 1D TG (high γ) regime. For $\gamma = 0.5$, a marked suppression of three-body collisional loss was observed (*21*). With $\gamma = 1$, changes in the collective excitation spectrum were reported (*22*), and changes in the 1D superfluid to Mott insulator transition were observed by adding an additional 1D optical lattice along the 1D axis (*23*). With the addition of a 1D lattice, the spatially modulated atoms can be described as quasiparticles with increased effective mass (*24*). In this way, a system with $\gamma = 0.5$ can be interpreted as having $\gamma_{eff} \sim 200$. The measured momentum distributions in such a system were found to fit well to a modified theoretical result derived for the lattice TG gas (*24*).

We create a TG gas with no periodic potential along the 1D axis. Our observations extend to $\gamma = 5.5$. We enter the strong coupling regime by using a combination of two independent light traps. A blue-detuned 2D optical lattice tightly confines nearly zero-temperature ^{87}Rb atoms in an array of parallel tubes, and a red-detuned crossed dipole trap weakly confines them along the tubes. As we explain below, the transverse confinement can thus be made tighter, which increases γ, without strengthening the axial confinement, which decreases γ. By changing trap intensities we scan γ, making the atoms either BEC-like or TG-like. We measure ε, the average 1D energy per particle (excluding the trap potential energy) and the equilibrium 1D cloud length. Our data fit well to the exact theory for the ground state of a TG gas in a harmonic trap (*25*), with no free parameters and over a wide range of coupling strengths. Our experiment provides a clear illustration of fermionization in a TG gas.

The interaction regimes of cold bosons in 1D can be understood by comparing the length of single-particle wave functions, ℓ, with the interparticle spacing, $r = 1/n_{1D}$, where n_{1D} is the linear density. The various regimes are illustrated in the wave function sketches of Fig. 1. In the mean field regime, $\ell \gg r$, and ℓ corresponds to the coherence length, which is the deBroglie wavelength associated with the 1D interaction energy (*25*). Long-range phase coherence makes such a trapped 1D gas superfluid. As ℓ approaches r, so that the system enters the TG regime, single-particle wave functions become spatially distinct. With less overlap, ℓ is not predominantly determined by the interaction energy, but by the kinetic energy associated with localizing the mutually repelling particles on a line. In the asymptotic TG limit, $\ell = r$, and the single-particle wave functions are completely distinct. The TG limit can be reached either by increasing the interaction energy (decreasing ℓ) or decreasing n_{1D} (increasing r). The absence of long-range phase coherence and of number fluctuations in space makes the 1D TG gas resemble a gas of classical hard spheres or noninteracting fermions. With its progressive loss of number fluctuations and phase coherence, the transition from a 1D BEC to a TG is similar to the superfluid to Mott insulator transition of a gas in a periodic potential (*26*), but without the manifest long-range spatial order (*21*).

Our experiment can be qualitatively understood as follows (Fig. 1, shaded sketches). Atoms near zero temperature are relatively tightly confined in two transverse dimensions, and loosely confined in an axial dimension. The system is then studied with constant axial confinement and atom number, and successively tighter transverse confinement. At first, the interactions are in the mean field limit, so the Bose gas acts like a 3D fluid. Squeezing the atoms transversely makes them spread out axially (increasing r) and increases ε (decreasing ℓ).

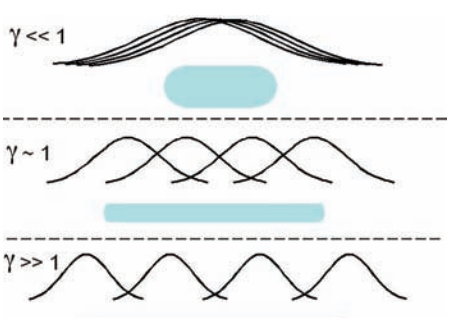

Fig. 1. Cartoon of 1D atom distributions. In each of three γ regimes, the upper drawing illustrates the size, ℓ, and separation, r, of single-particle wave functions. As γ increases, ℓ becomes smaller and r becomes larger, until the bosons, like fermions, become spatially distinct. The three shaded drawings below represent the atomic density in a 1D tube. In our experiment, γ is changed by transversely squeezing the tube. For $\gamma \ll 1$, the gas acts like a fluid and expands axially when squeezed transversely. As γ rises, transverse squeezing has less of an axial effect. For $\gamma \gg 1$, deep in the TG regime, transverse squeezing has no effect on the axial distribution (or energy).

Physics Department, The Pennsylvania State University, University Park, PA 16802, USA.

*To whom correspondence should be addressed. E-mail: dsweiss@phys.psu.edu

As ℓ and r approach each other ($\gamma > 1$) and the bosons start to fermionize, the rate at which both ℓ and r change decreases. We observe the stabilization of r by measuring the 1D cloud length. We also measure ε by removing the axial confinement and letting the atoms expand in 1D. With more squeezing, the interaction energy decreases, because although the higher 3D density tends to yield stronger interactions, the reduction in wave function overlap exerts a greater effect. With more localized wave functions, the kinetic energy starts to dominate. The net effect is that ε quickly approaches the asymptote to its high γ value. Very far in the TG limit ($\gamma \gg 1$), like classical beads on a string or like noninteracting fermions, transverse squeezing of TG atoms would have no effect on either r or ε.

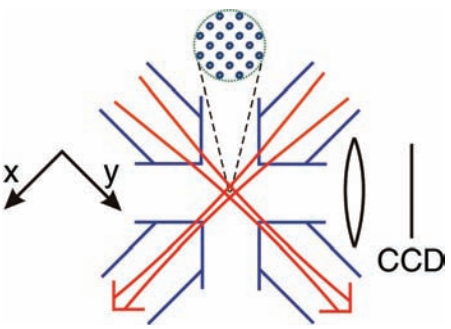

Fig. 2. Scheme illustrating the experiment. The large, blue-detuned crossed beam pairs form the 2D optical lattice that strongly confines atoms in 1D tubes (out of the page). The arrangement of the tubes is illustrated in the magnified circle. The smaller, red-detuned crossed traveling waves trap the atoms axially (out of the page, which corresponds to up in the experiment). The collection of tubes is imaged transversely, without resolving individual tubes.

The starting point for our experiment is a nearly pure ^{87}Rb BEC in the lowest internal energy state, which we produce by all-optical means every 3 s (*27*). The atoms are confined in a horizontal crossed dipole trap made with 1.06-μm yttrium-aluminum-garnet (YAG) laser light (*28*) (Fig. 2). The trap power, P, and waist size, w_0, are dynamically variable, but typically we perform the 1D experiments with $P = 12$ or 320 mW, $w_0 = 70$ μm, and 2×10^5 BEC atoms (supporting online text). We use high-intensity fluorescent imaging to measure cloud sizes (*29*) (supporting online text). By scanning P and progressively reducing the 3D trapped cloud, we determine the resolution of the optical system to be $w_{ir} = 20 \pm 1$ μm.

We create an ensemble of parallel 1D traps (*20*) by superimposing on the crossed dipole trap a 2D optical lattice (Fig. 2), made from two horizontal, orthogonal standing waves with slightly different frequencies (*30*). The lattice is generated by a Ti-sapphire laser, 3.2 THz to the blue of the D2 line, with a 600-μm waist and up to 700 mW per beam. The depth of the lattice, U_0, can thus reach 16 μK·k_B = 87 E_{rec}, where k_B is the Boltzmann constant and E_{rec} is the atom's recoil energy. The maximum transverse oscillation frequency, $\omega_\perp/2\pi$, is 70.7 kHz. The blue-detuned lattice anti-traps in the axial direction, but only very weakly for our atoms, which are in the transverse ground state. The net vertical oscillation frequency, ω_v, is reduced from its value in the crossed dipole trap by at most 2.8% by the lattice light, so we can scan the transverse confinement without affecting the axial confinement. The very large lattice beam waist and large w_0 compared with the initial cloud size means that $\omega_\perp$ and ω_v are nearly the same for the whole ensemble of ~6400 1D traps. The traps differ only in the number of atoms each contains, N_{tube}. For $P = 12$ mW (320 mW), $N_{tube} \sim 54$ (270) for the central tubes.

The 2D lattice is turned on slowly, to avoid nonadiabatic excitation of 1D breathing modes and keep the atoms in the lowest energy axial state. Adiabaticity is achieved by observing the in situ vertical cloud size after the lattice is turned on and keeping residual oscillations below 10% (supporting online text). When turned fully on, the lattice light causes spontaneous emission at a rate of 0.4 Hz, and background gas collisions occur at 0.4 Hz. Either event usually causes an atom to leave the trap, and we observe that 15% of the atoms are lost by the time we make our 1D measurements. To ensure that the remaining atoms are still near zero temperature, we reverse the procedure for turning on the lattice and measure how many atoms return to the BEC in the crossed dipole trap. Of the remaining atoms, 80% return to the 3D BEC, which implies that the thermal energy in 1D is not substantial.

Tunneling between tubes while the lattice is turned on may lead to a redistribution of atoms among the 1D tubes. We do not observe this in the measured horizontal width, w_h, when the atoms are trapped in both light traps. To the extent that tunneling does occur, it has a minimal effect, after the tubes are averaged, on our 1D calculations.

To measure ε, we suddenly turn off only the crossed dipole trap and let the atoms expand ballistically while they are still in the 1D tubes. With $P = 12$ mW, when $U_0 < 20\ E_{rec}$, the transverse width of the atomic ensemble (Fig. 3A, squares) increases, bal-

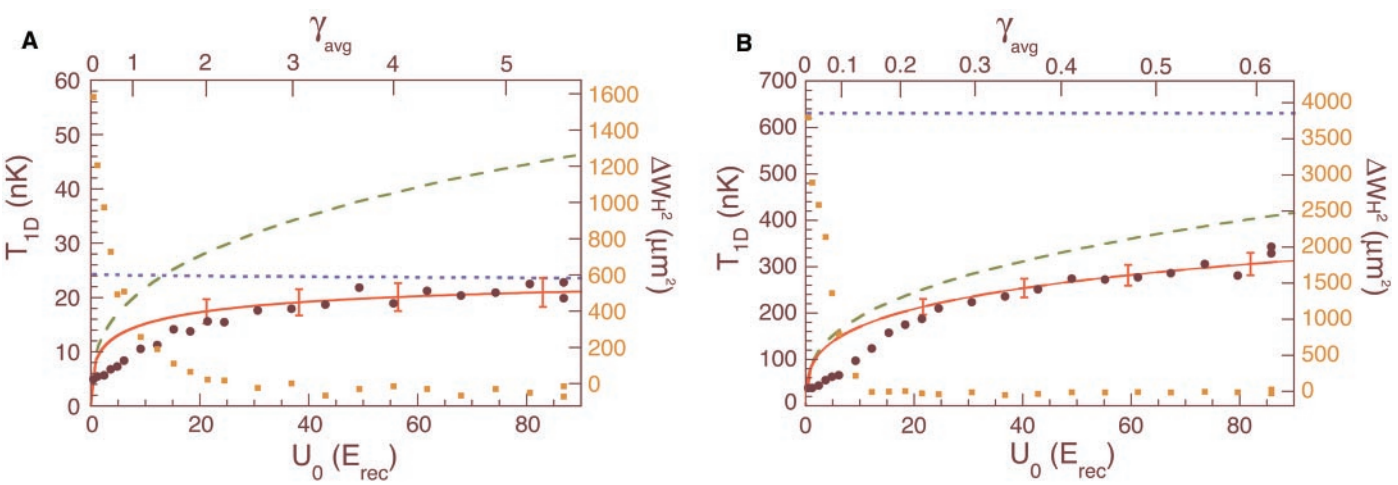

Fig. 3. Plot of the 1D temperature versus the transverse confinement. (**A**) At $P = 12$ mW, the atoms act like a TG gas. (**B**) At $P = 320$ mW, the atoms act like a BEC. The circles denote T_{1D}, which is proportional to ε. TG theory curves (short-dashed lines) are valid for $\gamma \gg 1$, mean field theory curves (long-dashed lines) are valid for $\gamma \ll 1$, and exact 1D Bose gas theory curves (solid lines) are valid for all values of γ. The theory curves have no free parameters. Error bars in the theory curve reflect uncertainty in the input experimental parameters, the most important being the crossed dipole trap size (±2 μm) and, secondarily, the atom number (±10%). See table S1 for detailed experimental parameters. The solid squares represent the change in the square of the horizontal width, Δw_h^2, measured from 7 to 17 ms after the crossed dipole trap has been shut off. The system is purely 1D only above $U_0 \sim 20\ E_{rec}$, when the interaction between tubes is negligible.

listically at the lowest U_0 values and like a random walk ($\Delta w_h \propto \sqrt{t}$) above 10 E_{rec}, which we attribute to tunneling between tubes. At higher values of U_0, however, the only expansion is vertical. There are thus no complications from transverse kinetic energy, mean field interactions between tubes, or spreading of 1D energy into other directions. When $U_0 \gtrsim 20\ E_{rec}$, all requirements for observing a TG gas are well realized in this system (*25*).

We take images 7 ms and 17 ms after the crossed dipole trap is turned off. All 1D strips in the 2D charge-coupled device image are summed together to obtain the linear distributions, which fit well to a Gaussian. At all values of U_0, expansion in 1D exactly resembles ballistic expansion. We extract ε from the measured 1D temperature, T_{1D}, by the simple relation, $\varepsilon = k_B T_{1D}/2$. We measure T_{1D} with $P = 12$ mW as a function of U_0, which changes the transverse confinement (Fig. 3A). We also calculate T_{1D} as a function of U_0 and N_{tube}, using the exact theory (solid curve, valid for all values of γ), mean field theory (long-dashed curve, valid for $\gamma \ll 1$), and TG theory (short-dashed curve, valid for $\gamma \gg 1$) (*25*). N_{tube} values are assigned to tubes according to the initial distribution in the crossed dipole trap, and a weighted average is taken (supporting online material). The theory curves have no free parameters. Agreement between experiment and the exact theory is excellent over the full range so that the system is reliably 1D. When γ_{avg}, the weighted average γ for all the tubes, is 5.5, T_{1D} is already quite close to its value in the TG limit. The insensitivity of T_{1D} to transverse squeezing is manifest in the data.

Figure 3B shows T_{1D} as a function of transverse confinement with the same lattice parameters as in Fig. 3A, but with $P = 320$ mW, where both N_{tube} and ω_v are larger, and γ is nine times smaller. Here the exact theory (solid curve) more closely resembles mean field theory (long-dashed curve), and T_{1D} does not level off to the same degree. The reliably 1D data ($U_0 \gtrsim 20\ E_{rec}$) in this limit also agree well with the exact theory (*25*), with no free parameters. The two limiting and the exact theory curves in Fig. 3, A and B, are each part of a universal family of curves parameterized by γ. The curves in Fig. 3B thus have the same shape as the leftmost part of the curves in Fig. 3A.

Unlike in Fig. 3A, where $P = 12$ mW, there is no transverse expansion between $U_o = 10$ and $20\ E_{rec}$ when $P = 320$ mW (Fig. 3B, squares). Because the lattice is the same in the two cases (and the other potential has been turned off), we know that the atoms are not isolated in their respective tubes. That suggests that the suppression of tunneling between tubes in this region is due to intertube mean field interactions. Although this is in itself an interesting effect (*15*), for the present purposes it means that the tubes are not independent 1D systems at those lattice depths.

Figure 4 shows the root mean square (rms) full length, w_{rms}, of the 1D trapped atom cloud as a function of U_0. With full lattice power, the aspect ratio of these 1D systems is 350. The density distribution in individual tubes is expected to vary between an inverted parabola (low γ) and the square root of an inverted parabola (high γ) (*25*). When either of these distributions, or the sum over tubes with these distributions, is numerically convolved with w_{ir}, the resulting distribution is nearly Gaussian. We experimentally observe Gaussian distributions of rms full length, w_{ex}. To compare experiment with theory, we deconvolve w_{ir} from Gaussian fits of the data, assuming that both the atomic distribution and the instrumental resolution are Gaussians, so $w_m = \sqrt{w_{ex}^2 - w_{ir}^2}$. Numerical calculations show that $w_m - w_{rms}$ ranges from 2 to 4% for our parameters. Because this difference is smaller than the dominant systematic error (our knowledge of w_{ir}), we do not adjust our measured widths to account for it.

Without free parameters, the measured lengths accord well with the exact 1D Bose gas theory (Fig. 4, solid curve) (*25*), applied to our ensemble of tubes (supporting online text). Mean field theory (Fig. 4, long-dashed curve) predicts larger lengths and a larger rate of increase with γ. By $\gamma_{avg} = 5.7$ (there are 12% fewer atoms in this scan than in the scan in Fig. 3A), the size is still ~20% short of the asymptotic size in the TG limit (Fig. 4, short-dashed curve). The remaining wave function overlap at $\gamma_{avg} = 5.7$ is reduced as γ grows mostly because r (and hence w_{rms}) increases. At $\gamma_{avg} = 5.7$, the total linear extent of the atoms is actually smaller in TG theory than in mean field theory. However, we plot the rms length, and because the TG distribution is flatter, its rms length is larger.

Fermionization is evident from the combination of Figs. 3A and 4. Figure 4 shows that the cloud length is smaller than the mean field value, so the 1D density is larger. But even with a larger 1D density, Fig. 3A shows that the total energy of the atoms is 2.5 times smaller than the mean field value. This can only result from substantially reduced wave function overlap.

In summary, we have constructed a set of parallel 1D Bose gases where axial and transverse trapping are mutually independent. We can therefore change the 1D coupling strength without changing the axial trapping, and realize a free Bose gas in the 1D TG regime. Reminiscent of fermions in a superconductor acting like bosons, strongly coupled 1D bosons act like fermions. By measuring the total 1D energy and the axial size of the atomic distribution, with both strong and weak coupling, we illustrate the large difference between the two coupling regimes.

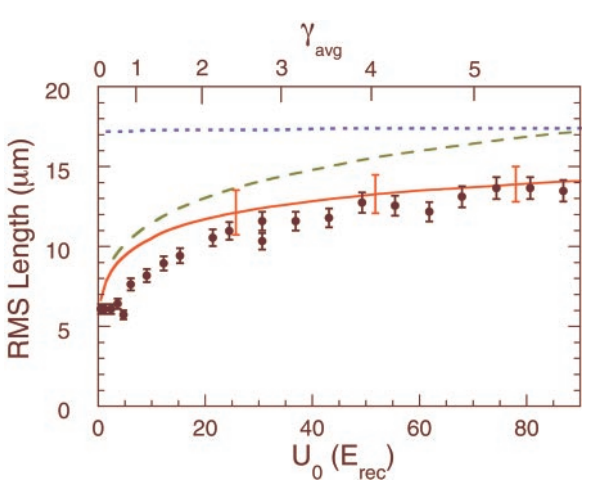

Fig. 4. Plot of the rms full length of the 1D atom cloud versus the transverse confinement at $P = 12$ mW. The circles represent the measured values, with the instrumental resolution deconvolved (see text). Error bars on the experimental points reflect residual trap excitations that arise when the lattice is turned on. The curves for TG theory (short-dashed line), mean field theory (long-dashed line), and exact 1D Bose gas theory (solid line) are shown (*11*). Error bars on the theory curve reflect uncertainties in experimental parameters and are dominated by a 5% uncertainty in w_{ir}. With no free parameters, the data conform to the exact theory (*11*) above $U_0 \sim 20\ E_{rec}$, where the system is purely 1D.

References and Notes

1. W. Ketterle, N. J. vanDruten, *Phys. Rev. A* **54**, 656 (1996).
2. M. Girardeau, *J. Math. Phys.* **1**, 516 (1960).
3. C. N. Yang, Y. P. Yang, *J. Math. Phys.* **10**, 1115 (1969).
4. L. Tonks, *Phys. Rev.* **50**, 955 (1936).
5. E. H. Lieb, W. Liniger, *Phys. Rev.* **130**, 1605 (1963).
6. L. Pitaevski, S. Stringari, in *Bose Einstein Condensation* (Clarendon, Oxford, 2003), pp. 323–338.
7. M. Olshanii, *Phys. Rev. Lett.* **81**, 938 (1998).
8. D. S. Petrov, J. V. Shlyapnikov, T. M. Walraven, *Phys. Rev. Lett.* **85**, 3745 (2000).
9. M. A. Cazalilla, *Phys. Rev. A* **67,** 053606 (2003).
10. S. Chen, R. Egger, *Phys. Rev. A* **68**, 063605 (2003).
11. M. Olshanii, V. Dunjko, *Phys. Rev. Lett.* **91**, 090401 (2003).
12. D. M. Gangardt, G. V. Shylapnikov, *Phys. Rev. Lett.* **90**, 010401 (2003).
13. E. H. Lieb, R. Seiringer, J. Yngvason, *Phys. Rev. Lett.* **91**, 150401 (2003).
14. G. P. Berman, F. Borgonovi, F. M. Izrailev, A. Smerzi, *Phys. Rev. Lett.* **92**, 030404 (2004).
15. A. F. Ho, M. A. Cazalilla, T. Giamarchi, *Phys. Rev. Lett.* **92**, 130405 (2004).

16. A. vanOtterlo *et al.*, *Phys. Rev. B* **52**, 16176 (1995).
17. G. Schmid, S. Todo, M. Troyer, A. Dorneich, *Phys. Rev. Lett.* **88**, 167208 (2002).
18. A. Görlitz, *Phys. Rev. Lett.* **87**, 130402 (2001).
19. M. Greiner, I. Bloch, O. Mandel, T. W. Hänsch, T. Esslinger, *Appl. Phys. B* **73**, 769 (2001).
20. M. T. DePue, C. McCormick, S. L. Winoto, S. Oliver, D. S. Weiss, *Phys. Rev. Lett.* **82**, 2262 (1999).
21. B. L. Tolra *et al.*, *Phys. Rev. Lett.* **92**, 190401 (2004).
22. H. Moritz, T. Söferle, M. Köhl, T. Esslinger, *Phys. Rev. Lett.* **91**, 250402 (2003).
23. T. Söferle, H. Moritz, C. Schori, M. Köhl, T. Esslinger, *Phys. Rev. Lett.* **92**, 130403 (2004).
24. B. Paredes *et al.*, *Nature* **429**, 277 (2004).
25. V. Dunjko, V. Lorent, M. Olshanii, *Phys. Rev. Lett.* **86**, 5413 (2001).
26. M. Greiner, O. Mandel, T. Esslinger, T. W. Hänsch, I. Bloch, *Nature* **415**, 39 (2002).
27. T. Kinoshita, T. Wenger, D. S. Weiss, in preparation.
28. D. J. Han, M. T. DePue, D. S. Weiss, *Phys. Rev. A* **63**, 023405 (2001).
29. M. T. DePue, S. L. Winoto, D. J. Han, D. S. Weiss, *Opt. Commun.* **180**, 73 (2000).
30. S. L. Winoto, M. T. DePue, N. E. Bramall, D. S. Weiss, *Phys. Rev A*, **59**, R19 (1999).
31. We thank M. Olshanii, K. Gibble, and J. Banavar for useful discussions and V. Dunjko for providing us with the exact 1D Bose gas theory curves. This work was supported by the NSF grant no. PHY-0137477.

Supporting Online Material
www.sciencemag.org/cgi/content/full/1100700/DC1
SOM Text
Table S1

25 May 2004; accepted 20 July 2004
Published online 29 July 2004;
10.1126/science.1100700
Include this information when citing this paper.

Observation of the Pairing Gap in a Strongly Interacting Fermi Gas

C. Chin,[1] M. Bartenstein,[1] A. Altmeyer,[1] S. Riedl,[1] S. Jochim,[1] J. Hecker Denschlag,[1] R. Grimm[1,2]*

We studied fermionic pairing in an ultracold two-component gas of ^{6}Li atoms by observing an energy gap in the radio-frequency excitation spectra. With control of the two-body interactions through a Feshbach resonance, we demonstrated the dependence of the pairing gap on coupling strength, temperature, and Fermi energy. The appearance of an energy gap with moderate evaporative cooling suggests that our full evaporation brought the strongly interacting system deep into a superfluid state.

The spectroscopic observation of a pairing gap in the 1950s marked an important experimental breakthrough in research on superconductivity (*1*). The gap measurements provided a key to investigating the paired nature of the particles responsible for the frictionless current in metals at very low temperatures. The ground-breaking Bardeen-Cooper-Schrieffer (BCS) theory, developed at about the same time, showed that two electrons in the degenerate Fermi sea can be coupled by an effectively attractive interaction and will form a delocalized, composite particle with bosonic character. BCS theory predicted that the gap in the low-temperature limit is proportional to the critical temperature T_c for the phase transition, in agreement with the experimental measurements. In general, the physics of superconductivity and superfluidity go far beyond the weak-coupling limit of BCS theory. In the limit of strong coupling, paired fermions form localized bosons, and the system can undergo Bose-Einstein condensation (BEC). The BCS limit and the BEC limit are connected by a smooth BCS-BEC crossover, which has been a subject of great theoretical interest for more than three decades (*2*–*5*). The formation of pairs generally represents a key ingredient of superfluidity in fermionic systems, and the gap energy is a central quantity to characterize the pairing regime.

The rapid progress in experiments with ultracold degenerate Fermi gases (*6*) has opened up a unique testing ground to study phenomena related to pairing and superfluidity at densities typically a billion times below the ones in usual condensed-matter systems. In cold-atom experiments, magnetically tuned scattering resonances (Feshbach resonances) serve as a powerful tool to control the two-body coupling strength in the gas (*7*). On the basis of such a resonance, a strongly interacting degenerate Fermi gas was recently realized (*8*). A major breakthrough then followed, with the creation of Bose-Einstein condensates of molecular dimers composed of fermionic atoms (*9*–*13*), which corresponds to the realization of a BEC-type superfluid in the strong coupling limit. By variation of the coupling strength, subsequent experiments (*12*, *14*–*18*) began to explore the crossover to a BCS-type system. This BEC-BCS crossover is closely linked to the predicted "resonance superfluidity" (*19*–*22*) and a "universal" behavior of a Fermi gas with resonant interactions (*23*, *24*). The observation of the condensation of atom pairs (*15*, *16*) and measurements of collective oscillations (*17*, *18*) support the expected superfluidity at presently attainable temperatures in Fermi gases with resonant interactions.

We prepared our ultracold gas of fermionic ^{6}Li atoms in a balanced spin-mixture of the two lowest sub-states $|1\rangle$ and $|2\rangle$ of the electronic $1s^2 2s$ ground state, employing methods of laser cooling and trapping and subsequent evaporative cooling (*9*). A magnetic field B in the range between 650 to 950 G was applied for Feshbach tuning through a broad resonance centered at the field $B_0 \approx 830$ G. In this high-field range, the three lowest atomic levels form a triplet of states $|1\rangle$, $|2\rangle$, and $|3\rangle$, essentially differing by the orientation of the nuclear spin ($m_I = 1, 0, -1$, where m_I is the nuclear magnetic quantum number). In the resonance region with $B < B_0$, the s-wave scattering length a for collisions between atoms in states $|1\rangle$ and $|2\rangle$ is positive. Here, two-body physics supports a weakly bound molecular state with a binding energy $E_b = \hbar^2/(ma^2)$, where $\hbar$ is Planck's constant h divided by 2π and m is the atomic mass. Molecules formed in this state can undergo BEC (*9*–*13*). At $B = B_0$, the two-body interaction is resonant ($a \rightarrow \pm\infty$), corresponding to a vanishing binding energy of the molecular state. Beyond the resonance ($B > B_0$), the scattering length is negative ($a < 0$), which leads to an effective attraction. Here, two-body physics does not support a weakly bound molecular level, and pairing can only occur because of many-body effects.

Our experimental approach (*9*, *14*) facilitated preparation of the quantum gas in various regimes with controlled temperature, Fermi energy, and interaction strength. We performed evaporative cooling under conditions (*25*) in which an essentially pure molecular Bose-Einstein condensate containing $N = 4 \times 10^5$ paired atoms could be created as a starting point for the experiments. The final laser power of the evaporation ramp allowed us to vary the temperature T. The Fermi energy E_F (Fermi temperature $T_F = E_F/k_B$, with Boltzmann's constant k_B) was controlled by a recompression of the gas, which we performed by increasing the trap laser power after the cooling process (*25*). We then varied the interaction strength by slowly changing the magnetic field to the desired final value. The adiabatic changes applied to the gas after evaporative cooling proceeded with conserved entropy (*14*). Lacking a reliable method to determine the temperature T of a deeply degenerate, strongly interacting Fermi gas in a direct way, we characterized the system by the temperature T' measured after an isentropic conversion into the BEC limit (*25*). For

[1]Institut für Experimentalphysik, Universität Innsbruck, Technikerstraße 25, 6020 Innsbruck, Austria. [2]Institut für Quantenoptik und Quanteninformation, Österreichische Akademie der Wissenschaften, 6020 Innsbruck, Austria.

*To whom correspondence should be addressed. E-mail: rudolf.grimm@uibk.ac.at

a deeply degenerate Fermi gas, the true temperature T is substantially below our observable T' (*25*, *26*), but a general theory for this relation is not yet available.

Radio-frequency (RF) spectroscopy has been introduced as a powerful tool to study interaction effects in ultracold Fermi gases (*27*–*29*). Molecular binding energies have been measured for ^{40}K atoms (*29*), for which the potential of the method to observe fermionic pairing gap energies has also been pointed out. RF spectroscopy has been applied to ^{6}Li atoms to study interaction effects up to magnetic fields of 750 G (*28*). One important observation was the absence of mean-field shifts in the strongly interacting regime. This effect can be attributed to the fact that, in the relevant magnetic-field range, all s-wave scattering processes between ^{6}Li atoms in the states $|1\rangle$, $|2\rangle$, and $|3\rangle$ are simultaneously unitarity-limited. This property of ^{6}Li is very favorable for RF spectroscopy because it suppresses shifts and broadening by mean-field effects.

We drove RF transitions from state $|2\rangle$ to the empty state $|3\rangle$ at ~80 MHz and monitored the loss of atoms in state $|2\rangle$ after weak excitation by a 1-s RF pulse, using state-selective absorption imaging (*14*). Our experiment was optimized to obtain a resolution of ~100 Hz, corresponding to an intrinsic sensitivity to interaction effects on the scale of ~5 nK, which is more than two orders of magnitude below the typical Fermi temperatures.

We recorded RF spectra for different degrees of cooling and in various coupling regimes (Fig. 1). We realized the molecular regime at $B = 720$ G ($a = +120$ nm). For the resonance region, we examined two different magnetic fields, because the precise resonance location B_0 is not exactly known. Our two values $B = 822$ G (*16*) and 837 G (*13*, *18*) may be considered as lower and upper bounds for B_0. We also studied the regime beyond the resonance with a large negative scattering length at $B = 875$ G ($a \approx -600$ nm). Spectra taken in a "hot" thermal sample at $T \approx 6T_F$ (where $T_F = 15$ μK) show the narrow atomic $|2\rangle \rightarrow |3\rangle$ transition line (Fig. 1, top) and serve as a frequency reference. We present our spectra as a function of the RF offset with respect to the bare atomic transition frequency.

Spectral signatures of pairing have been theoretically considered (*30*–*34*). A clear signature of the pairing process is the emergence of a double-peak structure in the spectral response as a result of the coexistence of unpaired and paired atoms. The pair-related peak is located at a higher frequency than the unpaired-atoms signal, because energy is required for pair breaking. For understanding of the spectra, both the homogeneous line shape of the pair signal (*31*, *33*) and the inhomogeneous line broadening due to the density distribution in the harmonic trap need to be taken into account (*34*). As an effect of inhomogeneity, fermionic pairing due to many-body effects takes place predominantly in the central high-density region of the trap, and unpaired atoms mostly populate the outer region of the trap where the density is low (*34*–*36*). The spectral component corresponding to the pairs thus shows a large inhomogeneous broadening in addition to the homogeneous width of the pair-breaking signal. For the unpaired atoms, the homogeneous line is narrow and the effects of inhomogeneity and mean-field shifts are negligible. These arguments explain why the RF spectra in general show a relatively sharp peak for the unpaired atoms together with a broader peak attributed to the pairs.

We observed clear double-peak structures already at $T'/T_F = 0.5$, which we obtained with moderate evaporative cooling down to a laser power of $P = 200$ mW (Fig. 1, middle, $T_F = 3.4$ μK). In the molecular regime $B = 720$ G, the sharp atomic peak was well separated from the broad dissociation signal (*29*), which showed a molecular binding energy of $E_b = h \times 130$ kHz $= k_B \times 6.2$ μK. For $B \rightarrow B_0$, the peaks began to overlap. In the resonance region [822 G and 837 G (Fig. 1)], we still observed a relatively narrow atomic peak at the original position together with a pair signal. For magnetic fields beyond the resonance, we could resolve the double-peak structure for fields up to ~900 G.

For $T'/T_F < 0.2$, realized with a deep evaporative cooling ramp down to an optical trap power of $P = 3.8$ mW, we observed the disappearance of the narrow atomic peak in the RF spectra (Fig. 1, bottom, $T_F = 1.2$ μK). This shows that essentially all atoms were paired. In the BEC limit (720 G), the dissociation line shape is identical to the one observed in the trap at higher temperature and Fermi energy. Here the localized pairs are molecules with a size much smaller than the mean interparticle spacing, and the dissociation signal is independent of the density. In the resonance region [822 G and 837 G (Fig. 1)], the pairing signal shows a clear dependence on density (Fermi energy), which becomes even more pronounced beyond the resonance (875 G). We attribute this to the fact that the size of the pairs becomes comparable to or larger than the interparticle spacing. In addition, the narrow width of the pair signal in this regime (Fig. 1, bottom, $B = 875$ G) indicates a pair localization in momentum space to well below the Fermi momentum $\hbar k_F = \sqrt{2mE_F}$ and thus a pair size exceeding the interparticle spacing.

To quantitatively investigate the crossover from the two-body molecular regime to the fermionic many-body regime, we measured the pairing energy in a range between 720 and 905 G. The measurements were performed after deep evaporative cooling ($T'/T_F < 0.2$) for two different Fermi temperatures, $T_F = 1.2$ μK and $T_F = 3.6$ μK (Fig. 2). As an effective pairing gap, we defined $\Delta\nu$ as the frequency difference between the pair-signal maximum and the bare atomic resonance. In the BEC limit, the effec-

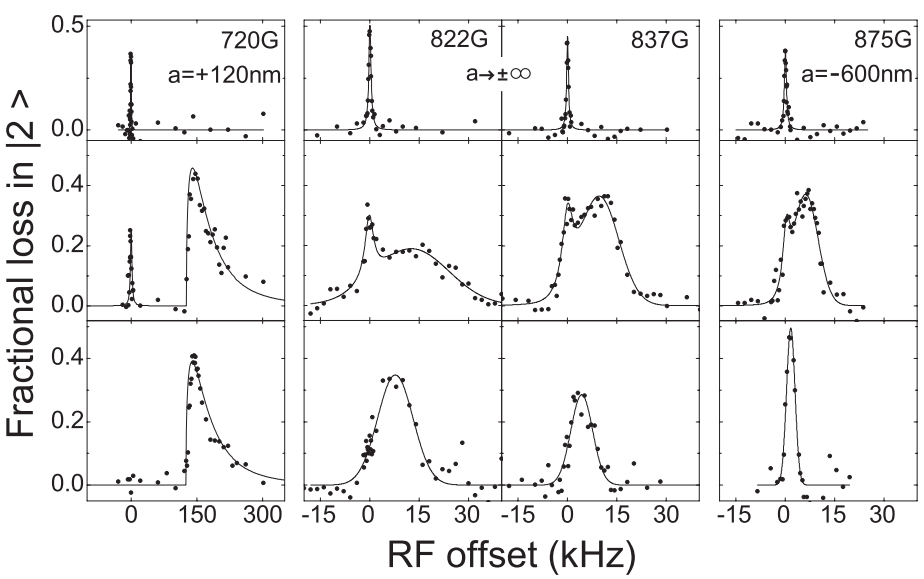

Fig. 1. RF spectra for various magnetic fields and different degrees of evaporative cooling. The RF offset ($k_B \times 1$ μK $\cong h \times 20.8$ kHz) is given relative to the atomic transition $|2\rangle \rightarrow |3\rangle$. The molecular limit is realized for $B = 720$ G (first column). The resonance regime is studied for $B = 822$ G and $B = 837$ G (second and third columns). The data at 875 G (fourth column) explore the crossover on the BCS side. Top row, signals of unpaired atoms at $T' \approx 6T_F$ ($T_F = 15$ μK); middle row, signals for a mixture of unpaired and paired atoms at $T' = 0.5T_F$ ($T_F = 3.4$ μK); bottom row, signals for paired atoms at $T' < 0.2T_F$ ($T_F = 1.2$ μK). The true temperature T of the atomic Fermi gas is below the temperature T', which we measured in the BEC limit. The solid lines are introduced to guide the eye.

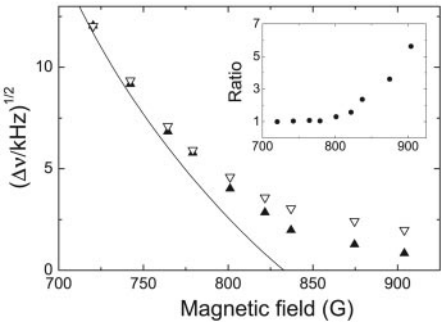

Fig. 2. Measurements of the effective pairing gap $\Delta\nu$ as a function of the magnetic field B for deep evaporative cooling and two different Fermi temperatures, $T_F = 1.2$ μK (solid symbols) and 3.6 μK (open symbols). The solid line shows $\Delta\nu$ for the low-density limit, where it is essentially given by the molecular binding energy (*25*). Inset: The ratio of the effective pairing gaps measured at the two different Fermi energies.

tive pairing gap $\Delta\nu$ simply reflects the molecular binding energy E_b (Fig. 2, solid line) (*25*). With an increasing magnetic field, in the BEC-BCS crossover, $\Delta\nu$ shows an increasing deviation from this low-density molecular limit and smoothly evolves into a density-dependent many-body regime where $h\Delta\nu < E_F$.

A comparison of the pairing energies at the two different Fermi energies (Fig. 2, inset) provides further insight into the nature of the pairs. In the BEC limit, $\Delta\nu$ is solely determined by E_b and thus does not depend on E_F. In the universal regime on resonance, E_F is the only energy scale, and we indeed observed the effective pairing gap $\Delta\nu$ to increase linearly with the Fermi energy. We found a corresponding relation $h\Delta\nu \approx 0.2\ E_F$. Beyond the resonance, where the system is expected to change from a resonant to a BCS-type behavior, $\Delta\nu$ was found to depend more strongly on the Fermi energy and the observed gap ratio further increased. We interpret this in terms of the increasing BCS character of pairing, for which an exponential dependence $h\Delta\nu / E_F \propto \exp(-\pi/2k_F|a|)$ is expected.

In a further series of measurements (Fig. 3), we applied a controlled heating method to study the temperature dependence of the gap in a way that allowed us to keep all other parameters constant. After production of a pure molecular Bose-Einstein condensate ($T' < 0.2T_F$) in the usual way, we adiabatically changed the conditions to $B = 837$ G and $T_F = 1.2$ μK. We then increased the trap laser power by a factor of nine (T_F increased to 2.5 μK), using exponential ramps of different durations. For fast ramps, this recompression was nonadiabatic and increased the entropy. By variation of the ramp time, we explored a range from our lowest temperatures up to $T'/T_F = 0.8$. The emergence of the gap with decreasing temperature is clearly visible in the RF spectra (Fig. 3). The marked increase of $\Delta\nu$ for decreasing temperature is

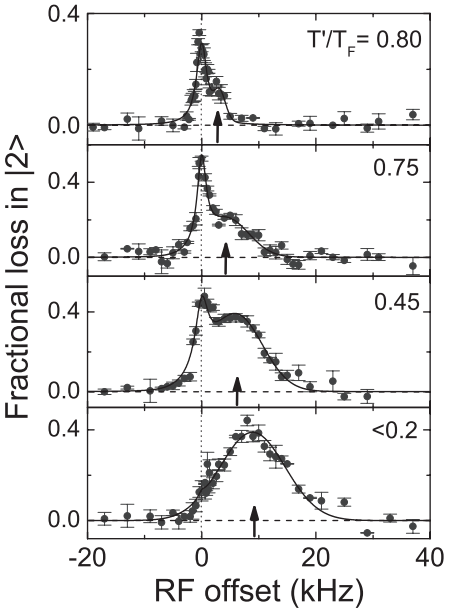

Fig. 3. RF spectra measured at $B = 837$ G and $T_F = 2.5$ μK for different temperatures T' adjusted by controlled heating. The solid lines are fits to guide the eye, using a Lorentzian curve for the atom peak and a Gaussian curve for the pair signal. The vertical dotted line marks the atomic transition, and the arrows indicate the effective pairing gap $\Delta\nu$.

in good agreement with theoretical expectations for the pairing gap energy (*5*).

The conditions of our experiment were theoretically analyzed for the case of resonant two-body interaction (*34*). The calculated RF spectra are in agreement with our experimental results and demonstrate how a double-peak structure emerges as the gas is cooled below $T/T_F \approx 0.5$ and how the atomic peak disappears with further decreasing temperature. In particular, the work clarifies the role of the "pseudo-gap" regime (*5*, *22*), in which pairs are formed before superfluidity is reached. According to the calculated spectra, the atomic peak disappears at temperatures well below the critical temperature for the phase-transition to a superfluid. A recent theoretical study of the BCS-BEC crossover at finite temperature (*36*) predicted the phase-transition to a superfluid to occur at a temperature that on resonance is only ~30% below the point where pair formation sets in.

We have observed fermionic pairing already after moderate evaporative cooling. With much deeper cooling applied, the unpaired atom signal disappeared from our spectra. This observation shows that pairing takes place even in the outer region of the trapped gas where the density and the local Fermi energy are low. Our results thus strongly suggest that a resonance superfluid is formed in the central region of the trap (*34*). Together with the observations of resonance condensation of fermionic pairs (*15*, *16*) and weak damping of collective excitations (*17*, *18*), our observation of the pairing gap provides a strong case for superfluidity in experiments on resonantly interacting Fermi gases.

References and Notes

1. M. Tinkham, *Introduction to Superconductivity* (McGraw-Hill, New York, ed. 2, 1996).
2. D. M. Eagles, *Phys. Rev.* **186**, 456 (1969).
3. A. J. Leggett, in *Modern Trends in the Theory of Condensed Matter*, A. Pekalski, R. Przystawa, Eds. (Springer-Verlag, Berlin, 1980), pp. 13–27.
4. P. Nozières, S. Schmitt-Rink, *J. Low Temp. Phys.* **59**, 195 (1985).
5. Q. Chen, J. Stajic, S. Tan, K. Levin, in preparation (available at http://arxiv.org/abs/cond-mat/0404274).
6. A. Cho, *Science* **301**, 750 (2003).
7. S. Inouye *et al.*, *Nature* **392**, 151 (1998).
8. K. M. O'Hara, S. L. Hemmer, M. E. Gehm, S. R. Granade, J. E. Thomas, *Science* **298**, 2179 (2002); published online 7 Nov 2002 (10.1126/science.1079107).
9. S. Jochim *et al.*, *Science* **302**, 2101 (2003); published online 13 November 2003 (10.1126/science.1093280).
10. M. Greiner, C. A. Regal, D. S. Jin, *Nature* **426**, 537 (2003).
11. M. W. Zwierlein *et al.*, *Phys. Rev. Lett.* **91**, 250401 (2003).
12. T. Bourdel *et al.*, *Phys. Rev. Lett.* **93**, 050401 (2004).
13. R. Hulet, paper presented at the Kauli Institute for Theoretical Physics Conference on Quantum Gases, Santa Barbara, CA, 10 to 14 May 2004.
14. M. Bartenstein *et al.*, *Phys. Rev. Lett.* **92**, 120401 (2004).
15. C. A. Regal, M. Greiner, D. S. Jin, *Phys. Rev. Lett.* **92**, 040403 (2004).
16. M. W. Zwierlein *et al.*, *Phys. Rev. Lett.* **92**, 120403 (2004).
17. J. Kinast, S. L. Hemmer, M. E. Gehm, A. Turlapov, J. E. Thomas, *Phys. Rev. Lett.* **92**, 150402 (2004).
18. M. Bartenstein *et al.*, *Phys. Rev. Lett.* **92**, 203201 (2004).
19. M. Holland, S. J. J. M. F. Kokkelmans, M. L. Chiofalo, R. Walser, *Phys. Rev. Lett.* **87**, 120406 (2001).
20. E. Timmermans, K. Furuya, P. W. Milonni, A. K. Kerman, *Phys. Lett. A* **285**, 228 (2001).
21. Y. Ohashi, A. Griffin, *Phys. Rev. Lett.* **89**, 130402 (2002).
22. J. Stajic *et al.*, *Phys. Rev. A.* **69**, 063610 (2004).
23. H. Heiselberg, *Phys. Rev. A.* **63**, 043606 (2001).
24. T.-L. Ho, *Phys. Rev. Lett.* **92**, 090402 (2004).
25. Materials and methods are available as supporting material on *Science* Online.
26. L. D. Carr, G. V. Shlyapnikov, Y. Castin, *Phys. Rev. Lett.* **92**, 150404 (2004).
27. C. Regal, D. Jin, *Phys. Rev. Lett.* **90**, 230404 (2003).
28. S. Gupta *et al.*, *Science* **300**, 1723 (2003); published online 8 May 2003 (10.1126/science.1085335).
29. C. A. Regal, C. Ticknor, J. L. Bohn, D. S. Jin, *Nature* **424**, 47 (2003).
30. P. Törmä, P. Zoller, *Phys. Rev. Lett.* **85**, 487 (2000).
31. J. Kinnunen, M. Rodriguez, P. Törmä, *Phys. Rev. Lett.* **92**, 230403 (2004).
32. H. P. Büchler, P. Zoller, W. Zwerger, in preparation (available at http://arxiv.org/abs/cond-mat/0404116).
33. R. B. Diener, T.-L. Ho, in preparation (available at http://arxiv.org/abs/cond-mat/0405174).
34. J. Kinnunen, M. Rodriguez, P. Törmä, *Science* **305**, 1131; published online 22 July 2004 (10.1126/science.1100782).
35. A. Bulgac, in preparation (available at http://arxiv.org/abs/cond-mat/0309358).
36. A. Perali, P. Pieri, L. Pisani, G. C. Strinati, *Phys. Rev. Lett.* **92**, 220404 (2004).

37. We thank P. Törmä for a stimulating exchange of results and very useful discussions and W. Zwerger and H. P. Büchler for many stimulating discussions. Supported by the Austrian Science Fund (FWF) within spezial forschungsbereich 15 (project part 15) and by the European Union in the frame of the Cold Molecules Training and Mobility of Researchers Network under contract no. HPRN-CT-2002-00290. C.C. is a Lise-Meitner research fellow of the FWF.

Supporting Online Material
www.sciencemag.org/cgi/content/full/1100818/DC1
Materials and Methods
References and Notes

27 May 2004; accepted 13 July 2004
Published online 22 July 2004;
10.1126/science.1100818
Include this information when citing this paper.

Pairing Gap and In-Gap Excitations in Trapped Fermionic Superfluids

J. Kinnunen, M. Rodríguez, P. Törmä*

We consider trapped atomic Fermi gases with Feshbach-resonance enhanced interactions in pseudogap and superfluid temperatures. We calculate the spectrum of radio-frequency (or laser) excitations for transitions that transfer atoms out of the superfluid state. The spectrum displays the pairing gap and also the contribution of unpaired atoms, that is, in-gap excitations. The results support the conclusion that a superfluid, in which pairing is a many-body effect, was observed in recent experiments on radio-frequency spectroscopy of the pairing gap.

Fermionic superfluidity and superconductivity appear in several systems in nature, such as metals, cuprates, and helium. In the limit of weak interparticle interaction, the Bardeen-Cooper-Schrieffer (BCS) theory of superconductivity has been successful in explaining the observed phenomenon as a Bose-Einstein Condensation (BEC) of weakly bound momentum-space pairs. In the limit of strong interactions, spatially small, strongly bound pairs are formed and undergo BEC. The intriguing question about the nature of the crossover from BCS pairing to BEC of dimers was theoretically addressed in 1980 (*1*, *2*) and is closely related to uncovering the nature of high-temperature superconductivity. Trapped fermionic atoms offer a system in which the crossover can be scanned by tuning the interparticle scattering length using Feshbach resonances (*3*–*7*). At the crossover region, the scattering length diverges and a universal behavior, independent of any length scale, is expected. The system is also genuinely mesoscopic as a result of the trapping potential for the atoms. Here, we consider spectroscopic signatures of pairing in these systems at the onset of the superfluid transition and show that the mesoscopic nature of the system leads to pronounced signatures from unpaired atoms, which can also be understood as in-gap excitations. The results are in agreement with the experimental results in (*8*).

The single-particle excitation spectrum of a fermionic superfluid is expected to show an energy gap. A spectroscopic method for observing the excitation gap in atomic Fermi gases has been proposed (*9*–*11*). Radio-frequency (RF) spectroscopy has been used for observing mean fields (*12*, *13*) and, very recently, the excitation gap (*8*). Laser or RF fields are used for transferring atoms out of the superfluid state to a normal one. The superfluid state originates from the pairing of atoms in two different internal states, say $|1\rangle$ and $|2\rangle$. The field drives a transition from $|2\rangle$ to a third state, $|3\rangle$. Atoms in state $|3\rangle$ are not paired; that is, they are in the normal state. The idea is closely related to observing the superconductor–normal metal current in metals and, similarly, it reflects the density of states and displays the excitation gap. In this case, however, the superfluid-normal interface is realized by internal states of the atom, not by a spatial boundary. The response, in the case of atoms, is qualitatively different from that of metals because of the exact momentum conservation in atomic transitions driven by homogeneous fields. Here, we calculate the response of this process, that is, the spectrum as a function of the detuning of the RF field, taking into account the mesoscopic nature of the sample, that is, the trapping potential. This leads to pronounced signatures that can be used to confirm the onset of the excitation gap and the superfluid transition.

In the high critical temperature (T_c) region of the BEC-BCS crossover, the BCS theory, in its simplest form, is expected to be incapable of describing the effects of strong interactions, such as the formation of a pseudogap. In atomic Fermi gases, the vicinity of the Feshbach resonance is associated with strong interactions, and preformed pairs causing a pseudogap to exist even above the critical temperature. The excitation gap, therefore, has contributions both from the superfluid gap (Δ_{sf}) and the pseudogap (Δ_{pg}). The many-body state is affected also by the existence of the molecular bound state, which actually causes the Feshbach-resonance phenomenon. These issues are considered in recent work on resonance superfluidity theory (*14*–*17*). We use such an approach for calculating the equilibrium state of the system (*18*).

The interaction with the RF or laser field is introduced as a perturbation, and the response is calculated to the second order in the perturbation Hamiltonian. This corresponds to a Fermi golden rule type of derivation of the spectrum and allows a treatment of the complex many-body state with reasonable accuracy. The transfer Hamiltonian H_T, describing the effect of the field, couples states $|2\rangle$ and $|3\rangle$ (*18*). The offset from the resonance of the transition between $|2\rangle$ and $|3\rangle$ is given by the RF field detuning $\delta = E_{RF} - (E_3 - E_2)$, where E_{RF}, E_3, and E_2 are the energies of the RF photon and of the states $|3\rangle$ and $|2\rangle$, respectively. The spectrum is obtained from the response $I(\delta) = \langle \dot{N}_3 \rangle$, where N_3 is the number of atoms in state $|3\rangle$, by neglecting terms of higher than second order in H_T in the derivation (*18*). In the case of metals, such quantity would give the current $I(V)$, where V is voltage, over the superconductor–normal metal tunneling junction.

Trapped atomic gases have an inhomogeneous density distribution $n(\mathbf{r})$; therefore, a spatially varying superfluid order parameter is expected. We treat the problem in the local density approximation, that is, we solve the equilibrium state by including $n(\mathbf{r})$ given by the Thomas-Fermi distribution as a position-dependent parameter (*18*, *19*). Figure 1 presents the position dependence of the atom density and the superfluid gap. This shows that only the atoms in the middle of the trap are condensed. Figure 2 shows the fraction of condensed atoms and the mean (averaged over r) superfluid gap and pseudogap as functions of temperature. The parameters used in calculating the results in Figs. 1 to 3 correspond to the experiments in figure 3 of (*8*) and are given in (*18*).

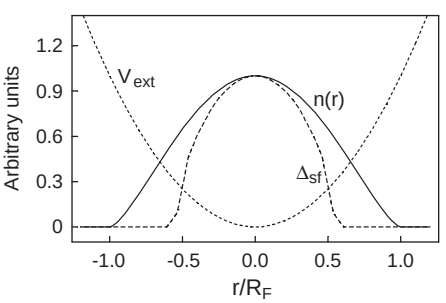

Fig. 1. The superfluid Δsf gap and the atom density n(r) as functions of position at temperature $T = 0.2\ T_F$, where T_F is the Fermi temperature. Resonance-superfluidity theory incorporating a pseudogap, together with Thomas-Fermi distribution in the local density approximation, is used. Only the atoms in the middle of the trap are condensed, whereas the atoms closer to the borders are either free or in the pseudogap regime. The critical temperature in the middle of the trap is $T_c \approx 0.3\ T_F$. V_{ext} is the external potential as a function of distance in units of Thomas-Fermi radius, r/R_F.

Department of Physics, NanoScience Center, Post Office Box 35, FIN-40014, University of Jyväskylä, Finland.

*To whom correspondence should be addressed. E-mail: paivi.torma@phys.jyu.fi

The spectra $I(\delta)$ at different temperatures are plotted in Fig. 3. The peak at the zero detuning, $\delta = 0$, originates from free (unpaired) atoms. Another peak, shifted right from the zero, appears with decreasing temperature. The shift reflects the excitation gap, that is, the energy needed for breaking a pair. The free-atom peak gradually vanishes when the temperature is lowered and the atoms at the borders of the trap become paired. The disappearance of the free-atom peak shows that the border atoms have reached the pseudogap regime (*18*) and that the atoms in the middle of the trap are well below the superfluid transition temperature (*20*). We have neglected the effect of the mean (Hartree-Fock) field energy shifts (*18*) because they appear absent in the experiments (*8*, *13*).

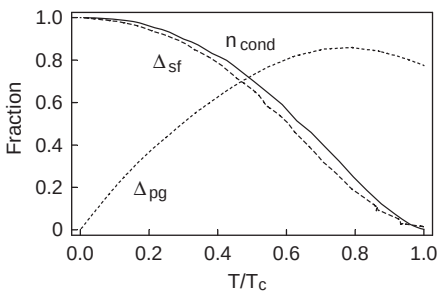

Fig. 2. The mean superfluid gap (Δ_{sf}) and pseudogap (Δ_{pg}) as functions of temperature. The fraction of condensed atoms n_{cond} is defined as the fraction of atoms for which the temperature is below the local critical temperature. The temperature $T \approx 0.7\ T_c$ corresponds to $T = 0.2\ T_F$, showing that the superfluid gap distribution in Fig. 1 corresponds to a condensate fraction of $n_{cond} \approx 0.3$.

In a corresponding spatially homogeneous system, instead of the free-atom peak at zero detuning, a quasiparticle peak, shifted left from the zero, appears at high temperatures (*11*). The shift is to the left, in the opposite direction of that of the pair peak, because thermal quasiparticles of the superfluid already possess the excess gap energy, that is, energy is gained in the RF transfer process (*21*). As Fig. 3 shows, such quasiparticle peaks appearing in a homogeneous system are now shadowed by trapping effects and by the free-atom peak. The unpaired atoms in Fig. 3 can, however, be understood as in-gap excitations or quasiparticles. Instead of the local density approximation, inhomogeneous superfluids can be described by the Bogoliubov–de Gennes equations. Solving the equations in a trap geometry (*10*, *22*) results in in-gap excitations whose energies lie below the maximum (at the point of highest density) gap energy. The wave functions of these excitations are located at the edges of the trap; they correspond to the free atoms at the borders of the trap in the local-density treatment. The free atoms in Fig. 3 and observed in (*8*) can thus be understood as in-gap excitations of an inhomogeneous superfluid.

The spectra in Fig. 3 are in excellent qualitative agreement with the experimental results in (*8*). They also agree well quantitatively with figure 3 of (*8*). The shift of the pair peak, which gives the excitation gap, is at temperatures $T' \leq 0.2\ T_F$, about $0.2\ E_F$ in (*8*) and $0.3\ E_F$ for $T \leq 0.1\ T_F$, according to our calculation. The widths of the peaks, which are determined by the gap, are about $0.3\ E_F$ and $0.4\ E_F$, respectively. The critical temperature at the center of the trap is in our case $T_c \sim 0.3\ T_F$, which may be used to estimate that in (*8*) it is ~0.2 to $0.25\ T_F$. The temperatures T' in the experiment are determined in the BEC limit as a result of the lack of precise thermometry in the unitarity limit. The adiabatic passage to the unitarity limit, where the spectra are actually measured, is expected to reduce the temperature as a result of entropy conservation so that $T < T'$ (*23*). This is consistent with the observation that the pair peak in Fig. 3 starts to appear at $T \sim 0.35\ T_F$ and is clearly visible at $T \sim 0.2\ T_F$, but in (*8*) it appears and is clearly visible already at higher (BEC limit) temperatures of $T' \sim 0.75\ T_F$ and $T' \sim 0.45\ T_F$, respectively. The sensitivity of the free-atom (quasiparticle) peak to temperature and the possibility of direct comparison between theory and experiment may offer a route for developing a precise thermometry for the crossover region.

We emphasize that those spectra in (*8*) where the free-atom peak has disappeared correspond to Fig. 3, H to J, where more than 80% of the atoms are condensed. This indicates that the pairing observed at the lowest temperatures in (*8*) corresponds to a superfluid. At higher temperatures, either a pseudogap or a combined effect of a superfluid gap and a pseudogap occurs. In summary, the results presented here support the conclusion that a superfluid, in which pairing is a many-body effect, was observed in (*8*). The mesoscopic nature of these novel Fermi superfluids shows up in an intriguing way.

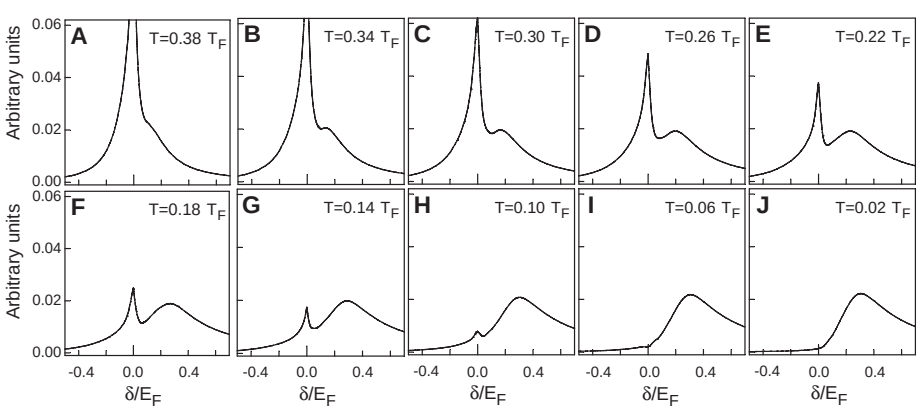

Fig. 3. The spectra of the considered RF transition as a function of the RF field detuning δ for several temperatures. The peak at $\delta = 0$ is caused by free atoms. A peak shifted to the right from the zero gradually appears for lower temperatures, corresponding to paired atoms; the shift of the peak from the zero detuning gives the energy gap in the single-particle excitation spectrum. The shift, that is, the gap, grows with decreasing temperature. The plots also show the disappearance of the free-atom peak when the atoms at the borders of the trap enter the pseudogap regime and become paired. The critical temperature in the middle of the trap is $T_c \approx 0.3\ T_F$. At the temperature $T = 0.1\ T_F$, more than 80% of the atoms are condensed. The parameters used in the calculation correspond to the experiments in Fig. 3 of (*8*). The gas is in the unitarity limit, that is, close to the Feshbach resonance, which is the expected high-T_c regime for the system. E_F, Fermi energy.

References and Notes

1. A. J. Leggett, *Modern Trends in the Theory of Condensed Matter* (Springer-Verlag, Berlin, 1980), p. 13.
2. P. Nozières, S. Schmitt-Rink, *J. Low Temp. Phys.* **59**, 195 (1985).
3. C. A. Regal, M. Greiner, D. S. Jin, *Phys. Rev. Lett.* **92**, 040403 (2004).
4. M. Bartenstein *et al.*, *Phys. Rev. Lett.* **92**, 120401 (2004).
5. M. W. Zwierlein *et al.*, *Phys. Rev. Lett.* **92**, 120403 (2004).
6. J. Kinast, S. L. Hemmer, M. E. Gehm, A. Turlapov, J. E. Thomas, *Phys. Rev. Lett.* **92**, 150402 (2004).
7. M. Bartenstein *et al.*, *Phys. Rev. Lett.* **92**, 203201 (2004).
8. C. Chin *et al.*, *Science* **305**, 1128; published online 22 July 2004 (10.1126/science.1100818).
9. P. Törmä, P. Zoller, *Phys. Rev. Lett.* **85**, 487 (2000).
10. G. M. Bruun, P. Törmä, M. Rodríguez, P. Zoller, *Phys. Rev. A.* **64**, 033609 (2001).
11. J. Kinnunen, M. Rodríguez, P. Törmä, *Phys. Rev. Lett.* **92**, 230403 (2004).
12. C. A. Regal, D. S. Jin, *Phys. Rev. Lett.* **90**, 230404 (2003).
13. S. Gupta *et al.*, *Science* **300**, 1723 (2003).
14. M. Holland, S. J. J. M. F. Kokkelmans, M. L. Chiofalo, R. Walser, *Phys. Rev. Lett.* **87**, 120406 (2001).
15. E. Timmermans, K. Furuya, P. W. Milonni, A. K. Kerman, *Phys. Lett. A* **285**, 228 (2001).
16. Y. Ohashi, A. Griffin, *Phys. Rev. Lett.* **89**, 130402 (2002).
17. J. Stajic *et al.*, *Phys. Rev. A.* **69**, 063610 (2004).
18. Materials and methods are available as supporting material on *Science* Online.

19. M. L. Chiofalo, S. J. J. M. F. Kokkelmans, J. N. Milstein, M. J. Holland, *Phys. Rev. Lett.* **88**, 090402 (2002).
20. The pronounced free-atom peak at the zero detuning clearly reflects the strong dependence of the order parameter on density and the trapping potential. In the case of a very smooth density dependence of the energy gap, one would expect simply a broadening of the pair peak. Such a behavior was actually observed in the experiments probing mean fields (*12*, *13*). There, only one peak was observed and the effect of the trapping potential was a considerable broadening of the peak.
21. Note that because not only energy but also momentum is exactly conserved in the transfer process, these particles cannot be transferred at zero detuning. This is in contrast to superconductor–normal metal junctions where thermal quasiparticle currents flow freely for below-gap voltages.
22. M. A. Baranov, *JETP Lett.* **70**, 396 (1999).
23. The precise relation between T' and T at the unitarity limit is not known, but the analysis in the case of a noninteracting Fermi gas (*24*) supports this argument.
24. L. D. Carr, G. V. Shlyapnikov, Y. Castin, *Phys. Rev. Lett.* **92**, 150404 (2004).
25. We thank C. Chin and R. Grimm for a stimulating exchange of results and very useful discussions. We acknowledge financial support from the Academy of Finland (Project Nos. 53903 and 205470) and the Emil Aaltonen Foundation.

Supporting Online Material
www.sciencemag.org/cgi/content/full/1100782/DC1
Materials and Methods
References and Notes

26 May 2004; accepted 13 July 2004
Published online 22 July 2004;
10.1126/science.1100782
Include this information when citing this paper.

Sudden Onset of Pitting Corrosion on Stainless Steel as a Critical Phenomenon

C. Punckt,[1] M. Bölscher,[1] H. H. Rotermund,[1] A. S. Mikhailov,[1] L. Organ,[2] N. Budiansky,[3] J. R. Scully,[3] J. L. Hudson[2]*

Stainless steels undergo a sharp rise in pitting corrosion rate as the potential, solution concentration, or temperature is changed only slightly. We report experiments using real-time microscopic in situ visualizations that resolve the nucleation and evolution of individual pits during the transition. They suggest that the sudden onset of corrosion is explained by an explosive autocatalytic growth in the number of metastable pits and that stabilization of individual pits takes place only later. This finding agrees with a theoretical approach treating the onset of pitting corrosion as a cooperative critical phenomenon resulting from interactions among metastable pits, and it extends perspectives on the control and prevention of corrosion onset.

All commonly used stainless steels and other passive-film–forming metals, which are designed to be corrosion-resistant, can nevertheless undergo localized pitting corrosion, which rapidly leads to their failure. The total annual costs due to corrosion in the United States are estimated at 3% of the gross national product (*1*), and a third of chemical plant failures are attributed to localized corrosion (*2*). Localized corrosion is preceded by the appearance of metastable pits: tiny corrosion seeds the size of a few micrometers developing on the metal surface, which is naturally protected by an oxide layer. Each pit produces a small spike of a few seconds duration in the electrical current, indicating an anodic reaction, and the spike then dies out. Experimental and theoretical studies have largely clarified the mechanism for the initiation of these microscopic pits as being caused by localized electrodissolution of metal at surface defects and inclusions (*3*–*8*).

[1]Abteilung Physikalische Chemie, Fritz-Haber-Institut der Max-Planck-Gesellschaft, Faradayweg 4-6, 14195 Berlin, Germany. [2]Department of Chemical Engineering, [3]Department of Material Science and Engineering, 102 Engineers' Way, University of Virginia, Charlottesville, VA 22904–4741, USA.

*To whom correspondence should be addressed. E-mail: hudson@virginia.edu

Pitting corrosion shows a sharp rise in corrosion rate that occurs with only a small change in conditions, such as applied potential, corrodant concentrations, or temperature (*9*). This corresponds to a sudden transition from a low-activity regime with a few metastable pits to a state with high pitting activity (*10*, *11*). The transition has been explained by a stabilization of individual pits (*12*). As an alternate explanation, we suggest that the onset of pitting corrosion represents a cooperative critical phenomenon. In previous investigations, temporal statistical correlations between the spikes in the total current have been found (*13*, *14*), indicating some memory in the pitting process (*15*). A stochastic spatiotemporal model of the corrosion onset has been proposed (*16*). According to this model, electrochemical reactions at a metastable pit change ion concentrations and weaken the protective film over defect sites. Each pit enhances the probability of appearance of further pits at defect sites within a wide zone of weakened film around it. We show below that autocatalytic reproduction of pits can take place. Sudden transitions are thus associated with an explosive growth in the number of active pits. Stabilization of individual pits would occur only after the transition.

To distinguish between different approaches, microscopic in situ visualizations of the onset of pitting corrosion are needed. Several experimental methods have been used to investigate pitting corrosion on stainless steels. Distributions and characteristics of pitting sites on metal surfaces have been determined through microscopic inspection after the termination of corrosion (*5*, *17*, *18*). Changes in the thickness of the oxide layer in the vicinity of an active pit and the topography of surfaces before and after pitting events have been measured via scanning techniques in which spatial or temporal resolution is restricted (*19*, *20*). Optical microscopy was applied in situ to observe relatively large, already stable pits (diameter >10 μm) (*21*), and individual metastable pits were visualized by using pH-sensitive agar gels (*22*, *23*) that indicated interactions among active pits.

We present detailed, time-resolved, in situ visualizations of the onset of pitting corrosion directly in the electrolyte, using two different techniques: ellipsomicroscopy for surface imaging (EMSI) and specially adapted high-resolution contrast-enhanced optical microscopy. Both techniques are accompanied by parallel monitoring of the current. Thus, the temporal and spatial development of metastable pits is followed during the transition to pitting corrosion, and we can also differentiate between active and inactive pits.

Ellipsometry, based on the detection of the polarization rotation of the light reflected from the surface, has been used in an electrochemical cell to measure average thicknesses of oxide layers on metal surfaces (*24*, *25*). In contrast to intrinsically slow scanning ellipsometry methods, EMSI permits real-time observation of ultrathin layers on the entire surface area (*26*). Figure 1A displays four snapshots from an EMSI video sequence at an early corrosion stage, with space/time diagrams along two line segments, and the electrical current (movie S1A). Bright areas extending up to 100 μm are observed, with the intensity gradually fading toward the periphery. We interpret the observed brightness as revealing changes in the thickness of the protective oxide layer on the surface around an active pit. Changes in solution concentration around a pit can be ruled out as a source

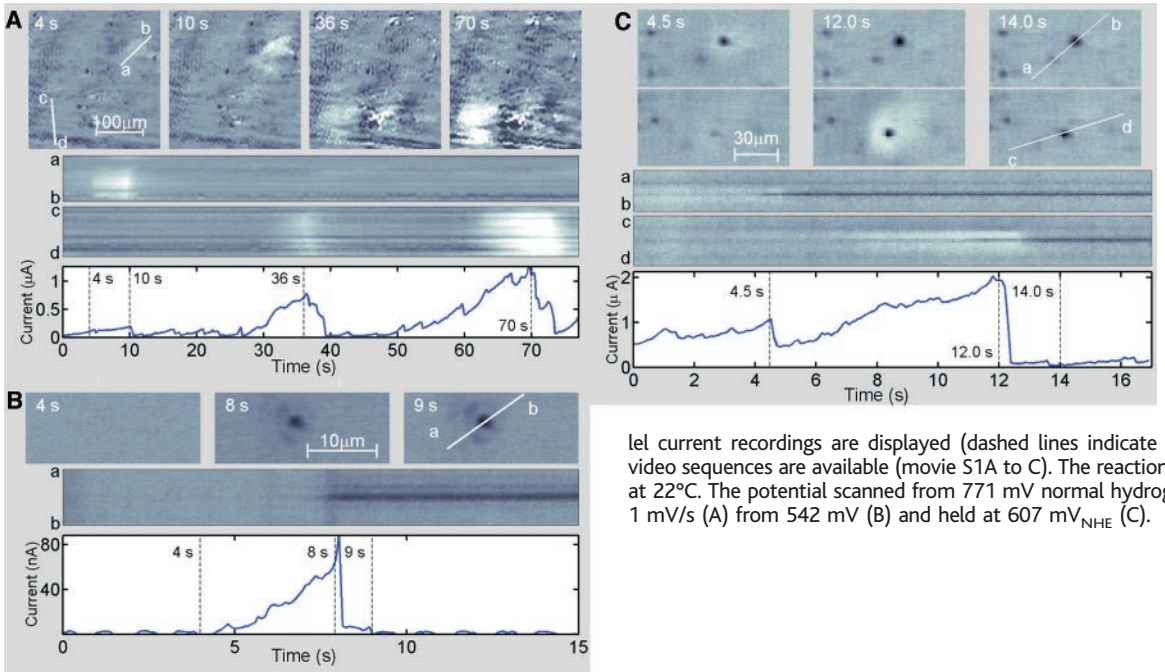

Fig. 1. Microscopic observations of individual pitting events. (**A**) EMSI visualizing oxide film damage. (**B**) Nucleation of single pit seen by contrast-enhanced microscopy. (**C**) Reactivation of single pits seen by contrast-enhanced microscopy. Below the snapshots in each part, space/time diagrams showing evolution along the lines marked *ab* or *cd* in the respective images and parallel current recordings are displayed (dashed lines indicate snapshot moments). Full video sequences are available (movie S1A to C). The reaction occurred in 0.05 M NaCl at 22°C. The potential scanned from 771 mV normal hydrogen electrode (mV_{NHE}) at 1 mV/s (A) from 542 mV (B) and held at 607 mV_{NHE} (C).

for the EMSI contrast [see supporting online material (SOM) text]. Each bright region is associated with a simultaneously measured current spike signaling the presence of an active pit (Fig. 1A, bottom panel). An area remains bright for 10 to 15 s, which is longer than the 4- to 10-s spikes seen in the current. The difference may result from the time required to repair the oxide layer.

The spatial resolution of EMSI is limited by geometrical restrictions to about 12 μm, and it cannot resolve individual pits. Therefore, we developed a contrast-enhanced optical microscope with a lateral diffraction-limited resolution of 2 μm. Figure 1B displays nucleation of a typical primary pit (movie S1B). Such pits are weak and accompanied by small spikes (here, 80 nA) in the current. They persist for a few seconds and then undergo passivation and the current drops. A black spot (passivated pit) remains because the corrosion has locally removed the metal surface.

Subsequently, pits can again become active. Two of these reactivation events are shown in Fig. 1C (movie S1C). The reactivated pits remain black, but activity can be identified by two effects: (i) Each reactivated pit produces a spike in the current. (ii) Moreover, we have noticed that sufficiently strong active pits are surrounded by a bright "halo" in the image. Such halos may be caused by a hemispherical concentration gradient of ions surrounding the active site that forms an effective microlens illuminating the surface. After the current drops to its noise level, the halo persists for 0.6 s, which is about the time needed for diffusion of the ions away from the pit, and then it disappears. An enlarged black spot remains on the surface at the previous location of the active pit, and further reactivation cycles are possible.

Fig. 2. Sudden onset of pitting corrosion observed with contrast-enhanced microscopy. (**Top**) Three snapshots of computer-processed optical microscopy images. Green stars show the nucleation of new pits. Red stars point out highly active pits (with halo). A full video sequence is available (movie S2). (**Bottom**) Total number of pits and total current on logarithmic scales as functions of time. The reaction occurred in 0.05 M NaCl at 22°C; the potential scanned from 693 mV_{NHE} at 1 mV/s.

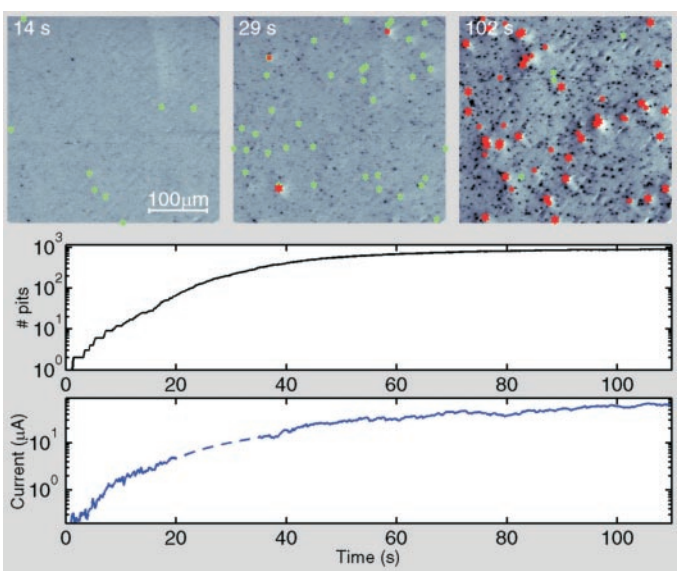

With the optical microscope, we monitored the sudden onset of pitting corrosion. Figure 2 displays three snapshots from a video sequence (movie S2). The images have been computer-processed to identify weak, newly appearing pits (green stars) and highly active pits that are surrounded by bright halos (red stars). The total number of pits (active or repassivated) present on the surface is shown as a function of time. During the first 20 s of the corrosion onset, the number of pits grows exponentially with time, as indicated by a linear increase on the logarithmic scale. During the time of the exponential growth in both the number of pits and the current, the experimental conditions remained approximately constant, with the change in applied potential being less than 20 mV. At longer times, the total number of pits saturates at a constant level.

In Fig. 3A, the rates of appearance of primary pits and highly active pits (with halos) are shown as functions of time. At the initial stage, characterized by the rapid increase in the total current, many pits are created. However, as saturation is approached, new pits cease to appear. The surface apparently possesses only a fixed number of sites for pit nucleation; that is, at defects and inclusion sites. When all such sites are exhausted, only reactivation of previously formed pits can occur. The lifetimes (durations of activity) of all relatively strong

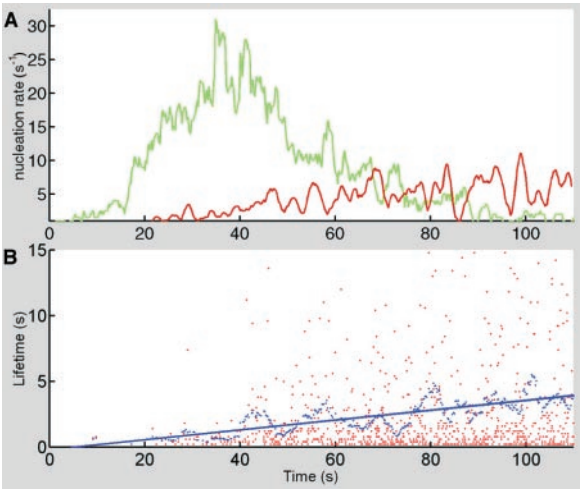

Fig. 3. Statistical analysis of pitting data. (**A**) Initiation rate of primary pits (green) and rate of appearance of active pits with halos (red) as functions of time. (**B**) Lifetimes of active pits (with halos) as a function of time moments of their activation (red dots). The blue dots indicate a 3-s moving mean, and the blue line shows a linear fit of the entire data set. Twenty-eight pits having lifetimes greater than 15 s are not shown in the distribution but are included in the mean.

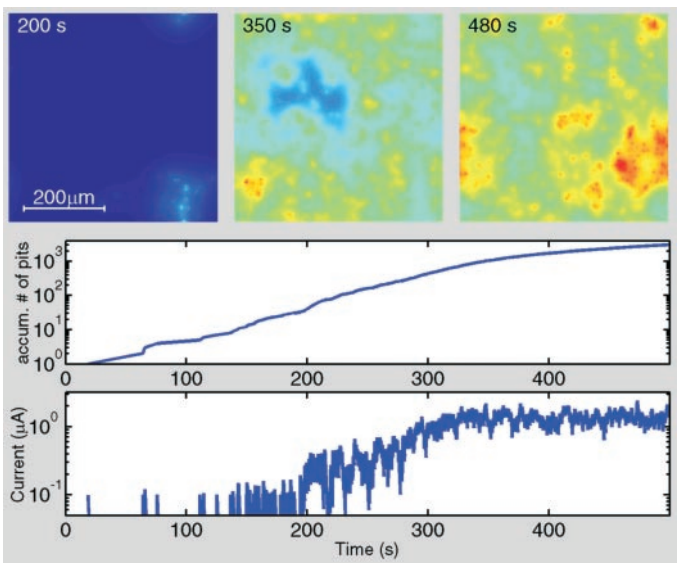

Fig. 4. Simulation of corrosion onset. (**Top**) Three snapshots showing evolution of the local film damage (a full video sequence is available as movie S3). Blue corresponds to low and orange to high film damage. (**Bottom**) Accumulated total number of pits and total current on a logarithmic scale as functions of time. Periodic boundary conditions; model parameters are given in the SOM text.

pits (marked as red stars in Fig. 2) were determined by computer processing of the video data. In Fig. 3B, these lifetimes are displayed as a function of the time when the activity of the respective pit began. Although all such pits were metastable, their lifetimes grew slowly. We have also analyzed the distribution of nearest-neighbor distances between the pits after their number had saturated, and we found a narrow exclusion zone that was a few micrometers wide, in agreement with the previous statistical investigations performed after reaction termination (*17*).

The observed critical phenomena agree with a simple phenomenological model of the corrosion onset (*23*) (SOM text). Reactions in a metastable pit produce aggressive species that move laterally away and into the bulk. These species act on the film and weaken this protective layer. When the pit activity is stopped and the aggressive agents disappear, the film heals slowly. Metastable pits are described as localized random events of a fixed short duration. The local generation rate of pits on the metal surface depends on the concentration of aggressive species in the electrolyte near the surface, the damage to the protective film, and the local potential. The potential drop caused by electrochemical reactions has an inhibitory effect which is, however, significant only within a few micrometers from an active pit. In contrast to this, aggressive agents and weakening of the protecting film enhance further pitting over distances of tens of micrometers from an existing active pit, and this effect persists even within tens of seconds after the pit has disappeared.

Thus, pitting effectively represents an autocatalytic process analogous to a chain reaction. Each metastable pit leads to the weakening of the protective film in the surrounding area of radius l_0 and within the time T_0, where l_0 is the characteristic lateral diffusion length of the aggressive agent in the electrolyte (equal to the diffusion boundary layer thickness) and T_0 is the recovery time of the protective layer. If inside this area the generation rate is increased to w_1, which is much higher than the rate of spontaneous pitting, the probability that another pit will be nucleated in such an area is estimated as $p \approx w_1 l_0^2 T_0$. Although this probability is small, autocatalytically induced pitting is negligible. On the other hand, if the parameter combination p is large, each pit gives rise to many further pits around it, and a chain explosion takes place. Hence, the approximate critical condition is that $w_1 l_0^2 T_0$ is of order unity.

Figure 4 shows a numerical simulation of the model (for the model equations and parameter values, see SOM text). Although the model is phenomenological and based on a number of simplifications, it does explain the observed features of sudden corrosion onset. Starting from the initial passive state, some individual pits independently nucleate and rapid pit reproduction begins, bringing the surface to high activity. The temporal evolution of the accumulated total number of active pits and the current are shown below on a logarithmic scale. The exponential growth of the number of pits is evident. The characteristic time and length scales, as well as the pit densities in the simulation, are consistent with the experimental observations.

In our experiments, all active pits remained metastable during the sharp rise in the corrosion rate. Thus, the transition to high corrosion rates was caused not by the stabilization of individual pits, but by the explosive growth in the number of metastable pits. Our theoretical analysis suggests that this can be a general property of the onset of pitting corrosion. It does not, of course, rule out subsequent stabilization of pits. The explosion instability, playing a crucial role in the process, can be suppressed by an increased rate of mass transfer of the reaction products that cause film weakening; by a solution modification (addition of inhibitors) leading to a faster recovery of the protective film; or by improvements in the alloy, reducing the number of surface defect sites. The developed experimental methods can be used for microscopic in situ visualization of various corrosion phenomena in different metals. Our analysis brings investigations of localized pitting corrosion into a conceptual framework of autocatalytic processes and nonequilibrium pattern formation phenomena in reaction-diffusion systems.

References and Notes

1. R. L. Jones, *Mater. Perform.* **35**, 63 (1996).
2. J. A. Collins, M. L. Monack, *Mater. Protect. Perform.* **12**, 11 (1973).
3. D. E. Williams, R. C. Newman, Q. Song, R. G. Kelly, *Nature* **350**, 216 (1991).
4. R. Ke, R. Alkire, *J. Electrochem. Soc.* **139**, 1573 (1992).
5. M. A. Baker, J. E. Castle, *Corros. Sci.* **34**, 667 (1993).

6. M. P. Ryan, N. J. Laycock, R. C. Newman, H. S. Isaacs, *J. Electrochem. Soc.* **145**, 1566 (1998).
7. G. S. Frankel, *J. Electrochem. Soc.* **145**, 2186 (1998).
8. M. P. Ryan, D. E. Williams, R. J. Chater, B. M. Hutton, D. S. McPhail, *Nature* **415**, 770 (2002).
9. Z. Szklarska-Smialowska, *Pitting Corrosion of Metals* (National Association of Corrosion Engineers, Houston, TX, 1986).
10. H. S. Isaacs, Y. Ishikawa, *J. Electrochem. Soc.* **132**, 1288 (1985).
11. P. C. Pistorius, G. T. Burstein, *Philos. Trans. R. Soc. Ser. A* **341**, 531 (1992).
12. D. E. Williams, C. Westcott, M. Fleischmann, *J. Electrochem. Soc.* **132**, 1796 (1985).
13. U. Bertocci, M. Koike, S. Leigh, F. Qiu, G. Yang, *J. Electrochem. Soc.* **133**, 1782 (1986).
14. T. T. Lunt, S. T. Pride, J. R. Scully, A. S. Mikhailov, J. L. Hudson, *J. Electrochem. Soc.* **144**, 1620 (1997).
15. B. Wu, J. R. Scully, J. L. Hudson, A. S. Mikhailov, *J. Electrochem. Soc.* **144**, 1614 (1997).
16. T. T. Lunt, J. R. Scully, V. Brusamarello, A. S. Mikhailov, J. L. Hudson, *J. Electrochem. Soc.* **149**, B163 (2002).
17. M. Reuter, K. E. Heusler, *Electrochim. Acta* **35**, 1809 (1990).
18. M. Büchler, T. Watari, W. H. Smyrl, *Corros. Sci.* **42**, 1661 (2000).
19. K. Sugimoto, S. Matsuda, Y. Ogiwara, K. Kitamura, *J. Electrochem. Soc.* **132**, 1791 (1985).
20. L. F. Garfias, D. J. Siconolfi, *J. Electrochem. Soc.* **147**, 2525 (2000).
21. Y. S. Lim, J. S. Kim, S. J. Ahn, H. S. Kwon, Y. Katada, *Corros. Sci.* **43**, 53 (2001).
22. H. S. Isaacs, G. Adzic, C. S. Jeffcoate, *Corrosion* **56**, 971 (2000).
23. K. Sasaki, H. S. Isaacs, *J. Electrochem. Soc.* **151**, B124 (2004).
24. L. Tronstad, *Nature* **124**, 373 (1929).
25. L. Tronstad, *Z. Phys. Chem.* **142**, 241 (1929).
26. H. H. Rotermund, G. Haas, R. U. Franz, R. M. Tromp, G. Ertl, *Science* **270**, 608 (1995).

27. The U.S. Department of Energy, Office of Basic Energy Sciences, Division of Materials Sciences and Engineering, supported this project under contract DEFG02-00ER45825. We thank G. Ertl and K. Doblhofer for fruitful discussions.

Supporting Online Material

www.sciencemag.org/cgi/content/full/305/5687/1133/DC1
SOM Text
Fig. S1
Movies S1 to S3

14 June 2004; accepted 16 July 2004

Decamethyldizincocene, a Stable Compound of Zn(I) with a Zn–Zn Bond

Irene Resa,[1] Ernesto Carmona,[1]* Enrique Gutierrez-Puebla,[2] Angeles Monge[2]

Unlike mercury, which has an extensive +1 oxidation state chemistry, zinc usually adopts the +2 oxidation state. Decamethyldizincocene, $Zn_2(\eta^5\text{-}C_5Me_5)_2$, an organometallic compound of Zn(I) formally derived from the dimetallic $[Zn–Zn]^{2+}$ unit, has been isolated from the low-temperature (–10°C) reaction of $Zn(C_5Me_5)_2$ and $Zn(C_2H_5)_2$ in diethyl ether. X-ray studies show that it contains two eclipsed $Zn(\eta^5\text{-}C_5Me_5)$ fragments with a Zn–Zn distance (± standard deviation) of 2.305(±3) angstroms, indicative of a metal-metal bonding interaction.

Of the Group 12 elements (zinc, cadmium, and mercury), the formal oxidation state of +1 is important only for mercury. For example, the dication Hg_2^{2+} is well known, whereas the oxidation state of the lighter metals, Zn and Cd, is almost invariably +2 (*1*, *2*). Only a few exceptions to this rule are known. The dication Cd_2^{2+} has been known for many years (*1*, *2*), and it has been structurally characterized by x-ray methods in $Cd_2(AlCl_4)_2$ (*3*) and by ^{113}Cd nuclear magnetic resonance (NMR) (*4*) in $Cd_2Tp^{Me2}{}_2$ [Tp^{Me2} is hydrotris(3,5-dimethylpyrazolyl)borate]. There is evidence for the formation of Zn_2^{2+} ions in $ZnCl_2$/Zn glasses at high temperatures (*5*) and in zeolite matrices (*6*). Very recently, the formation of mononuclear, paramagnetic Zn^+ in a microporous crystalline silicoaluminophosphate has been reported (*7*).

However, despite extensive research (*1*, *8*), molecular complexes of the metal-metal–bonded Zn_2^{2+} unit have not been reported. We unexpectedly succeeded in isolating a compound of this type, namely decamethyldizincocene, $Zn_2(\eta^5\text{-}C_5Me_5)_2$ (where Me is CH_3) (compound **1**), and we have characterized this molecule by chemical, spectroscopic, and x-ray methods.

Zincocene, $Zn(C_5H_5)_2$, and diethylzinc, $Zn(C_2H_5)_2$, have been reported to react at 60°C, for 1 hour, to give the half-sandwich complex $Zn(\eta^5\text{-}C_5H_5)(C_2H_5)$ in quantitative yield (*9*). We have found that the analogous reaction of $Zn(C_5Me_5)_2$ (*10*) and $Zn(C_2H_5)_2$ is fast at room temperature and produces a mixture of two compounds, **1** and **2** (Fig. 1), in a ratio that depends on the reaction conditions. In some instances, partial decomposition and generation of metallic zinc is observed (*11*), but this can be avoided by the careful exclusion of air.

Low-temperature ^1H NMR monitoring permits optimization of the synthesis of the two substances. Thus, in pentane at –60°C, the ethyl derivative $Zn(\eta^5\text{-}C_5Me_5)(C_2H_5)$ (compound **2**), is the only observable product, whereas the use of diethyl ether as the solvent at –10°C allows the isolation (*12*) of the unforeseen $Zn_2(\eta^5\text{-}C_5Me_5)_2$ (compound **1**) in ~45% isolated yield [based on $Zn(C_5Me_5)_2$; only minor amounts of **2** can be detected under these conditions].

Compound **2** is a half-sandwich derivative, with structure analogous to that of the known $Zn(\eta^5\text{-}C_5H_5)(C_2H_5)$ (*9*). Its ^1H NMR spectrum in C_6D_6 is simple and consists of a singlet at δ 1.98 resulting from the methyl protons of the C_5Me_5 ligand (relative intensity 15 H) and of one triplet and one quartet signals at δ 1.20 [the NMR coupling constant between ^1H nuclei separated by three chemical bonds ($^3J_{HH}$) = 8 Hz, 3 H] and 0.38 ($^3J_{HH}$ = 8 Hz, 2 H), respectively, as expected for a zinc-bound ethyl group. Corresponding $^{13}C\{^1H\}$ resonances are found at 9.8 (C_5Me_5), 12.9 (Zn-CH_2CH_3), and –8.2 parts per million (ppm) (Zn-CH_2CH_3). They are accompanied by a low-field signal at δ 107.8 attributable to the ring carbon atoms ($\eta^5\text{-}C_5Me_5$).

Compound **1** is exceedingly reactive toward oxygen and moisture, both in solution and in the solid state, particularly at temperatures above 0°C. As a crystalline solid, it burns spontaneously upon exposure to the atmosphere, but when kept under argon, or in a tube sealed under vacuum, it appears to be indefinitely stable at room temperature. Notwithstanding, storage at –20°C is advisable. Under dynamic vacuum (~10^{-3} mbar), it can be sublimed at temperatures near 70°C. Although partial decomposition occurs, the ^1H and $^{13}C\{^1H\}$ NMR spectra of the sublimate are identical to those of samples crystallized from pentane. It is highly soluble in common organic solvents such as pentane, benzene, diethyl ether, or tetrahydrofuran.

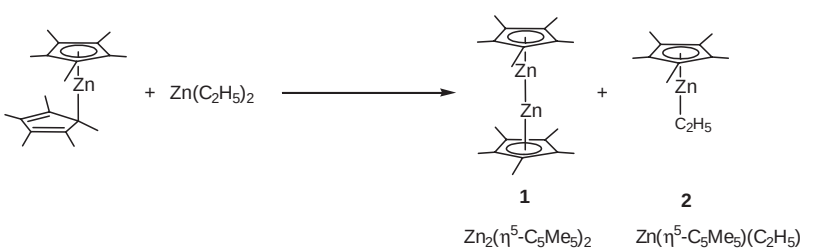

Fig. 1. Generation of compounds **1** and **2**.

[1]Instituto de Investigaciones Químicas–Departamento de Química Inorgánica, Universidad de Sevilla, Consejo Superior de Investigaciones Científicas, Américo Vespucio 49, 41092 Sevilla, Spain. [2]Instituto de Ciencia de Materiales de Madrid, Consejo Superior de Investigaciones Científicas, Campus de Cantoblanco, 28049 Madrid, Spain.

*To whom correspondence should be addressed. E-mail: guzman@us.es

The molecular structure of $Zn_2(\eta^5\text{-}C_5Me_5)_2$ was determined by x-ray crystallography (*13*). Two independent determinations have been carried out at –100°C (graphite monochromated Mo-K_α radiation, $\lambda = 0.71073$ Å) and –170°C (Cu-K_α radiation, $\lambda = 1.54184$ Å). Lower temperatures and longer wavelengths should enhance the contribution of the H atoms to the x-ray experiments, yet both studies have provided identical results. As shown in Fig. 2, compound **1** contains two metal-metal–bonded $Zn(\eta^5\text{-}C_5Me_5)$ units. Therefore, it would constitute a molecular complex of Zn(I). In addition, its structure differs from other cyclopentadienyl derivatives. The almost linear Cp^*_{centr}-Zn-Zn-Cp^*_{centr} geometry [where Cp* is C_5Me_5 and Cp^*_{centr}-Zn-Zn angles are 177.4 (±1)° on average], with a M–M bond unsupported by bridging ligands, has no precedent among either the transition metal (*14*, *15*) or the main group (*16*) metallocene families.

The most salient feature of the structure of **1** is doubtless the short Zn(1)–Zn(2) separation of 2.305 (±3) Å. This distance is substantially shorter than twice Pauling's single-bond metallic radius [2.50 Å (*17*)] and therefore indicative of Zn–Zn bonding interaction. Moreover, comparisons with the Cd–Cd distance of 2.58 Å found (*3*) in $Cd_2(AlCl_4)_2$ and with the Hg–Hg bond lengths of 2.49 to 2.59 Å reported for the mercury(I) halides (*1*, *18*) reveal comparable M–M bonding interactions in all of these compounds [the single-bond metallic radii of Zn, Cd, and Hg are 1.25, 1.41, and 1.44 Å, respectively (*17*)]. To rule out a doubly bridging hydride structure analogous to that recently described (*19*) for $[HC(CMeNXyl)_2]_2Zn_2(\mu\text{-}H)_2$ (where Xyl is C_6H_3-2,6-Me_2; the Zn–Zn separation of 2.4513 (±9) Å found in this complex is significantly longer than in **1**), a thorough study of the residual electron density has been performed (*20*). We found that the highest 10 peaks with electron density from 0.28 to 0.22 electrons per cubic angstrom (0.23 to 0.19 Å with Cu radiation) do not show any discontinuity. This finding, considered with the very short Zn–Zn separation in **1**, suggests that it is unlikely that the residual electron density arises from hydrogen atoms. Moreover, the hydride formulation may be discarded on the basis of the ^{1}H NMR (chemical and other data presented below). The coordination of the C_5Me_5 rings is symmetrical ($Zn\text{–}C_{ring}$ distances in the narrow interval of 2.27 to 2.30 Å) and the two $Zn\text{–}Cp^*_{centr}$ separations are identical within experimental error (~2.04 Å). Both rings are planar and adopt a parallel, eclipsed configuration.

The high-resolution mass spectrum of **1** shows the characteristic molecular ion envelope around the mass/charge ratio $[M^+](400)$ expected for $Zn_2(\eta^5\text{-}C_5Me_5)_2$. This result and the agreement between the experimental and calculated isotopic mass distributions (*12*) rules out the presence of hydride ligands in the molecular ion of **1**. Infrared and Raman spectra do not provide useful structural information, because they are dominated by the bands of the C_5Me_5 ligands. No definitive assignment of the Zn–Zn stretching mode can be made at this stage. The ^{1}H NMR spectrum of **1** recorded in C_6D_6 is a singlet at δ 2.02; no other resonances were found in the chemical shift range from +100 to –100 ppm in the temperature interval from –80° to +80°C (C_7D_8). Once more, this lack of resonance lines is not in accord with a hydride formulation (*19*, *21*) for **1**. Finally, $\eta^5\text{-}C_5Me_5$ coordination in solution is supported by the observation of a $^{13}C\{^1H\}$ signal at 108.5 ppm (δ 107.8 in **2**).

Preliminary chemical studies are also consistent with the structure proposed for **1**. As Fig. 3 shows, the parent compound, $Zn(C_5Me_5)_2$, reacts with CNXyl to give the half-sandwich iminoacyl species **3** as the only product (*12*). The analogous reaction of **1** yields this iminoacyl **3**, along with metallic zinc (*11*) (both in a preparative scale and by ^{1}H NMR monitoring; C_7D_8 solutions, from –60° to 20°C). In a blank test experiment, the volume of H_2 that would be evolved from a weighed sample of **1**, assuming a putative bis(hydride) formulation, was injected into 0.5 ml of C_6D_6 and gave the anticipated ^{1}H NMR resonance at δ 4.45 ppm. In contrast, no H_2 evolution was detected as a result of the reaction of **1** with CNXyl in a sealed NMR tube under the above conditions. Thus, apart from Zn and iminoacyl **3**, no other products are generated, in accord with an isocyanide-induced disproportionation of $Zn_2(C_5Me_5)_2$ into Zn plus $Zn(C_5Me_5)_2$, the latter being trapped as the iminoacyl complex **3**.

Both $Zn(C_5Me_5)_2$ and $Zn_2(\eta^5\text{-}C_5Me_5)_2$ react with H_2O (about –10°C, 10 molar excess, dilute diethyl ether solution), albeit with different reaction outcomes. The hydrolysis of the mononuclear Zn(II) metallocene yields C_5Me_5H (NMR) and a white precipitate of $Zn(OH)_2$ that converts into ZnO (*11*) upon heating at 50°C under a vacuum. The analogous reaction of the dizinc complex **1** generates C_5Me_5H, crystalline Zn (*11*) and $Zn(OH)_2$. Upon work-up at room temperature, H_2 liberation is observed (NMR) as a result of oxidation of metallic zinc by water, and after heating at 50°C under vacuum, ZnO is obtained as the only metal-containing product (*11*). Thus, in addition to the hydrolytic cleavage of the Zn-C_5Me_5 bonds, water induces the disproportionation of the Zn_2^{2+} unit to Zn plus Zn^{2+}.

Finally, the alcoholysis of the two Zn-C_5Me_5 complexes by Me_3COH provides related results (Fig. 4). The monozinc derivative gives the expected C_5Me_5H and $[Zn(OCMe_3)_2]_x$ (*22*) products, whereas the dizinc compound, $Zn_2(\eta^5\text{-}C_5Me_5)_2$, disproportionates to a mixture of Zn and $[Zn(OCMe_3)_2]_x$, as revealed by x-ray powder diffraction analysis.

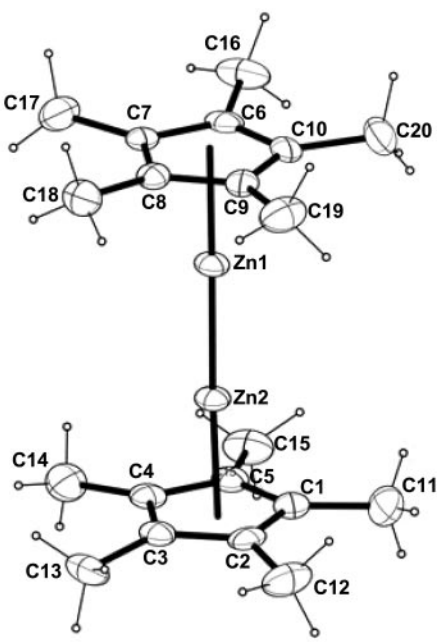

Fig. 2. Molecular structure of $Zn_2(\eta^5\text{-}C_5Me_5)_2$ (compound **1**).

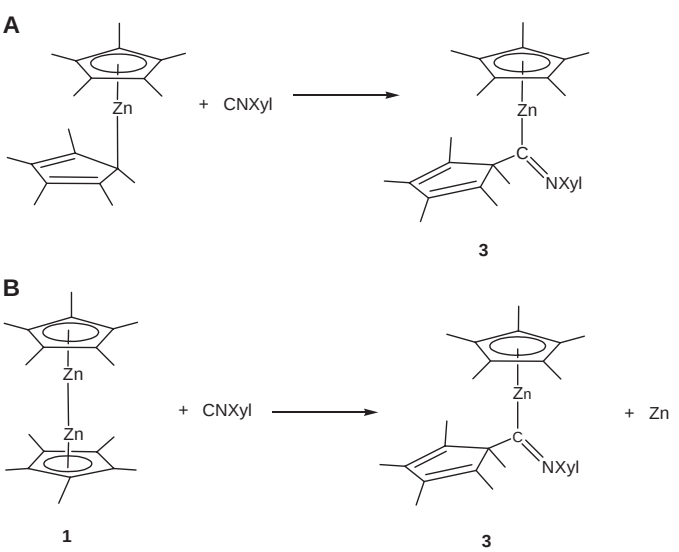

Fig. 3. Reactions of $Zn(C_5Me_5)_2$ (**A**) and $Zn_2(\eta^5\text{-}C_5Me_5)_2$ (**B**) with CNXyl.

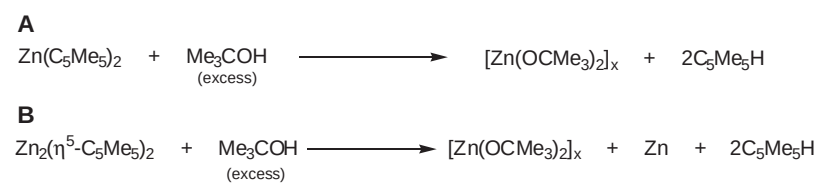

Fig. 4. Reactions of $Zn(C_5Me_5)_2$ (**A**) and $Zn_2(\eta^5\text{-}C_5Me_5)_2$ (**B**) with Me_3COH.

The alkoxide has been additionally identified by comparison of its infrared, ^1H, and $^{13}C\{^1H\}$ NMR spectra with those of an authentic sample prepared from $Zn(C_2H_5)_2$ and Me_3COH (*22*).

The synthesis of compound **1** suggests that related complexes of Cd and Hg could be isolated. It also seems plausible that the stabilization of the $[Zn–Zn]^{2+}$ unit does not require the existence of Zn–C bonds, which means that classical coordination compounds of the Zn_2^{2+} central unit are reasonable targets for future synthetic and structural studies.

References and Notes

1. F. A. Cotton, G. Wilkinson, C. A. Murillo, M. Bochmann, *Advanced Inorganic Chemistry* (Wiley, New York, ed. 6, 1999), chap. 15.
2. N. Wiberg, Ed., *Holleman-Wiberg Inorganic Chemistry* (Academic Press, New York, ed. 34, 2001), chap. XXIII.
3. R. Faggiani, R. J. Gillespie, J. E. Vekris, *J. Chem. Soc. Chem. Commun.* **1986**, 517 (1986).
4. D. L. Reger, S. S. Mason, *J. Am. Chem. Soc.* **115**, 10406 (1993).
5. D. H. Kerridge, S. A. Tariq, *J. Chem. Soc. A* **1967**, 1122 (1967).
6. F. Rittner, A. Seidel, B. Boddenberg, *Micropor. Mesopor. Mat.* **24**, 127 (1998).
7. Y. Tian, G. D. Li, J. S. Chen, *J. Am. Chem. Soc.* **125**, 6622 (2003).
8. P. O'Brien, in *Comprehensive Organometallic Chemistry II*, G. Wilkinson, F. G. A. Stone, E. Abel, Eds. (Pergamon, Oxford, UK, 1995), vol. 3, chap. 4.
9. J. T. B. H. Jastrzebski, J. Boersma, G. van Koten, W. J. J. Smeets, A. L. Spek, *Recl. Trav. Chim. Pays-Bas* **107**, 263 (1988).
10. R. Blom *et al.*, *Acta Chem. Scand. A* **40**, 113 (1986).
11. Data were identified by x-ray powder diffraction.
12. Materials and methods are available as supporting material on *Science* Online.
13. Two x-ray crystallographic analyses were carried out. The first made use of Bruker-Siemens Smart 1K charge-coupled device (CCD) diffractometer with a graphite monochromated Mo-K_α ($\lambda = 0.71073$ Å) radiation. Crystal data for **1** was as follows: $C_{20}H_{30}Zn_2$; molecular weight = 401.18; triclinic; space group $P\bar{1}$; Z = 2; T 173 (±2) K; a = 6.9329 (±3) Å, b = 10.8831 (±5) Å, c = 13.8384 (±7) Å, α = 109.777 (±1)°, β = 101.603 (±1)°, γ = 94.201 (±1)°, and V = 951.09 (±8) Å^3; goodness of fit = 0.988; R1[$I > 2\sigma(I)$] = 0.031; wR2 = 0.076 (all data). Atomic coordinates, bond lengths, and angles and other important parameters have been deposited with the Cambridge Crystallographic Data Centre as supplementary publication CCDC 233010. Details of the x-ray crystallographic analysis are also available on *Science* Online. The second analysis was carried out at –173°C (100 K), with the use of Cu-K_α ($\lambda = 1.54184$ Å) radiation, on a Bruker Smart 6000 CCD system equipped with a rotating anode. The results of the two determinations are very similar. Data from the second analysis can be obtained from the authors, upon request.
14. A compound initially formulated as $Co_2(\eta^5\text{-}C_5Me_5)_2$ by J. J. Schneider, R. Goddard, S. Werner, and C. Krüger [*Angew. Chem. Int. Ed. Engl.* **30**, 1124 (1991)] was subsequently shown to be $Co_2(\eta^5\text{-}C_5Me_5)_2(\mu\text{-}H)_3$[20].
15. J. L. Kersten *et al.*, *Angew. Chem. Int. Ed. Engl.* **31**, 1341 (1992).
16. P. Jutzi, N. Burford, *Chem. Rev.* **99**, 969 (1999).
17. L. Pauling, *The Nature of the Chemical Bond* (Cornell Univ. Press, Ithaca, NY, ed. 3, 1960), chap. 7.
18. E. Dorn, *J. Chem. Soc. Chem. Commun.* **1971**, 466 (1971).
19. H. Hao *et al.*, *Chem. Commun.* **2001**, 1118 (2001), and references therein.
20. In this refinement, the data with large 2θ angles were given higher weights, followed by a difference electron density synthesis with reflections with sinθ/λ.
21. R. Han, I. B. Gorrell, A. G. Looney, G. Parkin, *J. Chem. Soc. Chem. Commun.* **1991**, 717 (1991).
22. G. E. Coates, P. D. Roberts, *J. Chem. Soc. A* **1967**, 1233 (1967).

23. In memoriam of Professor Roberto Fernández de Caleya. We thank A. Justo (x-ray powder diffraction), M. A. Avilés (Raman spectra), and R. Fernández for their valuable help, and R. A. Andersen (University of California, Berkeley) for obtaining the mass spectrum of compound **1**. Supported by the Ministry of Science and Technology of Spain (to E.C., Project BQU2001-1995; and to I.R. for a research studentship).

Supporting Online Material

www.sciencemag.org/cgi/content/full/305/5687/1136/DC1
Materials and Methods
Tables S1 to S4
References

14 June 2004; accepted 7 July 2004

Regions of Strong Coupling Between Soil Moisture and Precipitation

The GLACE Team: Randal D. Koster,[1]* Paul A. Dirmeyer,[2] Zhichang Guo,[2] Gordon Bonan,[3] Edmond Chan,[4] Peter Cox,[5] C. T. Gordon,[6] Shinjiro Kanae,[7] Eva Kowalczyk,[8] David Lawrence,[9] Ping Liu,[10] Cheng-Hsuan Lu,[11] Sergey Malyshev,[12] Bryant McAvaney,[13] Ken Mitchell,[11] David Mocko,[10] Taikan Oki,[14] Keith Oleson,[3] Andrew Pitman,[15] Y. C. Sud,[1] Christopher M. Taylor,[16] Diana Verseghy,[4] Ratko Vasic,[17] Yongkang Xue,[17] Tomohito Yamada[14]

Previous estimates of land-atmosphere interaction (the impact of soil moisture on precipitation) have been limited by a lack of observational data and by the model dependence of computational estimates. To counter the second limitation, a dozen climate-modeling groups have recently performed the same highly controlled numerical experiment as part of a coordinated comparison project. This allows a multimodel estimation of the regions on Earth where precipitation is affected by soil moisture anomalies during Northern Hemisphere summer. Potential benefits of this estimation may include improved seasonal rainfall forecasts.

Atmospheric chaos severely limits the predictability of precipitation on seasonal time scales. Weather forecasts, which rely heavily on atmospheric initialization, rarely demonstrate skill beyond about a week. Hope for accurate seasonal forecasts lies with simulating the atmospheric response to slowly varying states of the ocean and land surface—components of the Earth system that can be predicted weeks to months in advance. A systematic response of the atmosphere to these boundary components would contribute skill to seasonal prediction.

The critical importance of the ocean surface in this regard is well known (*1*). Ocean temperature anomalies can be predicted a year or more in advance (*2*). Furthermore, the atmosphere responds particularly strongly (and predictably) to ocean temperature anomalies in certain regions—in "hot spots" of ocean-atmosphere coupling. The eastern equatorial Pacific is

[1]NASA Goddard Space Flight Center, Greenbelt, MD 20771, USA. [2]Center for Ocean-Land-Atmosphere Studies, Calverton, MD 20705, USA. [3]National Center for Atmospheric Research, Boulder, CO 80307, USA. [4]Meteorological Service of Canada, Toronto, Ontario M34 5T4, Canada. [5]Hadley Centre for Climate Prediction and Research, Exeter EX1 3PB, UK. [6]Geophysical Fluid Dynamics Laboratory, Princeton, NJ 08542, USA. [7]Research Institute for Humanity and Nature, Kyoto 602-0878, Japan. [8]CSIRO Atmospheric Research, Aspendale, Victoria 3195, Australia. [9]University of Reading, Reading, Berkshire RG6 6BB, UK. [10]Science Applications International Corporation, Beltsville, MD 20705, USA. [11]National Center for Environmental Prediction, Camps Springs, MD 20746, USA. [12]Princeton University, Princeton, NJ 08544, USA. [13]Bureau of Meteorology Research Centre, Melbourne, Victoria 3001, Australia. [14]University of Tokyo, Tokyo 153-8505, Japan. [15]Macquarie University, North Ryde, New South Wales 2109, Australia. [16]Centre for Ecology and Hydrology, Wallingford, Oxfordshire OX10 8BB, UK. [17]University of California, Los Angeles, CA 90095, USA.

*To whom correspondence should be addressed. E-mail: randal.d.koster@nasa.gov

the most famous oceanic hot spot, playing a key role in the El Niño–La Niña cycle (*3*).

Another potentially useful slowly varying component of the Earth system is soil moisture, which can influence weather through its impact on evaporation and other surface energy fluxes. Soil moisture anomalies can persist for months (*4*), and although a paucity of observations prevents an unambiguous demonstration of soil moisture impacts on precipitation (*5*), such impacts are often seen in atmospheric general circulation model (AGCM) studies (*6*, *7*). Indeed, some AGCM studies suggest that in continental midlatitudes during summer, oceanic impacts on precipitation are small relative to soil moisture impacts (*8*).

This suggests a question: Are there specific locations on the Earth's surface for which soil moisture anomalies have a substantial impact on precipitation? The identification of such hot spots would have important implications for the design of seasonal prediction systems and for the associated development of ground-based and satellite-based strategies for monitoring soil moisture, if such impacts were found to be local. In a broader sense, such identification is critical for understanding Earth's climate system and the limits of predictability therein.

Although AGCM studies (*9*–*12*) and even numerical weather prediction model studies (*13*) have addressed this question, published results are based on different experimental designs and reflect distinctive features of different model parameterizations. The coupling question, however, was recently addressed en masse by a dozen AGCM groups (*14*), all performing the same highly controlled numerical experiment. The experiments were coordinated by GLACE, the Global Land-Atmosphere Coupling Experiment (*15*). Each model contributing to GLACE generated several ensembles of boreal summer (June through August) simulations designed to quantify that model's land-atmosphere coupling strength (*16*) for that season. By combining the results across these models, we eliminate much of the undesired individual model dependence. We obtain, in effect, a unique result: a multimodel average depiction of the global distribution of land-atmosphere coupling strength. Given the limitations of the observational data, both now and in the foreseeable future, such a multimodel estimate of coupling strength distribution is arguably the best estimate attainable.

Each GLACE participant performed an ensemble of 16 simulations in which soil moisture varied between the simulations, and another ensemble in which the geographically varying time series of subsurface soil moisture was forced to be the same across the 16 simulations (*17*). Coupling strength—the degree to which all prescribed boundary conditions affect some atmospheric quantity X—can be estimated (*18*) for each of the two ensembles with the diagnostic Ω:

$$\Omega = (16\sigma^2_{<X>} - \sigma^2_X)/15\sigma^2_X \qquad (1)$$

where σ^2_X is the intraensemble variance of X and $\sigma^2_{<X>}$ is the corresponding variance of the ensemble-mean time series—the single time series generated by averaging across the 16 ensemble members at each time interval, chosen here to be 6 days. We are interested, of course, in precipitation; to reduce noise, however, we take X to be the natural logarithm of the precipitation. Performing statistics on the logarithms of precipitation is a common practice in hydrology and meteorology, because unmodified precipitation distributions tend to be highly skewed (*19*, *20*).

A study of the equation shows that outside of sampling error, Ω should vary from 0 to 1, with higher values implying a higher impact of the atmosphere's boundary conditions on precipitation. To isolate soil moisture's impact on precipitation from that of all other forcings, such as time-varying ocean temperatures and the seasonal variation of solar radiation, we compute the difference in the Ω values between the two ensembles. In simple terms, this Ω difference approximates the fraction of the precipitation variance explained by variations in soil moisture alone.

Figure 1 shows the global map of the Ω difference averaged across all of the participating models in GLACE. This multimodel estimation of land atmosphere coupling strength reveals several distinct hot spots. Hot spots appear in the central Great Plains of North America, the Sahel, equatorial Africa, and India. Less intense hot spots appear in South America, central Asia, and China.

The positions of the hot spots are not unexpected (*8*, *21*), particularly if the soil moisture influence is presumed to be local rather than remote. Consider first that in wet climates, for which soil water is plentiful, evaporation is controlled not by soil moisture but by net radiative energy. This is illustrated in Fig. 2, which shows how the Ω difference diagnostic, applied to evaporation rather than precipitation, varies (on average) with soil moisture. The Ω difference—the fraction of the evaporation variance explained by soil moisture variations—is indeed lowest when soil moisture is high. Because evaporation in wet climates is not highly sensitive to soil moisture variations, precipitation should not be sensitive to them, either.

Now consider that in dry climates, evaporation rates are sensitive to soil moisture but are also, of course, generally small, as demonstrated for the models by the dashed curve in Fig. 2. Intuitively, small evaporation rates should have a limited ability to affect precipitation. The atmosphere in dry regions is, in any case, predisposed to limit precipitation. Only in the transition zones between wet and dry climates, where the atmosphere is amenable to precipitation generation [in particular, where boundary-layer moisture can trigger moist convection (*22*)] and where evaporation is suitably high but still sensitive to soil moisture, can

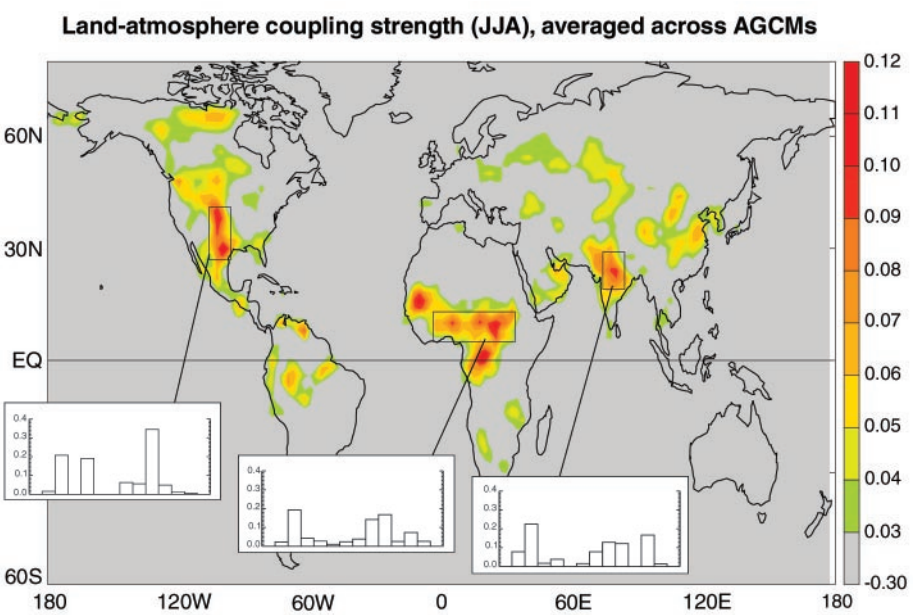

Fig. 1. The land-atmosphere coupling strength diagnostic for boreal summer (the Ω difference, dimensionless, describing the impact of soil moisture on precipitation), averaged across the 12 models participating in GLACE. (**Insets**) Areally averaged coupling strengths for the 12 individual models over the outlined, representative hotspot regions. No signal appears in southern South America or at the southern tip of Africa.

we expect soil moisture to influence precipitation. The major hot spots shown lie mainly in such transition zones (*23*).

The insets in the map (Fig. 1) show that not all of the GLACE models place hot spots in the regions indicated. In North America, for example, only half of the models show a statistically significant (*24*) coupling strength in the outlined region. The 12 models agree slightly more in the Sahelian and Indian hotspot regions; nevertheless, throughout the world, there exists extensive intermodel variability in the strength and positioning of the hot spots, a reflection of ongoing uncertainty in the proper way to represent the physical processes defining land-atmosphere coupling strength. Indeed, some of the models showing a small coupling strength in the insets also show a low coupling strength everywhere else on the planet. The intermodel variability highlights the importance of the averaging process leading to Fig. 1. The insets support the idea, stated above, that any single-model analysis of coupling strength will provide model-specific results. The patterns revealed by the averaging process are valuable because they show where many independent models agree that the land-atmosphere coupling is important.

The plotted hot spots indicate where a global initialization of soil moisture may enhance precipitation prediction skill during Northern Hemisphere summer (*25*, *26*). Under the assumption that the soil moisture impacts are predominantly local, the hot spots indicate where the routine monitoring of soil moisture, with both ground-based and space-based systems, will yield the greatest return in boreal summer seasonal forecasting. The hot spots are, in a sense, land-surface analogs to the ocean's "El Niño hot spot" in the eastern tropical Pacific.

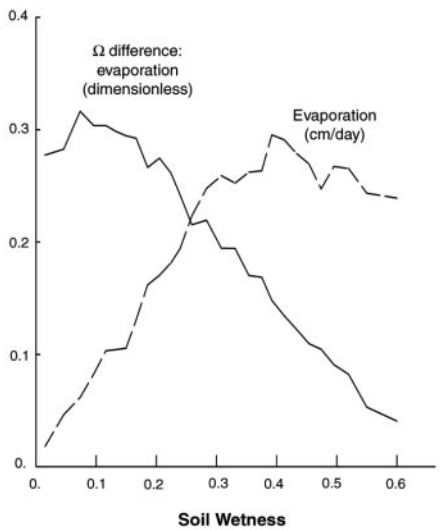

Fig. 2. Average relationship between soil wetness (the degree of saturation in the soil) and two separate aspects of the land-surface energy budget: the Ω difference for evaporation (solid curve, in dimensionless units) and the average evaporation rate (dashed curve, in cm/day). Both aspects should have suitably high values to allow soil moisture anomalies to be translated into precipitation anomalies; the plot shows that this mostly occurs for intermediate values of soil wetness, i.e., in the transition zones between wet and dry climates. The curves are derived by averaging the soil wetness, Ω difference, and evaporation fields across the 12 models, constructing scatter plots for the two relationships with data from nonice land points, and then binning the data according to soil wetness value.

References and Notes

1. J. M. Wallace *et al*., *J. Geophys. Res.* **103**, 14241 (1998).
2. B. P. Kirtman, P. S. Schopf, *J. Clim.* **11**, 2804 (1998).
3. E. M. Rasmusson, T. H. Carpenter, *Mon. Weather Rev.* **110**, 354 (1982).
4. Y. Vinnikov *et al*., *J. Geophys. Res.* **101**, 7163 (1996).
5. Historical soil moisture measurements are mostly confined to Asia (*27*). Even if global soil moisture fields did exist, using observations to establish that soil moisture affects precipitation is difficult because the other direction of causality is much stronger—precipitation has a first-order impact on soil moisture.
6. J. Shukla, Y. Mintz, *Science* **215**, 1498 (1982).
7. P. A. Dirmeyer, *J. Clim.* **13**, 2900 (2000).
8. R. D. Koster, M. J. Suarez, M. Heiser, *J. Hydrometeorol.* **1**, 26 (2000).
9. H. Douville, F. Chauvin, *Clim. Dyn.* **16**, 719 (2000).
10. P. A. Dirmeyer, *J. Hydrometeorol.* **4**, 329 (2001).
11. R. D. Koster, M. J. Suarez, *J. Hydrometeorol.* **4**, 408 (2003).
12. C. A. Schlosser, P. C. D. Milly, *J. Hydrometeorol.* **3**, 483 (2002).
13. C. M. Beljaars, P. Viterbo, M. J. Miller, A. K. Betts, *Mon. Weather Rev.* **124**, 362 (1996).
14. The participating AGCMs are from the following groups. (The order presented here is alphabetical and does not match the order of the histogram bars in Fig. 1.) (i) Bureau of Meteorology Research Centre (BMRC), Australia; (ii) The Canadian Center for Climate Modeling and Analysis (CCCma), Canada; (iii) Center for Climate System Research (CCSR), University of Tokyo, and National Institute for Environmental Studies (NIES), Japan; (iv) Center for Ocean-Land-Atmosphere Studies (COLA), United States; (v) Commonwealth Scientific and Industrial Research Organization (CSIRO), Australia; (vi) NASA/Goddard Space Flight Center Laboratory for Atmospheres, Climate and Radiation Branch, United States (GEOS); (vii) Geophysical Fluid Dynamics Laboratory (GFDL), United States; (viii) Hadley Center (HadAM3), UK; (ix) National Center for Atmospheric Research (NCAR), United States; (x) National Center for Environmental Prediction (NCEP), United States; (xi) NASA Seasonal-to-Interannual Prediction Project [now part of the Global Modeling and Assimilation Office (GMAO)], United States; and (xiii) University of California, Los Angeles (UCLA).
15. GLACE is a joint project of the Global Energy and Water Cycle Experiment (GEWEX) Global Land Atmosphere System Study (GLASS) and the Climate Variability Experiment (CLIVAR) Working Group on Seasonal-to-Interannual Prediction (WGSIP), all under the aegis of the World Climate Research Programme (WCRP).
16. Coupling strength in this report refers to the general ability of land surface moisture anomalies—either local or remote—to affect precipitation in a given region. Inferences regarding soil moisture measurement in the indicated hot spots require an assumption of local influence.
17. The prescribed soil moistures necessarily differed from model to model, because each time series had to be fully consistent with the individual model using it. The prescribed moistures for a given model came, in fact, from one of the model's simulations in the first, "variable soil moisture" ensemble. In GLACE, subsurface moisture refers to a soil moisture prognostic variable having an assigned effective depth of more than 5 cm from the surface. Soil moistures corresponding to shallower depths are not reset in the experiment. For details, see the experiment plan posted on the GLACE Web site: http://glace.gsfc.nasa.gov/.
18. R. D. Koster *et al*., *J. Hydrometeorol.* **3**, 363 (2002).
19. G. Drufuca, I. I. Zawadzki, *J. Appl. Meteorol.* **14**, 1419 (1975).
20. B. Kedem, L. S. Chiu, G. R. North, *J. Geophys. Res.* **95**, 1965 (1990).
21. Indirect (and thus limited in its own right) observational estimates (*28*) of the North American hot spot roughly agree with that shown in the figure.
22. Y. C. Sud, W. C. Chao, G. K. Walker, *J. Arid Environ.* **25**, 5 (1993).
23. Neither equatorial Africa nor the northernmost reaches of Canada are traditionally considered transition zones between wet and arid climates, and the appearance of hot spots in these regions is not so easily explained. On average, the models do show a pronounced sensitivity of evaporation to soil moisture in equatorial Africa, belying its intuitive status as an atmosphere-controlled evaporation regime.
24. For a single model at a single grid cell, an Ω difference of 0.06 is significant at the 95% confidence level. If the grid cells within a region are completely independent, then a regional (averaged over, say, 10 grid cells) Ω difference of 0.002 is significant at the 95% confidence level. The actual 95% confidence value for the bars in the histograms lies somewhere between these two values, because although multiple grid cells contribute to the regional average, the grid cells are not fully independent. A single exact value cannot be computed, because each AGCM uses its own horizontal grid resolution and simulates unique spatial correlation structures.
25. This study has focused on soil moisture effects alone. Vegetation properties and processes also have substantial impacts on climate in a number of regions. For example, Charney *et al*. (*29*) describe the importance of surface albedo on North American climate; Dickinson and Henderson-Sellers (*30*) show the impact of deforestation on Amazonian climate; and Xue *et al*. (*31*) demonstrate the importance of vegetation processes on east Asian climate. This issue, like the soil moisture issue, is a subject of continuing investigation.
26. The relative importance of sea surface temperature (SST) forcing in the indicated hot spots cannot be determined in this experiment, for two reasons. (i) The SST signal in either of the two ensembles cannot be separated from the strong seasonality signal associated with the Sun's transit across the sky over the 3-month simulation period. (ii) Only a single year of SSTs is prescribed, so the effect of interannually varying SSTs is not captured. As noted in the text, some studies (*8*) show a strong SST impact in the tropics and subtropics (encompassing the indicated hot spots in Africa and southern Asia) and a relatively weak impact in midlatitudes (encompassing the North American hot spot).
27. A. Robock *et al*., *Bull. Am. Meteorol. Soc.* **81**, 1281 (2000).
28. R. D. Koster, M. J. Suarez, R. W. Higgins, H. M. Van den Dool, *Geophys. Res. Lett.* **30**, 1241, 10.1029/2002GL016571 (2003).
29. J. Charney, W. J. Quirk, S. H. Chow, J. Kornfield, *J. Atmos. Sci.* **34**, 1366 (1977).
30. R. E. Dickinson, A. Henderson-Sellers, *Q. J. R. Meteorol. Soc.* **114**, 439 (1988).
31. Y. K. Xue *et al*., *J. Geophys. Res.* **109**, D03105, 10.1029/2003JD003556 (2004).

32. We thank the listed institutions for the computational support needed to perform the simulations. We also thank M. Kistler for help with the GLACE project Web page and T. Bell for statistical advice.

12 May 2004; accepted 7 July 2004

Modular Construction of Early Ediacaran Complex Life Forms

Guy M. Narbonne

Newly discovered, exceptionally preserved, soft-bodied fossils near Spaniard's Bay in eastern Newfoundland exhibit features not previously described from Ediacaran (terminal Neoproterozoic) fossils. All of the Spaniard's Bay taxa were composed of similar architectural elements—centimeter-scale frondlets exhibiting three orders of fracticality in branching. Frondlets were combined as modules atop semi-rigid organic skeletons to form a wide array of larger constructions, including frondose and plumose structures. This architecture and construction define the "rangeomorphs," a biological clade that dominated the Mistaken Point assemblage (575 to 560 million years ago) but does not appear to be ancestral to any Phanerozoic or modern organisms.

The Ediacara biota is a distinctive fossil assemblage of impressions of centimeter- to meter-scale, soft-bodied organisms that represent the oldest large and complex organisms and ecosystems in Earth history (*1*–*3*). The long-standing morphological view that the Ediacara biota contains the oldest animal megafossils is supported by the presence of probable animal embryos (*4*), burrows attributable to coelomic animals (*5*, *6*), and a community organization that resembles that of modern suspension-feeding animals (*7*, *8*). However, some Ediacaran taxa are more difficult to relate to living animal groups and have elicited interpretations that span virtually all extant kingdoms of macroscopic eukaryotes (*9*–*11*) as well as a hypothesized extinct kingdom (*12*).

Fossils of the Mistaken Point assemblage (575 to 560 million years ago) in eastern Newfoundland, Canada (Fig. 1) represent the oldest reliably dated examples of the Ediacara biota (*13*–*15*). In contrast to younger Ediacaran assemblages from Australia and Russia, which contain segmented forms that are at least broadly comparable with modern animal phyla (*16*–*18*), the Mistaken Point assemblage is dominated by fossils exhibiting fractal-like quilting and whose relationships with modern taxa are not obvious at even the phylum level (*12*). Previous research on the Mistaken Point assemblage has focused on southeastern Avalon Peninsula, particularly outcrops in the vicinity of Portugal Cove South and Mistaken Point (*7*, *8*, *11*–*12*, *15*, *19*–*23*). Preservation of these fossils as census populations beneath beds of volcanic ash provides a superb database for stratigraphic and ecological studies, but because of the grain size of the ash and subsequent penetrative tectonic deformation, fossil preservation is limited to two-dimensional impressions, with little resolution of features <1 to 2 mm in diameter (*8*, *19*, *20*).

A newly discovered and exquisitely preserved fossil assemblage in the Trepassey Formation of the Spaniard's Bay area of northern Avalon Peninsula (Fig. 1) provides more than an order of magnitude finer resolution of the fossils of the Mistaken Point assemblage. The fossils occur in a deep-water, turbiditic slope succession that contains decameter-scale slump beds and lacks any evidence that storm waves or light reached the sea floor. More than 100 frondose and plumose fossils are present on this surface. Their consistent unimodal current alignment, similar to that of other assemblages of the Mistaken Point biota (*19*, *20*), implies that they were tethered to the sea floor and were then buried in place. The fossils show no evidence of tectonic cleavage and are preserved as uncompressed external molds (or rarely as natural casts) within a muddy, distal $T_{D\text{-}E}$ turbidite, permitting resolution of features less than 30 μm in diameter on the best preserved specimens (Fig. 2). Their preservation within the fine sediment differs from the rapid preservation associated with microbial mats described from other Ediacaran localities (*24*); moreover, some Spaniard's Bay specimens partially decomposed before lithification, revealing internal structures previously unknown from the Ediacara biota (Fig. 3, B and D). Information provided from this unique taphonomic window helps to elucidate previously unknown attributes of the architecture and construction of the earliest Ediacaran organisms.

All taxa at the new Spaniard's Bay locality, and most of the 20 to 30 other taxa of the Mistaken Point assemblage elsewhere (*8*, *21*, *23*), are composed of varying constructions of the same architectural building block—a centimeter-scale module herein termed a "rangeomorph frondlet" (Fig. 2A). Each frondlet consists of inflated, self-similar branches that are indistinguishable from the "fractal pneus" defined by Seilacher (*12*). Pneus pass from the midline at an acute angle in an alternate pattern, but variable orientations of rangeomorph frondlets can give the appearance of asymmetric branch lengths or even branching on only one side of the frondlet (Fig. 2). The pattern of branching is remarkably self-similar over three orders of fracticality: Major branches with diameters ranging from 1 to 5 mm are composed of minor branches 0.3 to 0.6 mm in diameter, which, in the best preserved specimens, appear to be composed of tertiary branches <150 μm in diameter (Fig. 2, A to D). Partially overturned specimens reveal that both sides of a rangeomorph frondlet are identical and that each pneu has a circular cross section (Fig. 2, C and D).

Isolated rangeomorph frondlets at Spaniard's Bay exhibit a proximal stem (Fig. 2A) and are aligned parallel with the other fronds on the surface, and thus were probably miniature, free-living fronds attached to the sea floor.

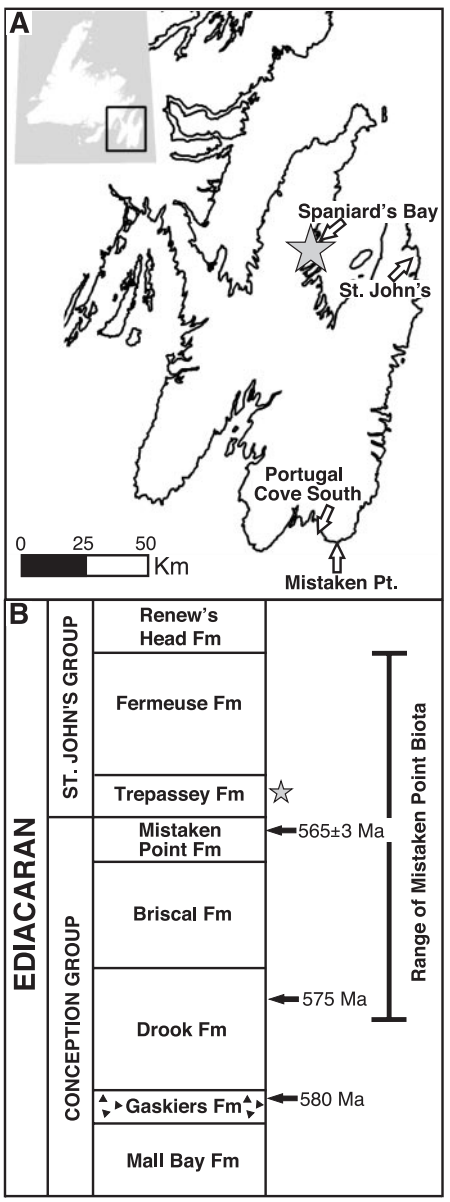

Fig. 1. Location (**A**) and stratigraphic setting (**B**) of the newly discovered bed of fossil rangeomorphs in the Trepassey Formation of the Spaniard's Bay area, eastern Newfoundland, Canada. The star (★) shows the geographic and stratigraphic position of the new fossil occurrence. U-Pb dates are from (*13*, *14*) and references therein.

Department of Geological Sciences and Geological Engineering, Queen's University, Kingston, Ontario K7L 3N6, Canada. E-mail: narbonne@geol.queensu.ca

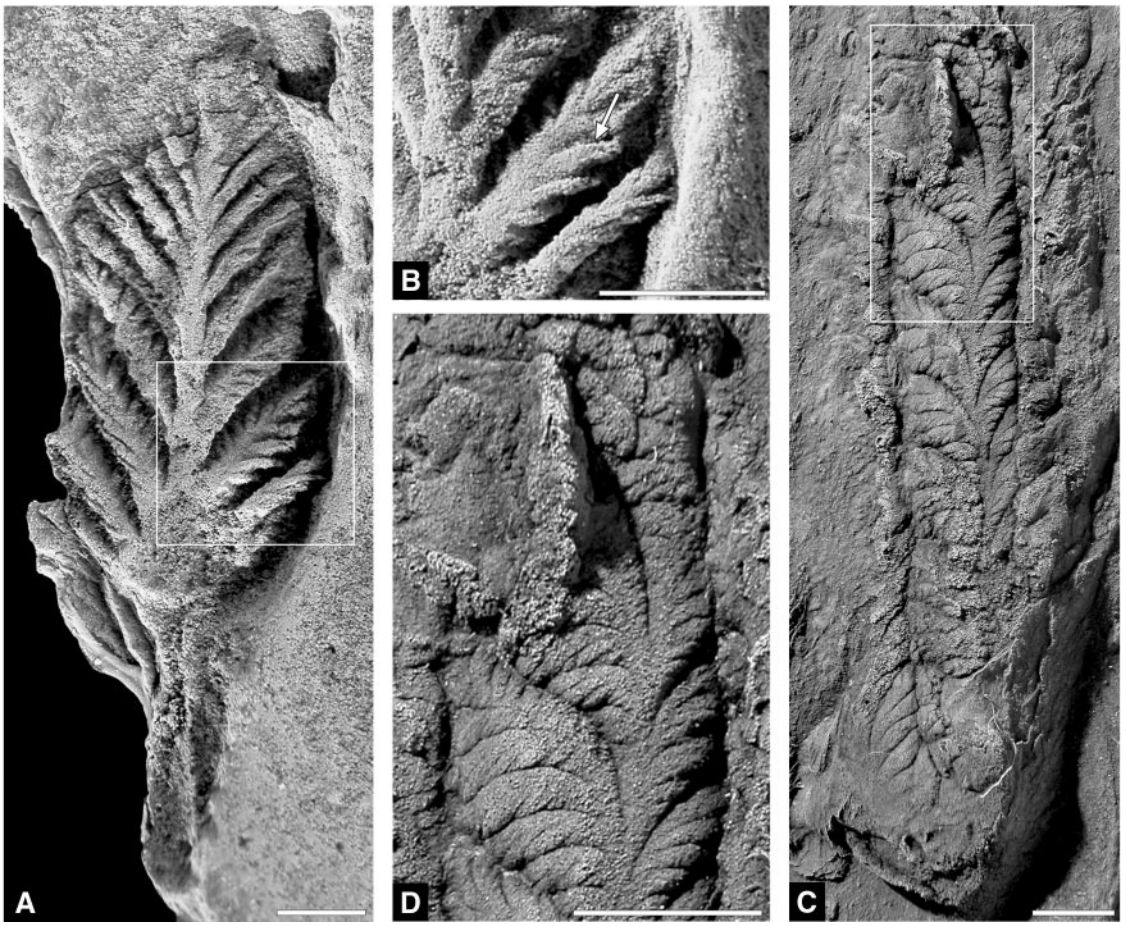

Fig. 2. Rangeomorph architecture from the Trepassey Formation at Spaniard's Bay. (**A**) Isolated rangeomorph frondlet. Specimen whitened with ammonium chloride. (**B**) Enlarged view of the area indicated in (A), showing details of the fractal-like branching pattern. The smallest branches are indicated by the arrow. (**C**) Plumose rangeomorph. Latex mold whitened with ammonium chloride. (**D**) Enlarged view of the area indicated in (C), showing details of the fractal-like branching pattern and the cylindrical cross section of the branches in the ripped and partially overturned frondlet in the upper left. Scale bars, 0.25 cm [(A) and (B)], 0.5 cm [(C) and (D)].

More commonly, rangeomorph frondlets were combined as modules to construct larger and more complicated structures (Fig. 2, C and D; Fig. 3, A to F).

The most familiar rangeomorph constructions are fronds, in which the rangeomorph frondlets were elevated above the sea floor by a stalk attached to a holdfast (Fig. 3, A to C). Previously described rangeomorph fronds are generally referred to *Rangea*, in which the rangeomorph frondlets are arranged in parallel arrays attached to multifoliate sheets surrounding the stalk (*25*–*27*). At least six different constructions of rangeomorph fronds are evident at different stratigraphic levels in the Mistaken Point assemblage (*28*). A new form at Spaniard's Bay differs from typical specimens of *Rangea* in exhibiting rangeomorph frondlets that are arranged as isolated, overlapping petal-shaped elements, each of which is attached at its proximal end to a central stalk (Fig. 3A). A second undescribed taxon at Spaniard's Bay exhibits rangeomorph frondlets that hang downward in a pendant array from a thin, presumably semi-rigid, zigzag central stalk with lateral struts (Fig. 3, B and C). The very close similarity in size and morphology between each "petal" of these fronds and the free-living rangeomorph frondlet (Fig. 2A) raises the distinct possibility that these fronds, and probably other rangeomorphs, were capable of vegetative reproduction.

Jenkins (*25*) regarded the cosmopolitan Ediacaran frond *Charnia* as a rangeomorph, a view supported by our reports of a rangeomorph pattern within individual segments of *C. masoni* (*21*) and *C. wardi* (*15*) lower in the Mistaken Point succession. One specimen at Spaniard's Bay (Fig. 3D) shows a *Charnia*-like quilted pattern of curved major branches arranged in an alternate pattern about the midline that are divided at right angles into secondary branches, but this has been removed in places to reveal struts of an internal organic skeleton beneath the inflated branches. All rangeomorph taxa at the Spaniard's Bay locality show evidence of an internal, semi-rigid, organic skeleton on which the rangeomorph frondlets were suspended above the sea floor, an internal feature not previously reported from rangeomorphs or any other Ediacaran taxa.

Five specimens of a "plumose rangeomorph" also occur at Spaniard's Bay (Fig. 2, C and D). Their construction superficially resembles that of a garden leek, with a basal holdfast surrounded by layered sheets that extended upward in a plumose pattern. Each sheet consists of a vane-like pattern of rangeomorph frondlets, connected at their proximal ends, that pass off the midline at an acute angle. The rangeomorph frondlets in each sheet are oriented with their distal tips pointing out and toward the base of the fossil. Plumose rangeomorphs are oriented parallel to the fronds on the surface, implying that they were also tethered to the sea floor.

Three other rangeomorph constructions are present in the Mistaken Point assemblage at other localities and stratigraphic levels, and these serve to emphasize the importance and diversity of rangeomorphs in early Ediacaran ecosystems. Bush-shaped rangeomorphs (Fig. 3E) are broadly similar in structure to the plumose forms but are more complex three-dimensional constructions with larger frondlet sheets, a more rounded shape, and lack of an obvious attachment disc. Specimens are similar to *Bradgatia* from Avalonian strata in central England (*29*) but are smaller, with frondlets that are more crowded and less distinct. Well-preserved specimens of the previously enigmatic "comb-shaped fossils" (*22*) from Mistaken Point suggest that these consist of a row of identical rangeomorph frondlets connected by a basal stolon. Spindle-shaped rangeomorphs (Fig. 3F) exhibit a vane-like pattern of rangeomorph frondlets that pass off the midline at right angles in an opposite or alternate pattern to end at the outer margin of the specimen. Par-

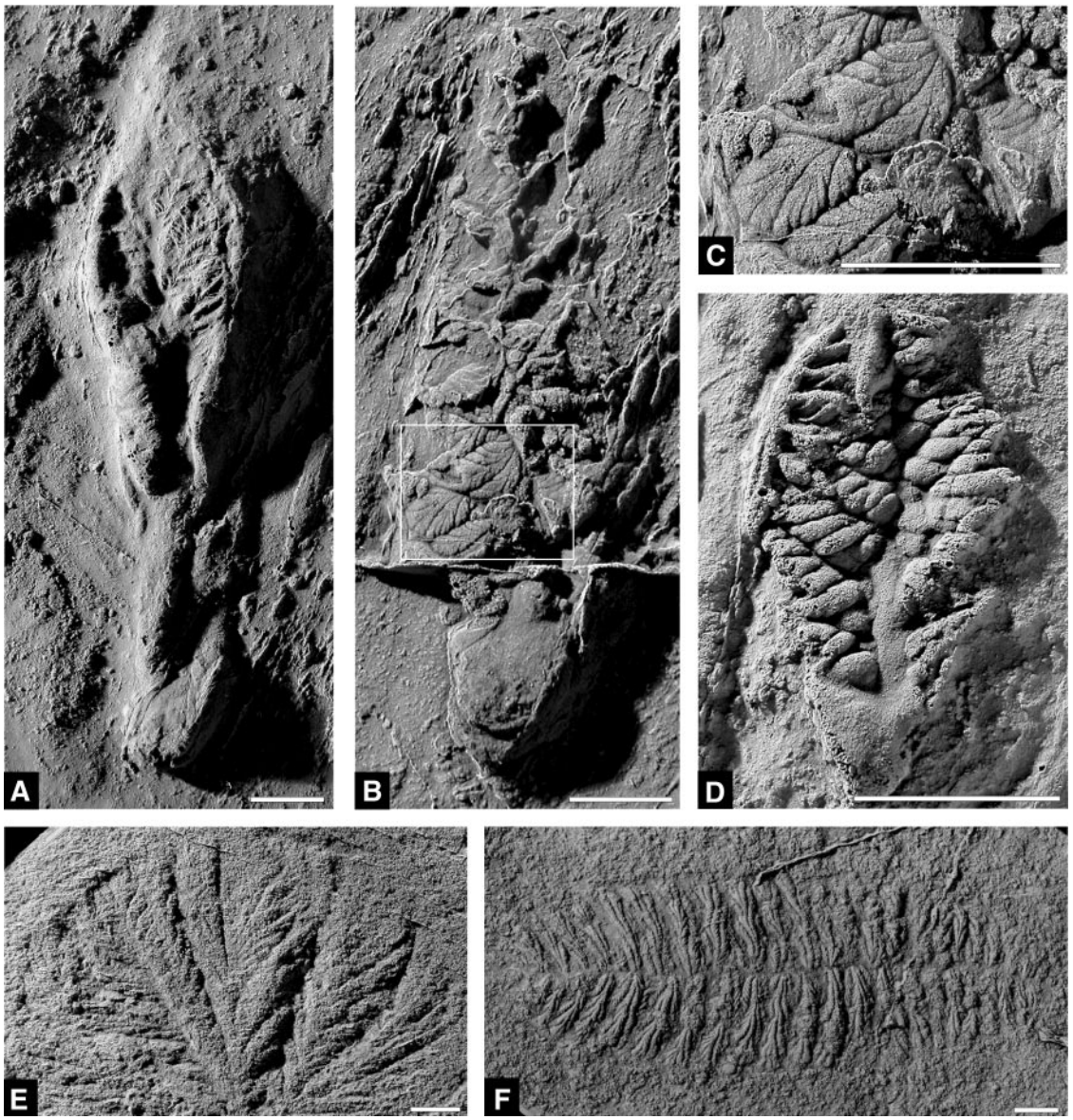

Fig. 3. Rangeomorph constructions from the Trepassey Formation at Spaniard's Bay (upper panels) and from the Mistaken Point Formation at Mistaken Point (lower panels). All specimens are latex molds whitened with ammonium chloride. (**A**) Long-stemmed rangeomorph frond with leaf composed of overlapping rangeomorph frondlets attached at their bases to the central stalk. Elements are partially deflated. (**B**) Short-stemmed rangeomorph frond with leaf composed of pendant rangeomorph frondlets hanging from a thin central stalk with side struts. (**C**) Enlarged view of the area indicated in (B). (**D**) *Charnia*-like frond with quilted array of major and minor branches overlying an internal organic skeleton. (**E**) Bush-shaped rangeomorph construction. (**F**) Spindle-shaped rangeomorph construction. Scale bars, 1 cm.

tially overturned specimens reveal that the other side of the specimen is identical (*12*). Crowding and fusion of adjacent rangeomorph frondlets in the spindles have caused them to become considerably elongated relative to the free-living rangeomorph frondlet, but their structure is otherwise indistinguishable. Spindle-shaped rangeomorphs were not aligned by currents (*19*, *20*) and probably functioned as recliners attached to the sea floor.

The morphologic features described above provide strong support for the view that rangeomorphs represent a single clade, a high-level taxon that went extinct in the terminal Proterozoic (*12*, *25*). It is probable that the Ediacara biota included stem groups for the Cambrian explosion of animals (*16*–*18*), but there are no obvious analogs for rangeomorph architecture and construction among modern taxa. Recent comparison of rangeomorph structure with the radial canals of fossil and recent ctenophores (*26*) seems remote from a morphological standpoint and is also inconsistent with the internal organic skeletons documented above. It would be tempting to regard the two-dimensional view of a rangeomorph frondlet as representing the bases of an array of open tubes that housed polyps or other filter-feeding organisms, but this is not consistent with partially overturned specimens that show that both sides are identical (Fig. 2D); the very small diameter of the secondary (300 to 600 μm) and tertiary (<150 μm) pneus would also specifically rule out cnidarian polyps as the originators of the tubes.

These modular constructions effectively partitioned food resources: Spindle-shaped rangeomorph recliners lay on the sea floor, whereas bush-, plume-, comb-, and frond-shaped rangeomorphs were elevated above the sea floor and fed from different levels within the water column (*7*). Rangeomorphs dominated the earliest Ediacaran ecosystems, with no evidence for burrowing, mobile, or metameric megascopic organisms among the taxa of the Mistaken Point assemblage. Rangeomorphs occur only sporadically in younger Ediacaran assemblages (*16*, *25*–*27*), perhaps as a result of competition with early animals, and have not been reported from any Phanerozoic assemblage including fossil Lagerstätten such as the Burgess Shale. It is difficult to relate rangeomorphs to any modern group of macroscopic organisms, and they appear to represent a "forgotten" architecture and construction that characterized early stages in the terminal Neoproterozoic evolution of complex multicellular life.

References and Notes

1. D. H. Erwin, J. Valentine, D. Jablonski, *Am. Sci.* **85**, 126 (1997).
2. G. M. Narbonne, *GSA Today* **8**, 1 (1998).
3. A. H. Knoll, *Life on a Young Planet: The First Three*

Billion Years of Evolution on Earth (Princeton Univ. Press, Princeton, NJ, 2003).
4. S. Xiao, Y. Zhang, A. H. Knoll, *Nature* **391**, 553 (1998).
5. M. A. Fedonkin, in *The Vendian System,* B. S. Sokolov, A. B. Iwanowski, Eds. (Springer-Verlag, Heidelberg, 1990), vol. 1, pp. 132–137.
6. R. J. F. Jenkins, *Precambrian Res.* **73**, 51 (1995).
7. M. E. Clapham, G. M. Narbonne, *Geology* **30**, 627 (2002).
8. M. E. Clapham, G. M. Narbonne, J. G. Gehling, *Paleobiology* **29**, 527 (2003).
9. T. D. Ford, *Proc. Yorks. Geol. Soc.* **31**, 211 (1958).
10. A. Yu. Zhuravlev, *Neues Jahrb. Geol. Palaeontol. Abh.* **190**, 299 (1993).
11. K. J. Peterson, B. M. Waggoner, J. W. Hagadorn, *Integr. Comp. Biol.* **43**, 127 (2003).
12. A. Seilacher, *J. Geol. Soc. (London)* **149**, 607 (1992).
13. M. W. Martin *et al.*, *Science* **288**, 841 (2000).
14. S. A. Bowring, P. M. Myrow, E. Landing, J. Ramenzani, *NASA Astrobiology Unit, General Meeting 2003*, Abstract 13045 (http://nai.arc.nasa.gov/institute/general_meeting_2003/AbstractBook.pdf).
15. G. M. Narbonne, J. G. Gehling, *Geology* **31**, 27 (2003).
16. J. G. Gehling, *Mem. Geol. Soc. India* **20**, 181 (1991).
17. J. G. Gehling, J. K. Rigby, *J. Paleontol.* **70**, 185 (1996).
18. M. A. Fedonkin, B. M. Waggoner, *Nature* **388**, 868 (1997).
19. A. Seilacher, *Palaios* **14**, 86 (1999).
20. D. A. Wood, R. W. Dalrymple, G. M. Narbonne, J. G. Gehling, M. E. Clapham, *Can. J. Earth Sci.* **40**, 1375 (2003).
21. G. M. Narbonne, R. W. Dalrymple, J. G. Gehling, *Geol. Assoc. Can. Field Guide B5* (2001).
22. S. B. Misra, *Geol. Soc. Am. Bull.* **80**, 2133 (1969).
23. M. M. Anderson, S. Conway Morris, *Proceedings of the Third North American Paleontological Convention* (Montreal, August 1982), vol. 1, part 1, pp. 1–8.
24. J. G. Gehling, *Palaios* **14**, 40 (1999).
25. R. J. F. Jenkins, *Paleobiology* **11**, 336 (1985).
26. J. Dzik, *J. Morphol.* **252**, 315 (2002).
27. D. Grazhdankin, *Paleobiology* **30**, 203 (2004).
28. Systematic paleontology will be presented elsewhere.
29. H. Boynton, T. D. Ford, *Mercian Geol.* **13**, 165 (1995).
30. Supported by a Natural Sciences and Engineering Research Council of Canada (NSERC) Discovery Grant. A. Daley, A. Ichaso, and R. W. Dalrymple contributed to the discovery and documentation of this fossil bed. C. Greentree, M. Mussa-Caleca, P. Pufahl, and M. Laflamme assisted with manuscript preparation. J. G. Gehling, R. W. Dalrymple, and M. Laflamme reviewed the manuscript.

28 April 2004; accepted 30 June 2004
Published online 15 July 2004;
10.1126/science.1099727
Include this information when citing this paper.

Intracellular Acidosis Enhances the Excitability of Working Muscle

Thomas H. Pedersen,[1] Ole B. Nielsen,[1] Graham D. Lamb,[2] D. George Stephenson[2]*

Intracellular acidification of skeletal muscles is commonly thought to contribute to muscle fatigue. However, intracellular acidosis also acts to preserve muscle excitability when muscles become depolarized, which occurs with working muscles. Here, we show that this process may be mediated by decreased chloride permeability, which enables action potentials to still be propagated along the internal network of tubules in a muscle fiber (the T system) despite muscle depolarization. These results implicate chloride ion channels in muscle function and emphasize that intracellular acidosis of muscle has protective effects during muscle fatigue.

Contraction in a twitch skeletal muscle fiber in response to a nerve impulse is the result of a complex series of events known as excitation-contraction-coupling (*1*) (ECC). ECC consists of (Fig. 1) (i) initiation and propagation of an action potential (AP) along the surface membrane and into the T system, (ii) activation of the voltage sensors (VSs) in the tubular wall, (iii) signal transmission to the sarcoplasmic reticulum (SR) from which the activator ion Ca^{2+} is released, and (iv) activation by Ca^{2+} of the Ca^{2+}-regulatory system associated with the contractile apparatus. Intense muscle activity leads to a decline in mechanical performance (power output, force, and velocity of shortening), which is generally known as muscle fatigue (*1–4*). Intracellular acidification of the working muscle associated with the production of lactic acid has been said to contribute to muscle fatigue (*2*). This is because intracellular acidification reduces the sensitivity of the contractile apparatus to Ca^{2+} and, under some circumstances, the maximum Ca^{2+}-activated force that is generated (*2*). However, the adverse actions of intracellular pH are not as great as originally thought (*5*, *6*). Another factor in muscle fatigue is reduced ability of the T system to conduct APs as a result of excitation-induced accumulation of K^+ in the T system (*3*, *4*). The accumulation of K^+ causes depolarization, which inactivates the

[1]Department of Physiology, University of Aarhus, DK-8000, Denmark. [2]Department of Zoology, La Trobe University, Bundoora, Melbourne, Victoria, 3086, Australia.

*To whom correspondence should be addressed. E-mail: G.Stephenson@zoo.latrobe.edu.au

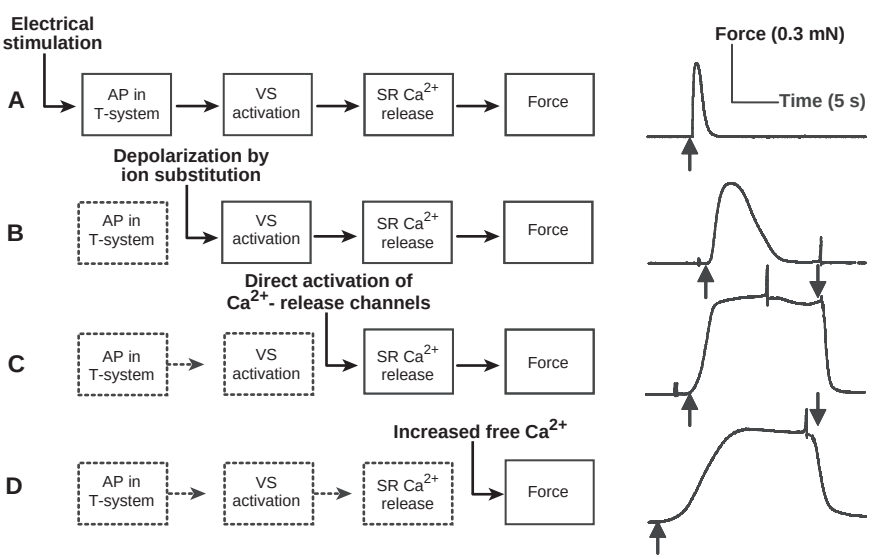

Fig. 1. Modes of activation of mechanically skinned muscle fibers. The force responses (right) were all obtained with the same preparation. Calibration bars for all force responses: vertical, 0.3 mN, and horizontal, 5 s. Upward-pointing arrows indicate time of activation and downward-pointing arrows indicate subsequent relaxation in a heavily buffered EGTA solution ($[Ca^{2+}] < 1$ nM). (**A**) Electrical stimulation initiates APs in the sealed T system. Shown is a tetanic contraction at 25 Hz stimulation with square pulses of 2-ms duration for 1s and field strength of 70 V/cm in a standard K-hexamethylene-diamine-tetraacetate (K-HDTA) solution with Cl^- (*10*, *11*, *21*). (**B**) Depolarization of the T system (by replacing all K^+ in the solution with Na^+) activates VSs independently of APs in the T system. The force response resulted from transfer of the preparation from a standard K-HDTA solution to depolarizing Na-HDTA solution (*5*). (**C**) Direct activation of SR Ca^{2+}-release channels, causing Ca^{2+} release from the SR, and force production when free $[Mg^{2+}]$ in the solutions was lowered from 1 mM to 0.015 mM (*5*). (**D**) Direct activation of the contractile apparatus in Ca^{2+}-buffered solutions (*5*, *10*, *11*, *21*). The preparation was transferred from the standard K-HDTA solution ($[Ca^{2+}] = 100$ nM) to heavily buffered Ca-EGTA solution ($[Ca^{2+}] = 30$ μM).

Na^+ channels responsible for the generation and propagation of APs (*3*, *7*). Unexpectedly, the loss of muscle excitability and force seen in depolarized muscles is greatly counteracted by intracellular acidification (*8*), although the underlying mechanism is not understood.

In this study, we used a muscle fiber preparation from the extensor digitorum longus (EDL) muscle of the rat in which the surface membrane is removed by microdissection, causing the T system to seal off and all steps in ECC to be maintained (*5*, *9*–*11*). This preparation allows direct access to the intracellular environment, thus permitting separate control of the intracellular pH and T system membrane potential. Such mechanically skinned muscle fibers can be activated at any individual step in the ECC process (i) by electrical stimulation that triggers APs in the T system (*10*, *11*), (ii) by direct activation of the VSs in the T system (*5*), (iii) by directly releasing Ca^{2+} from the SR (*5*), or (iv) by directly activating the contractile apparatus in Ca^{2+}-buffered solutions (*5*, *10*) (Fig. 1). Thus, it is possible to determine the separate and the combined effects of T system depolarization and intracellular acidification on T system excitability (that is, generation and propagation of APs in the T system) and to assess likely effects on muscle fatigue.

If the potential across the T system is reduced for a sustained period, a proportion of the VSs become dysfunctional (inactivated). This was achieved here by equilibrating the skinned fibers in solutions with decreased myoplasmic (intracellular) K^+ concentration ($[K^+]_i$) at constant $[K^+]_i[Cl^-]_i$ product ($[Cl^-]_i$ is the concentration of Cl^-) (*12*). The remaining (noninactivated) VSs were then activated by fully depolarizing the T system with application of a solution with all K^+ removed (Fig. 2A). The force responses to full depolarization were then plotted against the $[K^+]_i$ in the various equilibration solutions to show the inactivation behavior of the VSs. Because the inactivation curves of the VSs (Fig. 2B) at pH = 6.6 and pH = 7.1 were virtually the same, we conclude that the ECC steps starting from VS activation up to the activation of the contractile apparatus (Fig. 1) are largely unaffected by intracellular acidification. This is consistent with inactivation of VSs being unaffected by intracellular acidosis (*13*). The overlap of the two curves in Fig. 2B also confirms that the membrane potential across the T system at any given $[K^+]_i$ was essentially the same at pH values of 7.1 and 6.6. The values of membrane potential for the various $[K^+]_i$ were calculated from the Goldman-Hodgkin-Katz equation (*14*), assuming 4 mM for K^+ and 150 mM for Na^+ in the lumen of the sealed T system, relative permeability for K^+ as compared to Na^+ of 100:1, and passive distribution of Cl^- across the T system. In contrast, force responses to APs in the T system elicited by electrical stimulation (*10*, *11*) did display pH dependence (Fig. 2, C and D) (preparations were tetanically stimulated at 25 Hz at pH = 7.1 and at pH = 6.6). When the T system was moderately depolarized at $[K^+]_i$ values of 75 and 60 mM, there was a significantly greater loss of tetanic force at pH = 7.1 than at pH = 6.6 ($P < 0.05$, $n = 10$). The loss in force response with AP stimulation occurred at more negative potentials than did VS inactivation (compare Fig. 2D with Fig. 2B), showing that the force loss was due predominantly to AP failure rather than inadequate VS activation. These results indicate that intracellular acidosis protects against the loss of force caused by depolarization when activation is initiated by APs, as occurs in vivo, and

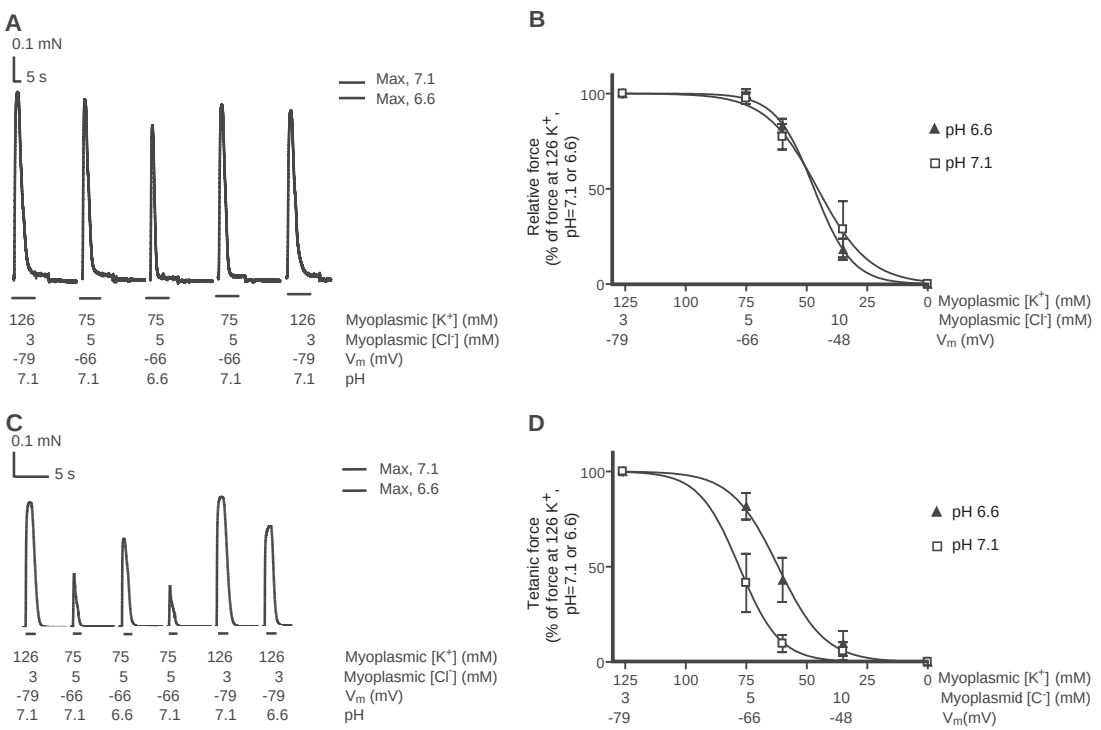

Fig. 2. Effect of pH and T system depolarization on force responses induced by direct VS activation (**A** and **B**) or tetanic stimulation at 25 Hz (**C** and **D**) in the presence of Cl^- in mechanically skinned fibers at 25° ± 2°C. EDL muscles of rats [Long Evans Hooded, 6-month-old males, killed by halothane overdose (*5*)] were placed in paraffin oil and skinned fibers were prepared as described (*5*, *10*, *11*, *21*) . Fibers were attached to a sensitive force transducer and bathed in solutions mimicking the myoplasmic environment (*5*, *10*, *11*, *21*). The K-HDTA standard solution at pH = 7.10 contained 126 mM K^+, 17 mM methylsulfate, 3 mM Cl^-, 40 mM Na^+, 40 mM $HDTA^{2-}$, 1 mM Mg^{2+} (free), 8 mM adenosine triphosphate, 10 mM creatine phosphate, 90 mM Hepes buffer, 0.05 mM Bapta [(1,2-bis*0*-aminophenoxy)ethane-*N*,*N*,*N*′,*N*′-tetraacetic acid], and 100 nM Ca^{2+}. The K-HDTA standard solution at pH = 6.60 was identical to the K-HDTA solution at pH = 7.10 with respect to all ions except that it contained 9 mM Pipes and Hepes was reduced to 80 mM to maintain osmotic balance (295 ± 2 mmol/kg). In solutions with decreased $[K^+]_i$, K^+ was replaced with NH_4^+ and methylsulfate with Cl^- to maintain constant $[K^+]_i[Cl^-]_i$ product. (A and C) Representative force traces from two individual fibers. Bars under traces represent the duration of stimulation [ion substitution for (A) and 25-Hz tetanic stimulation for (C)]. The voltage sensor–activated force response at pH = 6.6 (75 mM K^+) is only slightly smaller than the corresponding response at pH = 7.1, with the difference entirely due to the decrease in maximum Ca^{2+}-activated force at pH = 6.6, which was smaller by 19 ± 9% ($n = 49$) compared with that at pH = 7.1. The horizontal lines in (A) and (C) indicate the maximum Ca^{2+}-activated force generated at pH = 7.1 and pH = 6.6 in buffered Ca-EGTA solutions ($[Ca^{2+}] = 30$ μM) in which $HDTA^{2-}$ was replaced by $Ca\text{-}EGTA^{2-}$. Calibration bars: vertical, 0.1 mN, and horizontal, 5 s. Membrane potential in the various $[K^+]_i$ solutions was calculated from the Goldman-Hodgkin-Katz equation (*14*). For each data point *n* was from 5 to 8.

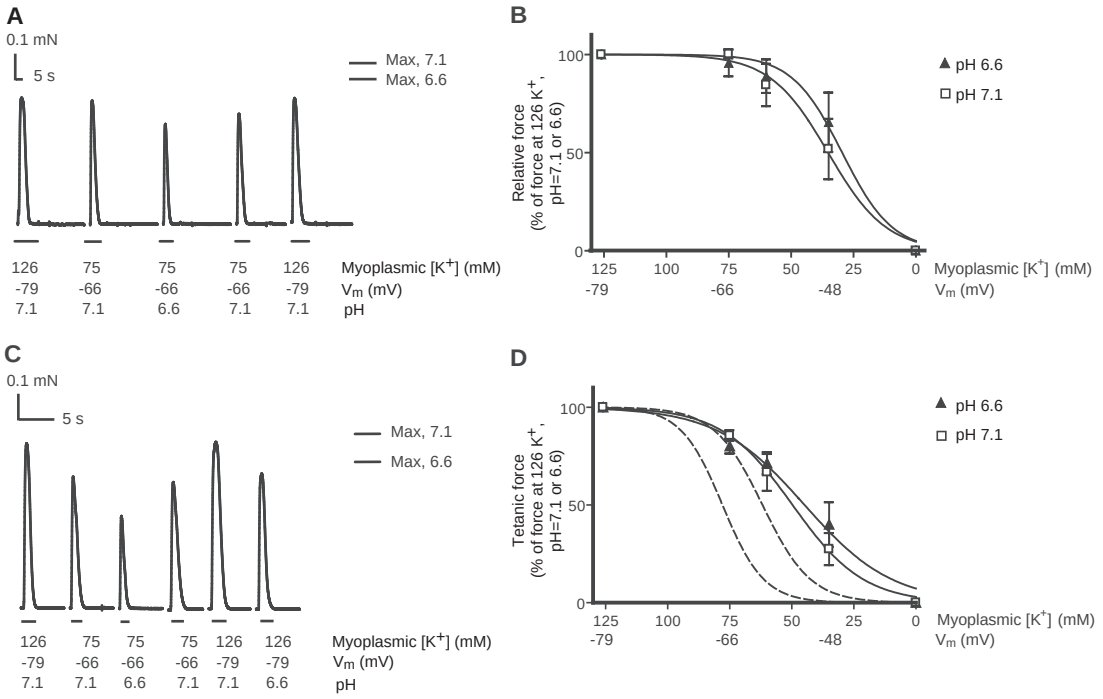

Fig. 3. Effect of pH and T system depolarization on force responses at 25° ± 2°C induced by direct VS activation (**A** and **B**) or tetanic stimulation at 25 Hz (**C** and **D**) in the absence of Cl^-. Before skinning, the muscles were equilibrated for 30 min in Cl^--free Ringer's solution containing 65 mM Hepes, 1.2 mM Ca^{2+}, 115 mM sodium methylsulfate, 4 mM K^+, 1.2 mM phosphate, and 5 mM glucose. NaOH was used to bring pH to 7.4. All intracellular solutions had the same composition as the solutions described in the legend of Fig. 2 except Cl^- was replaced with methylsulfate. Membrane potential in the various $[K^+]_i$ solutions was calculated as described (Fig. 2). (A and C) Representative force traces from two individual fibers. Bars under traces represent the duration of stimulation. (C) The horizontal lines indicate the maximum Ca^{2+}-activated force at pH values of 7.1 and 6.6 in heavily buffered Ca-EGTA solutions (Fig. 2). Calibration bars: vertical 0.1 mN, horizontal 5 s. The broken lines shown in (D) represent the curves from Fig. 2D.

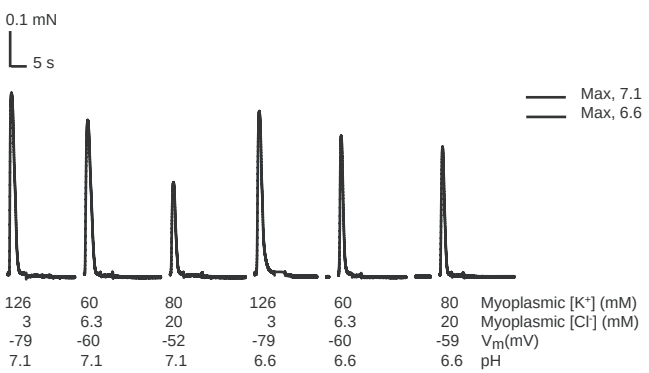

Fig. 4. Effect of pH on Cl^- permeability in the T system. Representative VS activated force responses in a mechanically skinned fiber equilibrated in solutions of different $[K^+]_i$ and $[Cl^-]_i$ at pH values of 7.1 and 6.6. Calibration bars: vertical, 0.1 mN; horizontal, 5 s. At constant $[K^+]_i[Cl]_i$ product, the membrane potentials were calculated as described in text, and at 80 K^+ and 20 Cl^- the membrane potential was estimated from Fig. 2B.

indicate that this protective effect may be due to enhanced excitability of the T system.

In rested muscle, Cl^- is the most membrane-permeant ion (*15*–*18*). The high membrane permeability to Cl^- at normal pH stabilizes the resting membrane potential, but the cost of this is that a comparatively large inward Na^+ current is needed to sustain a propagating AP (*16*, *18*). Because lowering pH reduces Cl^- conductance (*19*, *20*), we examined whether Cl^- plays a role in the protective effect of acidity. When experiments like those in Fig. 2, A to D, were repeated without Cl^- in the myoplasm and T system, the inactivation curve for tetanic stimulation at pH = 6.6 was no different from that at pH = 7.1 (Fig. 3, C and D). Compared with the inactivation curves in the presence of C1 (indicated with broken lines in Fig. 3D), both inactivation curves were shifted to the right (to lower $[K^+]_i$ and greater depolarization) but with a greater shift at pH = 7.1 than at pH = 6.6 (Fig. 3D). Thus, the pH effect seen in Fig. 2D is associated with the presence of Cl^-.

To evaluate whether intracellular acidosis decreases the Cl^- permeability of the T system, we did an experiment in which preparations were activated by ion substitution after equilibration in a solution with 80 mM K^+ and 20 mM Cl^-, which is about four times the $[Cl^-]_i$ needed to keep the $[K^+]_i[Cl^-]_i$ constant (Fig. 4). Under these conditions, Cl^- will tend to depolarize the T system more than the reduction in K^+ concentration would, and a high Cl^- permeability would therefore increase the level of chronic depolarization. Consequently the force response to maximal VS activation was expected to be reduced. The drop in force at 80 mM K^+ and 20 mM Cl^- was larger at pH = 7.1 than at pH = 6.6. From the inactivation curves in Fig. 2B, the membrane potential of the T system at 80 mM K^+ and 20 mM Cl^- was estimated to be –52 mV at pH = 7.1 and –59 mV at pH = 6.6 (*n* from 7 to 10). On the basis of the Goldman-Hodgkin-Katz equation, this change in membrane potential showed that the permeability of Cl^- in the T system was reduced by around 74% at pH = 6.6 compared to that at pH = 7.1. The fact that at pH = 6.6 the T system Cl^- permeability was not completely abolished may explain why the inactivation curve for tetanic stimulation at pH = 6.6 was not shifted as much as the inactivation curves were when Cl^- was totally removed (Fig. 3D).

We find that, in the presence of Cl^-, intracellular acidosis increases the excitability of the T system in depolarized muscles fibers, thus counteracting fatigue at a critical step in ECC. In this model of working muscle, acidic pH reduced Cl^- permeability, thereby reducing the size of the Na^+ current needed to generate a propagating AP. Thus, down-regulation of T system Cl^- permeability by intracellular acidosis is important for preserving a fully operational T system in working muscle.

References and Notes

1. D. G. Stephenson, G. D. Lamb, G. M. Stephenson, *Acta Physiol. Scand.* **162**, 229 (1998).
2. R. H. Fitts, *Physiol. Rev.* **74**, 49 (1994).
3. G. Sjøgaard, *Acta Physiol. Scand. Suppl.* **593**, 1 (1990).
4. O. M. Sejersted, G. Sjøgaard, *Physiol. Rev.* **80**, 1411 (2000).
5. G. D. Lamb, D. G. Stephenson, *J. Physiol.* **478**, 331 (1994).
6. H. Westerblad, D. G. Allen, J. Lännergren, *News Physiol. Sci.* **17**, 17 (2002).
7. R. L. Ruff, *Acta Physiol. Scand.* **156**, 159 (1996).

8. O. B. Nielsen, F. de Paoli, K. Overgaard, *J. Physiol.* **536**, 161 (2001).
9. B. S. Launikonis, D. G. Stephenson, *J. Gen. Physiol.* **123**, 231 (2004).
10. G. S. Posterino, G. D. Lamb, D. G. Stephenson, *J. Physiol.* **527**, 131 (2000).
11. G. S. Posterino, T. L. Dutka, G. D. Lamb, *Pflugers Arch.* **442**, 197 (2001).
12. A. L. Hodgkin, P. Horowitz, *J. Physiol.* **148**, 127 (1959).
13. E. M. Balog, R. H. Fitts, *J. Appl. Physiol.* **90**, 228 (2001).
14. B. Hille, *Ion Channels of Excitable Membranes* (Sinauer, Sunderland, MA, ed. 3, 2001).
15. A. F. Dulhunty, *J. Membr. Biol.* **45**, 293 (1979).
16. A. H. Bretag, *Physiol. Rev.* **67**, 618 (1987).
17. J. R. Coonan, G. D. Lamb, *J. Physiol.* **509**, 551 (1998).
18. T. J. Jentsch, V. Stein, F. Weinreich, A. A. Zdebik, *Physiol. Rev.* **82**, 503 (2002).
19. O. F. Hutter, A. E. Warner, *J. Physiol.* **189**, 403 (1967).
20. P. T. Palade, R. L. Barchi, *J. Gen. Physiol.* **69**, 325 (1977).
21. N. Ørtenblad, D. G. Stephenson, *J. Physiol.* **548**, 139 (2003).
22. This research was supported by the Danish Medical Research Council (22-02-0188), University of Aarhus, Australian Research Council, and National Health and Medical Research Council of Australia.

7 June 2004; accepted 27 July 2004

Local Nanomechanical Motion of the Cell Wall of *Saccharomyces cerevisiae*

Andrew E. Pelling, Sadaf Sehati, Edith B. Gralla, Joan S. Valentine, James K. Gimzewski*

We demonstrate that the cell wall of living *Saccharomyces cerevisiae* (baker's yeast) exhibits local temperature-dependent nanomechanical motion at characteristic frequencies. The periodic motions in the range of 0.8 to 1.6 kHz with amplitudes of ~3 nm were measured using the cantilever of an atomic force microscope (AFM). Exposure of the cells to a metabolic inhibitor causes the periodic motion to cease. From the strong frequency dependence on temperature, we derive an activation energy of 58 kJ/mol, which is consistent with the cell's metabolism involving molecular motors such as kinesin, dynein, and myosin. The magnitude of the forces observed (~10 nN) suggests concerted nanomechanical activity is operative in the cell.

Many biological processes taking place inside the living cell rely on the nanomechanical properties of cellular substructures and the cell membrane or wall itself. The atomic force microscope (AFM) (*1*) yields information on the integrity and local nanomechanical properties of mammalian and microbial cellular membranes under normal and stressed metabolic conditions (*2*–*11*). The sensitivity and ability to apply only minimal forces on a cell makes the AFM a useful nondestructive tool to study cellular nanomechanics. AFM has also been used to measure the natural beating motion in the 0.05 to 0.4 Hz range of cardiomyocytes (heart cells), which is a property related to the cell's physiology (*3*, *12*). In a low-noise environment, the AFM has the sensitivity to measure local nanoscale motion of cells. Here, we have used this capability to discover distinct periodic nanomechanical motion of yeast cells, which we relate to metabolic processes within the cell.

In a typical image of a dense layer of yeast cells air dried onto a mica surface (Fig. 1), yeast

Department of Chemistry and Biochemistry, University of California, Los Angeles, 607 Charles E. Young Drive East, Los Angeles, CA 90095, USA.

*To whom correspondence should be addressed. E-mail: gim@chem.ucla.edu.

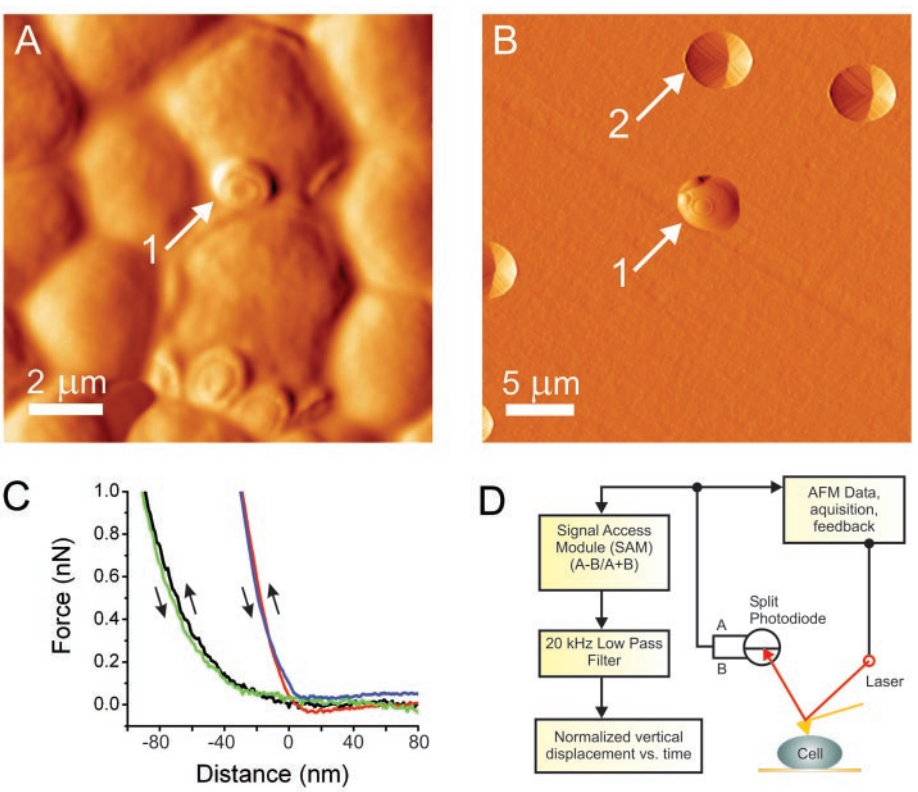

Fig. 1. Typical deflection mode images of yeast cells are shown in (**A** and **B**) [the color scale bar in (A) corresponds to deflections between 0 to 320 nm and 0 to 120 nm in (B)]. A dense layer of yeast cells dried onto mica and imaged in air is shown in (A). Yeast cells are about 5 μm in diameter and often have bud scars on the cell surface (arrow 1). Mechanical trapping is used to study live cells in YPD medium at 30°C. In (B), a typical image of a living yeast cell (arrow 1) trapped in a 5-μm filter pore is shown [empty pores (arrow 2) are easily distinguishable from trapped cells in the image]. Force-distance curves (**C**) can be obtained by monitoring the deflection of the cantilever as it is extended (up arrow) and retracted (down arrow) from the cell in order to measure the local cellular nanomechanical properties. The zero point on the displacement scale represents the point where the AFM tip first comes into contact with the cell. A force-distance curve on the cell body (black line, extension; and green line, retraction) and the bud scar (blue line, extension; and red line, retraction) are shown. Local nanomechanical spring constants (k_{cell}) can be determined from the slope of the linear portion of the curves. Bud scars always display higher k_{cell} because of the increased chitin content of the area (*8*). A schematic of the experimental setup (**D**) outlines the process of measuring the local nanomechanical motion of the cell wall. The AFM cantilever is positioned on top of a living cell, and the scan size is set to 0 nm. The deflection of the cantilever is measured with a photodiode. The signal is acquired with a breakout box (SAM, signal access module), low-pass filtered (20 kHz), and sampled using another computer at 40 kHz.

cells are approximately round and have a diameter of about 2 to 10 μm on average. The disk-shaped protrusion on the cell surface, clearly visible in Fig. 1A, is a bud scar. This structure forms on the cell after the process of division has taken place. Round microbial cells, such as yeast, are quite difficult to immobilize on a surface in liquid so they can be kept alive in order to be studied with the AFM. To circumvent this problem, a technique known as mechanical trapping is used to study single, living round-shaped microbial cells in AFM experiments without the use of chemical immobilizers under physiological conditions in fluid (*8*, *13*, *14*). Cells were first cultured and suspended in yeast extract, peptone, and dextrose (YPD) medium, by using standard techniques (*14*) and were studied at the end of log phase (*15*), which is when the cells are not dividing rapidly and are moving into stationary phase. The suspension was filtered through a polycarbonate membrane, whose ~5-μm pores act as mechanical traps for the cells. The filter was then attached to a petri dish, immediately covered with YPD medium, transferred to the AFM, and left to thermally equilibrate for 1 hour (*14*).

After initial AFM scans of the surface (Fig. 1B), individual cells were selected for force-distance curves to determine the contact force, which was minimized to less than 1 nN. Cantilevers with very low experimentally determined spring constants, k, were used to minimize damage to the cell wall [0.05 ± 0.01 N/m (*16*)]. The local spring constant of the cell wall (k_{cell}) was determined from the slope of the linear portion of the force-distance curve (*17*), which was similar to or slightly larger than that of the cantilever (Fig. 1C). Cell bodies have local k_{cell} of 0.06 ± 0.025 N/m (n = 15). Note that spring constants measured in the same manner on mammalian cells are invariably much lower (~0.002 N/m) (*17*). Yeast cells have a thick cell wall, which accounts for their high local stiffness (*8*). The observed variability in local k_{cell} has been attributed to the heterogeneous chemical makeup of the cell wall and the local nanomechanical properties at the time of measurement (*8*). The cantilever and cell wall can be considered as two springs in series (*14*). Given the cell's local stiffness, we can accurately measure the natural motion of the cell wall. Nanomechanical motion of the cell was observed by recording the cantilever motion (*3*, *7*, *12*) (Fig. 1D), while in contact with the cell, as a function of time in an acoustically isolated environment with a root mean square (rms) noise level of 0.06 nm. We examined nanomechanical motion between 22° and 30°C, using a controllable temperature stage (*14*).

The motion of the cell body of a typical yeast cell recorded at a temperature of 30°C is shown by several examples in Fig. 2. The signal observed is clearly oscillatory with average amplitude of 3.0 ± 0.5 nm (Fig. 2, A to E). The motion was typical for ~70% of the observation times at all temperatures (over 100 experiments were performed over a course of a year, on different individual cells and cell cultures). Occasionally the amplitude would be observed to go as high as 7 nm (Fig. 2F) or to drop as low as 1 nm (Fig. 2G). Fourier transforming the recorded motion revealed a characteristic frequency with a prominent peak at ~1.6 kHz (Fig. 3A). The observed frequencies at any given temperature were similar to within 5% on different cells in one experiment or on different runs with fresh samples of cells.

The results suggest that one of two principal mechanisms is responsible for the observed mechanical oscillations. The motion may be due to an active metabolic process or mechanical resonances and/or Brownian motion. We can differentiate these mechanisms by treating the cells with sodium azide (NaN_3), which is a

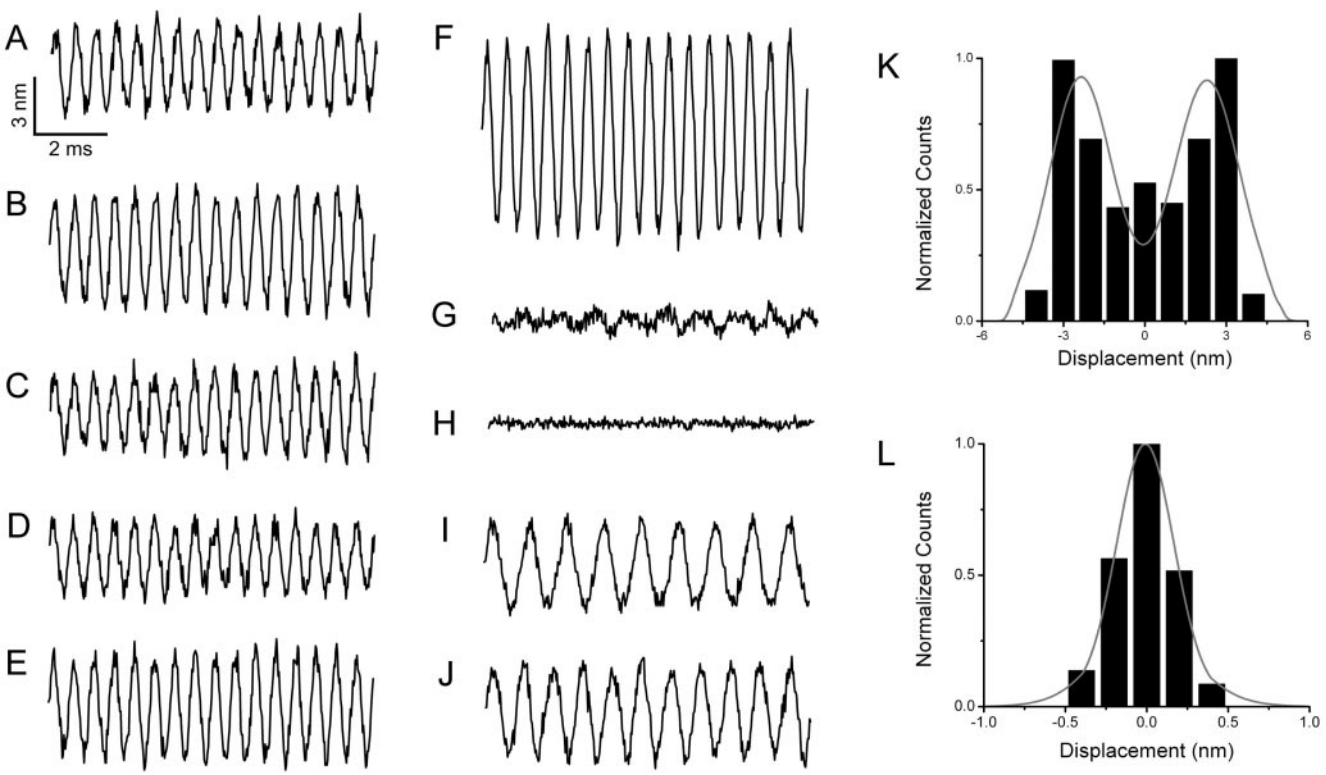

Fig. 2. Typical time traces of the motion of the cell wall of living yeast. All data shown are representative of more than 100 individual experiments carried out on different cells from different cell cultures. The data in (A to G) are from one single cell and data in (H to J) are measurements on different individual cells on different days. In most experimental runs (~70%), the amplitude of the motion was ~3 nm at 30°C (**A** to **D**) but is also consistent at other temperatures as well. Occasionally, amplitudes as large as 7 nm (**F**) and as small as 1 nm (**G**) were observed. In both extremes, the motion is clearly still oscillatory. When cells were maintained at 22°C (**I**) and 26°C (**J**), the amplitudes were similar, but the frequency decreased (see also Fig. 3). Exposure of the cells to sodium azide for 1 hour (*14*) caused the motion to cease (**H**). Living cells displayed a bimodal distribution of amplitudes [**K**, determined from the data in (A)] whereas cells treated with sodium azide always had a Gaussian distribution [**L**, determined from the data in (H)]. Gray lines are Gaussian fits to the data shown in (K and L).

well-known metabolic inhibitor that switches off ATP production in the mitochondria (*18*). Sodium azide is known not to change the mechanical properties of the cell wall, which we verified by measuring the local Young's modulus of the cell wall before and after exposure to the inhibitor (*14*). Likewise, AFM imaging indicated that the cells did not display any significant morphological changes from living cells. The motion observed in azide-treated cells clearly did not display oscillatory behavior and had an average amplitude of 0.4 ± 0.2 nm (Fig. 2H) with a Gaussian distribution of amplitudes whereas living cells always displayed a bimodal distribution (Fig. 2, K and L). Also, no specific frequency components were seen in the Fourier transform (Fig. 3D).

Nanomechanical oscillatory motion was observed to change in a systematic manner, with the frequency increasing significantly with temperature from 0.9 kHz (22°C) to 1.6 kHz (30°C) (Fig. 3); the average amplitude of the motion was similar (Fig. 2, I and J). The strong frequency dependence on temperature and metabolic state indicates that the nanomechanical motion is biologically driven and requires ATP.

An extensive series of control experiments was performed to exclude any contributions of possible artifacts from the AFM itself to the mechanical motion (*14*). No contact resonances between the AFM tip and the surface were observed when the tip was on hard or soft surfaces. Likewise, the mechanical resonance of the AFM cantilever was determined from a Fourier transform of the measured thermal fluctuations of the free cantilever in fluid at 30°C. The cantilevers used had a free resonance of 3.7 ± 0.3 kHz in fluid, far above the frequencies of the observed oscillations. Other resonances we considered were the *x*, *y*, and *z* modes of the piezoelectric tube scanner (2.3 kHz and 4.5 kHz, respectively), which were also out of the range of the frequencies of the cells.

In terms of mechanical resonances, the Young's modulus (E) is approximately proportional to the square of the resonant frequency (ω) (*19*). A measurement of the local Young's modulus of the yeast cell wall at all three temperatures also clearly showed that the average stiffness of the wall (0.72 ± 0.06 MPa at 22°C, 0.75 ± 0.04 MPa at 26°C, and 0.75 ± 0.06 MPa at 30°C) does not follow the expected trend for a mechanical resonator ($E \propto \omega^2$). The mechanical properties of the cell wall also did not change significantly after treatment with sodium azide (0.74 ± 0.05 MPa).

The above results clearly show that the changes in frequencies cannot be ascribed to mechanical resonances of the cell or small parasitic resonances in the AFM system. The observed temperature-dependent frequency shifts and disappearance of any oscillatory motion when the cells are exposed to sodium azide provide compelling evidence that the motion has metabolic origins.

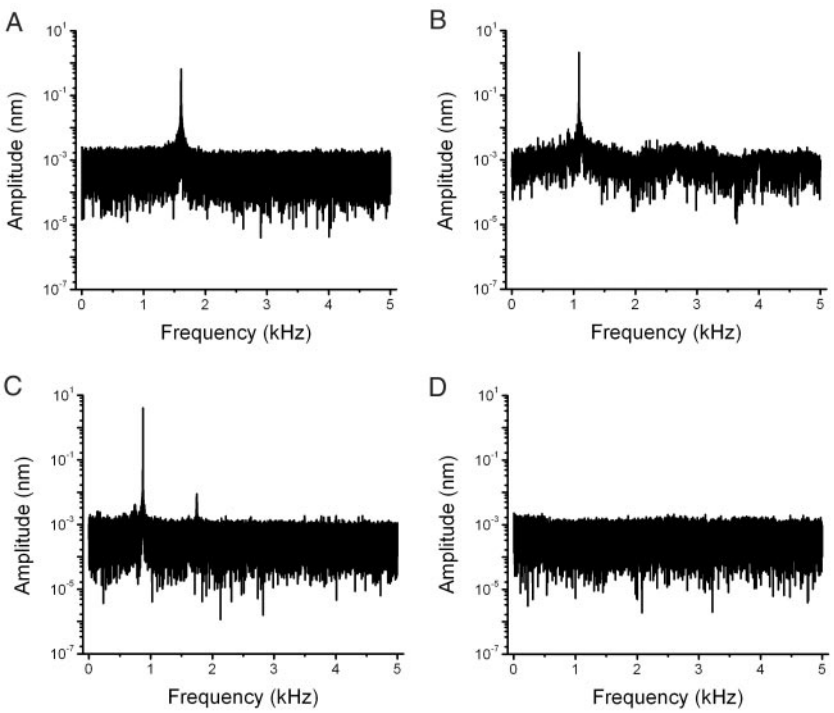

Fig. 3. Fourier transforms of the motion observed in Fig. 2 (note the amplitude is plotted on a logarithmic scale). Each spectrum is from different individual cells at each temperature but is reproducible to within 5% and is representative of many individual measurements. The Fourier transform of the motion at 30°C reveals a prominent peak at 1.634 kHz (**A**). At 26°C at frequency of 1.092 kHz (**B**) is observed and at 22°C a frequency of 0.873 kHz (**C**). Exposure of the cells to sodium azide causes the motion to cease, and no significant frequencies are observed in the Fourier transform (**D**).

This was confirmed from an expected temperature dependence of frequency (ν) that follows a straight line when plotted in an Arrhenius relation, $\ln[\nu]$ versus $1/T$. From the slope of the data, we determine an activation energy (E_a) of 58.15 ± 6.57 kJ mol^{-1} (Fig. 4). This value is consistent with the activation energies required to drive molecular motors such as myosin, kinesin and dynein, which occur in the range of 50 to 100 kJ mol^{-1} (*20*, *21*). These motor proteins exhibit dynamic behavior both inside and at the cell wall of yeast (*18*, *22*). Agreement in the value of the activation energies prompted us to compare our measured frequency with known values of linear velocity for motor proteins.

A calculated linear velocity can be determined by multiplying the observed frequencies by the amplitude of oscillation (~3.0 nm). This provides an indication of the operating speeds required for the proteins [2.6 to 4.9 μm s^{-1}, (*14*)]. Operating speeds of 0.2 to 8 μm s^{-1} for the myosins and 0.02 to 7 μm s^{-1} for the microtubule proteins kinesin and dynein (*23*) have been reported, which are comparable with operating speeds estimated from our nanomechanical measurements. Notably, many processes taking place inside the cell that are mediated by these proteins have been reported with operating speeds 1 to 2 orders of magnitude faster than the individual motor proteins (*23*). The force being generated at the cell wall can be determined by multiplying k_{cell} by the average amplitude of 3 nm, which yields a value of 0.2 nN. However, to determine the active force, we increased the contact force

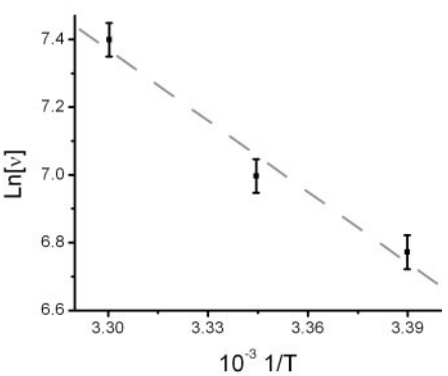

Fig. 4. Arrhenius plots can be constructed for temperature-dependent quantities such as the nanomechanical motion observed in this study. Generally, a temperature-dependent quantity (ν) will follow the relationship $\nu = \nu_0 \exp(-E_a/RT)$, where E_a is the activation energy, R is the universal gas constant, T is the temperature, and ν_0 the preexponential factor. The equation can be rearranged to take the form of a line where E_a can be determined from the slope: $\ln \nu = \ln \nu_0 - (E_a/RT)$. By plotting the natural logarithm of the frequency (in Hz) (data from Fig. 3, A to C) versus the temperature (1/Kelvin), we determine an E_a of 58.15 ± 6.57 kJ mol^{-1} from the slope of a weighted linear regression fit of the data (dashed line).

from the AFM cantilever on the cell until we noted a change in the amplitude of the motion, which occurred at ~10 nN (*14*). We can exclude that a single motor protein is driving the observed nanomechanical motion, because the forces observed at the cell wall (~10 nN) are far too large in magnitude. This may imply that large-scale forces are generated in yeast cells through the action of many proteins working in a concerted and cooperative manner.

Such cooperativity is known to occur during cell motility and muscle contraction. Spontaneous driven oscillations have been reported in a variety of cells [muscle cells, auditory cells, and structures such as flagella and cilia (*24*–*26*)], when molecular motors are elastically coupled to their environment by a microtubule or filament. For instance, these oscillations have been experimentally measured between about 1 Hz (muscle fibers) and 300 Hz (flagella) (*27*, *28*). Coupled molecular motors have also been theoretically predicted to be able to achieve frequencies as high as 10 kHz (*24*). These examples of biological processes involving concerted motor protein action lend strong support to our conclusion that a metabolically driven nanomechanical process occurs at the yeast cell wall. This process cannot be observed by traditional cytological methods and occurs in cells in their natural state.

Probing the nanomechanical motion of cell walls is not invasive and does not depend on the use of chemical dyes, fluorescent markers, or quantum dots. The speed of the motion, its response to metabolic inhibitors, and the Arrhenius temperature dependence are completely consistent with active metabolic processes driving the nanomechanical motion. The forces exerted are strongly suggestive of the concerted action of molecular motor proteins. The observed motion may be part of a communication pathway or pumping mechanism by which the yeast cell supplements the passive diffusion of nutrients and/or drives transport of chemicals across the cell wall. The current experiments were performed on yeast cells because they have a stiff cell wall. Extension of this experiment to mammalian cells will require the use of specially fabricated cantilevers with small spring constants comparable to the spring constant of the mammalian cell membrane (~0.002 N/m). Our experiments reveal a new aspect of yeast cell biology—the dynamic nanomechanical activity of the cell wall.

References and Notes

1. G. Binning, C. F. Quate, C. Gerber, *Phys. Rev. Lett.* **56**, 930 (1986).
2. E. A-Hassan *et al*., *Biophys. J.* **74**, 1564 (1998).
3. J. Domke, W. J. Parak, M. George, H. E. Gaub, M. Radmacher, *Eur. Biophys. J.* **28**, 179 (1999).
4. P. Zhang, A. M. Keleshian, F. Sachs, *Nature* **413**, 428 (2001).
5. C. Rotsch, F. Brate, E. Wisse, M. Radmacher, *Cell Biol. Int.* **21**, 685 (1997).
6. G. T. Charras, M. A. Horton, *Biophys. J.* **82**, 2970 (2002).
7. B. Szabó, D. Selmeczi, Z. Környei, E. Madarász, N. Rozlosnik, *Phys. Rev. E.* **65**, 041910 (2002).
8. A. Touhami, B. Nysten, Y. F. Dufrene, *Langmuir* **19**, 4539 (2003).
9. M. Arnoldi *et al*., *Phys. Rev. E.* **62**, 1034 (2000).
10. W. R. Bowen, R. W. Lovitt, C. J. Wright, *J. Colloid Interface Sci.* **237**, 54 (2001).
11. M. Gad, A. Itoh, A. Ikai, *Cell Biol. Int.* **21**, 697 (1997).
12. G. N. Maksym *et al*., *J. Appl. Physiol.* **89**, 1619 (2000).
13. S. Kasas, A. Ikai, *Biophys. J.* **68**, 1678 (1995).
14. Materials and methods are available as supporting material on *Science* Online.
15. M. Johnston, M. Calson, *The Molecular Biology of the Yeast* Saccharomyes*: Gene Expression* (Cold Spring Harbor Laboratory Press, Cold Spring Harbor, NY, 1992).
16. R. Levy, M. Maaloum, *Nanotechnology* **13**, 33 (2003).
17. J. H. Hoh, C. Schoenenberger, *J. Cell Sci.* **107**, 1105 (1994).
18. T. Doyle, D. Botstein, *Proc. Natl. Acad. Sci. U.S.A.* **93**, 3886 (1996).
19. C. M. Harris, *Shock and Vibration Handbook* (McGraw-Hill Book Company, New York, 1988).
20. K. Kawaguchi, S. Ishiwata, *Biochem. Biophys. Res. Comm.* **272**, 895 (2000).
21. K. Kawaguchi, S. Ishiwata, *Cell Motil. Cytoskel.* **49**, 41 (2001).
22. D. Ding, Y. Chikashige, T. Haraguchi, Y. Hiraoka, *J. Cell Sci.* **111**, 701 (1998).
23. J. Howard, *Nature* **389**, 561 (1997).
24. F. Jülicher, *C. R. Acad. Sci. (Paris) Ser. IV* **6**, 849 (2001).
25. A. Vilfan, T. Duke, *Phys. Rev. Lett.* **91**, 114101 (2003).
26. F. Jülicher, J. Prost, *Phys. Rev. Lett.* **78**, 4510 (1997).
27. K. Yasuda, Y. Shindo, S. Ishiwata, *Biophys. J.* **70**, 1823 (1996).
28. S. Kamimura, R. Kamiya, *Nature* **340**, 476 (1989).

29. A.E.P. and J.K.G. gratefully acknowledge C. Ventura (University of Sassari, Italy), M. A. Teitell (University of California, Los Angeles), H. E. Gaub (Ludwig Maximilian University, Munich), D. Kania (Veeco Digital Instruments), and V. Vesna (University of California, Los Angeles) for their insightful discussions and enthusiasm. A.E.P. and J.K.G. thank the Institute for Cell Mimetic Space Exploration, CMISE (a NASA URETI Institute), for partial support. E.B.G., S.S., and J.S.V. thank NIH for support from grant DK46828.

Supporting Online Material

www.sciencemag.org/cgi/content/full/305/5687/1147/DC1
Materials and Methods
Figs. S1 and S2
Tables S1 and S2
References and Notes

29 March 2004; accepted 12 July 2004

Requirement of Rac1 and Rac2 Expression by Mature Dendritic Cells for T Cell Priming

Federica Benvenuti,[1]*† Stephanie Hugues,[1]† Marita Walmsley,[2] Sandra Ruf,[2] Luc Fetler,[3] Michel Popoff,[4] Victor L. J. Tybulewicz,[2] Sebastian Amigorena[1]‡

Upon maturation, dendritic cells (DCs) acquire the unique ability to activate naïve T cells. We used time-lapse video microscopy and two-photon imaging of intact lymph nodes to show that after establishing initial contact between their dendrites and naïve T lymphocytes, mature DCs migrate toward the contacted lymphocytes. Subsequently, the DCs tightly entrap the T cells within a complex net of membrane extensions. The Rho family guanosine triphosphatases Rac1 and Rac2 but not Rho itself control the formation of dendrites in mature DCs, their polarized short-range migration toward T cells, and T cell priming.

In initiating T cell–dependent immune responses, DCs phagocytose antigen in peripheral tissues and migrate to the draining lymph nodes, where they interact with antigen-specific T cells (*1*). To efficiently prime naïve T cells, DCs need to undergo a process of maturation that implies up-regulation of the major histocompatibility complex (MHC) and peptide complexes and the costimulatory molecules at the surface (*2*). Upon maturation, DCs reorganize their actin cytoskeleton (*3*), projecting long and motile membrane extensions, called dendrites, which are likely to facilitate interactions with potentially reactive T cells (*4*, *5*). This type of membrane activity is generally controlled by the actin cytoskeleton, which is in turn regulated by small guanosine triphosphatases (GTPases) of the Rho family (*6*). Although the importance of the actin cytoskeleton and of small Rho family GTPases in T cells during T cell priming has been widely documented (*7*), their role in mature DCs is still unclear (*8*–*10*).

Interactions between mature DCs and naïve $CD4^+$ T cells during priming were analyzed in vitro with time-lapse video microscopy. DCs projected dendrite-like protrusions around their cell body before T cell contact (Fig. 1A and movie S1). These dendrites, which had an average length of 7 μm, enabled DCs to scan an area up to four times as large as their cell body surface. After an initial dendrite-mediated contact with a T cell, DCs projected numerous mobile membrane extensions and displaced their cell bodies to entangle the lymphocyte. These types of interactions have not been observed with immature DCs, which

[1]Unité INSERM 365, Institut Curie, 26 rue d'Ulm, 75005 Paris, France. [2]Division of Immune Cell Biology, National Institute for Medical Research, Mill Hill, London, NW7 1AA, UK. [3]UMR 168 CNRS/Institut Curie, 11 rue Pierre et Marie Curie, 75005 Paris, France. [4]Institut Pasteur, Unité des Toxines Microbiennes, 75015 Paris, France.

*Present address: International Centre for Genetic Engineering and Biotechnology, Padriciano 99, 34121 Trieste, Italy.
†These authors contributed equally to this work.
‡To whom correspondence should be addressed. E-mail: sebastian.amigorena@curie.fr

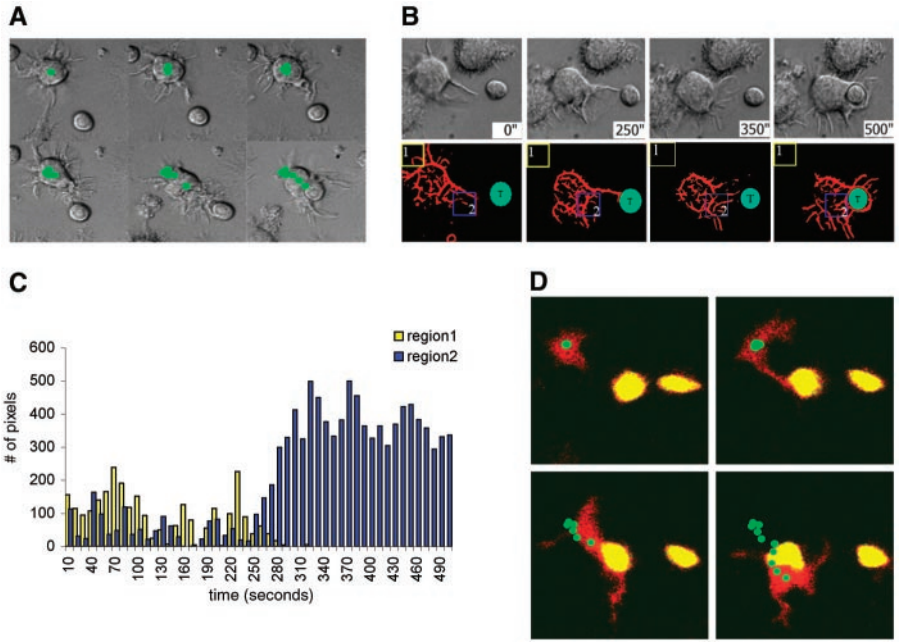

Fig. 1. Mature DCs extend polarized membrane extensions toward T cells during priming. (**A**) DIC images from movie S1 showing naïve $CD4^+$ T cells specific for the male antigen (H-Y)/I-A^b complex (*16*) and H-Y–loaded mature DCs. Green dot shows the successive positions of the DC body. (**B**) (Top) DIC images from movie S3A show the first phases of interaction between a mature DC and a naïve $CD4^+$ T cell. (Bottom) The corresponding images were treated with the mia filter (*17*) to quantify the membrane's projections as number of pixels (movie S3B). (**C**) Number of pixels in regions 1 and 2 during the first 500 s of a representative DC–T cell interaction are plotted. In 68% (n = 42) of the DC–T cell interactions, DCs extended membrane projections and displaced toward the T cell before any close apposition. No membrane extensions or DC displacements in the opposite direction were observed. (**D**) Two-photon imaging of a representative DC (red) polarizing toward a naïve T cell (yellow) in an intact lymph node (movie S5). The migratory path of the DC is illustrated by tracking the cell body centroid (green dots) in successive image stacks.

lack motile dendrites and are unable to entrap T cells (*11*) (movie S2).

To quantify the intensity and directionality of displacements and dendrite activity, two opposed regions surrounding the DC, either directed toward (Fig. 1B, bottom, blue box) or away from (yellow box) the T cell, were analyzed over time. Before establishing contact, DCs extended dendrites isotropically. Within the first few minutes after the initial dendrite-mediated contact with a T cell, abundant membrane extensions were projected in the direction of the T cell. The body of the DC then rapidly translated toward the T cell to establish a stable DC–T cell contact (Fig. 1, B and C, and movie S3, A and B). This process was observed in 68% (n = 42) of the DC–T cell interactions.

We also observed polarized membrane extensions and short-range migration toward the T cell in the absence of antigenic peptide and in MHC class II–deficient DCs (fig. S1 and movie S4). Although the polarization of the DC body must be driven by some signal, delivered to the DC upon a first contact with the T cell, it is not initiated by engagement of MHC class II molecules by the T cell receptor. The duration of the contacts, however, was strongly reduced in the absence of antigen or MHC class II molecules (*11*).

To address the relevance of these observations in a physiological environment, we performed two-photon microscopy on explanted lymph nodes (LNs) (Fig. 1D and movie S5). Only initial encounters between DCs and T cells were analyzed, omitting contacts that had already been established. In the absence of any contact, DCs projected membrane extensions randomly. After dendrite-mediated contact with a T cell (Fig. 1D), DCs (red) displaced toward the T cell (yellow) and established tight inter-

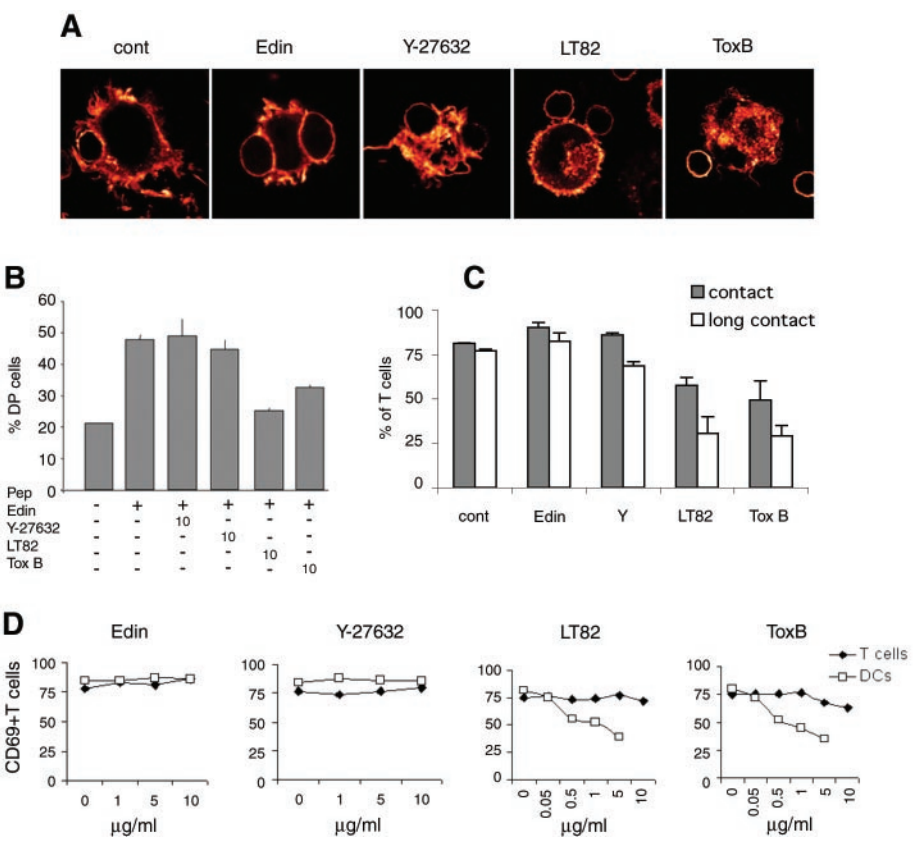

Fig. 2. Small GTPases of the Rho family regulate the antigen-presenting efficiency of DCs. (**A**) F-actin distribution (phalloidin labeling) in conjugates between DCs treated with the different inhibitors and naïve $CD4^+$ T cells. cont, untreated cells; Edin, Edin toxin from *Staphylococcus aureus*; Y-27632, a chemical inhibitor; LT82, *Clostrium sordellii* lethal toxin; Tox B, *Clostriudium difficile* toxin B. (**B**) Percentage of DC-T (DP) conjugates formed by treated DCs [as measured by fluorescence-activated cell sorting (FACS), peptide (pep) = 10 nM H-Y]. Error bars show mean + SD. (**C**) Effect of toxins on the number of T cells establishing at least one contact (gray bars) or contacts longer that 500′ (white bars) with toxin-treated or control DCs (measured with time-lapse video microscopy, $n \geq 50$ T cells). Error bars show mean + SD. (**D**) DCs (white squares) or T cells (black diamonds) were preincubated with the toxins and cultured with untreated T cells or DCs, respectively (10 nM H-Y peptide). Up-regulation of CD69 on T cells was measured by FACS after 12 hours of coculture.

actions (Fig. 1D and movie S5). The mean distance (±SD) between the two cell bodies at the time of the initial dendrite-mediated contact was 18.39 ± 8.68 μm. The speed of the DCs increased after a dendrite-mediated contact (from 2.61 ± 0.70 μm/min, $n = 9$, to 4.01 ± 1.13 μm/min, $n = 9$), but before formation of the conjugate. Once the conjugates were formed, the speed returned to values typical of unengaged DCs (2.28 ± 0.85 μm/min, $n = 9$) [supporting online material (SOM) text 1].

The potential role of Rho family GTPases in DC activities during T cell priming was first investigated with chemical inhibitors and bacterial toxins (fig. S2). Toxins that blocked Rho GTPases in DCs (fig. S3) also induced marked rearrangements of the actin cytoskeleton (fig. S4). However, only inhibitors that affect the Rac/cdc42/Ral pathway, not those that block Rho itself, resulted in a decreased ability of mature DCs to establish tight and long contacts with naïve T cells (Fig. 2, A to C, fig. S5, and movies S6 to S8). Consistently, treatment of DCs with Rac/cdc42/Ral-blocking toxins but not with Rho-blocking toxins resulted in a marked dose-dependent inhibition of T cell activation (Fig. 2D). Thus, Rho function in mature DCs was dispensable for the formation of stable DC–T cell conjugates and for T cell priming, whereas another Rho family GTPase was required.

The possible role of Rac GTPases in DCs during T cell priming was next analyzed with primary DCs derived from Rac1 conditional knockout mice (*Rac1*$^{-/-}$) (*12*–*14*), Rac2 knockout mice (*Rac2*$^{-/-}$) (*15*), and the double-knockout conditional strain derived from backcross of Rac1$^{-/-}$ and Rac2$^{-/-}$ (*Rac1/2*$^{-/-}$).

Immunoblot analysis of DCs grown from the bone marrow or isolated from the spleen of *Rac1*$^{-/-}$ and *Rac1/2*$^{-/-}$ mice showed an absence of Rac1 protein, confirming efficient deletion in this cell type (fig. S6). In both spleen and LNs, a significant reduction (45% and 55%, respectively) in the proportion of CD11c$^+$/CD8α$^+$ cells in *Rac1*$^{-/-}$ and *Rac1/2*$^{-/-}$ mice was found (Fig. 3A). This may reflect a selective defect in migration of CD8α$^+$ DCs to secondary lymphoid organs or a loss of expression of CD8α in Rac1-deficient DCs.

Homogeneous populations of CD8α$^-$ DCs were next differentiated in vitro from wild-type and mutant bone marrow precursors. Expression of CD11c and maturation markers was similar on wild-type and *Rac1/2*$^{-/-}$ cells (Fig. 3B). *Rac1/2*$^{-/-}$ DCs but not DCs deficient in either Rac1 or Rac2 presented severe alterations of the actin cytoskeleton (SOM text 2). Peptide-loaded wild-type or *Rac1/2*$^{-/-}$ splenic DCs were injected into wild-type mice to evaluate their ability to prime in vivo antigen-specific naïve CD4$^+$T cells. Up-regulation of CD69 on T cells primed by *Rac1/2*$^{-/-}$ DCs was inefficient, as compared with wild-type cells (Fig. 3C). This apparent defect in naïve T cell priming, however, was ascribed to defective migration of *Rac1/2*$^{-/-}$ DCs to the LNs (Fig. 3D). Signs of defective migration were also observed in vitro by tracking the movements of mature DCs on fibronectin-coated plates (Fig. 3E). Thus Rac1 and Rac2, although not required for DC differentiation and maturation, play a critical role in the biogenesis of dendrites and in mature DC migration.

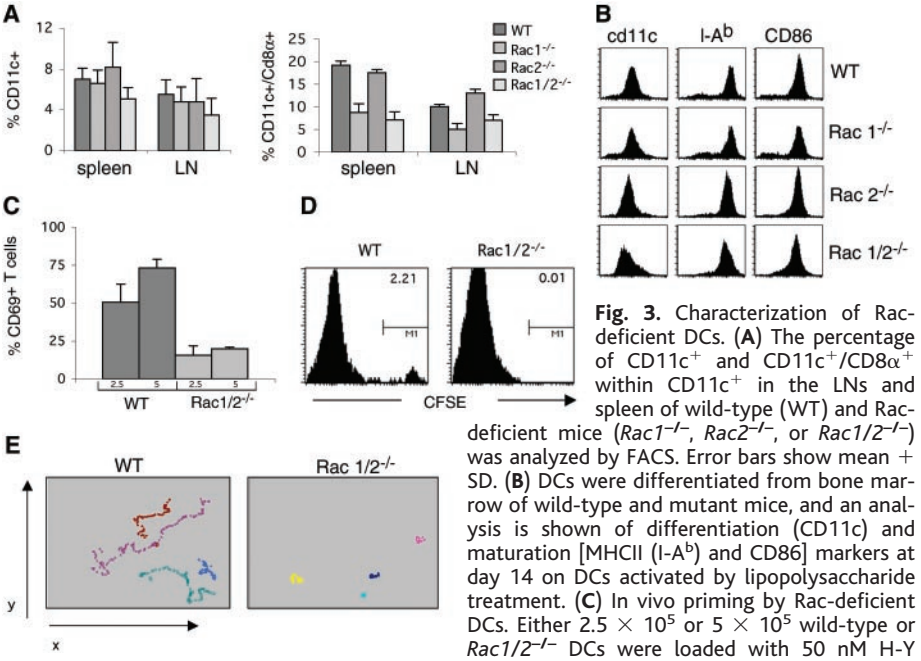

Fig. 3. Characterization of Rac-deficient DCs. (**A**) The percentage of CD11c$^+$ and CD11c$^+$/CD8α$^+$ within CD11c$^+$ in the LNs and spleen of wild-type (WT) and Rac-deficient mice (*Rac1*$^{-/-}$, *Rac2*$^{-/-}$, or *Rac1/2*$^{-/-}$) was analyzed by FACS. Error bars show mean + SD. (**B**) DCs were differentiated from bone marrow of wild-type and mutant mice, and an analysis is shown of differentiation (CD11c) and maturation [MHCII (I-A^b) and CD86] markers at day 14 on DCs activated by lipopolysaccharide treatment. (**C**) In vivo priming by Rac-deficient DCs. Either 2.5 × 10^5 or 5 × 10^5 wild-type or *Rac1/2*$^{-/-}$ DCs were loaded with 50 nM H-Y peptide and injected subcutaneously in female C57BL/6 hosts adoptively transferred with carboxyfluorescein diacetate succinimidyl ester (CFSE)–labeled CD4$^+$ naïve H-Y–specific T cells. The percentage of CFSE$^+$/CD69$^+$ T cells in draining LNs was measured 24 hours after injection. Error bars show mean + SD. (**D**) *Rac1/2*$^{-/-}$ DCs failed to migrate to LNs. We stained 5 × 10^5 wild-type or *Rac1/2*$^{-/-}$ DCs with CFSE and injected them subcutaneously into host mice. The histograms show the percentage of CD11c$^+$/CFSE$^+$ on total CD11c in draining LNs, 24 hours after injection. M_1 shows the marker region M_1. The numbers in the upper right corners indicate the percentage of cells in M_1. One representative of three experiments is shown. (**E**) Representative trajectories of four wild-type and four *Rac1/2*$^{-/-}$ DCs migrating on fibronectin for 30 min. Mean velocities (±SD): wild-type DCs, 1.03 ± 0.5 μm/min; *Rac1/2*$^{-/-}$ DCs = 0.12 ± 0.11 μm/min ($n = 20$ cells for each genotype).

To further investigate the role of Rac in the initial phases of DC–T cell interactions and in T cell priming, we filmed the interactions between Rac-deficient DCs and naïve T cells (SOM text 3). *Rac1/2*$^{-/-}$ DCs only established intermittent contacts with T cells and failed to displace toward or engulf T cells. Projections of dendrites were absent in *Rac1/2*$^{-/-}$ DCs, which seemed to "ignore" naïve T cells, even when short contacts were established (Fig. 4A and movie S9, A and B). The quantification of the number of pixels in regions 1 and 2 showed no preferential membrane activity or polarization toward the T cell (Fig. 4B). The lack of dendrites and directional cell body movements in *Rac1/2*$^{-/-}$ DCs resulted in a marked defect in the ability to establish, stabilize contact with, and engulf T cells (Fig. 4, C and D). We next tested the ability of Rac-deficient DCs to prime naïve T cells in vitro. *Rac1/2*$^{-/-}$ DCs showed a marked reduction in inducing early and late events of T cell activation (Fig. 4, E and F). *Rac1*$^{-/-}$ knockout DCs were slightly less efficient than wild-type and *Rac2*$^{-/-}$ cells, but the defect was only observed in three out of five experiments. The ability of *Rac1/2*$^{-/-}$ DCs to prime naïve T cells was restored when the same experiment was performed in round bottom plates, which physically forces cells to interact (Fig. 4E, flat and round). Therefore, we propose that this defective T cell priming is caused by the decreased dendrite activity and cell motility of mature *Rac1/2*$^{-/-}$ DCs, rather than by a defect in peptide loading or T cell activation.

These results show that the initial encounters between mature DCs and naïve T cells include two distinct steps, controlled by Rac1 and Rac2: (i) Initial interactions are mediated by dendrites, which are projected in all directions by mature DCs, and (ii) a first contact between the dendrites and a naïve T cell modifies the membrane activity of the mature DC, causing the directional projection of abundant membrane extensions toward the naïve T cell and the short range displacement of the cell body in the same direction. Immature DCs, which do not extend dendrites, and which do not polarize toward naïve T cells or entangle them in the course of the interaction, do not prime naïve T cells efficiently. We conclude that mature DCs have adapted their cytoskeletal activity to optimize the encounters and to stabilize interactions with naïve T cells.

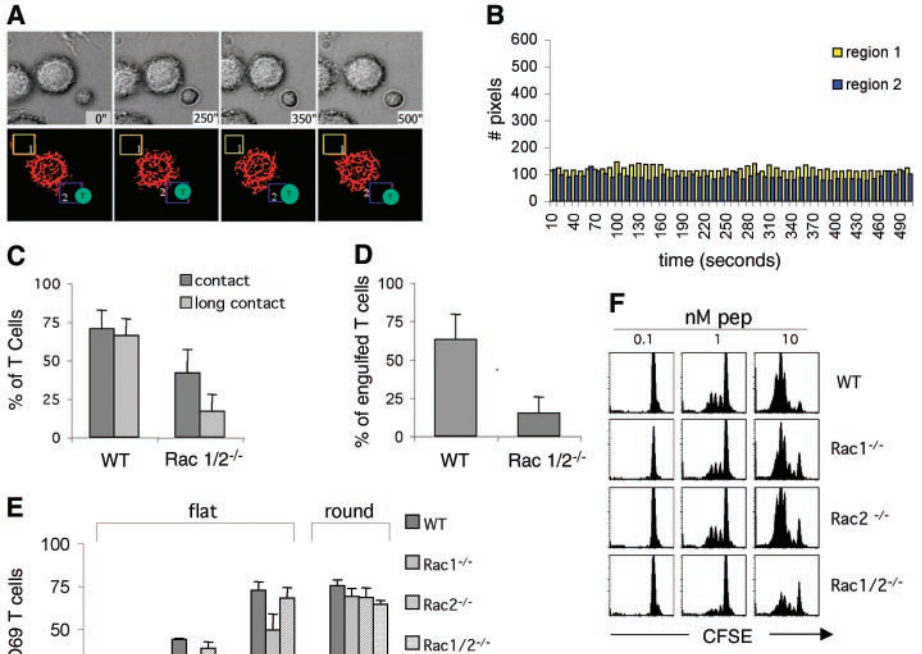

Fig. 4. Impaired ability of Rac-deficient DCs to interact with naïve T cells and to induce T cell priming. (**A**) Individual frames from movie S9A show the first 500 s of interaction between peptide-loaded mature *Rac1/2*$^{-/-}$ DCs (1:1) (top) and the corresponding mia-treated images (bottom and movie S9B). (**B**) The membrane activity in regions 1 and 2 was measured as in Fig. 1C and expressed as the number of pixels in each region over time. (**C**) The number of T cells establishing at least one contact (dark gray bars) or a contact longer that 500′ (light gray bars) with wild-type (WT) and *Rac1/2*$^{-/-}$ DCs was quantified (at least 100 T cells/genotypes). (**D**) Percentage of T cells that are engulfed by wild-type and *Rac1/2*$^{-/-}$ DCs during the interaction. (**E**) Up-regulation of CD69 on CD4^{+} T cells was measured by FACS after incubation with H-Y peptide–loaded mature DCs in flat or round bottom wells (one representative of five independent experiments is shown). Error bars show mean + SD. (**F**) T cell division, evaluated as loss of CFSE staining, was measured at day 3 by FACS after stimulation by wild-type or Rac-defective mature DCs loaded with the H-Y peptide (pep).

References and Notes

1. A. Lanzavecchia, F. Sallusto, *Curr. Opin. Immunol.* **13**, 291 (2001).
2. S. J. Turley *et al.*, *Science* **288**, 522 (2000).
3. F. Granucci *et al.*, *Blood* **102**, 2940 (2003).
4. T. R. Mempel, S. E. Henrickson, U. H. Von Andrian, *Nature* **427**, 154 (2004).
5. M. J. Miller, A. S. Hejazi, S. H. Wei, M. D. Cahalan, I. Parker, *Proc. Natl. Acad. Sci. U.S.A.* **101**, 998 (2004).
6. K. Burridge, K. Wennerberg, *Cell* **116**, 167 (2004).
7. M. L. Dustin, J. A. Cooper, *Nature Immunol.* **1**, 23 (2000).
8. M. M. Al-Alwan, G. Rowden, T. D. Lee, K. A. West, *J. Immunol.* **166**, 1452 (2001).
9. M. M. Al-Alwan *et al.*, *J. Immunol.* **171**, 4479 (2003).
10. M. Kobayashi *et al.*, *J. Immunol.* **167**, 3585 (2001).
11. F. Benvenuti *et al.*, *J. Immunol.* **172**, 292 (2004).
12. M. J. Walmsley *et al.*, *Science* **302**, 459 (2003).
13. R. Kuhn, F. Schwenk, M. Aguet, K. Rajewsky, *Science* **269**, 1427 (1995).
14. C. M. Wells, M. Walmsley, S. Ooi, V. Tybulewicz, A. J. Ridley, *J. Cell Sci.* **117**, 1259 (2004).
15. A. W. Roberts *et al.*, *Immunity* **10**, 183 (1999).
16. O. Lantz, I. Grandjean, P. Matzinger, J. P. Di Santo, *Nature Immunol.* **1**, 54 (2000).
17. Number of pixels corresponding to dendrites or membrane extension was quantified after applying on differential interference contrast (DIC) images a filter created with the Metamorph software [multi-dimensional image analysis (mia)].

18. F.B. was supported by INSERM and Fondation pour la Recherche Meédicale, S.H. was supported by "La Ligue Nationale Contre le Cancer." We thank J. B. Sibarita for his help with the Metamorph software, O. Lantz (Institut Curie) for Marilyn mice, and S. Ooi for help with maintenance of mouse colonies. Generation and maintenance of Rac-deficient mice was funded by the Medical Research Council, UK. Rac2$^{-/-}$ mice were kindly provided by D. A. Williams (Howard Hughes Medical Institute, Indiana University School of Medicine, USA).

Supporting Online Material

www.sciencemag.org/cgi/content/full/305/5687/1150/DC1
Materials and Methods
SOM Text
Figs. S1 to S6
Movies S1 to S9
References

14 April 2004; accepted 22 July 2004

Enhanced Dendritic Cell Antigen Capture via Toll-Like Receptor–Induced Actin Remodeling

Michele A. West,[1]* Robert P. A. Wallin,[1,2,3]* Stephen P. Matthews,[1] Henrik G. Svensson,[1] Rossana Zaru,[1] Hans-Gustaf Ljunggren,[3] Alan R. Prescott,[1] Colin Watts[1]†

Microbial products are sensed through Toll-like receptors (TLRs) and trigger a program of dendritic cell (DC) maturation that enables DCs to activate T cells. Although an accepted hallmark of this response is eventual down-regulation of DC endocytic capacity, we show that TLR ligands first acutely stimulate antigen macropinocytosis, leading to enhanced presentation on class I and class II major histocompatibility complex molecules. Simultaneously, actin-rich podosomes disappear, which suggests a coordinated redeployment of actin to fuel endocytosis. These reciprocal changes are transient and require p38 and extracellular signal–regulated kinase activation. Thus, the DC actin cytoskeleton can be rapidly mobilized in response to innate immune stimuli to enhance antigen capture and presentation.

Immature DCs respond to pathogen-derived products (*1*, *2*) by initiating a program of maturation that induces their migration to lymphoid organs and culminates in the enhanced expression of major histocompatibility complex (MHC)–peptide complexes, costimulatory molecules, and cytokines necessary for T cell activation (*3*–*5*). Much of the DC response to microbial products is dependent on changes at the transcriptional level (*6*, *7*). However, it is becoming clear that activation of TLRs can also trigger faster responses, for example, to the cellular machinery that supports antigen processing and presentation. Thus, endosomal/lysosomal proteolysis as well as membrane transport and fusion reactions are boosted (*8*–*12*), ubiquitinated proteins accumulate within specialized structures (*13*), and antigen presentation on both class I and class II MHC molecules is enhanced (*14*, *15*). Nevertheless, many of these adaptations take several hours to become evident. A further well-documented characteristic of

[1]Division of Cell Biology and Immunology, Wellcome Trust Biocentre, School of Life Sciences, University of Dundee, Dundee DD1 5EH, UK. [2]Microbiology and Tumor Biology Center, Karolinska Institutet, Stockholm, Sweden. [3]Center for Infectious Medicine, Department of Medicine, Karolinska Institutet, Karolinska University Hospital, Stockholm, Sweden.

*These authors contributed equally to this work.
†To whom correspondence should be addressed. E-mail: c.watts@dundee.ac.uk

DC maturation is the progressive down-regulation of endocytosis (*16*–*18*); yet, this seems paradoxical because, a priori, increased antigen capture upon encounter with a pathogen would seem desirable. To investigate this further in primary DCs, we undertook a detailed analysis of early events following TLR activation (*19*).

Murine bone marrow–derived DCs (BMDCs) and spleen-derived DCs (SDCs) were activated with TLR ligands, and their ability to take up the endocytosis marker fluorescein isothiocyanate (FITC)–dextran was assessed at early time points. Surprisingly, both types of DC accumulated several times as much FITC-dextran during a short pulse after lipopolysaccharide (LPS) treatment (Fig. 1A). However, this enhancement was transient, peaking after 30 or 45 min of LPS stimulation in BMDCs and SDCs, respectively (Fig. 1B, left). Longer-term down-regulation of endocytic capacity followed this acute stimulation (Fig. 1B, right). Ligands that stimulate DCs through other TLRs all transiently increased pinocytosis in BMDCs (Fig. 1C), but only if the appropriate TLR was expressed (fig. S1). We tested the lipopeptide $Pam3CS(K)_4$ (TLR2), poly I:C, which is a mimic of double-stranded RNA (TLR3) and an unmethylated CpG-containing oligonucleotide (ODN1668) mimicking bacterial DNA (TLR9). TLR4- and TLR3-stimulated FITC-dextran uptake persisted in DCs lacking the signaling adaptor MyD88, whereas the TLR9- and TLR2-dependent responses were abolished (Fig. 1D) (*20*). These results are consistent with other data indicating that TLR4 is coupled to both MyD88-dependent and independent signaling pathways, whereas TLR2 and TLR9 signaling is MyD88-dependent. TLR3 is known not to use the MyD88 adaptor (*21*).

Observation of DCs by video and fluorescence microscopy revealed the likely basis for enhanced FITC-dextran accumulation in LPS-exposed DCs: Membrane-ruffling activity was stimulated, leading to an enhanced accumulation of FITC-dextran–filled macropinosomes compared with control cells (Fig. 1E and movie S1). LPS-stimulated FITC-dextran uptake was abolished by cytochalasin D, which depolymerizes actin filaments (*20*). These results show that down-regulation of DC endocytosis by microbial products is actually preceded by a short-term enhancement of actin-dependent endocytic capacity.

To establish whether acute stimulation of antigen capture also enhanced antigen presentation, we pulsed DCs briefly (30 to 60 min) with antigen, either concurrently with LPS or for the same length of time but before LPS exposure (Fig. 2A). DCs were then chased for various times and cocultured with T cells. We assessed antigen presentation on class I MHC molecules using immune complexes containing ovalbumin (Ova-IC) (*22*) and on class II MHC molecules using tetanus toxin C fragment (TTCF). Coadministration of Ova-IC with LPS resulted in significantly enhanced cross-presentation of the ovalbumin peptide SIINFEKL to the T cell hybridoma B3Z compared with Ova-IC administration followed by LPS (Fig. 2B). This difference was not seen in DCs lacking TLR4 (Fig. 2C). Similarly, enhanced presentation on class II MHC was observed when TTCF was coadministered with LPS versus sequential administration of TTCF, then LPS (Fig. 2D). Similar results were obtained using the TLR2 ligand $Pam3CS(K)_4$ in both SDCs and BMDCs (Fig. 2, E and F).

TLR activation not only stimulated membrane-ruffling activity but also had a dramatic effect on F-actin–rich structures called podosomes. Podosomes are found in arrays on the ventral surface of macrophages (*23*, *24*), osteoclasts (*25*), and DCs (*26*–*28*). They are distinct from focal adhesions and are thought to be involved in cell migration and tissue invasiveness (*24*). A high proportion of DCs displayed clusters of podosomes (Fig. 3A), each encircled by a characteristic ring of vinculin (Fig. 3B). We expressed actin–green fluorescent protein (GFP) in liv-

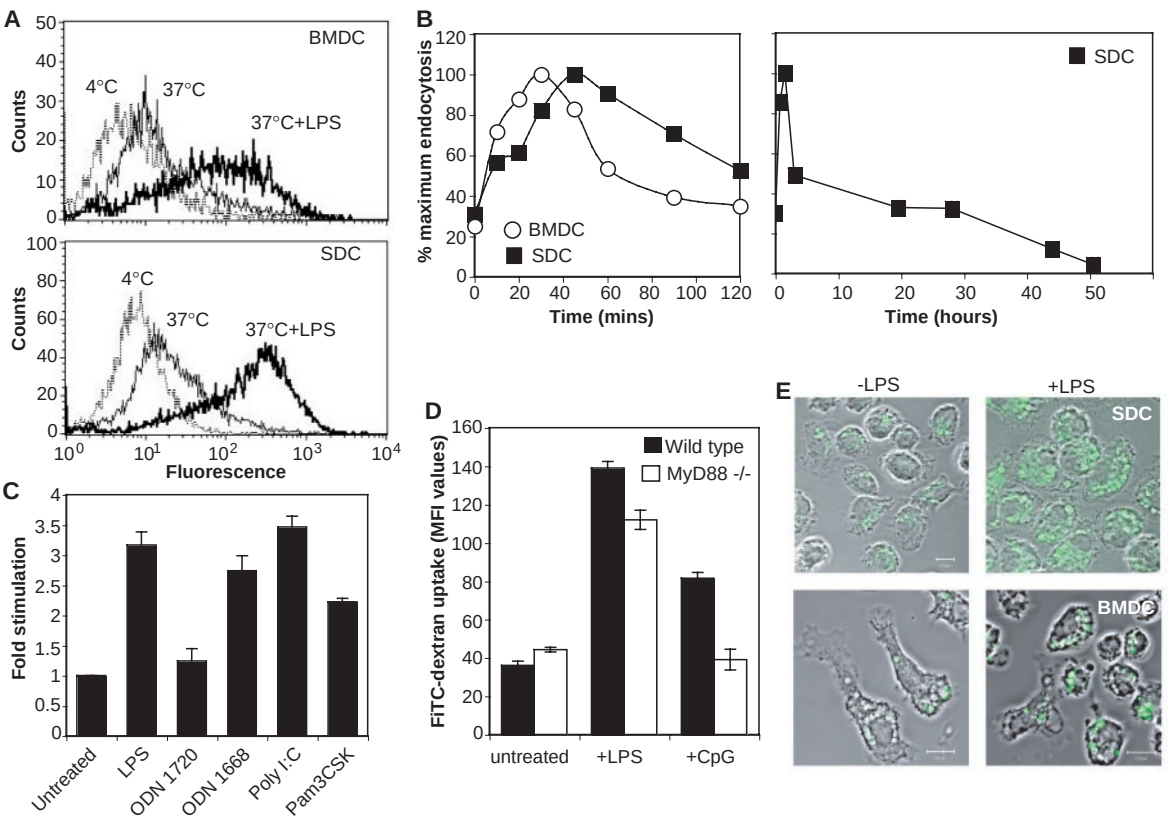

Fig. 1. Different TLR ligands transiently stimulate endocytosis in SDCs and BMDCs. (**A**) SDCs and BMDCs, with or without prior exposure (30 to 60 min) to 50 ng/ml LPS, were incubated with FITC-dextran for 10 min, washed, and analyzed by fluorescence-activated cell sorting. (**B**) As in (A), but FITC-dextran uptake (10 min pulse) was measured after different times of acute (left) or long-term (right) LPS treatment. (**C**) BMDCs were exposed to oligonucleotides ODN 1668 or control ODN 1720, poly I:C, or Pam3CSK, and FITC-dextran uptake was measured as in (A). Fold stimulation (mean fluorescence intensity values) is relative to FITC-dextran uptake in unstimulated DCs. (**D**) BMDCs from wild-type or MyD88-deficient mice were exposed to TLR ligands, and FITC-dextran uptake was assayed as in (A) and (B). Means ± SD of triplicates shown. (**E**) Combined phase contrast and fluorescence microscopy of DCs with or without LPS stimulation for 30 min, then exposure to FITC-dextran for 10 min. Scale bars, 10 μm.

ing DCs and monitored the behavior of podosome clusters. After photobleaching, podosomes rapidly reincorporated GFP-actin, which demonstrates that in DCs, as in other cells (*23*, *25*, *29*), podosomes are sites of rapid actin turnover (Fig. 3C and movie S2).

Although podosomes were a stable feature of the actin cytoskeleton in immature DCs when monitored over many hours, TLR activation induced podosome disassembly by 30 min in most DCs (Fig. 3, D and E) (*30*). Again, this effect was MyD88-independent for TLR4 and TLR3 but MyD88-dependent for TLR9 and TLR2 (Fig. 3E) (*20*). Interestingly, a more extended analysis revealed that the destabilization of podosomes induced by TLR signaling was transient. Podosomes disappeared precipitously 10 to 20 min after LPS challenge but then began to reappear at about 40 min and had almost fully recovered after 1.5 to 2 hours, even though LPS was still present (Figs. 3F and 4A and movie S3). Broadly, the same results were obtained in BMDCs, except that the disappearance and recovery of podosomes was slower (Fig. 4B). This cycle of podosome loss and recovery correlated inversely with the acute phase of enhanced endocytosis (Fig. 4, A and B). Thus, the few cells that retained podosomes after 30 min of LPS stimulation generally had fewer macropinosomes. Conversely, cells with large numbers of macropinosomes seldom had podosomes (Fig. 4C).

TLR ligands are known to activate protein and lipid-kinase signaling pathways leading ultimately to de novo gene transcription. However, as expected given the rapidity of the effects observed, actinomycin D had no effect on either enhanced endocytosis or podosome disassembly (fig. S2). The PI3-kinase inhibitor wortmannin blocked LPS-stimulated pinocytosis, but also basal pinocytosis (*20*), presumably because PI3 kinase is required for the terminal stages of macropinocytosis (*17*, *31*). It is difficult, therefore, to assess its role in LPS-stimulated pinocytosis. Wortmannin had no effect, however, on podosome disassembly (fig. S3). Both extracellular signal–regulated kinase 1/2 (ERK1/2) and stress-activated protein kinase 2 (SAPK2)/p38α mitogen-activated protein (MAP) kinases were activated by LPS in SDCs, and kinetics similar to the actin rearrangements were observed (fig. S3). Podosome disassembly, triggered by LPS, was completely blocked in the combined presence of PD184352, an inhibitor of MEK1 (the upstream activator of ERK1/2) and SB203580, an inhibitor of SAPK2/p38 (Fig. 4, D and E). These inhibitors did not block the appearance of DC maturation markers (fig. S4) and, notably, they did not inhibit rapid actin cycling through podosomes, demonstrating that they were not toxic (fig. S5). Because podosome disassembly and enhanced ruffling/macropinocytosis could be driven by distinct or similar signaling pathways, we tested the effect of MAP kinase inhibitors on LPS-stimulated FITC-dextran uptake. As shown in Fig. 4F, this was also substantially blocked by combined inhibition of p38 and ERK kinases. When tested individually, SB203580 and PD184352 partially inhibited LPS-stimulated endocytosis. SB203580 partially blocked podosome disassembly, whereas PD184352 had little effect (Fig. 4E).

Our results reveal previously unknown features of the TLR-induced DC maturation program at its earliest stages, including a transient phase of enhanced endocytosis that can be used to boost antigen capture and presentation. Although sampling of "self" by nonactivated DCs is emerging as an important mediator of tolerance under steady-state conditions (*32*), the capacity to up-regulate antigen capture under infectious conditions may favor presentation of pathogen-derived peptides. Our data further suggest that to fuel increased actin-dependent endocytosis, DCs disassemble other actin-rich structures, particularly podosomes. However, further studies are needed to demonstrate an obligatory link between these two events. Podosomes are still somewhat enigmatic elements of the actin cytoskeleton that grow, divide, and fuse with each other in a highly dynamic fashion at the leading lamella of macrophages (*23*) and in the differentiating osteoclast (*25*). Podosomes are proposed to play an important role in cell migration and tissue invasiveness (*24*), so it is particularly intriguing that TLR activation in DCs can induce dramatic perturbations in podosome stability and dynamics. Our data imply that optimal antigen sampling and DC migration are mutually exclusive events. Although podosomes returned after transiently disappearing, mature murine DCs (~30 hours of LPS) lacked podosomes (*20*), consistent with studies in human DCs (*28*).

LPS and other TLR ligands are well known to activate MAP kinase cascades (*33*), but here we report that acute modulation of the DC actin cytoskeleton is a downstream consequence. How MAP kinase activation simultaneously regulates enhanced ruffling/

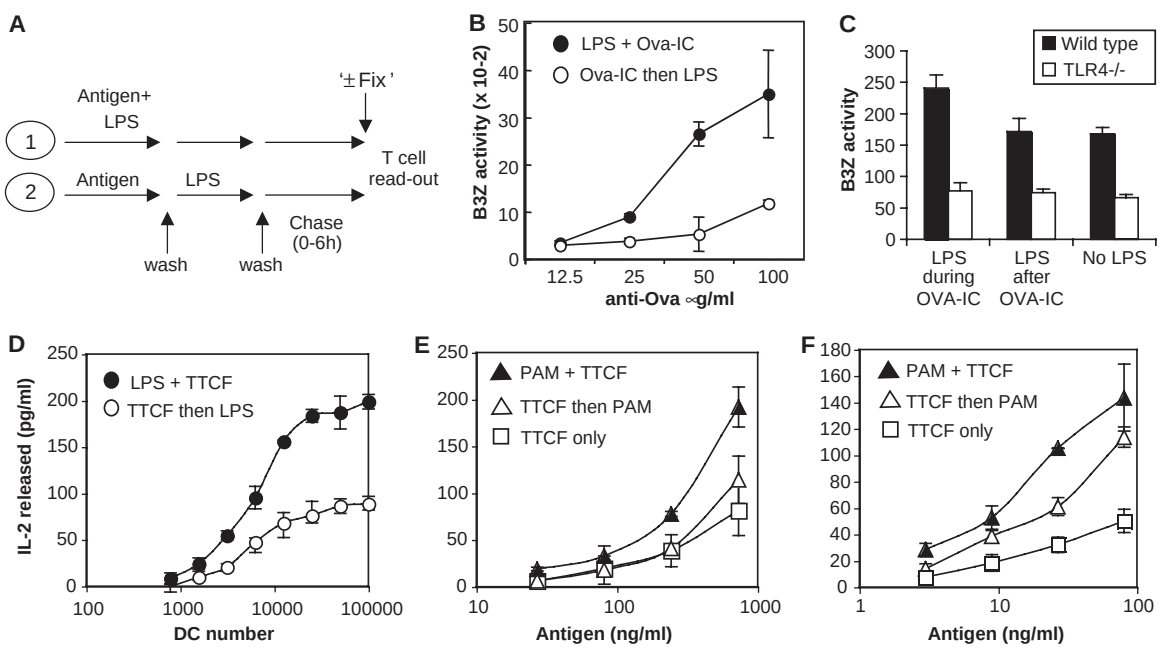

Fig. 2. Acute stimulation of antigen capture leads to enhanced antigen presentation. (**A**) Protocols for co-administration versus sequential administration of antigen and TLR ligands. Presentation of the ovalbumin epitope SIINFEKL or the tetanus-toxin epitope SGFNSSVITYPDAQLVP was detected by using T cell hybridomas B3Z (**B** and **C**) or 5B12 (**D** to **F**) on class I or class II MHC, respectively (*34*). B3Z cells were added to cells fixed after a 6-hour chase; 5B12 cells were added to live DCs after antigen-pulse manipulations. T cell stimulation was measured either by β-galactosidase luminescence assay (B3Z) or by enzyme-linked immunosorbent assay measurement of interleukin-2 release (5B12). DCs were either from spleen [(C) and (E)] or from bone marrow [(B), (D), and (F)]. Antigen was either ovalbumin immune complex (Ova IC, expressed as concentration of antibody to ovalbumin) or TTCF. In (D), dendritic cell numbers were titrated after pulsing with 0.5 μg/ml TTCF. Means ± SD of triplicate determinations are shown.

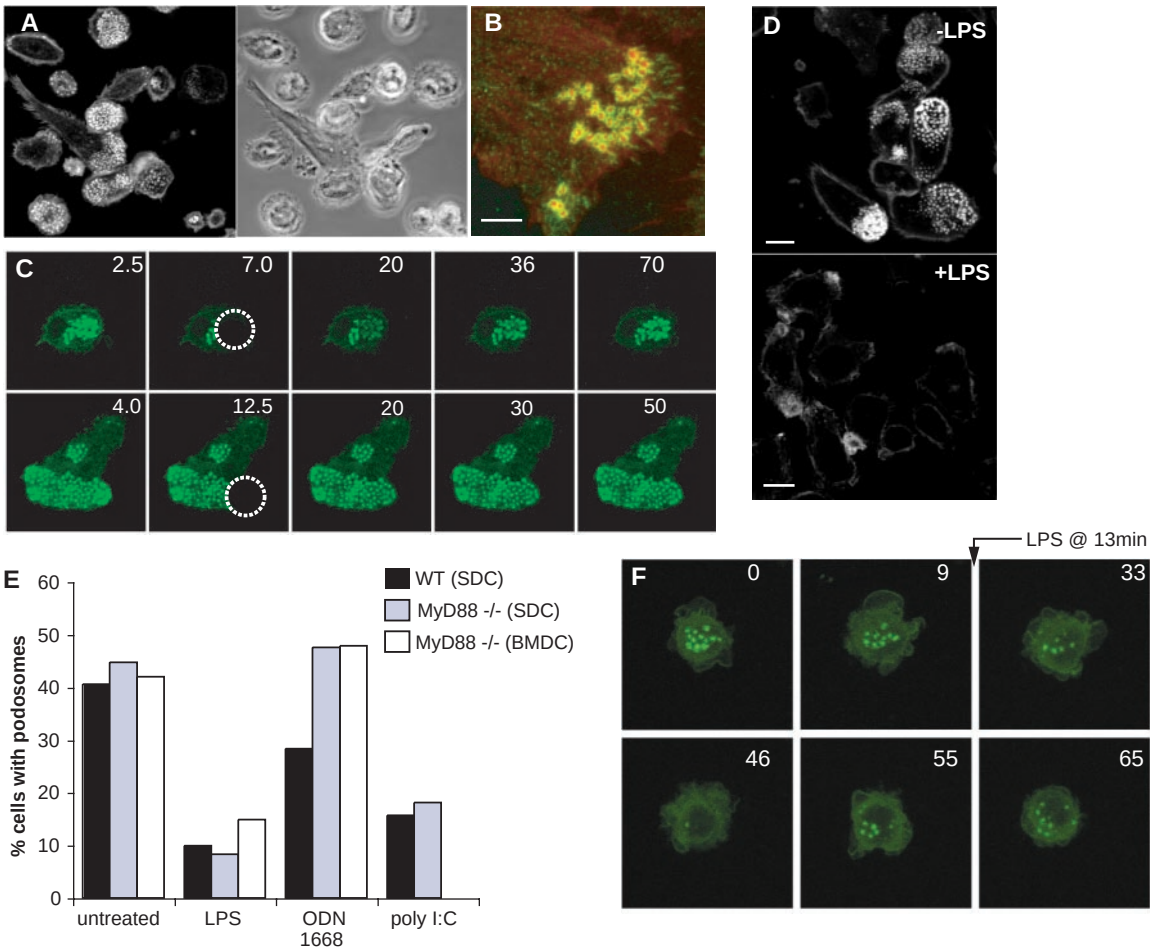

Fig. 3. DC podosome clusters are highly dynamic and acutely sensitive to TLR signaling. (**A**) Podosomes in SDCs. (**B**) Note characteristic actin core (red phalloidin staining) and peripheral (green) vinculin ring. Scale bar, 5 μm. (**C**) SDCs were transiently transfected with GFP-actin, and discrete areas (white dotted circles) were photobleached. Times are in seconds. (See also movie S2.) (**D**) Podosomes disassemble in LPS-treated cells. Scale bar, 10 μm. (**E**) Quantitation of TLR signaling–dependent podosome disassembly in MyD88 +/+ and −/− DCs scored at 40 min. (**F**) TLR4 signaling triggers a cycle of podosome disassembly and reassembly in living cells. Time points are in minutes, with LPS added at 13 min. (See also movie S3.)

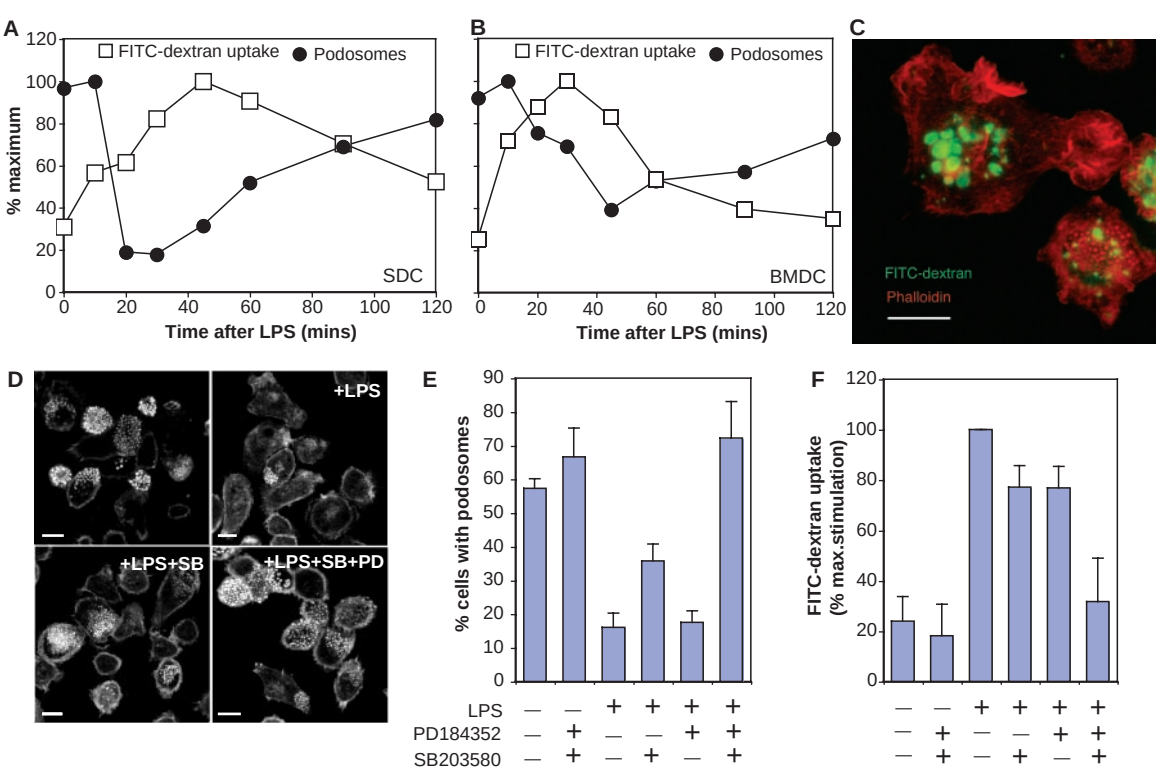

Fig. 4. Enhanced FITC-dextran uptake and podosome disassembly show reciprocal and reversible kinetics in SDCs (**A**) and BMDCs (**B**). (**C**) After 25 min of LPS, DCs retaining podosomes exhibit fewer pinosomes, and vice versa. FITC-dextran was included for the last 10 min. LPS-triggered podosome disassembly (**D** and **E**) and enhanced FITC-dextran uptake (**F**) is blocked in the presence of the combined ERK (PD184352) and p38 (SB203580) MAP kinase inhibitors. Typical images shown in (D) and quantitation in (E) and (F). Means ± SD of five experiments are shown in (E) and (F). Analysis was performed after 30 to 40 min of TLR activation. Scale bars, 10 μm.

pinocytosis and podosome disassembly remains to be determined. We did not observe major effects on the activation state of Rac or Cdc42 (fig. S6), so it seems likely that additional regulators of actin dynamics are targeted by the MAP kinases. Inhibition of both ERK and p38 kinases was required to fully block TLR-triggered effects on actin, which suggests that key downstream substrates can be activated by either pathway or that distinct ERK and p38 substrates deliver the effects observed. Because podosomes are continually turning over their actin content, consumption of the available actin pool and/or associated cofactors after a primary stimulation of actin-dependent endocytosis might indirectly result in podosome disassembly. Alternatively, separate signals may drive enhanced ruffling/pinocytosis and podosome disassembly in DCs, which may nonetheless be interdependent through a finite actin pool.

References and Notes

1. C. A. Janeway Jr., R. Medzhitov, *Annu. Rev. Immunol.* **20**, 197 (2002).
2. P. Matzinger, *Science* **296**, 301 (2002).
3. A. Lanzavecchia, F. Sallusto, *Cell* **106**, 263 (2001).
4. I. Mellman, R. M. Steinman, *Cell* **106**, 255 (2001).
5. P. Guermonprez, J. Valladeau, L. Zitvogel, C. Thery, S. Amigorena, *Annu. Rev. Immunol.* **20**, 621 (2002).
6. F. Granucci, C. Vizzardelli, E. Virzi, M. Rescigno, P. Ricciardi-Castagnoli, *Eur. J. Immunol.* **31**, 2539 (2001).
7. Q. Huang *et al.*, *Science* **294**, 870 (2001).
8. M. Kleijmeer *et al.*, *J. Cell Biol.* **155**, 53 (2001).
9. M. Boes *et al.*, *J. Immunol.* **171**, 4081 (2003).
10. A. Chow, D. Toomre, W. Garrett, I. Mellman, *Nature* **418**, 988 (2002).
11. E. S. Trombetta, M. Ebersold, W. Garrett, M. Pypaert, I. Mellman, *Science* **299**, 1400 (2003).
12. J. M. Blander, R. Medzhitov, *Science* **304**, 1014 (2004).
13. H. Lelouard *et al.*, *Nature* **417**, 177 (2002).
14. M. Cella, A. Engering, V. Pinet, J. Pieters, A. Lanzavecchia, *Nature* **388**, 782 (1997).
15. L. Delamarre, H. Holcombe, I. Mellman, *J. Exp. Med.* **198**, 111 (2003).
16. F. Sallusto, M. Cella, C. Danieli, A. Lanzavecchia, *J. Exp. Med.* **182**, 389 (1995).
17. M. A. West, A. R. Prescott, E. L. Eskelinen, A. J. Ridley, C. Watts, *Curr. Biol.* **10**, 839 (2000).
18. W. S. Garrett *et al.*, *Cell* **102**, 325 (2000).
19. Materials and Methods are available as supporting material on *Science* Online.
20. M. A. West *et al.*, data not shown.
21. S. Akira, *J. Biol. Chem.* **278**, 38105 (2003).
22. A. Regnault *et al.*, *J. Exp. Med.* **189**, 371 (1999).
23. J. G. Evans, I. Correia, O. Krasavina, N. Watson, P. Matsudaira, *J. Cell Biol.* **161**, 697 (2003).
24. S. Linder, M. Aepfelbacher, *Trends Cell Biol.* **13**, 376 (2003).
25. O. Destaing, F. Saltel, J. C. Geminard, P. Jurdic, F. Bard, *Mol. Biol. Cell* **14**, 407 (2003).
26. M. A. West *et al.*, *Eur. J. Immunol.* **29**, 3450 (1999).
27. S. Burns, A. J. Thrasher, M. P. Blundell, L. Machesky, G. E. Jones, *Blood* **98**, 1142 (2001).
28. S. Burns *et al.*, *Cell Motil. Cytoskel.* **57**, 118 (2004).
29. G. C. Ochoa *et al.*, *J. Cell Biol.* **150**, 377 (2000).
30. Only cells that have completely lost podosomes are scored as affected, which may underestimate the TLR signaling effect. CpG effects on endocytosis and podosome stability were generally less robust, probably because of lower and more variable expression of TLR9 in myeloid DCs.
31. N. Araki, M. T. Johnson, J. A. Swanson, *J. Cell Biol.* **135**, 1249 (1996).
32. R. M. Steinman, D. Hawiger, M. C. Nussenzweig, *Annu. Rev. Immunol.* **21**, 685 (2003).
33. J. Han, J. D. Lee, L. Bibbs, R. J. Ulevitch, *Science* **265**, 808 (1994).
34. Single-letter abbreviations for the amino acid residues are as follows: A, Ala; C, Cys; D, Asp; E, Glu; F, Phe; G, Gly; H, His; I, Ile; K, Lys; L, Leu; M, Met; N, Asn; P, Pro; Q, Gln; R, Arg; S, Ser; T, Thr; V, Val; W, Trp; and Y, Tyr.

35. We thank S. Rousseau and P. Cohen for helpful discussions, S. Akira for TLR and MyD88 knockout mice, and A. Chow and I. Mellman for advice on retroviral DC transfection. This work was supported by a Medical Research Council Programme Grant to C.W. and A.R.P. and by the Swedish Foundation for Strategic Research, Research Council, and Cancer Society.

Supporting Online Material

www.sciencemag.org/cgi/content/full/305/5687/1153/DC1
Materials and Methods
Figs. S1 to S6
Movies S1 to S3
References

14 April 2004; accepted 26 July 2004

NOBOX Deficiency Disrupts Early Folliculogenesis and Oocyte-Specific Gene Expression

Aleksandar Rajkovic,[1]* Stephanie A. Pangas,[2,4] Daniel Ballow,[1] Nobuhiro Suzumori,[2] Martin M. Matzuk[2,3,4]

Primordial ovarian follicles in mice form when somatic cells surround individual oocytes. We show that lack of *Nobox*, an oocyte-specific homeobox gene, accelerates postnatal oocyte loss and abolishes the transition from primordial to growing follicles in mice. Follicles are replaced by fibrous tissue in female mice lacking *Nobox* in a manner similar to nonsyndromic ovarian failure in women. Genes preferentially expressed in oocytes, including *Oct4* and *Gdf9*, are down-regulated in *Nobox*$^{-/-}$ mice, whereas ubiquitous genes such as *Bmp4*, *Kit*, and *Bax* remain unaffected. Therefore, *Nobox* is critical for specifying an oocyte-restricted gene expression pattern essential for postnatal follicle development.

Follicle formation in mice begins perinatally when germ cell cysts are invaded by pregranulosa cells to establish individual primordial follicles (*1*). As females age, primordial follicles are recruited from the resting pool to begin a growth phase. This transition from primordial to growing follicles is poorly defined at the molecular level. One hallmark of primordial follicle activation is growth of the oocyte, which, although still arrested in the first meiotic prophase, is transcriptionally active (*2*). Growing oocytes transcribe genes important for folliculogenesis (e.g., *Gdf9*, *Bmp15*, *Zp1-3*) (*3*) as well as those necessary for early embryonic development (e.g., *Mater*, *Zar1*) (*4*, *5*). *Figla* is a known oocyte-specific regulator of zona pellucida genes (*6*); however, the transcriptional control of the vast majority of oocyte-specific genes is poorly understood. Because stage-specific expression of these genes is necessary for proper oocyte growth and subsequent embryogenesis, transcription factors that regulate oocyte gene expression will be key mediators of fertility.

Nobox is an oocyte-specific homeobox gene expressed in germ cell cysts and in primordial and growing oocytes (*7*). To test whether *Nobox* is critical in folliculogenesis, we disrupted the *Nobox* locus in embryonic stem cells. We deleted 90% of the coding region, including exons that encode the homeodomain (fig. S1) (*8*). Female and male heterozygote matings produced expected Mendelian ratios, averaged 7.4 ± 2 pups per litter (n = 50 breeding pairs) over a 6-month period, and remained fertile for at least 9 months; the litter size was not statistically significantly different from the wild-type average (8.4 ± 2 pups per litter). Heterozygous (*Nobox*$^{+/-}$) and homozygous (*Nobox*$^{-/-}$) males were fertile and lacked gross anatomic abnormalities. Similarly, *Nobox*$^{+/-}$ females had normal gross anatomy and histology at 6 weeks of age (fig. S2, A and B). In contrast, all *Nobox*$^{-/-}$ females were infertile with atrophic ovaries that lacked oocytes at 6 weeks of age on the C57BL/6J/129S6/SvEv hybrid background (fig. S2, A and C).

Nobox$^{+/-}$ and *Nobox*$^{-/-}$ ovarian histology during early postnatal folliculogenesis (newborn to 14 days) was examined with the

[1]Departments of Obstetrics and Gynecology, [2]Pathology, [3]Molecular and Human Genetics, and [4]Molecular and Cellular Biology, Baylor College of Medicine, Houston, TX 77030, USA.

*To whom correspondence should be addressed. E-mail: rajkovic@bcm.tmc.edu

use of two germ cell markers, GCNA1 and MSY2 (Fig. 1). GCNA1 (germ cell nuclear antigen) is a nuclear marker for the germ cell lineage until the meiosis I diplotene/dictyate stage (*9*). MSY2 (germ cell–specific Y box protein) is a cytoplasmic marker for diplotene oocytes and persists in dictyate stages (*10*, *11*). Newborn ovaries from *Nobox*$^{+/-}$ and *Nobox*$^{-/-}$ mice stained with antibody to GCNA1 revealed germ cell cysts and primordial follicles (Fig. 1, A and B). Histomorphometric analyses showed that the relative numbers of oocytes, germ cell cysts, and primordial follicles were not significantly different between *Nobox*$^{+/-}$ and *Nobox*$^{-/-}$ newborn ovaries (fig. S3, A and B), indicating no loss of germ cells before birth. These data indicate that embryonic ovarian development, germ cell proliferation, and initial primordial follicle formation are grossly normal at the level of histology in newborn *Nobox*$^{-/-}$ females.

Nobox$^{+/-}$ and *Nobox*$^{-/-}$ ovaries stained with antibody to MSY2 showed different histology at postnatal day 3 (Fig. 1, C and D). *Nobox*$^{+/-}$ ovaries contained primary follicles (cuboidal granulosa cells surrounding larger oocytes greater than 20 μm in diameter) (Fig. 1C). In contrast, *Nobox*$^{-/-}$ ovaries contained more oocytes clustered in germ cell cysts and as primordial follicles (Fig. 1D). Secondary follicles (two layers of granulosa cells and oocyte diameters between 20 and 70 μm) were apparent by postnatal day 7 in the *Nobox*$^{+/-}$ mice stained with antibody to GCNA1 (Fig. 1E), but none were found in *Nobox*$^{-/-}$ ovary (Fig. 1F). Some follicles in *Nobox*$^{-/-}$ mice contained oocytes surrounded by cuboidal granulosa cells, but the oocyte size rarely exceeded 20 μm and the number of surrounding granulosa cells in a section was rarely greater than 7. Histomorphometric studies showed that *Nobox*$^{-/-}$ ovaries at day 7 had more oocytes in germ cell cysts, fewer primordial follicles, very few oocytes surrounded by cuboidal granulosa cells (primary follicles), and no secondary follicles (fig. S3, C and D). The loss of oocytes continued, such that by day 14, very few oocytes were visualized and most of them were degenerating (Fig. 1, G and H), and histomorphometric analysis revealed a greater loss of oocytes in *Nobox*$^{-/-}$ relative to *Nobox*$^{+/-}$ ovaries (fig. S3, E and F). Thus, although *Nobox*$^{-/-}$ ovaries are grossly normal at birth, a lack of *Nobox* inhibits the majority of oocyte and follicle growth beyond the primordial follicle stage and accelerates the loss of oocytes such that by 14 days postpartum, few remain.

Perturbations in meiosis and apoptosis can lead to the accelerated loss of oocytes (*12*). However, the presence of GCNA1 and MSY2 antigens in *Nobox*$^{-/-}$ mice argues that null oocytes can progress through prophase of meiosis I (Fig. 1). Additionally, the meiotic genes *Mlh1* and *Msh5* (*12*, *13*) were also expressed in the *Nobox*$^{-/-}$ ovary (fig. S4). Terminal deoxynucleotidyl transferase–mediated deoxyuridine triphosphate nick end labeling (TUNEL) revealed no differences in apoptosis between *Nobox*$^{+/-}$ and *Nobox*$^{-/-}$ ovaries at 3 and 7

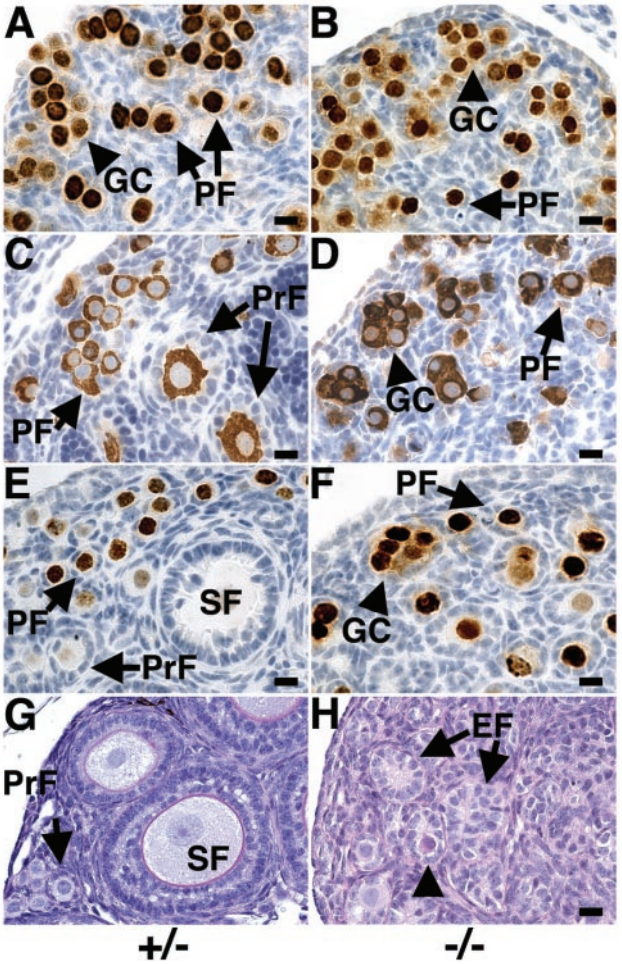

Fig. 1. Histology of *Nobox*$^{-/-}$ and control ovaries. Left panels, *Nobox*$^{+/-}$ ovaries; right panels, *Nobox*$^{-/-}$ ovaries. (**A** and **B**) Newborn *Nobox*$^{+/-}$ and *Nobox*$^{-/-}$ ovaries stained with antibody to GCNA1. GCNA1 localizes (brown staining) to oocyte nuclei within germ cell cysts (GC) and primordial follicles (PF). (**C** and **D**) Three-day-old *Nobox*$^{+/-}$ and *Nobox* $^{-/-}$ ovaries stained with antibody to MSY2 (cytoplasmic staining). Primary follicles (PrF) are present in *Nobox*$^{+/-}$ and absent in *Nobox*$^{-/-}$ ovaries. (**E** and **F**) Seven-day-old *Nobox*$^{+/-}$ and *Nobox*$^{-/-}$ ovaries stained with antibody to GCNA1. Secondary follicles (SF) are absent in null but present in heterozygous ovaries. (**G** and **H**) Fourteen-day-old *Nobox*$^{+/-}$ ovaries show presence of secondary follicles; *Nobox*$^{-/-}$ ovaries contain only empty follicular nests (EF) and degenerating oocytes (arrowhead). Scale bars, 20 μm.

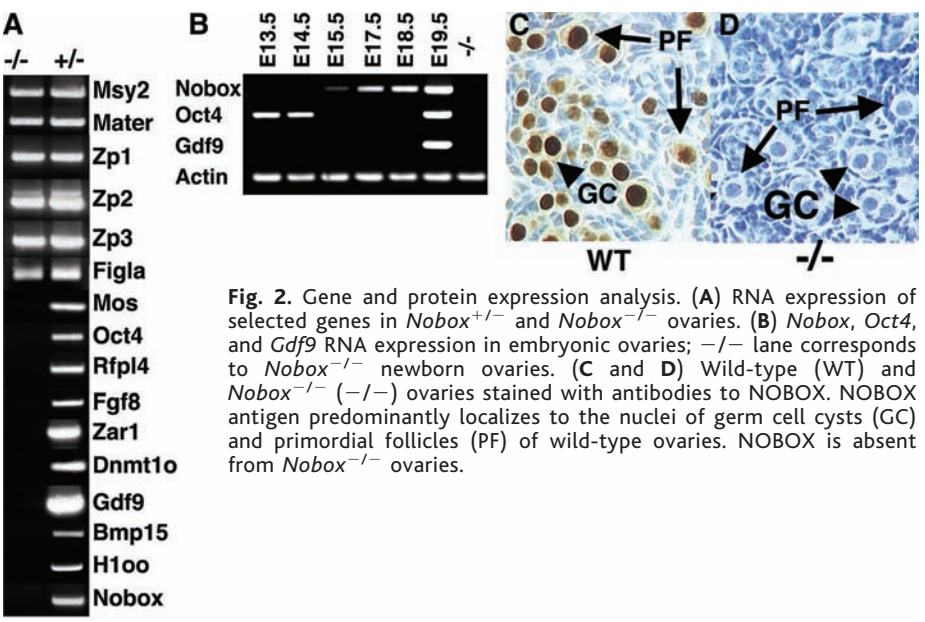

Fig. 2. Gene and protein expression analysis. (**A**) RNA expression of selected genes in *Nobox*$^{+/-}$ and *Nobox*$^{-/-}$ ovaries. (**B**) *Nobox*, *Oct4*, and *Gdf9* RNA expression in embryonic ovaries; −/− lane corresponds to *Nobox*$^{-/-}$ newborn ovaries. (**C** and **D**) Wild-type (WT) and *Nobox*$^{-/-}$ (−/−) ovaries stained with antibodies to NOBOX. NOBOX antigen predominantly localizes to the nuclei of germ cell cysts (GC) and primordial follicles (PF) of wild-type ovaries. NOBOX is absent from *Nobox*$^{-/-}$ ovaries.

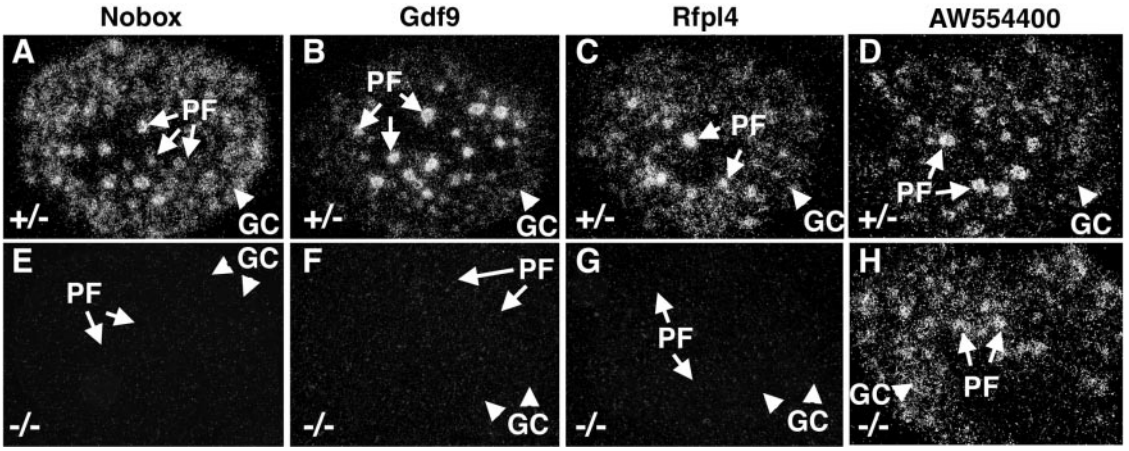

Fig. 3. In situ hybridizations. Newborn *Nobox*$^{+/-}$ ovaries (**A** to **D**) and *Nobox*$^{-/-}$ ovaries (**E** to **H**) were hybridized to antisense *Nobox*, *Gdf9*, *Rfpl4*, and *AW554400* riboprobes. Dark-field views are shown; corresponding bright-field panels are shown in fig. S7. *AW554400*, an expressed sequence tag that is expressed in *Nobox*$^{+/-}$ and *Nobox*$^{-/-}$ ovaries, served as a control for hybridization. GC, germ cell cysts; PF, primordial follicle.

days (fig. S5), and a number of pro- and antiapoptosis genes such as *Bcl2*, *Bcl2l2*, *Casp2*, and *Bax* were expressed in *Nobox*$^{+/-}$ and *Nobox*$^{-/-}$ mice (fig. S4).

A number of genes implicated in the primordial to primary transition were examined in *Nobox*$^{-/-}$ ovaries. Newborn ovaries were chosen for analysis because the same follicular types are present in *Nobox*$^{+/-}$ and *Nobox*$^{-/-}$ newborn ovaries and the histology is similar. Initiation of primordial follicle growth involves signaling by *Kitl* from granulosa cells to its receptor (*Kit*) on oocytes (*14*, *15*). This is likely not the mechanism for follicle arrest in *Nobox*$^{-/-}$ ovaries, because *Kitl* and its receptor *Kit* were expressed in *Nobox*$^{-/-}$ newborn ovaries (figs. S4 and S6). Numerous other genes implicated in early folliculogenesis were also expressed, such as growth and secreted factors *Fgf2*, *Bmp4*, and *Wnt4* and transcription factors *Gcnf* and *Foxo3a* (fig. S4). All of these genes were expressed in both *Nobox*$^{+/-}$ and *Nobox*$^{-/-}$ newborn ovaries. The common feature of all the above genes is that their expression is not limited to oocytes. Because *Nobox* is expressed exclusively in oocytes, we hypothesized that *Nobox* regulates oocyte-specific genes. Therefore, transcripts corresponding to genes preferentially expressed in oocytes were tested for expression in newborn null ovaries. *Figla*, *Mater*, *Zp1*, *Zp2*, and *Zp3* were expressed in *Nobox*$^{-/-}$ newborn ovaries (Fig. 2A). However, the transcripts corresponding to *Mos*, *Oct4*, *Rfpl4*, *Fgf8*, *Zar1*, *Dnmt1o*, *Gdf9*, *Bmp15*, and *H1oo* were down-regulated in *Nobox*$^{-/-}$ newborn ovaries (Fig. 2A); these findings suggest that *Nobox* either directly or indirectly regulates a subset of genes preferentially expressed in postnatal oocytes, some of which have been shown to play essential roles in oogenesis.

We studied whether *Nobox* expression precedes the expression of genes that it appears to regulate. The expression of *Nobox* transcripts was first detected at embryonic day 15.5, and the protein is abundantly expressed in germ cell cysts, primordial follicles, and later follicle stages (Fig. 2, B to D). *Gdf9* transcripts were first detected in newborn ovaries (Fig. 2B), and in situ hybridization showed that *Gdf9* transcripts localized faintly to germ cell cysts and primordial oocytes located in the medulla of the ovary (Fig. 3B) (fig. S7B). *Nobox* was abundantly expressed in the cortex of the ovary, where germ cell cysts reside, as well as in the medulla, where the *Gdf9*-positive primordial oocytes are located (Fig. 3A) (fig. S7A). *Rfpl4* expression was similar to that of *Gdf9* (Fig. 3C) (fig. S7C). *Oct4* is known to be expressed early in the development of the germ cell, but its transcription ceased after embryonic day 14 and reappeared in oocytes after birth (Fig. 2B) (*16*). *Nobox* RNA and protein expression preceded the reappearance of the expression of *Oct4* at the newborn stage (Fig. 2, B and C). Thus, the spatiotemporal pattern of *Nobox* expression precedes the expression of *Oct4*, *Gdf9*, and *Rfpl4*, consistent with the regulation of *Oct4*, *Gdf9*, and *Rfpl4* by *Nobox*.

Gdf9/Bmp15 double mutants arrest in early folliculogenesis with oocytes that reach more than 70 μm in diameter (*3*). Because both *Gdf9* and *Bmp15* were drastically down-regulated in *Nobox*$^{-/-}$ newborn ovaries, part of the phenotype observed in *Nobox*$^{-/-}$ ovaries is likely due to the lack of *Gdf9* and *Bmp15*. However, because these mutations do not phenocopy each other, one or more additional mechanisms must operate. The function of *Oct4*, *Fgf8*, *Rfpl4*, and *H1oo* in early folliculogenesis is unknown, but it is possible that a combinatorial derangement in the function of these genes, or another oocyte-expressed gene(s), causes the observed phenotype in ovaries that lack *Nobox*. In addition, NOBOX affected the transcription of *Zar1* and *Dnmt1o*, two critical early embryogenesis genes (Fig. 2A) (*5*). Thus, *Nobox* likely functions near the top of a signaling cascade that regulates genes necessary for oocyte and early embryo development.

The transition from primordial to growing follicles is important in regulating the size of the primordial follicle pool, reproductive lifespan, and fertility. Our results indicate that *Nobox* is an oocyte-specific homeobox gene that plays a crucial role in early folliculogenesis. *Nobox*$^{-/-}$ mice will help us to understand which genes are important in follicular growth as well as in oocyte death. Ultimately, *Nobox* (and the oocyte-specific genes that it regulates and with which it interacts) may allow us to understand nonsyndromic ovarian failure, achieve genetic control of mammalian reproductive life-span, and improve our ability to regulate fertility and generate mature eggs in vitro.

References and Notes

1. M. E. Pepling, A. C. Spradling, *Dev. Biol.* **234**, 339 (2001).
2. R. Bachvarova, in *Developmental Biology: A Comprehensive Synthesis*, L. W. Browder, Ed. (Plenum, New York, 1985), vol. 1, pp. 453–524.
3. C. Yan *et al.*, *Mol. Endocrinol.* **15**, 854 (2004).
4. Z. B. Tong *et al.*, *Nature Genet.* **26**, 267 (2000).
5. X. Wu *et al.*, *Nature Genet.* **33**, 187 (2003).
6. S. M. Soyal, A. Amleh, J. Dean, *Development* **127**, 4645 (2000).
7. N. Suzumori, C. Yan, M. Matzuk, A. Rajkovic, *Mech. Dev.* **111**, 137 (2002).
8. See supporting data on *Science* Online.
9. G. C. Enders, J. J. May 2nd, *Dev. Biol.* **163**, 331 (1994).
10. W. Gu *et al.*, *Biol. Reprod.* **59**, 1266 (1998).
11. J. Yu, N. B. Hecht, R. M. Schultz, *Biol. Reprod.* **65**, 1260 (2001).
12. W. Edelmann *et al.*, *Nature Genet.* **21**, 123 (1999).
13. W. Edelmann *et al.*, *Cell* **85**, 1125 (1996).
14. K. Manova, R. F. Bachvarova, *Dev. Biol.* **146**, 312 (1991).
15. Y. Matsui, K. M. Zsebo, B. L. Hogan, *Nature* **347**, 667 (1990).
16. M. Pesce, X. Wang, D. J. Wolgemuth, H. Scholer, *Mech. Dev.* **71**, 89 (1998).
17. Supported by NIH grant HD01426 and Basil O'Connor Grant 5-FY02-266 from the March of Dimes Birth Defects Foundation (A.R.) and by NIH grants HD33438 and HD42500 (M.M.M.). S.A.P. is an NIH Reproductive Biology Training Grant HD007165 postdoctoral fellow.

Supporting Online Material

www.sciencemag.org/cgi/content/full/305/5687/1157/DC1
Materials and Methods
Figs. S1 to S7
References

29 April 2004; accepted 19 July 2004

Uracil DNA Glycosylase Activity Is Dispensable for Immunoglobulin Class Switch

Nasim A. Begum,[1] Kazuo Kinoshita,[1] Naoki Kakazu,[2] Masamichi Muramatsu,[1] Hitoshi Nagaoka,[1] Reiko Shinkura,[1] Detlev Biniszkiewicz,[3] Laurie A. Boyer,[3] Rudolf Jaenisch,[3] Tasuku Honjo[1]*

Activation-induced cytidine deaminase (AID) is required for the DNA cleavage step in immunoglobulin class switch recombination (CSR). AID is proposed to deaminate cytosine to generate uracil (U) in either mRNA or DNA. In the second instance, DNA cleavage depends on uracil DNA glycosylase (UNG) for removal of U. Using phosphorylated histone γ-H2AX focus formation as a marker of DNA cleavage, we found that the UNG inhibitor Ugi did not inhibit DNA cleavage in immunoglobulin heavy chain (IgH) locus during CSR, even though Ugi blocked UNG binding to DNA and strongly inhibited CSR. Strikingly, UNG mutants that had lost the capability of removing U rescued CSR in UNG$^{-/-}$ B cells. These results indicate that UNG is involved in the repair step of CSR yet by an unknown mechanism. The dispensability of U removal in the DNA cleavage step of CSR requires a reconsideration of the model of DNA deamination by AID.

Activation-induced cytidine deaminase is essential for somatic hypermutation and CSR in B cells activated by antigen stimulation (*1–4*). The event that is essential for initiating CSR is AID-dependent double-strand breakages (DSBs) in the Sμ region and another switch (S) region. However, its molecular mechanism is controversial. The RNA-editing hypothesis postulates that AID deaminates cytosine in an unknown mRNA to generate a CSR endonuclease. This hypothesis is based on the structural and functional similarities between AID and apolipoprotein B (apoB) mRNA editing catalytic polypeptide 1 (APOBEC-1) (*1*, *3*, *5*, *6*). Evidence for the DNA deamination hypothesis comes from marked reduction in the class switching efficiency in UNG$^{-/-}$ B cells (*7*) and the DNA deamination activity of AID in vitro and in *Escherichia coli* (*8–12*). Phosphorylated histone H2AX (γ-H2AX) forms in the DNA domain next to a DSB soon after the DNA lesion (*13*, *14*); it recruits proteins involved in DNA repair and, thus, serves as a good marker of DNA cleavage sites. Because γ-H2AX focus formation in the IgH locus during CSR depends on AID (*15*) and the absence of H2AX severely reduces the efficiency of CSR (*16*), γ-H2AX focus formation in the IgH locus is an important marker for DSB during CSR. Here, we report evidence for involvement of UNG in a step after DSBs and the dispensability of removal by UNG in CSR, using γ-H2AX focus formation and UNG mutants, respectively. These results cannot be explained by the current DNA deamination model and are rather consistent with the RNA-editing hypothesis.

To understand the molecular mechanism of DNA cleavage during CSR, we set up chromatin immunoprecipitation (ChIP) assays using γ-H2AX–specific antibodies to monitor focus formation at the IgH locus in the mouse lymphoma cell line CH12F3-2, which switches efficiently to IgA after stimulation. The switch stimulus with CD40L, interleukin 4, and transforming growth factor–β (CIT) induced accumulation of γ-H2AX at the IgH locus (Sμ and Cμ) (Fig. 1A). This accumulation was specific to the IgH locus because many genes that do not encode immunoglobulins, including those for RAG1, CD19, CD5, and glyceraldehyde-3-phosphate dehydrogenase (GAPDH), were not coimmunoprecipitated by antibodies against γ-H2AX (Fig. 1B). Inversely, the Sμ association was specific to γ-H2AX and NBS1 but not to BRCA1 as reported (*15*) (Fig. 1C). The signal could be detected as early as 4 hours after CIT and tamoxifen (OHT) stimulation of CH12F3-2 derivative (AER) cells expressing

[1]Department of Medical Chemistry and Molecular Biology, Graduate School of Medicine, Kyoto University, Yoshida Sakyo-ku, Kyoto 606-8501, Japan. [2]Department of Molecular-Targeting Cancer Prevention, Graduate School of Medical Science, Kyoto Prefectural University of Medicine, Kajii-cho, Kamigyo-ku, Kyoto 602-8566, Japan. [3]Whitehead Institute for Biomedical Research, 9 Cambridge Center, Cambridge, MA 02142, USA.

*To whom correspondence should be addressed. E-mail: honjo@mfour.med.kyoto-u.ac.jp

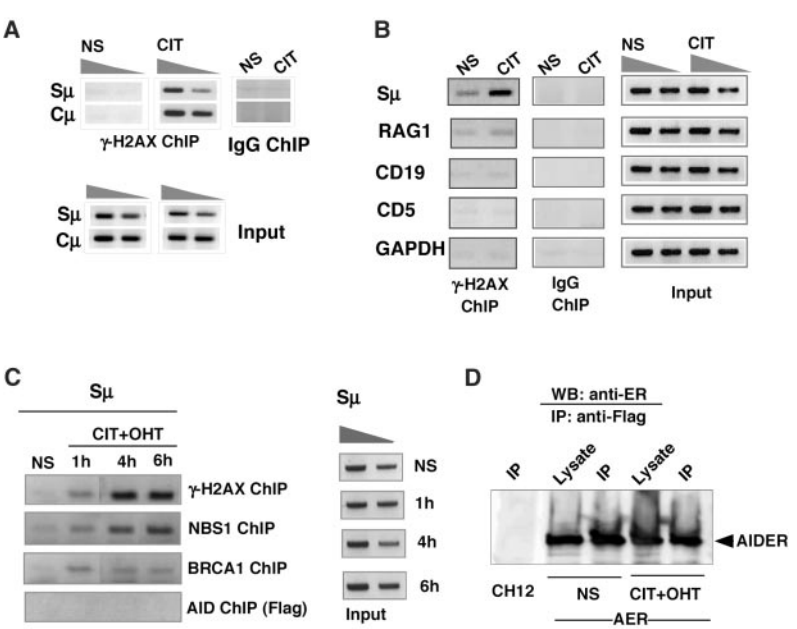

Fig. 1. Class switch–induced accumulation of γ-H2AX is specific to the IgH locus. γ-H2AX ChIP and polymerase chain reaction (PCR) were performed using cells that were not stimulated (NS) or were stimulated with CIT. Twofold serial dilutions of γ-H2AX and IgG ChIP (control) samples, as well as 5% input DNA, were analyzed by PCR using Sμ- and Cμ-specific primers. (**A**) γ-H2AX ChIP with the CH12F3-2 cell line stimulated (or not) with CIT for 24 hours. (**B**) γ-H2AX ChIP was done after 6 hours of CIT stimulation of CH12F3-2 cells. PCR of ChIP DNA was performed for Sμ and non-Ig genes indicated. (**C**) AER cells were stimulated (or not) as indicated with CIT and tamoxifen (OHT) and subjected to ChIP assay for Sμ using different Ab shown. (**D**) Immunoprecipitation (IP) of AIDER by anti-Flag M2 agarose beads, followed by Western blotting (WB) with antibodies against ER. About 5×10^5 cell equivalent amounts of lysates and IP were loaded per lane.

AID fused with the Flag-tagged hormone-binding domain (ER) of the estrogen receptor (AIDER) (*17*). However, anti-Flag ChIP to detect any association of AIDER with Sμ was negative, in disagreement with a previous report (*18*), although we could immunoprecipitate AIDER efficiently (Fig. 1, C and D).

To examine the effect of UNG inhibition on γ-H2AX ChIP, we generated a CH12F3-2–derivative line (UTT) with an expression vector containing Ugi and the internal ribosome entry site–green fluorescent protein (Ugi-IRES-GFP) gene that could be repressed by Tet. Ugi inactivates UNG by forming the UNG-Ugi complex (*19*). When Ugi was expressed, the cells showed low levels of IgA switching (1.6%) by CIT stimulation in contrast to when Ugi was not expressed (22%) (Fig. 2A). We then compared γ-H2AX ChIP of the Sμ region in CIT-stimulated UTT cells in the presence or absence of Ugi. As shown in Fig. 2B, γ-H2AX ChIP of the IgH locus (Sμ and Cμ), which depended on the switch stimulus, was not significantly affected by expression of Ugi, although Ugi strongly inhibited CSR.

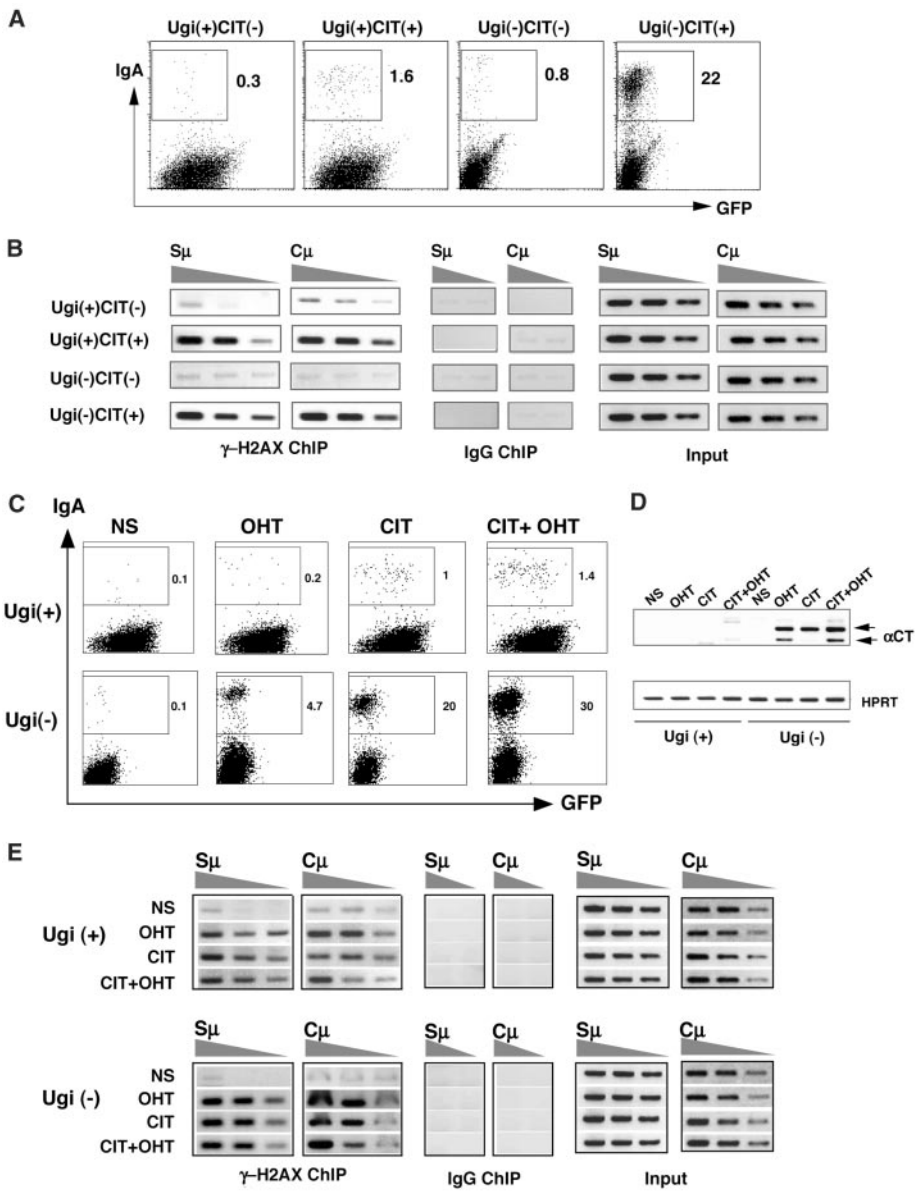

Fig. 2. Inhibition of UNG blocks IgA switching but not DSBs at the IgH locus. (**A**) UTT cells were stimulated by CIT in the presence or absence of Ugi expression, and surface IgA expression was determined at day 2. (**B**) γ-H2AX ChIP analysis of UTT cells after 24 hours stimulation. PCR of ChIP samples and 5% input DNA was carried out for Sμ and Cμ loci after twofold serial dilution. (**C**) UAR cells were stimulated as indicated, and surface IgA expression was examined at day 2 by fluorescence-activated cell sorting (FACS). Numbers indicate percentages of switched cells. (**D**) UAR cells were treated as indicated for 24 hours, and reverse transcription PCR (RT-PCR) of alpha circle transcript (αCT) and hypoxanthine-guanine phosphoribosyltransferase (HPRT, control) was performed. Arrows indicate spliced variants of αCT (*20*). (**E**) γ-H2AX ChIP analysis of UAR cells stimulated for 6 hours as indicated. ChIP DNA and 5% of input DNA were twofold serially diluted and analyzed by PCR for Sμ and Cμ.

To confirm that this observation depends on AID, we generated another derivative of CH12F3-2 (UAR) that expressed Ugi-IRES-GFP and AIDER under the regulation of Tet-repressible and constitutive promoters, respectively. As shown in Fig. 2C, Ugi expression drastically reduced class switching induced by stimulation with OHT, CIT, or both. CSR inhibition by Ugi was also demonstrated by the absence of circle transcripts (*20*) derived from looped-out circular DNA after CSR (Fig. 2D). By contrast, Ugi expression did not inhibit γ-H2AX ChIP of the IgH locus, which was induced in all activation conditions tested (Fig. 2E). The results indicate that γ-H2AX focus formation at the IgH locus depends on AID, but not on UNG, although, overall, CSR is markedly reduced by inhibition of UNG.

To substantiate the above conclusion, immunohistochemistry and fluorescence in situ hybridization (FISH) assays were carried out with CSR-stimulated UAR cells to detect the γ-H2AX focus formation at the IgH locus (Fig. 3A). The number of IgH loci that overlapped with foci detected by γ-H2AX antibody immunostaining was estimated by blind tests and found to increase to a similar level, by CIT and OHT stimulation, regardless of the absence or presence of Ugi (Fig. 3B). The results indicate that AID-induced DSBs are independent of UNG activity.

Accumulation of point mutations and deletions in the germline Sμ region during CSR is known to reflect DNA cleavage during CSR (*15*, *21*, *22*). We therefore examined whether Ugi inhibits the Sμ mutation in UAR cells stimulated by CIT and OHT. Ugi expression did not show significant changes in the mutation rate (Fig. 3C) and base specificity of mutations (fig. S1). The results also support the conclusion that UNG is required, not for Sμ cleavage, but probably for subsequent repair steps during CSR.

To understand the role of UNG in CSR, we examined whether well-defined loss-of-function mutants of UNG (*19*, *23*) could rescue CSR in $UNG^{-/-}$ B cells. D145N, N204V, and H268L mutants of human UNG (*24*) have less than 0.6% uracil DNA glycosylase activity but retain the ability to bind DNA (*23*). Therefore, we reasoned that the above mutations may have milder or different phenotypes on CSR than inhibition of DNA binding by Ugi expression (*19*). Because the amino acid sequences of human and mouse UNG are highly homologous (92% identity and 96% similarity) and the mutated residues above are conserved in all UNG homologs so far identified, we generated mouse counterparts of the mutants (fig. S2). The mouse UNG mutants were expressed in $UNG^{-/-}$ B cells by a retrovirus vector, and class switching to IgG1 was assayed by surface immunoglobulin staining. Surprisingly, all the mutants could recover wild-type levels of CSR in $UNG^{-/-}$ B cells (Fig. 4, A and B). In

contrast, double mutants D145N+N204V and H268L+D145N were incapable of recovering CSR, which suggests a structural requirement for an unknown function of UNG. All of these UNG mutants had little, if any, uracil DNA glycosylase activity in extracts of transfected $UNG^{-/-}$ B cells, although protein expression levels of these mutants were similar to wild-type (Fig. 4, C and D). It is of note that N204V has no binding activity to U (table S1). These results indicate that the reduction of CSR in $UNG^{-/-}$ mice is not owing to loss of U removal activity but to loss of a yet-unknown activity of UNG.

Although $UNG^{-/-}$ B cells have only one-tenth the efficiency of wild-type class switching activity (*7*), $UNG^{-/-}$ cells appear to remove U efficiently by alternative enzymes, because the general mutation frequency in the mutant mice was not strikingly enhanced (*25*). It should be examined whether U removal activity of any enzyme other than UNG is required for CSR. Although B cells with UNG mutations in patients with hyper-IgM syndrome (HIGM) were reported to be defective in generation of stimulation-induced DSBs in Sμ (*26*), the reason for this apparent discrepancy is elusive. Unexpectedly, an F242S mutant equivalent to the P2 patient mutation was active for both U removal and CSR (Fig. 4).

The residual CSR activity in $UNG^{-/-}$ mice indicates that UNG is important but not essential for CSR (*7*). Its DNA binding activity rather than catalytic activity appears to be critical because Ugi almost completely inactivates UNG as well as CSR. Interestingly, UNG without the capability of removing U is required for replication of vaccinia virus DNA (*27*). The severe combined immunodeficient (SCID) mutant mouse has no activity of the DNA-dependent protein kinase catalytic subunit (DNA-PKcs) but shows about 50% CSR activity for all isotypes (*28*). By contrast, B cells of DNA-PKcs null mice cannot switch to any isotypes except for IgG1 with 30 to 50% efficiency (*29*). Recently, ATPase-defective mutation of MSH2 was also reported to have milder phenotypes on CSR than those from MSH2 deficiency (*30*). Requirement of the proteins but not of their known catalytic activities implies that they may serve as a scaffold to recruit other members of the repair machinery. On the basis of these results, we propose that UNG and other mismatch repair proteins recruit different error-prone polymerases to repair cleaved ends generated during CSR and somatic hypermutation. Perturbation of somatic hypermutation base specificity in $UNG^{-/-}$ B cells (*7*) could be explained by the change of error-prone polymerases recruited.

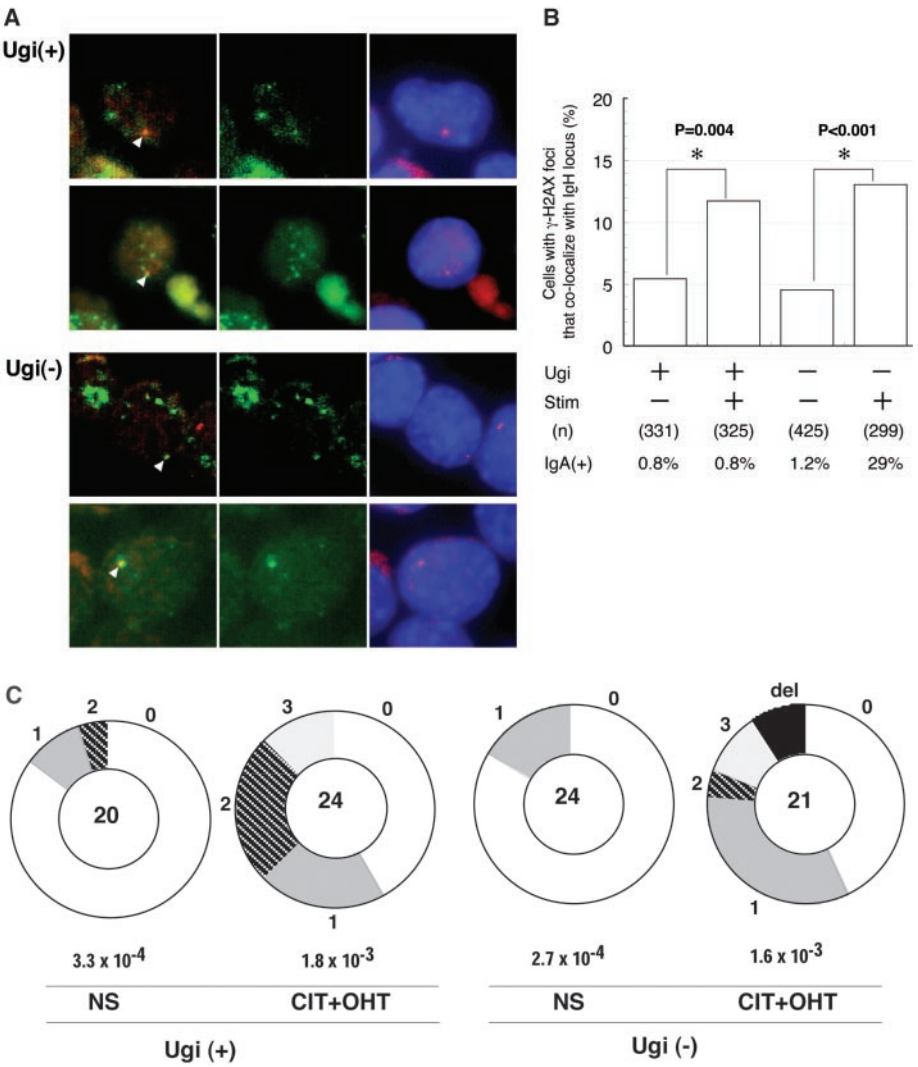

Fig. 3. Immunohistochemistry and FISH assay for γ-H2AX focus formation in the presence of Ugi. (**A** and **B**) UAR cells were stimulated with CIT and OHT for 24 hours in the presence or absence of Ugi. (A) Fixed cells were immunostained with antibodies against γ-H2AX (green), and FISH was done using fluorescence-labeled IgH probe (red). Two representative cases of colocalization (arrow head) after CSR-induced stimulation in each of UNG-inhibited [Ugi(+)] and uninhibited [(Ugi(–)] conditions are shown. Rightmost panel shows DAPI (blue)-stained images of the nuclei. (B) Frequencies of cells with γ-H2AX foci that colocalize with IgH loci in the four different culture conditions. Numbers of cells analyzed are shown in parentheses. IgA(+) means percentage of surface IgA-positive cells measured by FACS 48 hours after stimulation. (**C**) Effect of Ugi on mutational frequency in the Sμ region. UAR cells were activated for 6 days by CIT and OHT, with or without Ugi expression, and the upstream region of Sμ core repeats was amplified by PCR. Pie charts represent the proportion of clones (total clones in centers) with given numbers of mutations/deletions (numbers outside the pie slices). Total mutation frequencies are shown below. The frequency of stimulation-induced mutations is significant in the presence ($P < 0.001$) or absence ($P < 0.003$) of Ugi.

References and Notes

1. T. Honjo, K. Kinoshita, M. Muramatsu, *Annu. Rev. Immunol.* **20**, 165 (2002).
2. T. Honjo, M. Muramatsu, S. Fagarasan, *Immunity* **20**, 659 (2004).
3. M. Muramatsu *et al.*, *Cell* **102**, 553 (2000).
4. P. Revy *et al.*, *Cell* **102**, 565 (2000).
5. S. Anant, N. O. Davidson, *Curr. Opin. Lipidol.* **12**, 159 (2001).
6. S. Ito *et al.*, *Proc. Natl. Acad. Sci. U.S.A.* **101**, 1975 (2004).
7. C. Rada *et al.*, *Curr. Biol.* **12**, 1748 (2002).
8. A. R. Ramiro, P. Stavropoulos, M. Jankovic, M. C. Nussenzweig, *Nature Immunol.* **4**, 452 (2003).
9. S. K. Dickerson, E. Market, E. Besmer, F. N. Papavasiliou, *J. Exp. Med.* **197**, 1291 (2003).
10. P. Pham, R. Bransteitter, J. Petruska, M. F. Goodman, *Nature* **424**, 103 (2003).
11. J. Chaudhuri *et al.*, *Nature* **422**, 726 (2003).
12. A. Sohail, J. Klapacz, M. Samaranayake, A. Ullah, A. S. Bhagwat, *Nucleic Acids Res.* **31**, 2990 (2003).
13. J. A. Downs, N. F. Lowndes, S. P. Jackson, *Nature* **408**, 1001 (2000).
14. E. P. Rogakou, D. R. Pilch, A. H. Orr, V. S. Ivanova, W. M. Bonner, *J. Biol. Chem.* **273**, 5858 (1998).
15. S. Petersen *et al.*, *Nature* **414**, 660 (2001).
16. A. Celeste *et al.*, *Science* **296**, 922 (2002); published online 4 April 2002.
17. T. Doi, K. Kinoshita, M. Ikegawa, M. Muramatsu, T. Honjo, *Proc. Natl. Acad. Sci. U.S.A.* **100**, 2634 (2003).
18. Y. Nambu *et al.*, *Science* **302**, 2137 (2003).
19. C. D. Mol *et al.*, *Cell* **82**, 701 (1995).
20. K. Kinoshita, M. Harigai, S. Fagarasan, M. Muramatsu, T. Honjo, *Proc. Natl. Acad. Sci. U.S.A.* **98**, 12620 (2001).

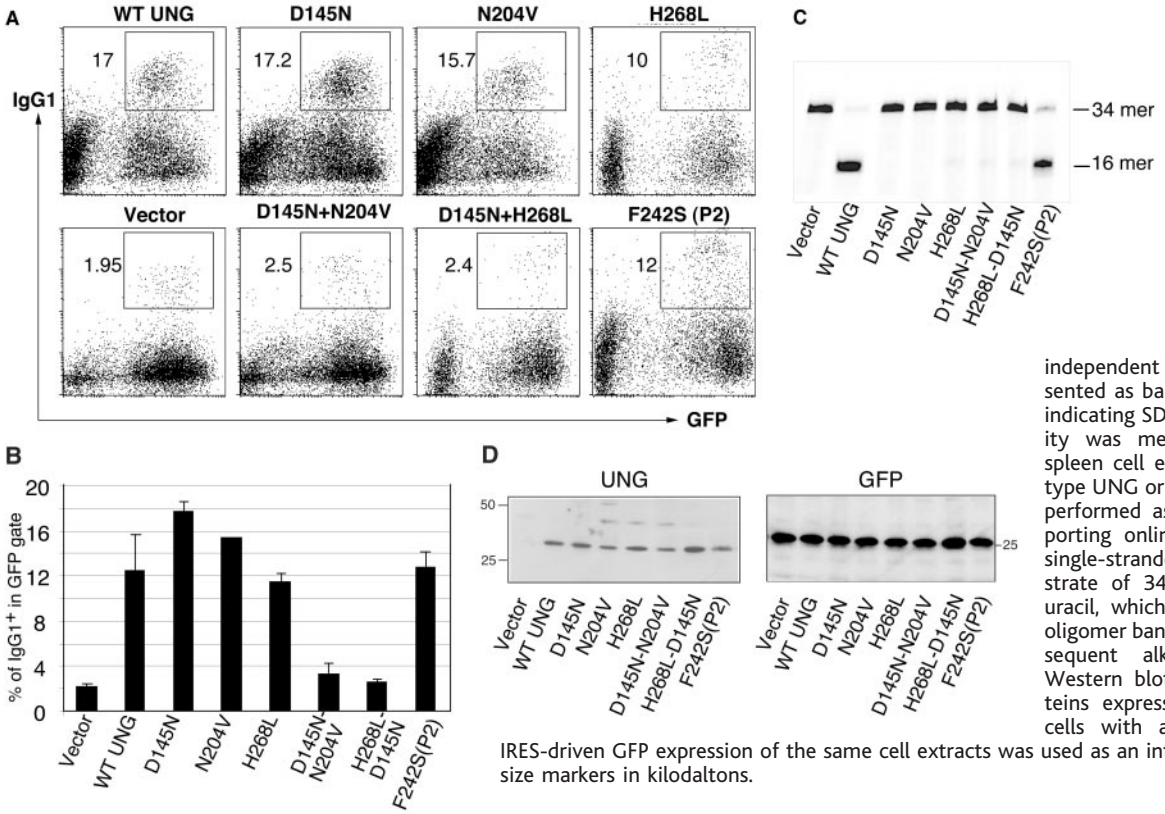

Fig. 4. Removal of U by UNG is dispensable for CSR. (**A**) IgG1 switching profiles of activated $UNG^{-/-}$ spleen cells at day 3 after retroviral introduction of wild-type (WT) and mutants of UNG are shown. Numbers indicate percentages of $IgG1^+$ cells in GFP^+ gated cells. (**B**) Percentages of IgG^+ cells in GFP^+ cells were calculated from three independent experiments and presented as bar graphs with error bars indicating SD. (**C**) In vitro UNG activity was measured using $UNG^{-/-}$ spleen cell extracts expressing wild-type UNG or mutants. The assay was performed as described in the supporting online material by using a single-stranded oligonucleotide substrate of 34-oligomer containing a uracil, which is converted to a 16-oligomer band by U removal and subsequent alkaline treatment. (**D**) Western blot of UNG mutant proteins expressed in $UNG^{-/-}$ spleen cells with antibody against UNG. IRES-driven GFP expression of the same cell extracts was used as an internal control. Numbers, size markers in kilodaltons.

21. H. Nagaoka, M. Muramatsu, N. Yamamura, K. Kinoshita, T. Honjo, *J. Exp. Med.* **195**, 529 (2002).
22. R. Shinkura *et al*., *Nature Immunol.* **5**, 707 (2004).
23. C. D. Mol *et al*., *Cell* **80**, 869 (1995).
24. Single-letter abbreviations for the amino acid residues are as follows: D, Asp; F, Phe; H, His; L, Leu; N, Asn; S, Ser; and V, Val.
25. H. Nilsen *et al*., *Mol. Cell* **5**, 1059 (2000).
26. K. Imai *et al*., *Nature Immunol.* **4**, 1023 (2003).
27. F. S. De Silva, B. Moss, *J. Virol.* **77**, 159 (2003).
28. G. C. Bosma *et al*., *J. Exp. Med.* **196**, 1483 (2002).
29. J. P. Manis, D. Dudley, L. Kaylor, F. W. Alt, *Immunity* **16**, 607 (2002).
30. A. Martin *et al*., *J. Exp. Med.* **198**, 1171 (2003).

31. We are grateful to S. Fagarasan and T. Doi for critical comments and for support by Center of Excellence grant (12CE2006) from the Ministry of Education, Culture, Sports, Science, and Technology of Japan.

Supporting Online Material
www.sciencemag.org/cgi/content/full/305/5687/1160/DC1
Materials and Methods
Figs. S1 and S2
Table S1
References and Notes

29 March 2004; accepted 12 July 2004

Gefitinib-Sensitizing *EGFR* Mutations in Lung Cancer Activate Anti-Apoptotic Pathways

Raffaella Sordella, Daphne W. Bell, Daniel A. Haber, Jeffrey Settleman*

Gefitinib (Iressa, AstraZeneca Pharmaceuticals) is a tyrosine kinase inhibitor that targets the epidermal growth factor receptor (EGFR) and induces dramatic clinical responses in nonsmall cell lung cancers (NSCLCs) with activating mutations within the EGFR kinase domain. We report that these mutant EGFRs selectively activate Akt and signal transduction and activator of transcription (STAT) signaling pathways, which promote cell survival, but have no effect on extracellular signal–regulated kinase signaling, which induces proliferation. NSCLC cells expressing mutant EGFRs underwent extensive apoptosis after small interfering RNA–mediated knockdown of the mutant *EGFR* or treatment with pharmacological inhibitors of Akt and STAT signaling and were relatively resistant to apoptosis induced by conventional chemotherapeutic drugs. Thus, mutant EGFRs selectively transduce survival signals on which NSCLCs become dependent; inhibition of those signals by gefitinib may contribute to the drug's efficacy.

Receptor tyrosine kinases of the EGFR family regulate essential cellular functions, including proliferation, survival, migration, and differentiation, and appear to play a centralrole in the etiology and progression of solid tumors (*1*, *2*). EGFR is frequently overexpressed in breast, lung, colon, ovarian, and brain tumors, prompting the development of specific pharmacological inhibitors such as gefitinib (Iressa, AstraZeneca Pharmaceuticals), which disrupts EGFR kinase activity by binding the adenosine triphosphate (ATP) pocket within the catalytic domain (*3*). Gefitinib has induced substantial clinical responses in about 10% of patients with chemotherapy-refractory NSCLC (*4*–*7*). Nearly all gefitinib-responsive lung cancers harbor somatic mutations within the EGFR kinase domain, whereas no mutations have been seen in nonresponsive cases (*8*, *9*). These heterozygous mutations include small in-frame deletions and missense substitutions clustered within the ATP-binding pocket.

Center for Molecular Therapeutics, Massachusetts General Hospital Cancer Center and Harvard Medical School, Building 149, 13th Street, Charlestown, MA 02129, USA.

*To whom correspondence should be addressed. E-mail: settleman@helix.mgh.harvard.edu

With use of transient transfections of mutant EGFRs, we showed previously that both types of mutations lead to increased EGF-dependent receptor activation as measured by autophosphorylation of Tyr^{1068} (Y1068), one of the prominent C-terminal phosphorylation sites of EGFR (*8*). To enable studies of qualitative differences in signaling by mutant EGFRs, we generated stable lines of nontransformed mouse mammary epithelial cells (NMuMg) expressing wild-type or mutant EGFRs (*10*) and analyzed EGF-mediated autophosphorylation of multiple tyrosine residues linked to activation of distinct downstream effectors (Fig. 1A) (*1*). Cell lines were generated that expressed either wild-type EGFR or one of two recurrent mutations detected in tumors from gefitinib-responsive patients: the missense mutation $Leu^{858} \rightarrow Arg^{858}$ (L858R) and the 18–base pair inframe deletion, delL747-P753insS (fig. S1). Notably different tyrosine phosphorylation patterns were observed between wild-type and the two mutant EGFRs at several C-terminal sites (Fig. 1B). EGF-induced phosphorylation of Y1045 and Y1173 was almost indistinguishable between wild-type and mutant EGFRs, whereas phosphorylation of Y992 and Y1068 was substantially increased in both mutants. Interestingly, Y845 was highly phosphorylated in the L858R missense mutant, but not in the wild-type or the deletion mutant, and hence appears to be unique in distinguishing between the two types of EGFR mutations. The differential EGF-induced tyrosine phosphorylation pattern seen with wild-type and mutant receptors was reproducible in transiently transfected COS7 cells, ensuring against potential cell type–specific effects (fig. S2). These observations suggest that the gefitinib-sensitive mutant EGFRs have the potential to transduce signals that are qualitatively distinct from those mediated by wild-type EGFR. These differences may result directly from structural alterations within the catalytic pocket affecting substrate specificity or from altered interactions with accessory proteins that modulate EGFR signaling.

The establishment of cell lines stably transfected with mutant EGFRs made it possible to compare the phosphorylation status of the major downstream targets of EGFR in a shared cellular background. EGF-induced activation of extracellular signal–regulated kinase 1 (Erk1) and Erk2 via Ras, of Akt via phospholipase C γ and phosphatidylinositol 3-kinase (PI3K), and

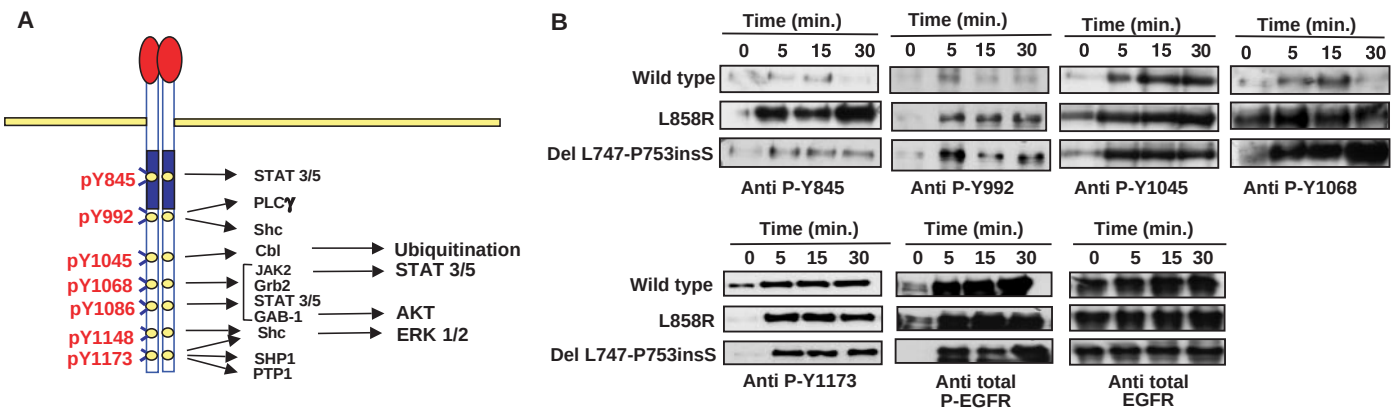

Fig. 1. (**A**) Schematic representation of the autophosphorylation sites in the EGFR and the activation of the corresponding major signal transduction pathways. (**B**) Time course of ligand-induced phosphorylation of the various Tyr residues of the delL747-P753insS and L858R EGFR mutants, as compared with wild-type EGFR, after the addition of EGF (30 ng/ml) to stably transfected NMuMg. The phosphorylation of EGFR was determined by immunoblotting of whole cell lysates collected at the indicated times post-EGF treatment with antibodies that specifically recognize the phosphorylated Tyr^{845}, Tyr^{992}, Tyr^{1045}, Tyr^{1068}, and Tyr^{1173} of EGFR. Total phosphorylation of EGFR expressed in transfected cells was determined with the use of the py20 antibody. Total EGFR expression is also indicated.

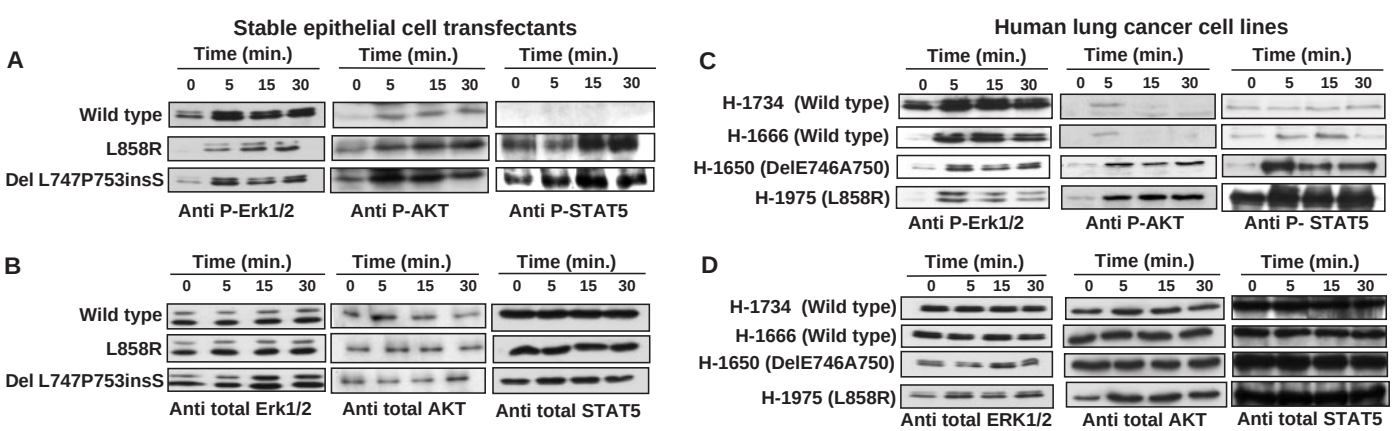

Fig. 2. Selective activation of Akt and STAT5 by mutant EGFRs. (**A**) Time course of ligand-induced activation of specific signal transduction pathway downstream of the delL747-P753insS and L858R EGFR mutants, as compared with wild-type EGFR in stably-transfected NMuMg cells, after the addition of 30 ng/ml of EGF to serum-starved cells. Phosphorylation of Erk1 and Erk2 was determined by immunoblotting with an antibody that specifically recognizes the phosphorylated Thr^{202} and Tyr^{204} residues. For AKT and STAT5, phospho-specific antibodies against Ser^{471} and Tyr^{694}, respectively, were used. (**B**) Total Erk1, Erk2, Akt, and STAT5 from the corresponding cell lysates used in (A) was determined by immunoblotting with the relevant antibodies. (**C** and **D**) An analysis of NSCLC human cell lines that harbor either wild-type *EGFR* or heterozygous activating mutations in *EGFR*, analogous to that performed on the stable transfectants in (A) and (B). In both sets of experiments, the expression of mutant EGFRs is associated with selective activation of Akt and STAT5 but not of Erk1 and Erk2.

of signal transducer and activator of transcription 3 (STAT3) and STAT5 via Janus kinase 2 (JAK2) are essential downstream pathways mediating oncogenic effects of EGFR (*1*). EGF-induced Erk activation was essentially indistinguishable among cells expressing wild-type EGFR or either of the two activating EGFR mutants (Fig. 2, A and B). In contrast, phosphorylation of both Akt and STAT5 was substantially elevated in cells expressing either of the mutant EGFRs (Fig. 2, A and B). Increased phosphorylation of STAT3 was similarly observed in cells expressing mutant EGFRs (*11*). The unaltered Erk activation by the mutant EGFRs is consistent with the absence of increased phosphorylation of Y1173, an important docking site for the Shc and Grb-2 adaptors that leads to Ras activation and subsequent Erk phosphorylation (*1*). The increased Akt and STAT phosphorylation after activation of the mutant EGFRs is consistent with the increase in Y992 and Y1068 phosphorylation, both of which have been previously linked to Akt and STAT activation (*1*). Thus, the selective EGF-induced autophosphorylation of C-terminal tyrosine residues within EGFR mutants is correlated well with the selective activation of downstream signaling pathways.

To extend these observations to lung cancer cells in which *EGFR* mutations appear to drive tumorigenesis, we studied lines derived from five NSCL tumors. NCI-H1975 carries the recurrent heterozygous missense mutation L858R and NCI-H1650 has the in-frame deletion delE746-A750, whereas NCI-358, NCI-H1666, and NCI-H1734 express wild-type *EGFR* (fig. S3). As in transfected cells, EGF-induced autophosphorylation of Y992 and Y1068 was markedly elevated in the two lines with endogenous *EGFR* mutations, as was phosphorylation of Akt and STAT5 but not Erk (Fig. 2, C and D, and fig. S4).

The oncogenic activity of EGFR reflects the activation of signals that promote both cell proliferation and cell survival (*12*). Although these pathways exhibit overlap, Ras-mediated activation of the Erk kinases contributes substantially to the proliferative activity of EGFR, whereas activation of Akt and STATs is largely linked to an anti-apoptotic function (*12–17*). The two lung cancer cell lines harboring *EGFR* mutations exhibited increased cell number over time relative to cells expressing wild-type EGFR when maintained in the presence of EGFR in low serum concentration (Fig. 3A). However, the proliferation rate and cell density at confluence were comparable at normal serum concentrations (*11*). In contrast, apoptotic pathways were markedly different in lung cancer cells with mutant EGFRs: Small interfering RNA (siRNA)–mediated specific inactivation of mutant *EGFR* in these cell lines resulted in rapid and massive apoptosis. About 90% of NCI-H1975 cells transfected with L858R-specific siRNA died within 96 hours, as did NCI-H1650 cells transfected with delE746-

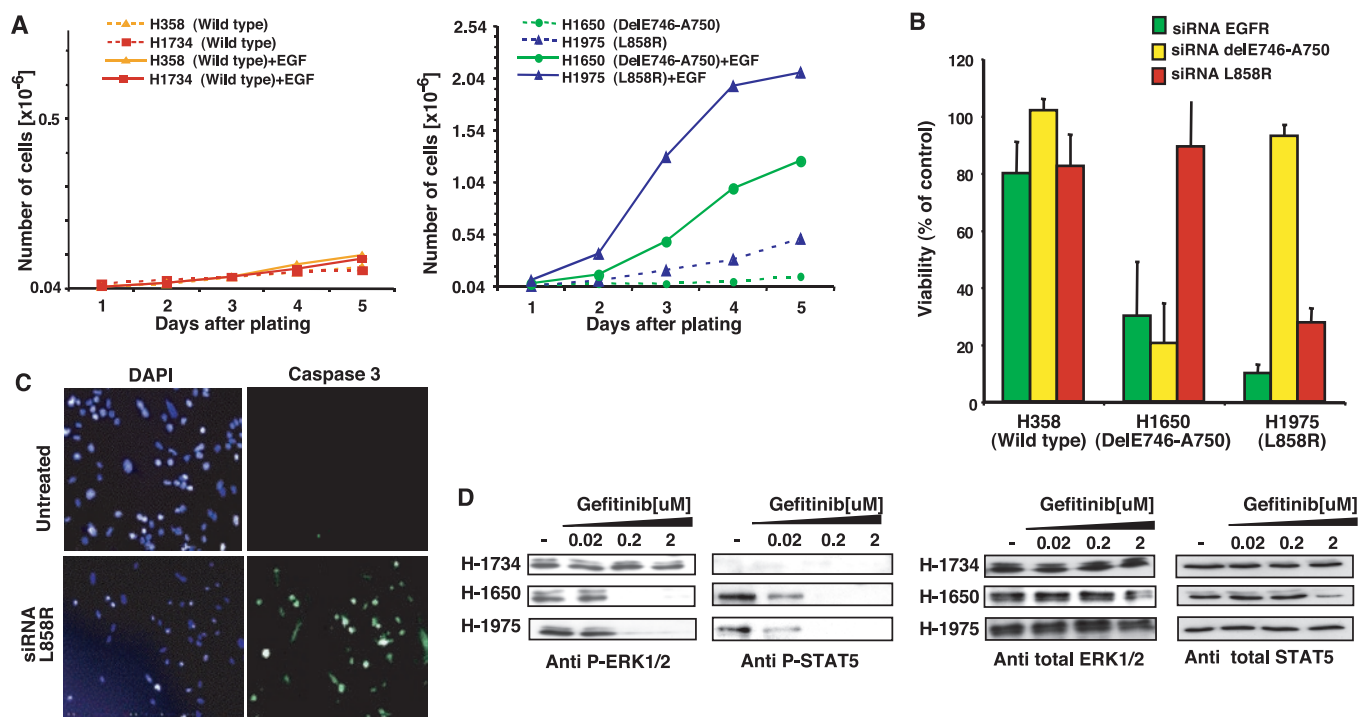

Fig. 3. Expression of mutant EGFRs provides an essential cell survival signal in NSCLC. (**A**) Growth curves for two NSCLC cell lines expressing only wild-type *EGFR* (left) and two lines with the indicated heterozygous *EGFR* mutations (right) maintained in the presence or absence of 100 ng/ml of EGF. The scale of the graph to the left is expanded in order to visualize each of the curves. (**B**) siRNA-mediated specific knockdown of the mutant *EGFR* allele in NSCLC cell lines results in rapid and massive apoptosis. H1975 cells transfected with siRNA targeting the endogenous L858R missense transcript, but not those transfected with siRNA against the delE746A-750 transcript, showed 90% decreased viability relative to untreated cells (control) as measured by the MTT assay within 96 hours of transfection. Similarly, H1650 cells expressing the delE746A-750 mutant were susceptible to siRNA targeting the endogenous mutation but not the L858R transcript. H358 cells expressing wild-type EGFR were unaffected by the mutant-specific siRNAs, and siRNA directed against wild-type EGFR (which also targets the mutants) had no detectable effect on cells expressing only wild-type EGFR but effectively induced apoptosis in lines expressing mutant EGFR. Each column reflects the average of four different experiments, each performed in triplicate. Error bars indicate standard deviation. (**C**) The decreased number of viable cells after siRNA treatment in (B) is due to an increase in apoptosis as revealed by immunostaining of fixed cells with an antibody directed specifically against cleaved caspase-3. Cells were co-stained with 4′,6′-diamidino-2-phenylindole (DAPI) to reveal nuclei. (**D**) The H1650 and H1975 lung cancer cell lines, which express endogenous *EGFR* kinase domain mutations, exhibit comparably increased drug sensitivity with respect to Erk as well as STAT5 phosphorylation. The activity of Erk1, Erk2, and STAT5 was determined by immunoblotting with phospho-specific antibodies. Cells were untreated or pretreated for 3 hours with increasing concentrations of gefitinib and then stimulated with 30 ng/ml of EGF for 15 min. Total Erk1, Erk2, and STAT5 protein were also determined by immunoblotting and are shown in the lower panels.

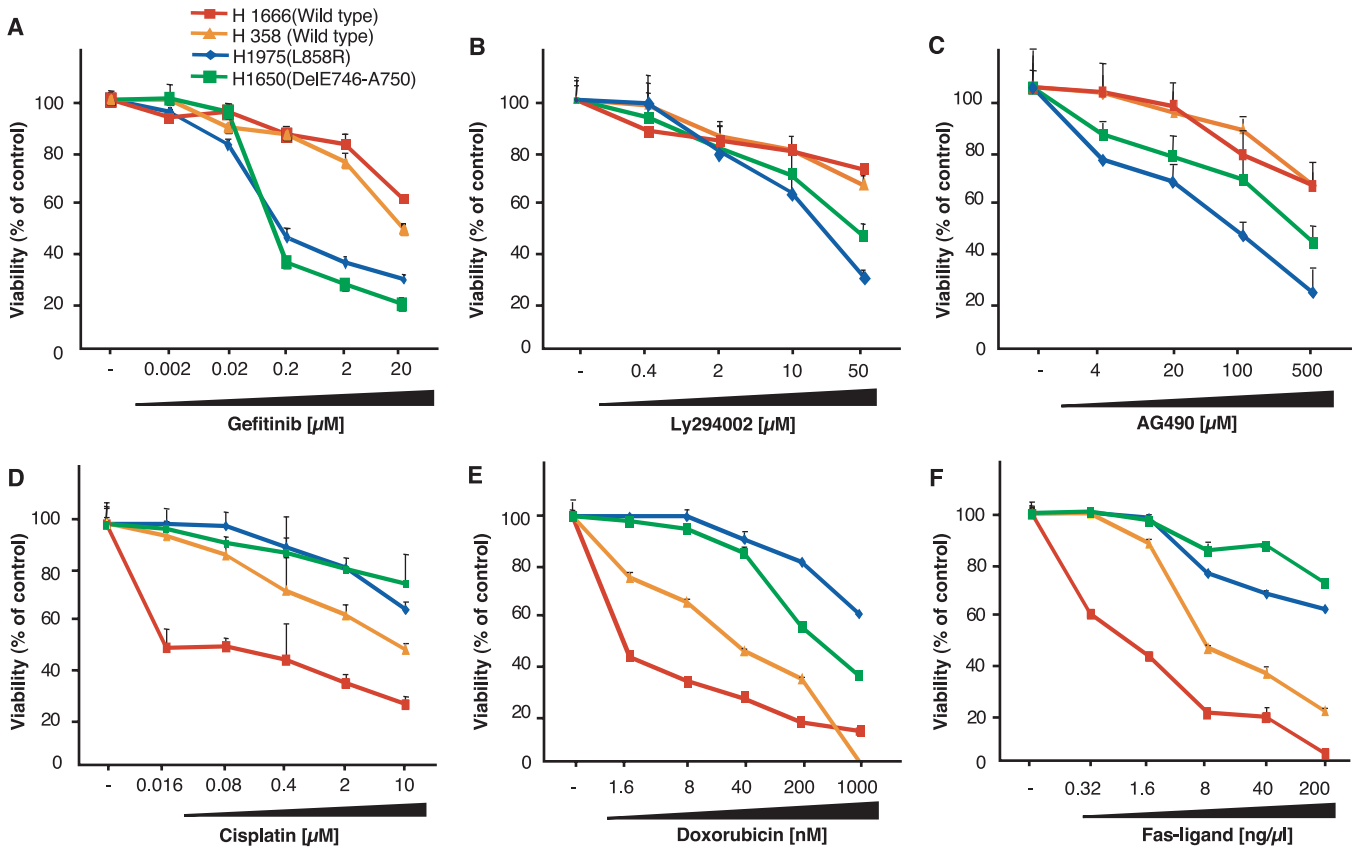

Fig. 4. NSCLC lines expressing EGFR mutants exhibit increased sensitivity to Akt and STAT inhibition and increased resistance to chemotherapeutic drugs. (**A**) The H1650 and H1975 lung cancer cell lines with endogenous *EGFR* mutations show increased sensitivity to gefitinib relative to lung cancer lines expressing wild-type EGFR. Cells were treated for 72 hours in the presence of increasing concentration of gefitinib, and their viability was then measured with the MTT assay and plotted as a percentage of the viability of untreated cells (control). (**B** and **C**) NSCL tumor lines harboring EGFR kinase domain mutations exhibit increased sensitivity to pharmacological inhibitors of anti-apoptotic signaling mediated by the PI-3K–Akt pathway (B) and the Jak-STAT pathway (C). The PI-3K inhibitor Ly294002 (Eli Lilly) was used at the indicated concentrations to disrupt Akt activation, and the Jak inhibitor AG490 was used at the indicated concentrations to disrupt STAT activation. (**D** to **F**) NSCL tumor lines harboring EGFR kinase domain mutations exhibit significantly increased resistance to the chemotherapeutic agents cisplatin (D) and doxorubicin (E) as well as the pro-apoptotic Fas ligand (F) relative to NSCL tumor lines expressing wild-type EGFR. Cells were treated with increasing concentrations of cisplatin, doxorubicin, or Fas ligand in the presence of 100 ng/ml of EGF, and their viability was determined after 96 hours with use of the MTT assay. Error bars represent standard deviation.

A750-specific siRNA (Fig. 3, B and C). SiRNA specific for either *EGFR* mutation had no effect on cells expressing the alternative mutation, and siRNA that targets both wild-type and mutant *EGFR* had minimal effect on the viability of cells expressing only wild-type receptor but induced rapid cell death in lines expressing *EGFR* mutants (Fig. 3B). The ability of siRNAs to specifically target the corresponding *EGFR* alleles was confirmed in transfected COS7 cells by immunoblotting (fig. S5). Thus, expression of mutant EGFRs appears essential for suppression of pro-apoptotic signals in lung cancers harboring these mutations. The fact that lung cancer cells expressing only wild-type receptors do not display a similar dependence on EGFR expression may also account for the relative gefitinib-insensitivity of human tumors that overexpress wild-type EGFR.

The effectiveness of gefitinib in lung cancers harboring mutant EGFRs may reflect both its inhibition of critical anti-apoptotic pathways on which these cells have become strictly dependent as well as altered biochemical properties of the mutant receptors. We previously reported that mutant EGFRs are more sensitive to gefitinib inhibition of EGF-dependent autophosphorylation than wild-type receptors (*8*). This increased drug sensitivity by mutant receptors was also observed for both Erk and STAT5 activation (Fig. 3D). Thus, although EGF-induced signaling by mutant receptors demonstrates selective activation of downstream effectors via differential autophosphorylation events, their enhanced inhibition by gefitinib is uniform and may reflect altered drug binding to the mutant ATP pocket.

To establish the relevance of increased Akt and STAT signaling in EGFR-mediated NSCLC survival, we targeted these pathways with specific pharmacological inhibitors. Lung cancer cells harboring *EGFR* mutations were 100-fold more sensitive to gefitinib than cells with wild-type receptor (Fig. 4A). Cells expressing mutant EGFRs were also more sensitive to pharmacological inhibition of Akt or STAT signaling than cells expressing only wild-type EGFR (Fig. 4, B and C). Although EGFR-mutant lung cancer cells exhibited increased sensitivity to disruption of Akt- and STAT-mediated anti-apoptotic signals, they demonstrated markedly increased resistance to cell death signals induced by the commonly used chemotherapeutic agents doxorubicin and cisplatin and the pro-apoptotic Fas ligand (Fig. 4, D to F). Enhanced Akt and STAT signaling in cells with mutant EGFR might therefore provide an additional therapeutic target and raises the possibility that conventional chemotherapy may be less effective against these tumors.

"Oncogene addiction" has been proposed to explain the apoptosis of cancer cells after suppression of a proliferative signal on which they have become dependent (*18*). Interestingly, imatinib mesylate (Gleevec, Novartis)

efficiently triggers cell death in chronic myeloid leukemias expressing the BCR-ABL translocation product and in gastrointestinal stromal tumors expressing activating c-Kit mutations, both of which frequently exhibit constitutive STAT activation that is effectively inhibited by the drug (*19*, *20*). Similarly, in lung cancer cells with EGFR kinase mutations, gefitinib responsiveness may result in large part from its effective inhibition of essential anti-apoptotic signals transduced by the mutant receptor.

References and Notes

1. R. N. Jorissen *et al.*, *Exp. Cell Res.* **284**, 31 (2003).
2. H. S. Earp, T. L. Dawson, X. Li, H. Yu, *Breast Cancer Res. Treat.* **35**, 115 (1995).
3. A. E. Wakeling *et al.*, *Cancer Res.* **62**, 5749 (2002).
4. J. Baselga *et al.*, *J. Clin. Oncol.* **20**, 4292 (2002).
5. M. Fukuoka *et al.*, *J. Clin. Oncol.* **21**, 2237 (2003).
6. G. Giaccone *et al.*, *J. Clin. Oncol.* **22**, 777 (2004).
7. M. G. Kris *et al.*, *JAMA* **290**, 2149 (2003).
8. T. J. Lynch *et al.*, *N. Engl. J. Med.* **350**, 2129 (2004).
9. J. G. Paez *et al.*, *Science* **304**, 1497 (2004).
10. Materials and methods are available as supporting material on *Science* Online.
11. R. Sordella *et al.*, unpublished data.
12. S. Grant, L. Qiao, P. Dent, *Front. Biosci.* **7**, d376 (2002).
13. F. Chang *et al.*, *Leukemia* **17**, 1263 (2003).
14. F. Chang *et al.*, *Leukemia* **17**, 590 (2003).
15. F. Chang *et al.*, *Int. J. Oncol.* **22**, 469 (2003).
16. V. Calo *et al.*, *J. Cell. Physiol.* **197**, 157 (2003).
17. T. J. Ahonen *et al.*, *J. Biol. Chem.* **278**, 27287 (2003).
18. I. B. Weinstein, *Science* **297**, 63 (2002).
19. T. Kindler *et al.*, *Leukemia* **17**, 999 (2003).
20. G. P. Paner *et al.*, *Anticancer Res.* **23**, 2253 (2003).

21. We thank P. Harris for technical assistance, T. Lynch and members of the Haber and Settleman laboratories for helpful discussions, and M. Betson for critical comments on the manuscript. This work was supported by grants from the Sandler Family Foundation (to D.A.H. and D.W.B.), NIH (PO1 95281 to D.A.H. and D.W.B.), the Doris Duke Charitable Foundation (to D.A.H.), the Samuel Waxman Cancer Research Foundation (to J.S.), and the Saltonstall Scholarship (to J.S.).

Supporting Online Material

www.sciencemag.org/cgi/content/full/1101637/DC1
Materials and Methods
Figs. S1 to S5

18 June 2004; accepted 19 July 2004
Published online 29 July 2004;
10.1126/science.1101637
Include this information when citing this paper.

New Products

Leica
For more information
847-405-7026
www.leica-microsystems.com
www.scienceproductlink.org

Fluorescence Microscope System

The Leica TCS 4Pi fluorescence microscope system represents a leap in resolution in commercial three-dimensional (3D) fluorescence microscopy and opens up new dimensions for research in cell and developmental biology. 4Pi microscopy makes use of a special phase-corrected and wavefront-corrected, double-objective imaging system linked to a confocal scanner to enable a fourfold to sevenfold increase in axial resolution compared with confocal and two-photon microscopy. Even in live specimens, axial sections of about 100 nm can be obtained. The system maintains all of the advantages of fast scanning.

Pierce
For more information
800-874-3723
www.piercenet.com
www.scienceproductlink.org

Biotin Label Transfer Kit

The ProFound Sulfo-SBED Biotin Label Transfer Kit for Western Blot Applications provides researchers performing protein:protein interaction studies with an in vitro method of discovering new interactions or confirming data from co-immunoprecipitation, pull-down, or yeast two-hybrid experiments. The label transfer method has emerged as a powerful new tool in protein interaction analysis because of its ability to capture weakly or transiently integrating systems.

Berthold Technologies
For more information
+49 7081 177 128
www.bertholdtech.com
www.scienceproductlink.org

Multimode Reader

Mithras is a versatile multimode microtiter plate reader that can read absorbance, luminescence, fluorescence (top and bottom), fluorescence polarization, AlphaScreen, FRET (fluorescence resonance energy transfer), and BRET (bioluminescence resonance energy transfer). The Mithras LB 940 operates with dedicated optical paths to ensure the best available performance in each technology. The unit's software supports a multitude of functions, including standard curves and kinetic data reduction. For medium-throughput environments such as assay development or secondary screening, the instrument can be equipped with a stacker.

Eastman Kodak
For more information
877-SIS-HELP
www.kodak.com
www.scienceproductlink.org

Digital Imaging of Multiple Fluorochromes

A new digital imaging system enables high-sensitivity detection of one or more fluorochromes in Western blotting assays. The Kodak Image Station 2000MM Multimodal Imaging System features selectable, multi-wavelength illumination allowing for specific excitation and differential detection of multiple fluorochromes in gene expression assays such as Western blots. With this system, a Western blot can be probed with multiple antibodies simultaneously, improving throughput compared with stripping and re-probing blots in a serial fashion. The system's software allows images to be pseudocolored and overlayed to view both simultaneously. The instrument offers quantitative imaging of luminescent-, fluorescent-, radiographic-, and colorimetric-labeled biomolecules in a variety of common assay formats, including membranes, electrophoresis gels, plates, tissues, and in vivo assays. With true 14-bit imaging performance, mega-pixel resolution, a 10× optical zoom, and comprehensive image analysis capability, the IS2000MM produces high-performance molecular imaging results for the widest range of sample formats on one easy-to-use imaging platform.

Sigma-Aldrich
For more information
800-521-8956
www.sigma-aldrich.com
www.scienceproductlink.org

Custom Peptide Library Technology

The PEPscreen peptide synthesis platform allows high-throughput synthesis of custom peptide libraries (6 to 20 amino acids) comprising thousands of peptides at 70% purity. Higher purity is available on request. Peptides are synthesized in quantities from 0.5 to 2 mg in which 100% of the peptides are analyzed by matrix-assisted laser-desorption ionization–time-of-flight mass spectrometry. The platform allows peptide libraries to be synthesized, analyzed, and delivered in less than seven days. The peptide libraries can be used in diverse applications such as epitope mapping, interaction profiling, substrate specificity profiling, vaccine development, immunogen detection, peptide microarray production, protein–protein or receptor–ligand interactions, and alanine scans.

Molecular Research Center
For more information
888-841-0900
www.mrcgene.com
www.scienceproductlink.org

TRI Reagent

TRI Reagent is a reliable, cost-effective, and efficient method for RNA isolation or for the simultaneous isolation of RNA, DNA, and protein from a single biological sample. TRI Reagent now comes with an improved protein extraction protocol that significantly reduces the time required for protein recovery, provides a more manageable protein pellet, and improves total protein recovery. It allows comprehensive analysis of gene expression in a variety of cell and tissue samples.

Millipore
For more information
800-MILLIPORE
www.millipore.com
www.scienceproductlink.org

Literature

Protein Blotting Handbook contains optimized protocols for all of the essential protein blotting techniques, including Western, dot, slot, and immunoblotting. This third edition contains additional protocols, a new troubleshooting section, and photographs of sample blots. The handbook also has a review of new methods such as matrix-assisted laser desorption ionization–time-of-flight analysis of blotted proteins.

Newly offered instrumentation, apparatus, and laboratory materials of interest to researchers in all disciplines in academic, industrial, and government organizations are featured in this space. Emphasis is given to purpose, chief characteristics, and availability of products and materials. Endorsement by *Science* or AAAS of any products or materials mentioned is not implied. Additional information may be obtained from the manufacturer or supplier by visiting www.scienceproductlink.org on the Web, where you can request that the information be sent to you by e-mail, fax, mail, or telephone.

Published by AAAS